

# Three-dimensional Elastodynamic Modeling of Frictional Sliding with Application to Inter-sonic Transition

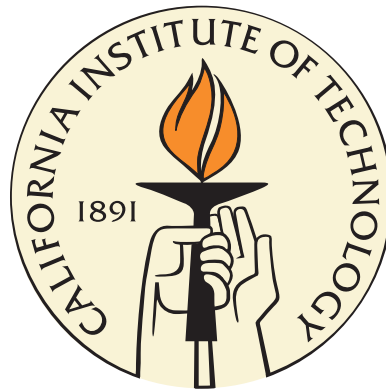
Thesis by

Yi Liu

In Partial Fulfillment of the Requirements

for the Degree of

Doctor of Philosophy



California Institute of Technology

Pasadena, California

2009

(Defended September 22, 2008)

© 2009

Yi Liu

All Rights Reserved

# Acknowledgements

I have been exceptionally fortunate to have spent my time as a graduate student working with a number of colleagues who were not only great scientists, but wonderful and interesting people. Now the time has finally come to express my thanks to them.

First and foremost, I would like to express my sincere gratitude to my thesis advisor, Professor Nadia Lapusta, for her guidance, inspiration, and support over years. Nadia introduced me to the field of earthquake mechanics and pointed out interesting problems in this area of research. Nadia's patience is remarkable: she is always willing to spend hours with me going through research problems, and help me see connections between seemingly unrelated results and make everything fit together. She has always supported and encouraged me. This thesis would not have been possible without her crucial contribution and insights.

I would like to thank all other members of my committee, Profs. Jean-Philippe Avouac, Kaushik Bhattacharya, Thomas H. Heaton, Ares J. Rosakis, and Guruswami Ravichandran for reviewing my thesis and providing valuable suggestions/criticism. Profs. Bhattacharya and Ravichandran have given me constant support during my study at Caltech and valuable suggestions for my future career development.

My sincere appreciation extends to my colleagues in Nadia's group. Frequent discussions with Yoshihiro Kaneko helped me understand many key concepts about geophysics and inspired me with many scientific ideas. Xiao Lu has been a good friend of mine since college, and he helped me a

lot with computer software and hardware. It was very pleasant to work with Ting Chen and Ajay Harish about numerical algorithms.

I am also indebted to my former advisors Profs. Wei Yang and Keqin Zhu at Tsinghua University. The course Elasticity, taught by Prof. Yang, ignited my initial interest in solid mechanics. Prof. Zhu supervised my undergraduate thesis, which later became my first published scientific paper. It was his encouragement that made me determined to pursue graduate study abroad.

I sincerely appreciate the help and friendship of Xin Guo, Lin Zhu, Zhiyi Li, Fei Wang, Chunhui Gu, Xiaobai Li, Xiaosong Niu, Ke Wang, Jing Yang, Wei Liang, Li Liu, Jie Chen, Yue Yang, Changling Pang, Tao Liu, Lin Shi, Yue Zhou, Vikram Gavini, Tamer Elsayed, Kook Oh Chang, and many others. They have made my life at Caltech more exciting and wonderful.

My final thanks are reserved for my family. I thank my parents and sister for their love and care. I want to thank my lovely wife, Dr. Ling Zheng. It is her love, friendship, and support that made this work possible, and I will always be grateful for that. With her, life becomes meaningful.

# Abstract

Spontaneous slip on frictional interfaces involves both short-lived inertially-driven events and long-term quasi-static sliding. An example of considerable practical importance is the response of faults in the Earth's crust to tectonic loading. The response combines earthquakes that cause destructive ground motions and aseismic slip. Numerical models are needed to study the physics and mechanics of such complex behavior. In part, the models can help understand the observed slip patterns and interpret them in terms of constitutive properties of rocks determined in the lab.

This thesis contains two main contributions. The first one is the development and implementation of a 3D methodology for simulations of spontaneous long-term interface slip punctuated by rapid inertially driven ruptures. Our approach is the first one to combine long-term deformation histories and the resulting stress redistribution on faults with full inclusion of inertial effects during simulated earthquakes in the context of 3D models. It reproduces all stages of earthquake cycles, from accelerating slip before dynamic instability, to rapid inertially driven propagation of earthquake rupture, to post-seismic slip, and to interseismic creep, including aseismic transients. The second main contribution is the discovery of the potentially dominating effect of favorable heterogeneity on intersonic transition in earthquakes, in both 2D models of single dynamic ruptures and 3D models of long-term fault slip. Studies of intersonic ruptures are practically important as they have the potential to cause strong ground motion farther from the fault than subsonic ruptures. Our conclusion that rheological boundaries promote transition to intersonic speeds in 3D rupture models is completely unexpected, as the neighboring stably slipping regions inhibit fast, inertially driven slip. The result could not be established in earlier studies, as it requires the computational methodology developed here that combines inertial effects, long-term slip histories, and 3D fault models.

The thesis also develops test problems for dynamic rupture propagation and evaluates simplified quasi-dynamic approaches.

The obtained results emphasize that dynamic ruptures should be considered in the context of the entire slip history of the fault, as such approach allows dynamic ruptures to occur under stress conditions established by prior slip, which leads to characteristic stress distributions that are not considered in single-event simulations. The developed 3D methodology can be applied to a number of problems in earthquake physics and mechanics that involve interaction of seismic and aseismic slip.

# Contents

<b>Acknowledgements</b>	<b>iii</b>
<b>Abstract</b>	<b>v</b>
<b>Contents</b>	<b>vii</b>
<b>List of Figures</b>	<b>xi</b>
<b>List of Tables</b>	<b>xxv</b>
<b>1 Introduction</b>	<b>1</b>
<b>2 Modeling 3D spontaneous rupture with boundary integral method</b>	<b>10</b>
2.1 Problem formulation . . . . .	10
2.2 3D boundary integral method . . . . .	12
2.3 Test problem . . . . .	16
2.4 Cohesive zone and constraints on discretization . . . . .	17
2.5 Comparison of numerical results . . . . .	24
2.5.1 Grid dependence of solutions . . . . .	24
2.6 Comparison of high-resolution solutions . . . . .	29
2.7 Discussion . . . . .	31
2.7.1 Resolution criterion . . . . .	31
2.7.2 Scale collapse . . . . .	32
2.7.3 Computational resources required and associated parameter limitations . . . . .	33

2.7.4	Significance of BI/DFM agreement . . . . .	34
2.8	Extension to bimaterial fault interface . . . . .	35
2.9	Conclusion . . . . .	36
2.10	Appendix: closed-form expression for kernels used for bimaterial faults . . . . .	37
<b>3</b>	<b>3D modeling of spontaneous earthquake sequences and aseismic slip</b>	<b>39</b>
3.1	Methodology . . . . .	39
3.1.1	Truncation of elastodynamic response . . . . .	40
3.1.2	Fault constitutive response: rate and state friction laws . . . . .	42
3.1.3	Criteria for spatial discretization . . . . .	45
3.1.4	Computational procedure . . . . .	46
3.1.5	Model of a strike-slip fault . . . . .	47
3.2	Simulation example: fault with a homogeneous seismogenic region . . . . .	48
3.2.1	Parameters of the fault model . . . . .	48
3.2.2	Fault response: dynamic events and aseismic slip, including transients . . . . .	51
3.2.3	Parameters of simulated earthquakes . . . . .	52
3.2.4	Effect of parameter distributions near the free surface . . . . .	57
3.3	Parameter validation . . . . .	59
3.3.1	Spatial discretization . . . . .	59
3.3.2	Frequency-independent truncation . . . . .	61
3.3.3	Frequency-dependent truncation . . . . .	61
3.4	Long-term interaction of slip with compact heterogeneity . . . . .	62
3.4.1	Supershear burst in the first event . . . . .	62
3.4.2	No supershear burst in subsequent events . . . . .	64
3.4.3	Effect of heterogeneity on long-term behavior . . . . .	65
3.4.4	Fault interaction with heterogeneity of higher normal stress . . . . .	65
3.5	Comparison of fully dynamic and quasi-dynamic approaches . . . . .	66
3.5.1	Generalized quasi-dynamic formulation . . . . .	68

3.5.2	Similarity of quasi-dynamic solutions and their differences with fully dynamic results . . . . .	70
3.5.3	Cohesive zone size and numerical resolution in quasi-dynamic simulations . .	72
3.6	Conclusions . . . . .	73
3.7	Appendix . . . . .	75
3.7.1	Convolution kernels . . . . .	75
3.7.2	Updating field variables . . . . .	77
<b>4</b>	<b>Transition of mode II cracks from sub-Rayleigh to intersonic speeds in the presence of favorable heterogeneity</b>	<b>81</b>
4.1	Burridge-Andrews mechanism on homogeneous fault . . . . .	81
4.2	Methodology . . . . .	84
4.3	Advancing main rupture towards a pre-existing subcritical crack: An example of abrupt sub-Rayleigh-to-intersonic transition . . . . .	87
4.4	Advancing main crack towards a patch of higher prestress: dependence on patch size, prestress, and location . . . . .	91
4.5	Conclusions and discussion . . . . .	101
4.5.1	Abrupt change of crack tip speeds . . . . .	102
4.5.2	Prestress levels for intersonic transition and propagation . . . . .	103
4.5.3	Transition distance . . . . .	104
4.5.4	Importance of crack initiation procedure . . . . .	104
4.5.5	Propagation speeds in the intersonic regime . . . . .	106
4.5.6	Implications for earthquake dynamics . . . . .	106
4.6	Appendix . . . . .	107
4.6.1	Interonic loading field due to an accelerating sub-Rayleigh mode II crack . .	107
4.6.2	Expressions for stress transfer functional in the spectral boundary integral method . . . . .	109
4.6.3	Some aspects of crack tip behavior during abrupt intersonic transition . . . .	111

<b>5</b>	<b>Intersonic rupture in 3D simulations of earthquake sequences and aseismic slip: effect of rheological boundaries and weaker patches</b>	<b>113</b>
5.1	Fault model . . . . .	114
5.2	Connection between rate and state friction and linear slip-weakening friction during dynamic rupture . . . . .	118
5.3	Intersonic transition due to rheological boundaries for Case I of a homogeneous seis- mogenic region . . . . .	122
5.3.1	Effects of stress concentration at rheological boundaries on intersonic transition	126
5.4	Intersonic transition due to favorable compact heterogeneity . . . . .	130
5.4.1	Weaker patch as favorable heterogeneity for intersonic transition . . . . .	133
5.4.2	Initiation of secondary cracks in the weaker patch by an intersonic loading field	135
5.4.3	Influence of the location of the weaker patch . . . . .	138
5.5	Discussion . . . . .	139
5.5.1	Influence of seismic ratio $\bar{S}$ on rupture behavior . . . . .	139
5.5.2	Distribution of seismic ratio over seismogenic region . . . . .	141
5.5.3	Significance of rheological boundaries for rupture dynamics . . . . .	143
5.5.4	Effect of weaker patches on earthquake sequences . . . . .	144
5.5.5	Effect of rupture speed on slip distribution . . . . .	145
5.5.6	On friction behavior during dynamic rupture . . . . .	146
5.6	Conclusion . . . . .	147
5.7	Appendix: calculation of horizontal rupture speed $c(x, z)$ . . . . .	148
<b>6</b>	<b>Conclusions and future work</b>	<b>150</b>
	<b>Bibliography</b>	<b>153</b>

# List of Figures

- 1.1 An example of interaction between earthquakes and aseismic quasi-static slip. Earthquakes redistribute stress on faults, causing slow postseismic slip or afterslip in surrounding areas, as shown here on the example of 2005 Nias-Simeulue earthquake in Sumatra (from Hsu et al., 2006). The postseismic slip, in turn, redistributes stress and may trigger other seismic events. The figure shows compilation of inferred seismic and postseismic slip, illustrating the approximately complimentary nature of seismogenic and aseismic regions. Distribution of seismic slip is indicated by white contours at intervals of 2 m; color indicates cumulative postseismic slip during the 9 months after the earthquake. Black and red vectors indicate GPS observations and their match using the inferred postseismic slip, respectively. White and red stars are epicenters of 2004 Aceh-Andaman and 2005 Nias-Simeulue earthquakes, respectively. Pink and green dots denote earthquakes with body wave magnitude  $m_b > 4.5$  before and after the 2005 event. The regions of high seismicity correspond to the transition between regions of seismic and aseismic slip. The question mark indicates the region where afterslip may have occurred but it is not detectable by the existing GPS network. White tick marks on the northern and southern boundaries of the postseismic slip model indicate depths along the megathrust. . . . . 3

1.2	An example of inferred intersonic propagation in a large strike-slip earthquake. The 2002 Denali (Alaska) earthquake produced a surface rupture of about 340 km (dark blue line). Modeling of near-fault accelerometer records suggests that the rupture in a segment of about 40 km (red line) may have propagated with intersonic speeds, with an average speed of 5.3 km/s (Ellsworth et al., 2004). . . . .	5
2.1	(a) A planar fault interface ( $y = 0$ ) is embedded in an infinite uniform elastic medium. (b) On the fault interface, the square in the center is the nucleation area. The triangles are the receivers at which we compare time-histories of slip, slip rate, and shear stress. Relative to an origin at the center of the fault, the receiver PI has $z$ coordinate 0 km and $x$ coordinate 7.5 km, and the receiver PA has $x$ coordinate 0 km and $z$ coordinate 6.0 km. The stress parameters are specified in Table 2.1. . . . .	12
2.2	Cohesive zone during rupture, along both in-plane and anti-plane directions, for BI0.1 (dashed curve), DFM0.1 (dash-dotted curve), and DFM0.05 (solid curve) solutions . . .	23
2.3	Differences in time of rupture, relative to reference solution, shown as a function of grid interval $\Delta x$ . Differences are RMS averages over the fault plane. Open circles are BI solutions, relative to BI0.1 (the smallest grid-interval BI case). Solid circles are DFM solutions, relative to DFM0.05 (the smallest grid-interval DFM case). The dashed lines show the (approximate) dependence of time step $\Delta t$ on $\Delta x$ . The upper axis characterizes the calculations by their characteristic $\bar{N}_c$ values, where $\bar{N}_c$ is median cohesive zone width in the in-plane direction divided by $\Delta x$ . Note the power-law convergence of both methods as the grid size is reduced. The 90% confidence intervals on the power-law exponents suggested by the regression lines are: BI [2.44–3.04]; DFM [2.77–3.15], indicating approximately equal convergence rates for the two methods. . .	25

2.4	Differences in final slip (diamonds) and peak slip velocity (circles), relative to reference solution, shown as a function of grid interval $\Delta x$ . Differences are RMS averages over the $x$ and $z$ axes of the fault plane. Open symbols are BI solutions, relative to BI0.1 (the smallest grid-interval BI case). Solid symbols are DFM solutions, relative to DFM0.05 (the smallest grid-interval DFM case). Note the power-law convergence of both methods as the grid size is reduced. The 90% confidence intervals on the power-law exponents suggested by the regression lines are: BI displacement [1.07–1.99]; DFM displacement [1.31–1.84]; BI velocity [1.04–1.33]; DFM velocity [1.02–1.33]. Outliers at $\Delta x = 0.2$ km and 0.6 km were not used in estimating the BI displacement slope. . . .	27
2.5	Contour plot of the rupture front for the dynamic rupture test problem. Solid curves are for DFM0.05 (grid size $\Delta x = 0.05$ km); dotted curves are for DFM0.1 (grid size $\Delta x = 0.1$ km); dashed curves are for BI0.1 (grid size $\Delta x = 0.1$ km). . . . .	28
2.6	Time histories at the two fault-plane points marked in Figure 2.1. PI is on the in-plane ( $x$ ) axis, and PA is on the anti-plane ( $z$ ) axis. Shear stress, slip, and slip velocity are shown for solutions DFM0.05, DFM0.1, and BI0.1. The time histories of BI0.1 and DFM0.05 are virtually identical, with DFM0.1 also very close. . . . .	30
2.7	A planar fault separating materials of different elastic properties. Some theories and numerical simulations suggest that there is a preferred rupture propagation direction along bimaterial fault (Weertman, 1980; Adams, 1995; Shi and Ben-Zion, 2006). . . .	35
2.8	Contour plot of the rupture time on the bimaterial fault for the Southern California Earthquake Center (SCEC) Code Validation Project Problem, Version 7. Red curves are for BI method, and black curves are for DFM method. Contour lines are plotted every 0.5 seconds. Rupture propagation along horizontal direction is asymmetric due to different material properties across the fault. . . . .	36

- 3.1 (a) A model of a planar interface embedded in an infinite and homogeneous elastic medium. (b) A vertical strike-slip fault in an elastic half-space. The top part of the fault is governed by rate and state friction, and the bottom part is steadily moving due to tectonic loading. . . . . 40
- 3.2 Properties of the simulated fault segment. (a) Rate and state friction acts on the top 24 km of the fault. A potentially seismogenic region of velocity-weakening properties (shown in white) is surrounded by velocity-strengthening regions (shown in yellow). Below  $z = -24$  km, steady motion of 32 mm/year is imposed. (b) Depth dependence of friction parameters  $(a - b)$ ,  $a$ , and  $L$  in the seismogenic region. The distributions are piecewise linear between the following points:  $(a - b)|_{z=0} = 0.008$ ,  $(a - b)|_{z=4} = -0.004$ ,  $(a - b)|_{z=13.5} = -0.004$ ,  $(a - b)|_{z=17.5} = 0.015$ ,  $(a - b)|_{z=24} = 0.024$ ,  $a|_{z=0} = 0.019$ ,  $a|_{z=4} = 0.015$ ,  $a|_{z=17.5} = 0.015$ ,  $a|_{z=24} = 0.024$ ,  $L|_{z=0} = 24$  mm,  $L|_{z=4} = 8$  mm,  $L|_{z=24} = 8$  mm. . . . . 43
- 3.3 Long-term histories of slip and slip velocity history at two representative fault locations, P1 from the velocity-weakening region and P2 from the velocity-strengthening region. Slip velocity is plotted on the logarithmic scale. (a),(c) Point P1 (9 km,-8 km) exhibits stick-slip behavior. It is virtually locked for most of the time (with slip velocity three orders of magnitude below the plate rate) but occasionally slips very fast, with maximum slip velocity on the order of 1 m/s. (b),(d) Point P2 (-18 km,-8 km) moves throughout the simulated time. After each dynamic event, it has postseismic slip, with maximum slip velocity on the order of  $10^{-6}$  m/s. . . . . 49

- 3.4 Snapshots of spatial slip-velocity distribution during a typical earthquake cycle for  $L = 8$  mm ( $h^*/W_{\text{seis}} = 0.8$ ). Slip history between the 9th and 10th events is illustrated. Colors represent slip velocity on the logarithmic scale. White and bright yellow correspond to seismic slip rates, orange and red correspond to aseismic slip, and black corresponds to locked portions of the fault. Each panel shows the time  $t$  of the snapshot in years (in the upper-right corner) and the corresponding time step  $\Delta t$  in seconds (at the bottom of each panel). Panels A–C also show the time in seconds elapsed since the time of panel A. The simulations reproduce dynamic events (panels A–C and K–L), postseismic slip (panels D–E), and the interseismic period (panel F). Aseismic transient slip occurs between panels F and J and it is shown in panels G8–I8 of Figure 3.6 on a different slip-velocity scale. . . . . 53
- 3.5 Snapshots of spatial slip-velocity distribution during a typical earthquake cycle for  $L = 4$  mm ( $h^*/W_{\text{seis}} = 0.4$ ). Slip history between the 2nd and 3d events is illustrated. Colors and time markings have the same meaning as in Figure 3.4. Compared with the case with  $L = 8$  mm (Figure 3.4), dynamic events in the case with  $L = 4$  mm have smaller nucleation size, nucleate closer to the rheological transition (panels A, L), have more unilateral propagation, and develop faster rupture speeds (panels A–C). Consistent with the smaller value of  $h^*/W_{\text{seis}}$ , the velocity-weakening region experiences less aseismic slip, with large portion of the region still locked when a seismic event nucleates (panels A, J–L). Smaller aseismic transients still occur between panels F and J; they are shown in panels G4–I4 of Figure 3.6. . . . . 54

- 3.6 Snapshots of spatial slip-velocity distribution illustrating aseismic transients. White dashed rectangles show the extent of the velocity-weakening region. Panels G8–I8 correspond to the simulation with  $L = 8$  mm. The aseismic transient travels around the locked portion of the fault. The average rupture speed between panels G8 and I8 is about 10 km/s and the maximum slip velocity is about  $10^{-7}$  m/s. The aseismic slip accumulated in the seismogenic region is equivalent to that of a  $M_w = 5.8$  earthquake. Panels G4–I4 correspond to the simulation with  $L = 4$  mm. The spatial extent of the transients is smaller. Again, the transients travel around the locked portion of the fault. Comparison of the two cases shows that the transients are confined to the band of the velocity-weakening region next to rheological transition which experiences slow slip in the interseismic period. The width of the band scales with the nucleation size and its estimate  $h^*$ . That is why smaller values of  $h^*/W_{\text{seis}}$  lead to smaller and more localized aseismic transients. . . . . 55
- 3.7 Slip accumulation along the line  $z = -8$  km for the case of the homogeneous seismogenic region. Red dashed lines illustrate fast slip; they are plotted every 2 s when maximum slip velocity over the fault exceeds 1 mm/s. Green solid lines are plotted every 5 years, representing slip accumulation in interseismic periods. (a) The case with  $L = 8$  mm settles into a periodic two-event pattern. (b) The case with  $L = 4$  mm results in periodic events. In the latter case, dynamic ruptures propagate faster and are more pulse-like. In both cases, points at the nucleation zones accumulate less slip seismically than points elsewhere on the fault. . . . . 56

3.8 Shear stress as a function of slip during a representative dynamic event (the 9th one in the sequence) for four locations on the fault with (a)  $L = 8$  mm and (b)  $L = 4$  mm. In both cases, dynamic rupture propagates from the left side of the fault to the right side, passing the velocity-weakening locations (-3 km, -8 km), (3 km, -8 km), (9 km, -8 km), and then influencing the velocity-strengthening location (18 km, -8 km) as the rupture arrests in the velocity-strengthening region. Zero slip for each point is chosen as the slip when shear stress at the point reaches its peak during the dynamic event. We see that the effective dependence of stress on slip is similar to linear slip-weakening friction, with the slip-weakening rate  $W \approx \sigma b/L$ . The velocity-strengthening point has a smaller values of  $b$  than the other three points and hence a smaller slope. In the case with  $L = 8$  mm, rupture accelerates while propagating through the points shown (Figure 3.7a), leading to different effective peak strength and slip-weakening distances for the three velocity-weakening points. In the case with  $L = 4$  mm, the rupture has nearly reached its limiting speed and it is almost steady (Figure 3.7b), leading to similar behavior of the velocity-weakening points. . . . . 58

3.9 Accumulation of slip along the line  $x = 3$  km, for the fault with the homogenous seismogenic region and the case of  $L = 8$  mm. Lines have the same meaning as in Figure 3.7. Different near-surface parameter distributions are explored. (a) In the case of Section 3.2.1–3.2.2 and Figures 3.3–3.8 with constant normal stress and depth-dependent  $L$ , dynamic events do not reach the free surface, arresting in the velocity-strengthening region. The free surface accumulates large slip deficit, which is compensated by aseismic slip. (b) For depth-independent  $L$  and normal stress decreasing towards the free surface (the same distributions as in the 2D model of Lapusta et al. (2000)), dynamic ruptures propagate all the way to the free surface, consistently with the results of Lapusta et al. (2000). (c) When distributions of parameters  $a$  and  $b$  in the case of panel (b) are modified to match the distributions of  $\sigma a$  and  $\sigma b$  of the case in panel (a), the near-surface behavior becomes very similar to the case of panel (a). . . . . 58

- 3.10 Fully dynamic simulations with different cell sizes  $\Delta x$ . (a),(b) Slip accumulation along the line  $z = -8$  km for  $\Delta x = 50$  m and 400 m, respectively. The results can be compared with Figure 3.7a that shows slip accumulation for  $\Delta x = 100$  m. (c) Slip-velocity history of the fault location (9 km,  $-8$  km) during the 5th event for  $\Delta x = 50$  m, 100 m, 200 m, and 400 m. Zero in time corresponds to rupture arrival at the location (6 km,  $-8$  km). The values  $\Delta x = 50$  m and 100 m are both several times smaller than the quasi-static cohesive zone size  $\Lambda_0 = 300$  m and produce resolution-independent results.  $\Delta x = 200$  m provides less adequate resolution and  $\Delta x = 400$  m leads to very different results. The numerical resolution in our simulations is dictated by the cohesive zone size, as the nucleation size  $h^*$ , another important length scale, is several times larger. . . . . 59
- 3.11 Fully dynamic simulations with different values of the truncation parameter  $\alpha$ . (a),(b) Slip accumulation along the line  $z = -8$  km for  $\alpha = 2$  and  $1/3$ , respectively. The results can be compared with Figure 3.7a that shows slip accumulation for  $\alpha = 3/2$ . (c) Slip-velocity history of the fault location (12 km,  $-8$  km) during the 5th event for  $\alpha = 1/3, 1/2, 3/2, 1$ , and 2. Zero in time corresponds to rupture arrival at the location (6 km,  $-8$  km). Larger values of  $\alpha$  lead to inclusion of longer slip histories in the dynamic response calculation.  $\alpha = 2, 3/2$ , and 1 produce similar results, while  $\alpha = 1/2$  and  $1/3$  cause differences as discussed in the text. . . . . 60
- 3.12 Slip-velocity history of the fault location (12 km,  $-8$  km) during the first event in fully dynamic simulations with different values of the truncation parameter  $\rho_c$ . Zero in time corresponds to the rupture arrival at the location (3 km,  $-8$  km). Larger values of  $\rho_c$  make the frequency-dependent truncation closer to the frequency-independent one. Our frequency-dependent truncation with  $\rho_c = 3\pi/2$  approximately corresponds to the truncation parameters in Lapusta et al. (2000).  $\rho_c \geq 100$  produce the same results as the frequency-independent truncation. . . . . 61

- 3.13 Snapshots of slip-velocity distribution during the first (top row) and second (bottom row) events for the case with a stronger patch. The slip-velocity range shown is different from Figures 3.4–3.6 and chosen to emphasize the rupture front. The number in the upper-right corner of each snapshot indicates the elapsed time (in seconds) since the first snapshot for each event. During the first event, dynamic rupture interacts with the stronger patch and produces a supershear burst. During the second event, no interaction or supershear propagation occurs; the stronger patch is indicated by a red circle in this case. Rupture behavior of the first event does not repeat in the slip history of the fault due to redistribution of shear stress. . . . . 63
- 3.14 Distribution of shear stress along the line  $z = -8$  km during the 1st and 2nd events, at the time when the horizontal rupture front (at this depth) arrives approximately at the center of the fault ( $x = 0$  km). In the 1st event, the patch has similar shear stress  $\tau$  as the surrounding area but 20% larger normal stress  $\sigma$ , resulting in smaller nondimensional prestress  $\tau/\sigma$  than the rest of the fault. However, in the second event,  $\tau$  inside the patch is about 20% larger than in the surrounding area, resulting in homogeneous nondimensional prestress  $\tau/\sigma$ . This redistribution of shear stress due to prior slip history eliminates the interaction of dynamic rupture with the patch observed in the first event. . . . . 65
- 3.15 Snapshots of slip velocity during the first three events for  $\sigma_h = 1.4\sigma$ ,  $1.6\sigma$ , and  $2.0\sigma$ . Black circles are plotted to indicate the location of the heterogeneity. Due to redistribution of shear stress with slip, the interaction of dynamic rupture with heterogeneity becomes insignificant after the first three events. . . . . 67
- 3.16 Earthquake recurrence period  $T$  for different heterogeneity strengths  $\sigma_h$ . Higher normal stress inside the patch increases the shear stress drop in dynamic events, and thus tends to increase  $T$ . On the other hand, higher normal stress decreases the earthquake nucleation size, and thus facilitates earthquake occurrence. . . . . 68

- 3.17 Accumulation of slip along the line  $z = -8$  km for the case with a stronger patch. Lines have the same meaning as in Figure 3.7. (a) Results for the fully dynamic simulation. The slip pattern of the fault with a small stronger patch (which occupies less than 1% of the seismogenic area) is different from the one with the homogeneous seismogenic region (Figure 3.7a). (b) The standard quasi-dynamic formulation ( $\beta_s = 1$ ) results in a modified slip pattern, smaller slip velocity, slower rupture speeds, and smaller slip per event. (c),(d) Larger values of  $\beta_s = 1$  or smaller radiation terms in the quasi-dynamic formulation accelerate rupture speed and increase slip velocity. However, all quasi-dynamic simulations produce similar slip patterns that are qualitatively different from the fully-dynamic one. . . . . 69
- 3.18 Comparison of fully dynamic and quasi-dynamic simulations of one dynamic event (the first event in the sequence). (a),(b) Slip-velocity and slip histories of the fault location (9 km, -8 km). Zero time corresponds to the time of rupture arrival at the point (6 km, -8 km). Slip velocity and slip per event in quasi-dynamic simulations is significantly smaller than in the fully-dynamic one. Simulations with larger  $\beta_s$  produce faster rupture speeds, larger slip velocity, and larger slip per event. However, when scaled appropriately, the quasi-dynamic results all collapse onto the same curves (insets in panels (a) and (b)). (c),(d) Rupture speed as a function of rupture tip location along  $z = -8$  km. The quasi-dynamic simulation with  $\beta_s = 4$  has larger rupture speeds than the fully-dynamic simulation. All quasi-dynamic simulations have nearly identical scaled rupture speed  $c/(\beta_s c_s)$ , as shown in panel (d). . . . . 70

- 3.19 Cohesive zones in quasi-dynamic simulations. (a) Shear stress distribution along the horizontal line  $z = -8$  km at the time of rupture front arrival at point  $(-7.9$  km,  $-8$  km) during the first event in the simulation with  $\beta_s = 1$ . Crosses indicate locations of spatial cells ( $\Delta x = 50$  m). The rupture speed at that time is 0.12 km/s. The cohesive zone size is 0.3 km. The bottom panel shows the accumulation of slip in that case, with the double arrow indicating the distance plotted in the main panel. (b) Shear stress distribution along the horizontal line  $z = -8$  km at the time of rupture front arrival at  $(0.24$  km,  $-8$  km) km during the first event in the simulation with  $\beta_s = 4$ . The rupture speed at that time is 2.45 km/s. Despite the different value of  $\beta_s$  and the different rupture speed, the cohesive zone size is still 0.3 km. In quasi-dynamic simulations, the cohesive zone size does not shrink during rupture propagation and its size is independent of the parameter  $\beta_s$ . . . . . 72
- 3.20 Elastodynamic kernels  $K_{III}(\rho)$  and  $K_{II}(\rho)$ . (a),(b) Values of the kernels for relatively small kernel arguments. (c),(d) Comparison of kernels with the leading terms in their asymptotic expansions. For  $\rho \gg 1$ ,  $K_{III}(\rho) \sim O(\rho^{-3/2})$  and  $K_{II}(\rho) \sim O(\rho^{-1/2})$ .  $K_{II}(\rho)$  decays much slower than  $K_{III}(\rho)$  as  $\rho$  increases. . . . . 75
- 4.1 (a) Linear slip-weakening friction law.  $\tau_c$  is the shear strength of the interface and  $\delta$  is slip (or relative displacement in shear) across the interface. (b) A prescribed crack interface is embedded in an infinite, elastic, and homogeneous space. The main crack is initiated from a region around  $x = 0$ . This work considers interaction of the main crack with a region of heterogeneity that exists in front of the main crack and may initiate a secondary crack. Depending on the model, the heterogeneity is a pre-existing subcritical crack, a patch with higher prestress, or a patch with lower peak friction strength. When discussing crack tips and their speeds for both main and secondary cracks, we always refer to crack tips that propagate in the direction of increasing  $x$ , or to the right in all figures, unless specified otherwise. . . . . 82

4.2 (a) Shear stress distribution for a mode II crack spontaneously propagating on an interface governed by linear slip-weakening friction. A peak in shear stress travels with the shear wave speed in front of the crack. The interface has uniform friction properties and uniform prestress  $\tau^o$  given by  $(\tau^o - \tau^d)/(\tau^s - \tau^d) = 0.53$ . (b) Rupture time along the interface, i.e., the time at which each point along the interface first acquires nonzero speeds. A daughter crack appears in front of the main crack at the location  $x/L^c = 13.5$  and propagates with intersonic speeds as described by the Burridge-Andrews mechanism. Here and in the text the word “intersonic” refers to speeds between the shear wave speed  $c_s$  and the dilatational wave speed  $c_p$ . For lower prestress, the daughter crack would appear further along the interface or not at all. . . . . 83

4.3 Stress distribution on the interface for different initiation procedures. To compare stress fields created by the main crack, no heterogeneity at  $\bar{x} = 12$  is imposed for these simulations. The more abrupt initiation procedure that results in a higher shear stress peak is discussed in Section 4.4. . . . . 88

4.4 Stress distribution around the main crack and pre-existing subcritical crack at  $\bar{t} = 0$  (solid green line). The main crack centered at  $\bar{x} = 0$  is poised to propagate spontaneously for  $t > 0$ , while the secondary crack centered at  $x = 12L^c$  remains a subcritical crack. Prestress outside of zones affected by cracks is equal to  $\bar{\tau}^o = 0.33$ .  $\bar{\tau}_{BA} = 0.53$  (black dashed line) is the prestress level required for intersonic transition at the location  $\bar{x} = 13.5$  by the Burridge-Andrews mechanism. . . . . 88

4.5 Left panel: Rupture time along the interface for the case with a preexisting subcritical crack. Under the stress field of the advancing main crack, the secondary subcritical crack begins to spread at  $\bar{t} = c_s t / L^c = 7.9$  and eventually propagates with intersonic speeds. Note that the results of simulations with two resolutions,  $N^c = 200, \beta = 4$  and  $N^c = 1200, \beta = 4$ , are almost indistinguishable on the scale of the plot. More resolution comparisons are shown in Figure 4.6. Right panel: Rupture speed of the secondary crack. It approaches the Rayleigh-wave speed and then abruptly jumps to intersonic speeds. Rupture speed is determined for the case with resolution  $N^c = 1200, \beta = 4$  by dividing the interface into intervals of 24 cells each, computing average rupture speed over each interval, and plotting the obtained value with respect to the middle of the interval. Care is taken to make the location of the rupture speed jump correspond to a beginning or end of an interval. . . . . 89

4.6 Propagation of the secondary crack in the region where sub-Rayleigh-to-intersonic transition occurs. Rupture time of each spatial cell is indicated using different symbols for different resolution. For progressively finer resolution (i.e., larger  $N^c$ ), transition occurs within one cell size  $\Delta x$  and one time step  $\Delta t$ , which means that, in the limit of  $\Delta x \rightarrow 0$  and  $\Delta t \rightarrow 0$ , the rupture front abruptly jumps from speeds numerically equal to  $c_R = 0.92c_s$  to an intersonic speed. . . . . 90

4.7 Snapshots of slip velocity (left) and shear stress distributions (right) on the interface during sub-Rayleigh-to-intersonic transition for the case  $N^c = 1200, \beta = 4$ , zooming in on the crack tip. Slip velocity is plotted on the logarithmic scale. For plotting convenience, slip velocity shown is the actual slip velocity plus  $10^{-6}$  and hence zero slip velocity appears as  $10^{-6}$  on the plot. At time  $\bar{t} = c_s t / L^c = 15.02$ , the crack tip propagates with the speed numerically equal to  $c_R$ . At  $\bar{t} = 15.04$ , sliding initiates just *one* cell ahead of the crack tip and propagates with intersonic speeds. . . . . 91

- 4.8 Shear stress distribution around the main crack (left panel) and the patch of higher prestress (right panel) at  $\bar{t} = 0$  ( $\bar{\tau}^o = 0.33$ ). In the left panel, the solid green and dashed red lines correspond to the smooth and more abrupt initiation procedures, respectively.  $\bar{\tau}_{BA} = 0.53$  is the level of prestress required to achieve Burridge-Andrews intersonic transition at the location  $\bar{x} = 13.5$  with the smooth initiation procedure. . . . . 92
- 4.9 Influence of patch parameters on eventual intersonic vs. sub-Rayleigh propagation for three different values of background prestress and more abrupt initiation of the main crack. The horizontal and vertical axes indicate the patch prestress and patch size, respectively. Red filled dots indicate simulated cases for which rupture has sustained intersonic speeds beyond the higher-stressed patch. Black open dots indicate simulated cases for which rupture stays sub-Rayleigh. Dashed green lines indicate approximate boundaries of different behavior. The value  $\alpha$  of the patch prestress is discussed in the text. . . . . 94
- 4.10 Influence of patch parameters on intersonic vs. sub-Rayleigh propagation for smooth initiation of the main crack that results in a smaller shear stress peak. The horizontal and vertical axes indicate the patch prestress and patch size, respectively. Red filled dots indicate simulated cases for which rupture has sustained intersonic speeds beyond the higher-stressed patch. Black open dots indicate simulated cases for which rupture stays sub-Rayleigh. Dashed green lines indicate approximate boundaries of different behavior. The value  $\alpha$  of the patch prestress, blue star, and two cases marked by small red squares are discussed in the text. . . . . 95

4.11 Rupture time for different patch sizes, with  $\bar{\tau}^o = 0.25$  ( $S = 3$ ) and more abrupt initiation of the main crack. Left panel: Patch prestress  $\bar{\tau}_h^o = 0.85$ . Rupture eventually propagates with intersonic speeds for  $\bar{L}_h = L_h/L^c = 0.075$  and  $0.34$  and sub-Rayleigh speeds for  $\bar{L}_h = 0.055$  and  $0.20$ . Behavior for these and other patch sizes is discussed in the text. Right panel: Patch prestress  $\bar{\tau}_h^o = 0.70$ , note a different scale of  $\bar{x}$ . The behavior is much simpler than for  $\bar{\tau}_h^o = 0.85$ . Cases with different  $\bar{L}_h$  are marked by letters A–E at the location  $\bar{x} = 12 + 2\bar{L}_h$  where the secondary crack for each case leaves the patch.  $\bar{L}_h = 0.08$ , line A: the secondary crack is overtaken by the main crack for this and smaller  $\bar{L}_h$ .  $\bar{L}_h = 0.1, 0.105, 0.11, 0.115, 0.12$ , line B: for  $0.1 \leq \bar{L}_h \leq 0.115$ , the secondary crack accelerates to  $c_R$  and abruptly transitions to intersonic speeds, but reverts back to sub-Rayleigh speeds after short (but progressively longer) intersonic propagation; for  $\bar{L}_h = 0.12$ , the crack manages to stay intersonic and results in eventual intersonic propagation.  $\bar{L}_h = 0.20, 0.30, 0.45$ , lines C, D, E: same behavior as for  $\bar{L}_h = 0.12$  . . . . . 98

4.12 Snapshots of stress and slip velocity for the cases of  $\bar{L}_h = 0.075$  (solid green line) and  $\bar{L}_h = 0.20$  (black dashed line with smaller dashes) with  $\bar{\tau}^o = 0.25$ ,  $\bar{\tau}_h^o = 0.85$ , and more abrupt initiation of the main crack. Propagation of the main crack with no patch of higher prestress is also shown (red dashed line with larger dashes). . . . . 100

4.13 Left:  $G(1/v_r, 1/c) = (\tilde{\tau}(c) - \tau^o)/(\tau^o - \tau^d)$  for different  $c > c_s$  and rupture speed  $v_r$ . Right: Mode II kernel  $M(u)$  of the space-time representation of  $f(x, t)$  . . . . . 109

5.1 (a) A buried strike-slip fault model which is 180 km long and 36 km wide. The region where friction acts is  $L_{\text{fric}} = 120$  km long and  $W_{\text{fric}} = 24$  km wide. It is separated into a potentially seismogenic velocity-weakening region (white color,  $L_{\text{seis}} = 60$  km,  $W_{\text{fric}} = 10$  km), and a velocity-strengthening region (yellow color). The outside region moves with the constant loading rate  $V_{\text{pl}} = 10^{-9}$  m/s = 32 mm/year. Figure (b) and (c) show distributions of friction parameters  $a$  and  $b$  along horizontal line  $z = 0$  km and vertical line  $x = 0$  km in Cases I and II, respectively. . . . . 115

5.2	Distribution of shear stress at the beginning of each simulation along $z = 0$ km (left panel) and $x = 0$ km (right panel) . . . . .	118
5.3	Typical behavior of a location within the seismogenic region, with (0 km, 0 km) used as an example. (a)–(c) Shear stress vs. slip, shear stress vs. time, slip vs. time for Case I. Zero time is the starting time of the third event, and slip is set to be zero at the zero time. Seismic ratio at this location is $2.08 > S_{\text{crit},3\text{D}} (= 1.19)$ in this event. Nonetheless, rupture passes this location with an intersonic speed. $\tau_p$ , $\tau_i$ , $\tau_d$ , and $\tau_e$ are defined in the text. (d) Shear stress vs. slip for Case II. Zero time is the starting time of the third event. Seismic ratio is 2.21, and rupture passes this location with a subsonic speed. For both Cases I and II, $V_{\text{dyn}}$ is of the order of 1 m/s, and $T$ is of the order of 100 years. Larger $a$ results in higher seismic ratio $S$ in Case II, making Case II less susceptible to intersonic propagation. . . . .	121
5.4	(a) Slip accumulation along the horizontal line $z = 0$ km in Case I. Red dashed lines are plotted every 1 second when maximum slip velocity on the fault exceeds 1 mm/s, representing slip accumulation during seismic periods, and green solid lines are plotted every 5 years, representing slip accumulation in aseismic periods. The 1st, 3rd, 5th and 9th events have global intersonic propagation. (b) Maximum slip velocity on the logarithmic scale vs. time in years. Each vertical line represents a seismic event. . . .	122

5.5	<p>Snapshots of slip velocity in the third and sixth events for Case I. Slip velocity is shown on the logarithmic scale, ranging from <math>10^{-12}</math> m/s to 1 m/s. White and bright yellow correspond to seismic slip velocity, and black corresponds to locked portions of the fault. The white dashed boxes in the top panels indicate the location of the velocity-weakening region. Zero time is the starting time of each event. The time interval between two successive panels is 2.22 s. The blue dashed line is plotted to indicate the position of the rupture front (at depth <math>z = 0</math> km) if it propagates with the shear wave speed of 3 km/s. The two events have similar initial rupture propagation (before the time of 7.78 s), but afterwards the third event propagates appreciably faster than the sixth event. . . . .</p>	124
5.6	<p>(a) and (b): Rupture time of the third and sixth events for Case I; (c) and (d): Horizontal rupture speed <math>c(x, z)</math> for the same events . . . . .</p>	125
5.7	<p>(a) Rupture speed <math>c^*(x)</math> as a function of strike distance <math>x</math> for the third and sixth events in Case I. The third event has global intersonic propagation, but the sixth event does not. (b) Average slip <math>\bar{\delta}(x)</math> as a function of strike distance <math>x</math> for the third and sixth events in Case I . . . . .</p>	127
5.8	<p>Distribution of initial shear stress <math>\tau_i</math> for the third (intersonic) and sixth (subsonic) events of Case I . . . . .</p>	127
5.9	<p>(a) Interseismic slip accumulation along central vertical line <math>x = 0</math> km between the second and third events of Case I (red dashed line) and slip distribution assumed in a 2D anti-plane model (blue solid line). (b) The corresponding shear stress accumulation . . . . .</p>	129
5.10	<p>Distribution of seismic ratio <math>S = (\tau_p - \tau_i)/(\tau_i - \tau_d)</math> on the fault (within velocity-weakening seismogenic region) for the third and sixth event of Case I . . . . .</p>	130
5.11	<p>(a) Slip accumulation along the horizontal line <math>z = 0</math> km in Case II, with a homogeneous velocity-weakening region. All events after the first one are subsonic. (b) Maximum slip velocity on the logarithmic scale vs. time in unit of years. . . . .</p>	131

5.12	Snapshots of slip velocity on the fault for the third event of Cases II and IIIh1. The blue line is plotted to indicate the shear wave speed $c_s$ of 3 km/s. A weaker patch of lower peak resistance in Case IIIh1 makes the entire rupture transition to intersonic speeds. . . . .	132
5.13	(a) Fault model of Case IIIh1: a buried strike-slip fault model with a weaker patch (red) centered at (-5 km, 0 km). Figure (b) and (c) show the distributions of friction parameters $a$ and $b$ along horizontal line $z = 0$ km and vertical line $x = 0$ km in Cases IIIh1 and IIIh2, respectively. In Case IIIh2, the heterogeneity is of the same size as in Case IIIh1 but centered at (5 km, 0 km). . . . .	133
5.14	(a) Slip accumulation along the horizontal line $z = 0$ km in Case IIIh1. (b) Maximum slip velocity in logarithmic scale vs. time in unit of years . . . . .	134
5.15	(a) Slip accumulation along the horizontal line $z = 0$ km in Case IIIb. (b) Maximum slip velocity in logarithmic scale vs. time in unit of years . . . . .	134
5.16	Figure (a), (b), and (c): rupture time of the third event for Case II, IIIh1, and IIIh2, respectively; Figure (c), (d), and (e): horizontal rupture speed $c(x, z)$ on the fault of the third event for Case II, IIIh1, and IIIh2, respectively. The black dashed boxes in Figures (e) and (f) indicate the locations of the weaker patch. Global intersonic transition occurs in Case IIIh1 and IIIh2, and the transition occurs approximately at the location of the weaker patch. . . . .	136
5.17	Distribution of seismic ratio $S = (\tau_p - \tau_i)/(\tau_i - \tau_d)$ on the fault (within velocity-weakening seismogenic region) of the third event for Cases II, IIIh1, and IIIh2, respectively. Due to low seismic ratio in the patch in Case IIIh1 and IIIh2, secondary cracks are initiated there in front of the main rupture, and driven to intersonic speeds by the intersonic loading stress field in front of the shear wave front of the main rupture. . . . .	137

5.18	Initiation of an intersonic secondary rupture in the third event of Case IIh1. (a)–(c): Snapshots of shear stress distribution along the strike distance at $z = 4$ km depth, next to a rheological boundary, at the times $t = 6.1$ s, 7.1 s, and 8.1 s, respectively. (d)–(f): Corresponding snapshots of slip velocity. Red solid lines represent the location of the weaker patch. Blue dashed lines represent the horizontal locations of shear stress peak. The secondary rupture initiates in the weaker patch ahead of the shear stress peak, consistent with our findings in Chapter 4. . . . .	139
5.19	(a) Average shear stress $\bar{\tau}_i$ before each event in Case I. (b) Effective seismic ratio $\bar{S}$ for each event in Case I. Red solid dots represent intersonic events and blue empty circles represent subsonic events. . . . .	140
5.20	Effective seismic ratio $\bar{S}$ and average initial shear stress $\bar{\tau}_i$ before each dynamic event for Cases II, IIh1, and IIh2. Red solid dots represent intersonic events and blue empty circles represent subsonic events. . . . .	141
5.21	Distribution of stress drop $\Delta\tau = \tau_i - \tau_e$ for the third and sixth events of Case I. The distribution is heterogeneous due to the presence of rheological boundaries. . . . .	144
5.22	Distribution of final slip $\delta_e(x, z)$ on the fault due to the third (intersonic) and sixth (subsonic) events for Case I. In each panel, the red star indicates the event hypocenter. . . . .	146
5.23	Rupture time along the line $z = -4$ km in the third event of Case IIh1. The black solid line is the original rupture time $t_r$ , and the red dashed line is the adjusted rupture time $t_r^*$ , used to compute horizontal rupture speed. . . . .	148

# List of Tables

2.1	Stress and frictional parameters for test problem . . . . .	16
2.2	Test problem calculations . . . . .	17
3.1	Parameters of our simulations. For depth-dependent quantities marked with the asterisk “*”, the typical value over the velocity-weakening (potentially seismogenic) region is specified. . . . .	56
4.1	Values of $S$ , $L^{\text{nucl}}/L^c$ , and numerical resolution of $L^c$ and $\Lambda_o$ for different prestress levels $\tau^o$ . $N^c = 100$ is the lowest resolution used. Numerical convergence has been verified by considering $N^c$ equal to 200, 400, and, in some cases, 1200, which increases the resolution of the cohesive zone by a factor of two, four, and twelve, respectively. . . . .	86
5.1	Case-independent parameters . . . . .	117
5.2	Case-dependent parameters . . . . .	117
5.3	Some simulated quantities from dynamic events . . . . .	126

# Chapter 1

## Introduction

Frictional interfaces respond to loading with both stick-slip behavior and steady sliding. An example of considerable practical importance is the relative displacement or slip on faults in the Earth's crust. Driven by slow tectonic motion equivalent to centimeters of slip per year, fault processes involve both seismic events or earthquakes and complex patterns of quasi-static aseismic slip (Figure 1.1). Understanding the physics and mechanics of this behavior is a fascinating scientific problem. In this thesis, we first develop computational tools for three-dimensional (3D) modeling of dynamic rupture and long-term fault slip. Then the tools are applied to the fundamentally and practically important phenomenon of intersonic transition and propagation of dynamic rupture.

In Chapter 2, we present a 3D spectral boundary-integral (BI) numerical algorithm for modeling dynamic rupture processes on a frictional interface, and compare it with a finite difference method (DFM) developed by Day and Dalguer (Day et al., 2005). BI methods have been widely used to investigate spontaneous propagation of cracks in elastic media (Das, 1980; Andrews, 1985; Das and Kostrov, 1988; Cochard and Madariaga, 1994; Perrin et al., 1995; Geubelle and Rice, 1995; Ben-Zion and Rice, 1997; Kame and Yamashita, 1999; Aochi et al., 2000; Lapusta et al., 2000; Lapusta and Rice, 2003). The main idea of BI methods is to confine the numerical consideration to the crack path, by expressing the elastodynamic response of the surrounding elastic media in terms of integral relationships between displacement discontinuities and tractions along the path. These relationships involve convolutions in space and time of either displacement discontinuities and their histories or tractions and their histories. Such an approach eliminates the necessity to simulate

wave propagation through elastic media, because that wave propagation is accounted for through the convolutions. The challenge is then to determine the appropriate convolution kernels, which is possible to do analytically only for relatively simple situations such as crack propagation in an infinite, uniform elastic solid. It may be possible to consider more complex problems (such as a layered elastic medium) by precalculating convolution kernels numerically as briefly discussed in [Lapusta et al. \(2000\)](#), but to our knowledge this has not yet been implemented. This makes BI methods more restrictive than finite-element or finite-difference methods. However, BI methods are more efficient (Chapter 2) and allow extensions to simulations of long-term deformation histories punctured by rapid dynamic events ([Lapusta et al., 2000](#), Chapter 3).

Since spontaneous rupture problems are highly nonlinear and do not have analytical solutions, it is necessary to compare our implementation of the boundary integral methodology and finite difference algorithms. The nonlinearity is attributable to the fact that rupture evolution and arrest are not specified a priori, and they are determined as part of the problem solution. That is, the problem is a mixed-boundary value problem in which the respective (time-dependent) domains of the kinematic and dynamic boundary conditions have to be determined as part of the problem solution itself. In the absence of a strict mathematical proof that either method converges to an exact solution for spontaneous rupture problems, the comparison provides validation for both numerical approaches, because these numerical methods have a high degree of independence. The boundary integral method may be called a semi-analytical method, because it discretizes only the fault surface points; the reaction of the continuum to slip at those points is represented exactly, through a closed-form Green's function. In contrast, the finite difference method uses a volume discretization to approximate the differential equations of motion throughout the 3D problem domain.

The 3D dynamic rupture methodology of Chapter 2 allows us to simulate one instance of earthquake rupture. However, even if the goal is to understand only the behavior of large destructive dynamic events, it is still important to consider the entire earthquake cycle, since slow aseismic slip may determine where earthquakes would nucleate as well as modify stress and other initial conditions before dynamic rupture ([Figure 1.1](#)). Modeling long-term slip histories of faults is quite

challenging because of the variety of temporal and spatial scales involved. Slow loading requires hundreds to thousands of years in simulated time and fault zone dimensions are in tens to hundreds of kilometers. At the same time, rapid changes in stress and slip rate at the propagating dynamic rupture tip occur over distances on the order of meters and times on the order of a small fraction of a second.

Several approaches to modeling long-term histories of fault slip have been proposed (e.g., [Shibazaki and Matsu'ura, 1992](#); [Cochard and Madariaga, 1996](#); [Kato, 2004](#); [Duan and Oglesby, 2005](#); [Liu and Rice, 2005](#); [Hillers et al., 2006](#); [Ziv and Cochard, 2006](#); [Aagaard and Heaton, 2008](#)) but all of them adopted simplified treatments of either slow tectonic loading and hence aseismic slip, or inertial effects during dynamic rupture, or transition between interseismic periods and dynamic rupture. [Lapusta et al. \(2000\)](#), based on prior studies ([Tse and Rice, 1986](#); [Rice and Ben-Zion, 1996](#); [Ben-Zion and Rice, 1997](#)), developed a methodology capable of capturing both seismic and aseismic slip and the gradual process of earthquake nucleation. However, the model of [Lapusta et al. \(2000\)](#) is two-dimensional (2D) and neglects variations in the along-strike fault dimension. Therefore it cannot be directly compared to observations and cannot be used to study a number of important problems such as interaction of fault slip with compact fault heterogeneities. In 2D models, the fault is simplified to a line, and any heterogeneity in stress or friction properties blocks the entire fault. In 3D models, the fault is represented as a surface that can include local heterogeneities and complex patterns of frictional and other properties.

In Chapter 3, we develop 3D methodology for simulating long-term history of spontaneous seismic and aseismic slip on a vertical planar strike-slip fault subjected to laboratory-derived rate and state friction and slow tectonic loading. The algorithm is able to resolve all stages of earthquake cycle in detail, including gradual nucleation processes, dynamic rupture propagation, postseismic slip, and aseismic processes throughout the loading period. Our approach builds on the studies of [Lapusta et al. \(2000\)](#), with a number of modifications required in 3D such as a different truncation procedure. The potential of the methodology is illustrated by simulations of long-term slip on a fault segment with relatively simple distributions of fault properties. The slip response of the fault model combines

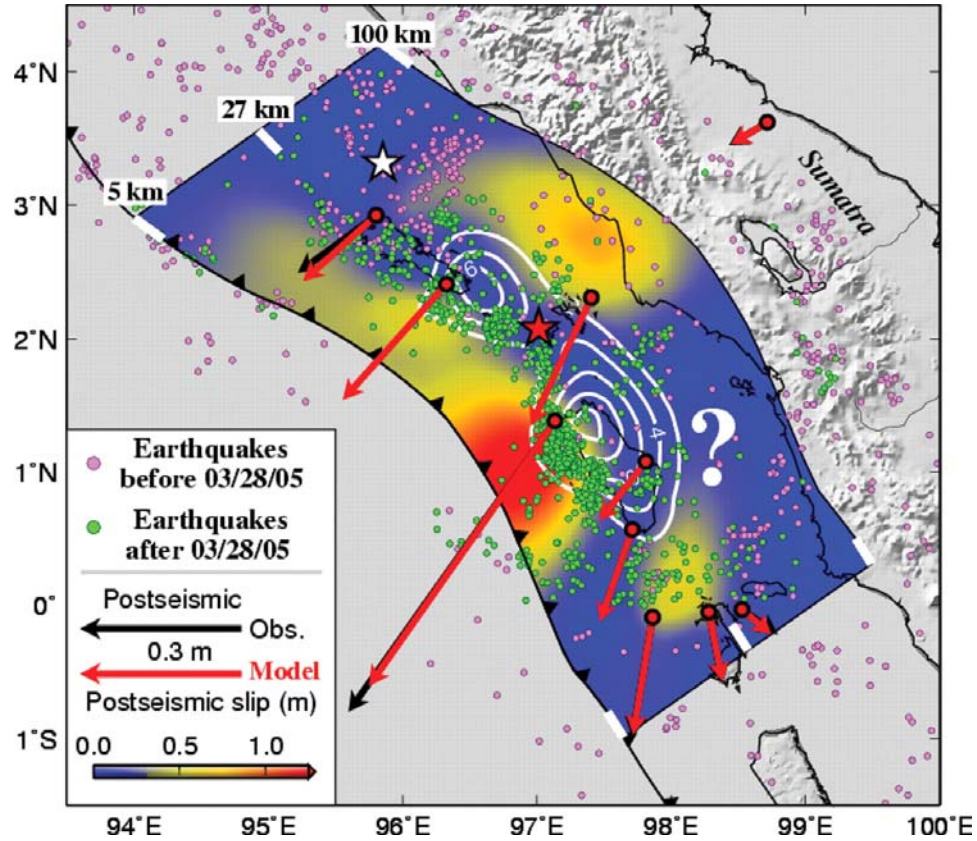


Figure 1.1: An example of interaction between earthquakes and aseismic quasi-static slip. Earthquakes redistribute stress on faults, causing slow postseismic slip or afterslip in surrounding areas, as shown here on the example of 2005 Nias-Simeulue earthquake in Sumatra (from [Hsu et al., 2006](#)). The postseismic slip, in turn, redistributes stress and may trigger other seismic events. The figure shows compilation of inferred seismic and postseismic slip, illustrating the approximately complementary nature of seismogenic and aseismic regions. Distribution of seismic slip is indicated by white contours at intervals of 2 m; color indicates cumulative postseismic slip during the 9 months after the earthquake. Black and red vectors indicate GPS observations and their match using the inferred postseismic slip, respectively. White and red stars are epicenters of 2004 Aceh-Andaman and 2005 Nias-Simeulue earthquakes, respectively. Pink and green dots denote earthquakes with body wave magnitude  $m_b > 4.5$  before and after the 2005 event. The regions of high seismicity correspond to the transition between regions of seismic and aseismic slip. The question mark indicates the region where afterslip may have occurred but it is not detectable by the existing GPS network. White tick marks on the northern and southern boundaries of the postseismic slip model indicate depths along the megathrust.

a range of seismic and aseismic phenomena. The model is used to explore the effect of several physical and numerical parameters.

We then consider two application examples that demonstrate (i) the importance of conducting long-term simulations even if the main emphasis is on the behavior of dynamic rupture and (ii) the necessity of including inertial effects in long-term simulations of slip. In the first example, we study how fault slip interacts with compact heterogeneity in the form of a patch of higher normal stress over many earthquake cycles. This kind of problem cannot be addressed with a 2D fault model. Such patches can result on natural faults from slight local non-planarity of the fault surface. 3D simulations of single dynamic events suggest that such fault heterogeneities can strongly influence the development of dynamic ruptures, in part, inducing intersonic rupture speeds (e.g., [Dunham et al., 2003](#)). However, in simulations of single dynamic events, specified initial conditions, such as initial shear stress, have a determining effect on the resulting dynamic rupture. Our methodology for earthquake cycle modeling allows us to simulate the interaction of slip with heterogeneity under conditions that naturally develop in the model due to prior seismic and aseismic slip, and to compare that evolved behavior with the one due to arbitrarily chosen initial conditions. We do find significant differences between dynamic rupture behavior in the first and subsequent events, demonstrating the importance of simulating long-term slip histories. In the second example, the fully dynamic formulation developed in this work is compared with quasi-dynamic approaches, which have been widely used in earthquake studies (e.g., [Rice, 1993](#); [Cochard and Madariaga, 1994](#); [Ben-Zion and Rice, 1995](#); [Rice and Ben-Zion, 1996](#); [Hori et al., 2004](#); [Kato, 2004](#); [Hillers et al., 2006](#); [Ziv and Cochard, 2006](#)). Quasi-dynamic approaches significantly simplify the treatment of inertial effects during simulated earthquakes by ignoring wave-mediated stress transfers. Results of our comparison underscore the importance of including full inertial effects. We also explore the possibility of improving the standard quasi-dynamic formulation by decreasing the radiation damping term, as suggested by [Lapusta et al. \(2000\)](#).

In Chapter 4 and 5, we apply the developed computational tools to the phenomenon of intersonic transition. Understanding sub-Rayleigh-to-intersonic transition of shear cracks is a fundamental

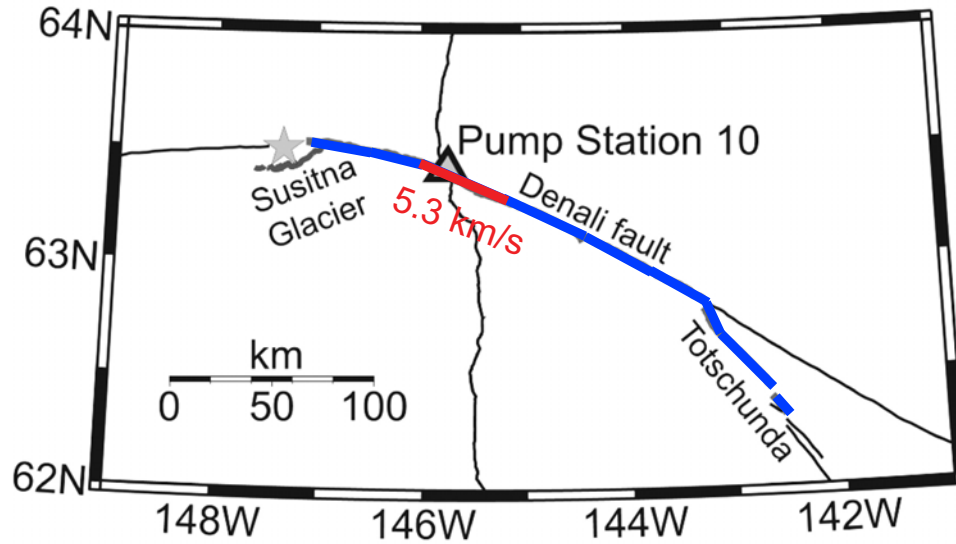


Figure 1.2: An example of inferred intersonic propagation in a large strike-slip earthquake. The 2002 Denali (Alaska) earthquake produced a surface rupture of about 340 km (dark blue line). Modeling of near-fault accelerometer records suggests that the rupture in a segment of about 40 km (red line) may have propagated with intersonic speeds, with an average speed of 5.3 km/s (Ellsworth et al., 2004).

problem in fracture mechanics with important practical implications for earthquake dynamics and seismic radiation. The word “intersonic” refers to speeds between the shear wave speed  $c_s$  and the dilatational wave speed  $c_p$ , the range which is often called “supershea” in the geophysical literature. Although average rupture speeds for earthquakes are often subsonic in general, seismic data for several earthquakes points to intersonic propagation. Examples are 1979 Imperial Valley earthquake (Archuleta, 1984; Spudich and Cranswick, 1984), 1992 Landers earthquake (Olsen et al., 1997), 1999 Izmit earthquake (Bouchon et al., 2001), 2001 Kunlun earthquake (Bouchon and Vallée, 2003), and 2002 Denali earthquake (Ellsworth et al., 2004, Figure 1.2). While this evidence is indirect, as it is obtained through analysis of seismic data, it presents a compelling case that intersonic propagation and hence sub-Rayleigh-to- intersonic rupture transition can occur during earthquakes.

Direct evidence for the possibility of spontaneous intersonic transition and propagation has been obtained in the laboratory. Inter-sonic crack propagation of mode II cracks was observed on weak interfaces under impact loading conditions (Rosakis et al., 1999; Rosakis, 2002). Needleman and Rosakis (1999) numerically modeled those experiments and qualitatively reproduced their crack

speed histories. [Xia et al. \(2004\)](#) reported experimental observations of spontaneous sub-Rayleigh-to-intersonic transition of mode II cracks propagating along a frictionally held homogeneous interface. [Xia et al. \(2005\)](#) experimentally observed a change in rupture speed from sub-Rayleigh to intersonic along a bimaterial interface.

Studies of sub-Rayleigh-to-intersonic transition have important practical implications. On the one hand, understanding which parameters and conditions do, and do not, lead to intersonic rupture propagation in models can help constrain properties and stress conditions on natural faults where rupture speeds of large earthquakes have been inferred. On the other hand, it is important to know which conditions can lead to intersonic propagation on faults and how likely intersonic ruptures are to occur. This is because intersonic ruptures can cause much stronger shaking far from the fault than subsonic ruptures can, as Mach fronts generated by intersonic ruptures carry large stresses and particle velocities far from the fault ([Bernard and Baumont, 2005](#); [Dunham and Archuleta, 2005](#); [Bhat et al., 2007](#)).

Theoretical and numerical studies of sub-Rayleigh-to-intersonic transition date back to [Burridge \(1973\)](#) and [Andrews \(1976\)](#). Large strike-slip earthquakes are dominated by in-plane sliding and some of their dynamics can be understood by considering them as mode II cracks. [Burridge \(1973\)](#) considered a self-similar mode II crack and found that a shear stress peak propagates with the shear wave speed  $c_s$  in front of the crack. [Andrews \(1976\)](#) performed numerical simulations of spontaneous crack propagation on a uniformly prestressed interface governed by a linear slip-weakening law, and demonstrated that a growing shear stress peak nucleates a daughter crack in front of the main rupture. The daughter crack propagates with intersonic speeds from its very beginning. This processes of intersonic transition is often called the Burridge-Andrews mechanism. Since the work of [Burridge \(1973\)](#) and [Andrews \(1976\)](#), a number of theoretical and numerical studies have addressed the issue of sub-Rayleigh-to-intersonic transition and/or intersonic propagation, as discussed in Chapter 4.

In Chapter 4, we take a broader look at the Burridge-Andrews mechanism and find, through numerical simulations of spontaneous mode II crack propagation, that sub-Rayleigh-to- intersonic

transition occurs in a number of models where a crack is subjected to an intersonic loading stress field. The Burridge-Andrews mechanism falls under that category, as a daughter crack initiates at the location of the shear stress peak and finds itself under the influence of the stress field of the advancing main crack. The stress field creates intersonic loading in front of the shear stress peak. We consider interaction of an advancing mode II crack (main crack) with a location susceptible to nucleation of a secondary dynamic crack, such as a pre-existing subcritical crack, a patch of higher prestress, or a patch of lower peak friction strength. Such locations are called collectively by “favorable heterogeneity” in this thesis. For a range of parameters, a secondary dynamic crack initiates at the location before the shear stress peak arrives, acquires intersonic speeds, and maintains intersonic propagation for large distances. We call the crack secondary to reserve the term “daughter” for cracks that initiate at the location of the shear stress peak in front of the main crack in the absence of pre-existing heterogeneity. Our results show, in part, that nucleating a daughter crack at the shear wave peak, a feature that propagates with the shear wave speed, is not essential for the subsequent intersonic propagation of the daughter crack. In our models, intersonic rupture transition can be achieved and subsequent intersonic crack propagation can be maintained under background prestress levels that are lower than the ones predicted by the Burridge-Andrews mechanism, and transition lengths depend on the position of favorable heterogeneities. Observations of transition lengths in earthquakes are sometimes interpreted using the Burridge-Andrews mechanism to infer parameters of fault friction (e.g., [Xia et al., 2004](#)). If intersonic transition is governed by presence of heterogeneities as presented in Chapter 4, such inferences may be misleading.

The results of Chapter 4 suggest that heterogeneity can have significant effect on intersonic transition and propagation. However, the 2D in-plane model of Chapter 4 contains a number of simplifications that can affect its applicability to natural earthquakes. First, Chapter 4 considers 2D models of in-plane sliding to make comparison with earlier studies ([Burridge, 1973](#); [Andrews, 1976](#)) and develop intuition about the role of favorable heterogeneity. However, large strike-slip earthquakes occur on faults that have long strike lengths (hundreds of km) but limited depth extent (15–20 km or so). Hence their dynamics, while dominated by in-plane sliding, are also influenced

by 3D aspects, especially the finite fault width, which have been shown to have adverse effects on intersonic transition (Day, 1982a; Madariaga and Olsen, 2000; Fukuyama and Olsen, 2002; Dunham, 2006). Second, stress and strength distributions on faults in the Earth’s crust can be much more complicated than assumed in Chapter 4. Certain types of heterogeneous stress distributions result in slower rupture speeds than the speeds that would correspond to mean values of stress (Day, 1982b). While one can assume any prestress distribution for a simulation of one instance of dynamic rupture, stress distribution on faults before a large earthquake is the result of a complicated history of seismic and aseismic sliding. That history would tend to redistribute stress and may exclude some prestress distributions before a large earthquake and hence certain rupture behaviors, as demonstrated in Chapter 3. Hence it is important to simulate long deformation histories of faults, to be able to study simulated earthquakes and intersonic transition under prestress distributions that naturally arise as the result of prior sliding history. Third, we find that the initiation procedure of the main crack significantly affects intersonic transition at the heterogeneity and subsequent propagation. Hence it is important to consider ruptures nucleating in a realistic model under slow tectonic loading.

We remove these simplifications in Chapter 5 by using the methodology developed in Chapter 3 to study intersonic transition and rupture propagation in the context of a 3D fault model and long-term fault slip. The adopted rate-and-state fault model is similar to that of Chapter 3, with a potentially seismogenic region of steady-state velocity-weakening properties surrounded by stable regions of steady-state velocity-strengthening properties. However, the fault is longer along its strike to allow for larger events, as intersonic transition is typically observed for relatively large earthquakes. We simulate long-term slip history in this fault model for a range of friction parameters and find that the rheological boundary between regions of velocity-weakening and velocity-strengthening properties acts as favorable heterogeneity, promoting intersonic transition of dynamic ruptures. During interseismic periods (i.e., periods between two large earthquakes), velocity-strengthening regions stably move with slip velocity comparable to the plate loading rate, while the velocity-weakening region is almost locked, with slip velocity several orders of magnitude smaller than the plate loading rate. The disparity in slip concentrates stress next to rheological boundaries and causes

continuing “creep-in” of the stable slip into the locked region, creating areas of high fault stress. Once earthquake rupture nucleates, it propagates faster over these areas of higher stress than over the rest of the seismogenic region, transitioning to intersonic speeds in some cases. The occurrence of intersonic transition in our 3D model depends on the combination of friction properties and fault stress that develops in the model before large earthquakes. It can be explained by considering the seismic ratio (Andrews, 1976) on the fault before large events, as discussed in Chapter 5. Since the presence of rheological boundaries on natural faults can be inferred from laboratory studies and fault observations (e.g., Blanpied et al., 1991; Marone et al., 1991; Blanpied et al., 1995; Ellsworth et al., 2000; Marone, 1998; Lyons and Sandwell, 2002; Schaff et al., 2002; Waldhauser et al., 2004; Shearer et al., 2005) as further discussed in Chapter 5, this factor can significantly contribute to intersonic transition on natural faults.

We then consider whether intersonic transition in 3D models of long-term slip can be further promoted by favorable compact fault heterogeneity, as suggested by the 2D single-event study of Chapter 4. We find a parameter regime in which there is no intersonic transition in the long-term history of the 3D fault model without the compact heterogeneity, and then we add a patch of lower effective peak frictional resistance to the model. Our simulations show that adding such a patch indeed qualitatively modifies the behavior of the model, resulting in occasional intersonic earthquakes. The transition distance is determined by the location of the patch, consistently with conclusions in Chapter 4.

Note that the phenomenon of intersonic transition due to rheological boundaries discovered in our work could not be established in prior studies, as those studies either considered single dynamic events, or simulated long deformation histories without inclusion of full inertial effects during simulated earthquakes, or studied 2D models. Single-event simulations do not include the effect of stress concentration along rheological boundaries, since the stress concentration arises as a result of prior long-term slip. Long-term simulations without the inclusion of inertial effects carried by stress waves cannot simulate intersonic transition, as this is an inertially driven phenomenon. Finally, 2D models simplify the fault plane to a line and cannot reproduce areas of higher stress at

rheological boundaries parallel to the direction of rupture propagation.

The 3D elastodynamic computational methodology developed in this thesis can be used to study a number of other problems that require 3D models and proper treatment of both long-term quasi-static deformation and inertial effects during simulated earthquakes, as discussed in Chapter 6.

## Chapter 2

# Modeling 3D spontaneous rupture with boundary integral method

In this chapter, we develop a 3D spectral boundary integral algorithm to simulate spontaneous rupture and assess its accuracy and efficiency by comparing simulated results with a finite difference method (Day, 1982b; Dalguer and Day, 2004). This comparison is necessary as spontaneous rupture problems are highly nonlinear and do not have analytic solutions. This comparison also provides useful data for testing new numerical methods. At the end of this chapter, we expand the algorithm to simulate spontaneous rupture on the fault separating solids with different elastic properties.

Sections 2.1–2.7 are based on Day, Dalguer, Lapusta and Liu (2005).

### 2.1 Problem formulation

We consider a problem of a planar surface  $\Sigma$  embedded in an isotropic, linearly elastic infinite space.

The linearized equations of motion for the space are

$$\boldsymbol{\sigma} = \mu \left( \frac{c_p^2}{c_s^2} - 2 \right) (\nabla \cdot \mathbf{u}) \mathbf{I} + \mu (\nabla \mathbf{u} + \mathbf{u} \nabla), \quad (2.1)$$

$$\ddot{\mathbf{u}} = \frac{c_s^2}{\mu} (\nabla \cdot \boldsymbol{\sigma}), \quad (2.2)$$

where  $\boldsymbol{\sigma}$  is the stress tensor,  $\mathbf{u}$  is the displacement vector,  $c_s$  and  $c_p$  are the S and P wave speeds, respectively,  $\mu$  is the shear modulus, and  $\mathbf{I}$  is the identity tensor.

The surface  $\Sigma$  has a (continuous) unit normal vector  $\mathbf{n}$ . A discontinuity in the displacement vector is permitted across the interface  $\Sigma$ . On  $\Sigma$  we define limiting values of the displacement vector,  $\mathbf{u}^+$  and  $\mathbf{u}^-$ , by

$$\mathbf{u}^\pm(\mathbf{x}, t) = \lim_{\varepsilon \rightarrow 0} \mathbf{u}(\mathbf{x} \pm \varepsilon \mathbf{n}, t). \quad (2.3)$$

We denote the discontinuity of the vector of tangential displacement (slip) by  $\boldsymbol{\delta} \equiv (\mathbf{I} - \mathbf{nn}) \cdot (\mathbf{u}^+ - \mathbf{u}^-)$ , its time derivative (slip rate) by  $\dot{\boldsymbol{\delta}}$ , and their magnitudes by  $\delta$  and  $\dot{\delta}$ , respectively. The traction vector  $\boldsymbol{\sigma} \cdot \mathbf{n}$  is continuous across  $\Sigma$ . The shear traction vector  $\boldsymbol{\tau}$  is given by  $(\mathbf{I} - \mathbf{nn}) \cdot \boldsymbol{\sigma} \cdot \mathbf{n}$  with the magnitude  $\tau$ , bounded by a non-negative frictional strength  $\tau_c$ .

We formulate the jump conditions at the interface as follows:

$$\tau_c - \tau \geq 0, \quad (2.4)$$

$$\tau_c \dot{\boldsymbol{\delta}} - \boldsymbol{\tau} \dot{\boldsymbol{\delta}} = 0. \quad (2.5)$$

Equation (2.4) stipulates that the shear traction be bounded by the (current value of) frictional strength, and equation (2.5) stipulates that any nonzero velocity discontinuity be opposed by an antiparallel traction (i.e., the negative side exerts traction  $-\tau$  on the positive side) with magnitude equal to the frictional strength  $\tau_c$ . But note that (2.5) has been written in a form such that it remains valid when  $\dot{\boldsymbol{\delta}}$  is zero. In fact, when equality does not pertain in (2.4), (2.5) can be satisfied only with  $\dot{\boldsymbol{\delta}}$  equal to zero.

The frictional strength evolves according to some constitutive functional which may in principle depend upon the history of the velocity discontinuity, and any number of other mechanical or thermal quantities, but is here simplified to the well-known slip-weakening form, introduced by [Ida \(1972\)](#) and [Palmer and Rice \(1973\)](#) by analogy to cohesive zone models of tensile fracture. In that form,  $\tau_c$  is the product of compressive normal stress  $-\sigma_n$  (as  $\sigma_n = \mathbf{n} \cdot \boldsymbol{\sigma}$  is positive in tension) and a

coefficient of friction  $f(l)$  that depends on the slip path length  $l$  given by  $\int_0^t \dot{\delta}(t') dt'$ ,

$$\tau_c = -\sigma_n f(l). \quad (2.6)$$

For this comparison, we use the linear slip-weakening friction (the same as in Chapter 4), where  $f(l)$  is given by:

$$f(l) = \begin{cases} f_s - (f_s - f_d)l/d_0, & l < d_0; \\ f_d, & l \geq d_0; \end{cases} \quad (2.7)$$

where  $f_s$  and  $f_d$  are coefficients of static and dynamic friction, respectively, and  $d_0$  is the critical slip-weakening distance (e.g., [Ida, 1972](#); [Andrews, 1976](#); [Day, 1982b](#); [Madariaga et al., 1998](#); [Dalguer et al., 2001](#)). In the event that the normal stress and frictional parameters are constant over the entire fault, as will be the case in the test problem considered here, this idealized model results in constant fracture energy  $\Gamma$  with  $\Gamma = |\sigma_n|(f_s - f_d)d_0/2$ . This simple model provides an adequate basis for testing the numerical methods, though it may have significant shortcomings as a model for earthquakes, in which interface frictional properties may be better represented by more complicated relationships that account for rate and state effects (e.g., [Dieterich, 1979](#); [Ruina, 1983](#)) and thermal phenomena such as flash heating and pore pressure evolution (e.g., [Lachenbruch, 1980](#); [Mase and Smith, 1985, 1987](#); [Rice, 2006](#)). Moreover, the energy dissipation may not be confined mostly to the fracture surface, but rather distributed in a damage zone of finite thickness around the surface ([Andrews, 1976, 2005](#); [Dalguer et al., 2003a,b](#)).

Jump conditions (2.4–2.5), combined with the friction law (2.6–2.7) and appropriate initial stress conditions on  $\Sigma$ , provide a model of fault behavior which is complete in the sense that no memory variables have to be specified to explicitly track the state of rupture at each point. That is, these conditions alone can model initial rupture (when the initial transition from inequality to equality occurs in 2.4), arrest of sliding (when 2.4 undergoes a transition from equality back to inequality), and reactivation of slip (if condition 2.4 switches back again from inequality to equality).

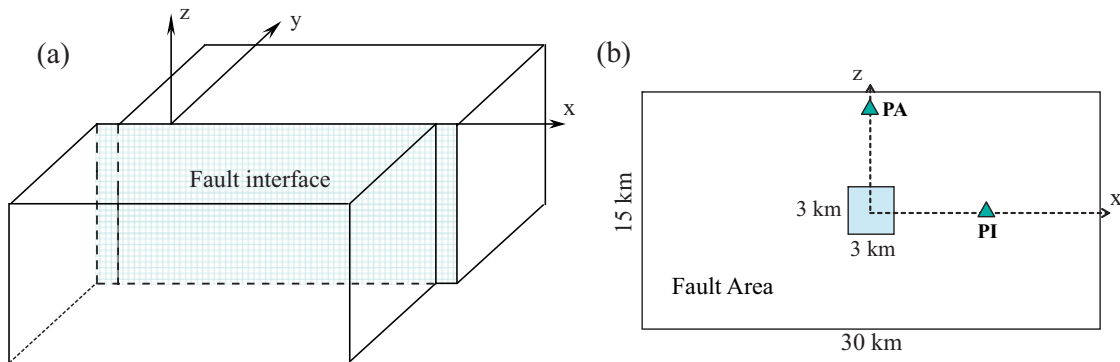


Figure 2.1: (a) A planar fault interface ( $y = 0$ ) is embedded in an infinite uniform elastic medium. (b) On the fault interface, the square in the center is the nucleation area. The triangles are the receivers at which we compare time-histories of slip, slip rate, and shear stress. Relative to an origin at the center of the fault, the receiver PI has  $z$  coordinate 0 km and  $x$  coordinate 7.5 km, and the receiver PA has  $x$  coordinate 0 km and  $z$  coordinate 6.0 km. The stress parameters are specified in Table 2.1.

## 2.2 3D boundary integral method

We employ the spectral formulation of the boundary integral method for planar interfaces pioneered by Perrin et al. (1995) for 2D anti-plane problems and extended by Geubelle and Rice (1995) to 3D fracture problems. The 3D formulation allows for displacement discontinuities that are both normal (opening) and tangential (slip) to the crack interface. Geubelle and Rice (1995) applied the formulation to numerical simulations of tensile cracking. Here we adopt the formulation for the shear case, with slip only and no opening. Hence the displacements normal to the interface are continuous in our case.

The test problem we consider involves a planar interface in an infinite uniform elastic medium (Figure 2.1). The tractions,  $\tau_\nu(x, z; t) = \sigma_{y\nu}(x, 0, z; t)$ ,  $\nu = x, y, z$  on the planar interface  $y = 0$  are expressed as the sum of the “loading” tractions  $\tau_\nu^0(x, z; t)$  that would act on the interface in the absence of any displacement discontinuity on that interface plus additional terms due to time-dependent relative slip (or tangential displacement discontinuities  $\delta_\nu(x, z; t)$ ) on the interface, in the

form

$$\tau_\nu(x, z; t) = \tau_\nu^0(x, z; t) + f_\nu(x, z; t) - \frac{\mu}{2c_s} \dot{\delta}_\nu(x, z; t), \quad \nu = x, z \quad (2.8)$$

$$\tau_y(x, z; t) = \sigma_{yy}(x, 0, z; t) = \tau_y^0(x, z; t). \quad (2.9)$$

In (2.8),  $f_\nu(x, z; t)$  are functionals of tangential displacement discontinuities; these stress-transfer functionals incorporate much of the elastodynamic response and involve convolution integrals. The last term on the left of (2.8),  $-(\mu/2c_s)\dot{\delta}_\nu(x, z; t)$ , is separated to reduce the singularity of the convolution integrals (Cochard and Madariaga, 1994).  $\dot{\delta}_\nu(x, z; t)$ , as before, denote the time derivatives of the tangential displacement discontinuities. Equation (2.8) reflects the elastodynamic fact that tangential displacement discontinuities (or slips) on a planar interface between identical elastic solids do not alter the stress normal to the interface, and hence the time dependence of normal stress in the shear case can be imposed only externally (through dynamic loading, for example). The normal stress would be altered by the displacement discontinuity normal to the interface, by nonplanarity of the sliding surface, or by sliding on a planar interface between dissimilar elastic solids. However, we do not consider any of those cases here.

The loading tractions  $\tau_\nu^0(x, z; t)$  are the stresses that would result along the interface due to external loading if the interface were restricted against any slip. Hence they need to be computed from the prescribed loading before the formulation (2.8–2.9) can be applied. In the test cases considered here, the tractions before the sliding starts are given and there is no additional loading, and hence  $\tau_\nu^0(x, z; t)$  are just equal to the initial tractions prescribed. To study earthquake problems in general, one can assume some (simplified) loading scenarios, for example, one in which,  $\tau_\nu^0(x, z; t)$ ,  $\nu = x, z$ , grow with time in a prescribed manner.

The method is called “spectral” because it relates the functionals  $f_\nu(x, z; t)$ ,  $\nu = x, z$ , to displacement discontinuities  $\delta_\nu(x, z; t)$  in the Fourier domain. For our numerical implementation, we represent the displacement discontinuities and stress-transfer functionals by their truncated Fourier series. The interface is discretized into rectangular elements, with  $N_\nu$  (even) being the number of

elements in the  $\nu$  direction, and we write

$$\begin{aligned}\delta_\nu(x, z; t) &= \sum_{k=-N_x/2}^{N_x/2} \sum_{m=-N_z/2}^{N_z/2} D_\nu(k, m; t) \exp\left(2\pi i \left(\frac{kx}{\lambda_x} + \frac{mz}{\lambda_z}\right)\right), \\ f_\nu(x, z; t) &= \sum_{k=-N_x/2}^{N_x/2} \sum_{m=-N_z/2}^{N_z/2} F_\nu(k, m; t) \exp\left(2\pi i \left(\frac{kx}{\lambda_x} + \frac{mz}{\lambda_z}\right)\right), \nu = x, z.\end{aligned}\quad (2.10)$$

In (2.10),  $\lambda_x$  and  $\lambda_z$  are the dimensions of the interface region simulated, replicated periodically. The periods  $\lambda_x$  and  $\lambda_z$  have to be chosen larger than the domain over which the rupture propagation takes place, to assure that the influence of waves arriving from the periodic replicates of the rupture process is negligible. Let us denote the wave vectors of Fourier components by  $\hat{\mathbf{q}} = (\hat{k}, \hat{m})$  with

$$\hat{k} = 2\pi k/\lambda_x, \quad \hat{m} = 2\pi m/\lambda_z, \quad \hat{q} = |\hat{\mathbf{q}}| = \sqrt{\hat{k}^2 + \hat{m}^2}.\quad (2.11)$$

The Fourier coefficients  $F_\nu(k, m; t)$  of the functionals and  $D_\nu(k, m; t)$  of the displacement discontinuities are then related by:

$$\begin{aligned}\begin{pmatrix} F_x(k, m; t) \\ F_z(k, m; t) \end{pmatrix} &= -\frac{\mu}{2\hat{q}} \begin{bmatrix} \hat{k}^2 & \hat{m}\hat{k} \\ \hat{m}\hat{k} & \hat{m}^2 \end{bmatrix} \int_0^t C_{\text{II}}(\hat{q}c_s(t-t')) \begin{pmatrix} D_x(k, m; t') \\ D_z(k, m; t') \end{pmatrix} q c_s dt' \\ &\quad -\frac{\mu}{2\hat{q}} \begin{bmatrix} \hat{m}^2 & -\hat{m}\hat{k} \\ -\hat{m}\hat{k} & \hat{k}^2 \end{bmatrix} \int_0^t C_{\text{III}}(\hat{q}c_s(t-t')) \begin{pmatrix} D_x(k, m; t') \\ D_z(k, m; t') \end{pmatrix} q c_s dt',\end{aligned}\quad (2.12)$$

where  $C_{\text{II}}(\rho)$  and  $C_{\text{III}}(\rho)$  are convolution kernels corresponding to mode II and III of the standard deformation decomposition in fracture mechanics. Equation (2.12) assumes that there are no displacement discontinuities before  $t = 0$ . The convolution kernels are:

$$C_{\text{II}}(\rho) = \frac{J_1(\rho)}{\rho} + 4\rho \left[ W\left(\frac{c_p}{c_s}\rho\right) - W(\rho) \right] - 4\frac{c_s}{c_p} J_0\left(\frac{c_p}{c_s}\rho\right) + 3J_0(\rho),\quad (2.13)$$

$$C_{\text{III}}(\rho) = \frac{J_1(\rho)}{\rho},\quad (2.14)$$

$$W(\rho) = \int_{\rho}^{\infty} \frac{J_1(\eta)}{\eta} d\eta = 1 - \int_0^{\rho} \frac{J_1(\eta)}{\eta} d\eta, \quad (2.15)$$

where  $J_0(\rho)$  and  $J_1(\rho)$  denote Bessel functions.

The formulation that involves expression (2.12) is referred to as “displacement” formulation, because the convolutions in (2.12) are done on the histories of Fourier coefficients of displacement discontinuities. To separate the static (long-term) and transient dynamic responses, the integrals in (2.12) can be integrated by parts to obtain

$$\begin{aligned} \begin{Bmatrix} F_x(k, m; t) \\ F_z(k, m; t) \end{Bmatrix} &= -\frac{\mu}{2\hat{q}} \begin{bmatrix} \hat{k}^2 & \hat{m}\hat{k} \\ \hat{m}\hat{k} & \hat{m}^2 \end{bmatrix} \left\{ 2 \left( 1 - \frac{c_s^2}{c_p^2} \right) \begin{pmatrix} D_x(k, m; t) \\ D_z(k, m; t) \end{pmatrix} - \int_0^t K_{\text{II}}(\hat{q}c_s(t-t')) \begin{pmatrix} \dot{D}_x(k, m; t') \\ \dot{D}_z(k, m; t') \end{pmatrix} dt \right\} \\ &\quad - \frac{\mu}{2\hat{q}} \begin{bmatrix} \hat{m}^2 & -\hat{m}\hat{k} \\ -\hat{m}\hat{k} & \hat{k}^2 \end{bmatrix} \left\{ \begin{pmatrix} D_x(k, m; t) \\ D_z(k, m; t) \end{pmatrix} - \int_0^t K_{\text{III}}(\hat{q}c_s(t-t')) \begin{pmatrix} \dot{D}_x(k, m; t') \\ \dot{D}_z(k, m; t') \end{pmatrix} dt \right\}, \quad (2.16) \end{aligned}$$

where

$$K_{\text{II}}(\rho) = \int_{\rho}^{\infty} C_{\text{II}}(\eta) d\eta = 2 \left( 1 - \frac{c_s^2}{c_p^2} \right) - \int_0^{\rho} C_{\text{II}}(\eta) d\eta, \quad (2.17)$$

$$K_{\text{III}}(\rho) = \int_{\rho}^{\infty} C_{\text{III}}(\eta) d\eta = 1 - \int_0^{\rho} C_{\text{III}}(\eta) d\eta. \quad (2.18)$$

The spectral BI formulation has several advantages over the purely space-time formulation. In the latter, stress-transfer functionals  $f_{\nu}(x, z; t)$  are written as integrals on both space and time, because the tractions at a particular location on the interface depend on the slip information within the relevant space-time cone determined by the speed of the propagation of elastic waves. Hence, in the discretized space-time formulation, the value of the stress-transfer functional for each cell would be determined by the histories of displacement discontinuities for all relevant cells. In the spectral formulation, the Fourier coefficients of the functionals corresponding to the wave vector  $\hat{\mathbf{q}}$  depend only on the Fourier coefficients of the displacement discontinuity corresponding to the same vector  $\hat{\mathbf{q}}$ , as can be seen in (2.12) or (2.16). Hence, the space-related integration is eliminated at the cost of introducing Fourier transforms. However, Fourier transforms take less computational time than

space integration, even when the necessity to simulate larger domains is taken into consideration, as discussed in Lapusta et al. (2000) for a 2D case. Another advantage is having the transient elastodynamic response separated into Fourier modes. The convolution kernels in (2.16) are oscillating with decaying amplitude and hence at large enough times the convolutions can be truncated. In addition, the arguments of the kernels contain the magnitude of the wave vector, which is larger for higher modes. Hence, the convolution for the higher modes can be truncated sooner than for the lower modes, and such mode-dependent truncation can save a lot of computational time, as discussed in Lapusta et al. (2000) for a 2D case. Moreover, such mode-dependent truncation may serve as means to suppress numerical high-frequency noise, although this has not yet been studied systematically. Note that separation of the response into the static part (involving the current values of displacement discontinuities) and the dynamic part (involving convolution integrals on velocity discontinuities) as accomplished by (2.16) ensures that regardless of how the convolutions are truncated, the final static stress response is fully accounted for. Even though justifiable truncation produces results very close to those obtained with no truncation, we do not use truncation in this work, to ensure that the comparison with other numerical methods (e.g., finite difference method) is not complicated by the (minor) effects of the truncation.

The solution is obtained by making the tractions (2.8) on the interface agree with the jump conditions (2.4–2.5) that involve the frictional strength (2.6–2.7). The shear traction vector  $\boldsymbol{\tau}$  and the compressive normal stress  $\sigma_n$  that enter (2.4–2.7) are given in terms of tractions  $\tau_\nu(x, z; t)$  by

$$\boldsymbol{\tau} = (\tau_x, \tau_z); \tau = \sqrt{\tau_x^2 + \tau_z^2}; \sigma_n = \tau_y. \quad (2.19)$$

## 2.3 Test problem

To assess the accuracy of our boundary integral method, we simulate a test problem and compare it with a well-established finite element method (Day, 1982b; Dalguer and Day, 2004). The numerical test entails solving the spontaneous rupture problem for a planar fault embedded in a uniform infinite

elastic isotropic space. The formulation and parameters of the test case correspond to Version 3 of the Southern California Earthquake Center (SCEC) benchmark problem developed for the 2nd SCEC Spontaneous Rupture Code-Validation Workshop of 2004 (Harris et al., 2004, 2008). The problem geometry is shown in Figure 2.1(b). We take the fault plane to be the  $x - z$  plane. The shear prestress is aligned with the  $x$  axis, and the origin of the coordinate system is located in the middle of the fault, as shown in Figure 2.1(b). The fault and prestress geometries are such that the  $x$  and  $z$  axes are axes of symmetry (or antisymmetry) for the fault slip and traction components. As a result, the  $x - y$  plane undergoes purely in-plane motion, and the  $z - y$  plane purely anti-plane motion.

Rupture is allowed within a fault area 30 km in the  $x$  direction and 15 km in the  $z$  direction. A homogeneous medium is assumed, with a P wave velocity of 6000 km/s, S wave velocity of 3464 m/s, and density of 2670 kg/m<sup>3</sup>. The distributions of the initial stresses and frictional parameters on the fault are specified in Table 2.1. The nucleation occurs in 3 km  $\times$  3 km square area that is centered on the fault, as shown in Figure 2.1. The rupture initiates because the initial shear stress in the nucleation patch is set to be slightly (0.44%) higher than the initial static yield stress in that patch. Then the rupture propagates spontaneously through the fault area, following the linear slip-weakening fracture criterion (2.6–2.7). The rupture cannot propagate beyond the 30 km  $\times$  15 km region due to the high static frictional strength set outside the region, and the region boundaries send arrest waves that ultimately stop the rupture. The duration of the simulation until the full arrest of the slip is about 12 s.

We computed eight BI solutions and seven DFM solutions to the test problem, with grid intervals and time steps shown in Table 2.2. All BI solutions use a uniform mesh. Grid intervals for the BI solutions range from 0.1 km to 0.75 km. The smallest grid interval was  $x = 0.1$  km (with time step 0.00962 s), and the corresponding solution is denoted BI0.01. The other BI solutions are given similar designations—for example, the case  $x = 0.75$  km (with time step 0.07217 s) is denoted BI0.75. DFM solutions use grid sizes  $x$  ranging from 0.05 km (with time step 0.005 s) to 0.3 km (with time step 0.020 s), with a naming convention analogous to that used for the BI solutions.

Table 2.1: Stress and frictional parameters for test problem

Parameters	Within Fault Area of 30 km $\times$ 15 km		Outside Fault Area
	Nucleation	Outside Nucleation	
Initial shear stress $\tau_0$ , MPa	81.6	70.0	70.0
Initial normal stress $-\sigma_n$ , MPa	120.0	120.0	120.0
Static friction coefficient $f_s$	0.677	0.677	$+\infty$
Dynamic friction coefficient $f_d$	0.525	0.525	0.525
Static yield stress $\tau_s = -f_s\sigma_n$	81.24	81.24	$+\infty$
Static yield stress $\tau_d = -f_d\sigma_n$	63.0	63.0	63.0
Dynamic stress drop $\Delta\tau = \tau_o - \tau_d$ ,MPa	18.6	7.0	7.0
Strength excess $\tau_s - \tau_o$ , MPa	-0.36	11.24	$+\infty$
Critical slip distance $d_0$ ,m	0.40	0.40	0.40

Although our principal objective is to compare the BI and DFM solutions, comparison of the various BI (or DFM) solutions with each other is also informative, in that it helps establish the degree to which grid-size invariance has been achieved in the numerical solutions. The BI and DFM calculations were done independently, initially as a part of a blind test of spontaneous rupture algorithms coordinated by SCEC ([Harris et al., 2004](#)).

Table 2.2: Test problem calculations

Calculation Name	Spatial Step $\Delta x$ , km	Time Step $\Delta t$ , s	Median Resolution $\bar{N}_c$	Minimum Resolution $N_c^{\min}$
BI0.1	0.1	0.00962	4.4	3.3
BI0.15	0.15	0.01443	2.9	2.2
BI0.2	0.2	0.01924	2.2	1.6
BI0.25	0.25	0.02406	1.7	1.3
BI0.3	0.3	0.02887	1.5	1.1
BI0.5	0.5	0.04811	0.9	0.65
BI0.6	0.6	0.05774	0.7	0.54
BI0.75	0.75	0.07217	0.6	0.43
DFM0.05	0.05	0.005	8.7	6.5
DFM0.075	0.075	0.00625	5.8	4.3
DFM0.10	0.10	0.008	4.4	3.3
DFM0.15	0.15	0.0125	2.9	2.2
DFM0.20	0.20	0.016	2.2	1.6
DFM0.25	0.25	0.015	1.7	1.3
DFM0.30	0.30	0.020	1.5	1.1

## 2.4 Cohesive zone and constraints on discretization

An important dimensionless measure of the resolution of numerical methods is the ratio  $N_c$  of the size (also called width or length)  $\Lambda$  of the cohesive (or slip-weakening) zone to the grid spacing  $\Delta x$ , i.e., the number of fault-plane node points (measured in the direction of rupture propagation) defining the cohesive zone:

$$N_c = \Lambda/\Delta x. \quad (2.20)$$

The cohesive zone is the portion of the fault plane behind the crack tip where the shear stress decreases from its static value to its dynamic value and slip path-length  $l$  satisfies  $0 < l < d_0$  (e.g., [Ida, 1972](#)). In the cohesive zone, shear stress and slip rate vary significantly, and proper numerical resolution of those changes is crucial for capturing the maximum slip rates and the rupture propagation speeds.

Here we review some concepts of linear fracture mechanics and simple estimates for the cohesive-zone size in two-dimensional cases of Mode II and Mode III, following and combining results by [Palmer and Rice \(1973\)](#), [Andrews \(1976\)](#), [Andrews \(2004\)](#), [Rice \(1980\)](#), and [Freund \(1990\)](#). Note that while the rupture considered here is three-dimensional, it proceeds in Mode II or in-plane mode along the  $x$  axis and in Mode III or anti-plane mode along the  $z$  axis of the fault plane. Following standard treatment in fracture mechanics, we consider a planar semi-infinite crack with constant shear traction  $\tau_d = -\sigma_n f_d$  everywhere on the crack surfaces except for the cohesive zone  $0 < \xi < \Lambda$  behind the crack tip (given by  $\xi = 0$ ), where the shear traction  $\tau(\xi)$  varies from the peak shear stress  $\tau_s = -\sigma_n f_s$  to  $\tau_d$ . While our crack is not semi-infinite, this is a good approximation for the region near the crack tip. Let us assume that the cohesive-zone width is small enough relative to the overall rupture size that we can employ the small-scale yielding limit of fracture mechanics ([Rice, 1968](#)). In that limit, the stress field that surrounds the cohesive zone is assumed to be dominated by the singular part of the crack field, characterized by the stress intensity factor  $K$ , which is either  $K_{II}$  for Mode II or  $K_{III}$  for Mode III. Finally, we consider the crack propagation to be steady, with the constant crack (or rupture) speed  $v$ . The results obtained with the assumptions of steady rupture

should still be reasonably accurate for the unsteady case, provided that the crack speed does not change significantly over propagation distances comparable to the cohesive zone length or several times that (Freund, 1990). In the following, we use subscripts II or III to indicate that the quantity is related to Mode II or III; the same quantities with no subscript participate in expressions valid for both Mode II and III.

The balance of the energy release rate  $G$  and fracture energy  $\Gamma$  at the crack tip can be written as (e.g., Freund, 1990):

$$G \equiv A(v)K^2/(2\mu^*) = \Gamma \quad (2.21)$$

where  $\mu_{\text{III}}^* = \mu$ ,  $\mu_{\text{II}}^* = \mu/(1 - \nu)$ ,  $\mu$  is the shear modulus,  $\nu$  is the Poisson's ratio,  $\Gamma$  is the fracture energy, and functions  $A(v)$  are known dimensionless functions of crack tip speed  $v$  (Freund, 1990). The fracture energy  $\Gamma$  is given by the cohesive zone law; in our case:

$$\Gamma = d_0(\tau_s - \tau_d)/2. \quad (2.22)$$

Since the cohesive zone presence eliminates the singularity at the crack tip,  $K$  and  $\tau(\xi)$  must be related by (e.g., Rice, 1980; Freund, 1990):

$$K = \sqrt{\frac{2}{\pi}} \int_0^\Lambda \frac{\tau(\xi) - \tau_d}{\sqrt{\xi}} d\xi. \quad (2.23)$$

A useful estimate of the cohesive zone size can be derived from equation (2.21–2.23) if we assume that the traction distribution within the cohesive zone is a function only of  $\xi/\Lambda$ , i.e.,

$$\tau(\xi) = \tau_s - (\tau_s - \tau_d)f(\xi/\Lambda), \quad f(0) = 0, \quad f(1) = 1. \quad (2.24)$$

Then from (2.23), the cohesive zone width  $\Lambda$  can be expressed as

$$\Lambda = C_1 \frac{K^2}{(\tau_s - \tau_d)^2}, \quad C_1 = \sqrt{\frac{2}{\pi}} \int_0^1 \frac{1 - f(\varsigma)}{\sqrt{\varsigma}} d\varsigma. \quad (2.25)$$

To estimate the constant  $C_1$ , we assume that the traction distribution within the cohesive zone is linear, i.e.,  $\tau(\xi) = \tau_s - (\tau_s - \tau_d)\xi/\Lambda$ , in which case  $C_1 = 9\pi/32$ . Note that our cohesive relation comes from friction laws (2.6–2.7), and the shear tractions are given as a linear function of slip-path length  $l$ , not space variable  $\xi$ . However, simulations show that this is a good assumption, as shear tractions within the cohesive zone are approximately linear with  $\xi$ . Determining  $K^2$  from equations (2.21–2.23) and substituting into (2.25), we obtain:

$$\Lambda = \Lambda_0 A^{-1}(v), \quad \Lambda_0 = C_1 \frac{\mu^* d_0}{(\tau_s - \tau_d)}, \quad (2.26)$$

where

$$\begin{aligned} \mu_{\text{III}}^* &= \mu, \quad \mu_{\text{II}}^* = \mu/(1 - \nu), \quad A_{\text{III}}^{-1} = (1 - v^2/c_s^2)^{1/2}, \\ A_{\text{II}}^{-1} &= \frac{(1 - \nu)c_s^2 D}{v^2(1 - v^2/c_s^2)^{1/2}}, \quad D = 4(1 - v^2/c_p^2)^{1/2}(1 - v^2/c_s^2)^{1/2} - (2 - v^2/c_s^2)^2; \\ C_1 &= 9\pi/32 \text{ for linear } \tau(\xi). \end{aligned} \quad (2.27)$$

In (2.26), since  $A^{-1}(0^+) = 1$ ,  $\Lambda_0$  denotes the cohesive zone size that the crack has when its speed is  $v = 0^+$  (the crack is barely moving).  $A^{-1}(v)$  are decreasing functions of the rupture speed  $v$ , and  $A^{-1}(0^+) \rightarrow 0$  as  $v \rightarrow c_R$  (Rayleigh wave speed) for Mode II or  $v \rightarrow c_s$  (shear wave speed) for Mode III. Hence we see that as the crack velocity increases, the cohesive zone undergoes Lorentz contraction in the direction of rupture propagation, its width collapsing as  $A^{-1}(v)$  given in (2.27).

$\Lambda_0$  provides a convenient upper bound for the cohesive zone size (it is an upper bound in the sense that any nonzero rupture speed would shrink this zone even further as predicted by equation (2.26)). The expression for  $\Lambda_0$  with  $C_1 = 9\pi/32$  was originally derived by [Palmer and Rice \(1973\)](#) and then discussed in [Rice \(1980\)](#). In numerical simulations, one should definitely resolve  $\Lambda_0$  with more than one spatial element, as we discuss further at the end of this section.

To come up with an estimate for the cohesive zone size  $\Lambda$  that accounts also for the effect of rupture speeds and their change with the propagation distance, we need to make some reasonable

assumptions about the development of the stress intensity factor  $K$  as the rupture propagates. We can then use (2.21) to estimate the rupture speeds  $v$ , and corresponding contraction factor  $A^{-1}(v)$ , that would result from such  $K$ . Under wide range of conditions (e.g., Freund, 1990; Broberg, 1999),  $K$  can be factored as

$$K = k(v)K^{\text{ref}}, \quad (2.28)$$

where  $k(v)$  are known dimensionless functions of the rupture speed and  $K^{\text{ref}}$  is the equilibrium stress intensity factor that depends on the given applied loading and characteristic crack dimension but is independent of the rupture speed. Note that equation (2.28) is derived for a semi-infinite crack propagating in an infinite medium and does not account for effects of boundaries or finite crack size. For example, in the case of a finite crack, the stress field of the opposite crack tip influences  $K$ , so its precise value depends upon the past history of rupture. We neglect this memory and other potential effects, and consider the case in which  $K^{\text{ref}}$  is only determined by stress released on the fault, given by the stress drop  $\Delta\tau = \tau_o - \tau_d$ , and the length of the rupture  $2L$ . The dimensional considerations dictate the form

$$K^{\text{ref}} = C_2 L^{1/2} \Delta\tau, \quad (2.29)$$

where  $C_2$  is a constant of order 1. For the case of a static Mode II or Mode III crack of length  $2L$  embedded in an infinite elastic medium,  $C_2 = \sqrt{\pi}$ .

Now we can substitute the assumed stress intensity factor (2.28–2.29) into the crack tip balance (2.21–2.22) and then solve the resulting equation for the crack speed  $v$  and hence the Lorentz contraction factor  $A^{-1}(v)$ . This is possible to do analytically only for the Mode III case. The result is

$$A_{\text{III}}^{-1} = (1 - v^2/c_s^2)^{1/2} = \frac{2L_0/L}{1 + (L_0/L)^2}, \quad (2.30)$$

where  $2L_0$  is the size of the crack when  $v = 0^+$  or  $2L_0$  is the critical crack length, given by

$$L_0 = \frac{\mu d_0 (\tau_s - \tau_d)}{C_2^2 (\tau_o - \tau_d)^2} = \frac{\mu d_0 (S + 1)}{C_2^2 \Delta\tau}. \quad (2.31)$$

In (2.31),  $S = (\tau_s - \tau_o)/(\tau_o - \tau_d)$  is the dimensionless seismic ratio (Andrews, 1976; Das and Aki, 1977), and, for a static Mode II or Mode III crack,  $C_2^2 = \pi$ . For the parameters of the test problem,  $2L_0 = 3$  km which motivates the 3-km choice for nucleation region size in the test problem. Note that the nucleation region is overstressed which ensures that slip there starts right away.

We can combine these results in two ways. First, substituting the Lorentz factor (2.30) into the cohesive zone expression (2.26), we obtain:

$$\Lambda = \Lambda_0 \frac{2L_0/L}{1 + (L_0/L)^2}, \quad (2.32)$$

which shows how the zero-speed cohesive zone size  $\Lambda_0$  decreases as the rupture lengthens (or propagates). Additionally, by writing out explicitly  $\Lambda_0$  and  $L_0$  in the numerator of (2.32), we get

$$\Lambda = \frac{C_1}{C_2^2} \left( \frac{\mu d_0}{\Delta\tau} \right)^2 \left( \frac{1}{1 + L_0^2/L^2} \right) L^{-1}. \quad (2.33)$$

In (2.33), the only dependence upon the seismic ratio  $S$  is contained in the critical crack half-length  $L_0$ . For crack sizes  $L$  large compared to the critical crack size  $L_0$ , we get

$$\Lambda = \frac{C_1}{C_2^2} \left( \frac{\mu d_0}{\Delta\tau} \right)^2 L^{-1}, \quad L \gg L_0, \quad (2.34)$$

where, based on the values of  $C_1$  and  $C_2$  introduced above,  $C_1/C_2^2 = 9/16$ . Note that, under the assumptions made, the cohesive zone size  $\Lambda$  is independent of  $(\tau_s - \tau_d)$  and hence, for a given  $\Delta\tau$ , of the relative strength factor  $S$ . Physically, the absence of strong dependence on  $(\tau_s - \tau_d)$  arises from the following tradeoff: reducing  $(\tau_s - \tau_d)$  increases the zero-speed cohesive zone length  $\Lambda_0$  (equation 2.26), but it also increases the rupture velocity occurring at a given rupture distance  $L$ , producing a compensating Lorentz contraction (equations 2.30 and 2.31). Note also that the cohesive zone size is inversely proportional to the crack half-length  $L$ . For  $L \gg L_0$ , the crack half-length  $L$  would be approximately equal to the propagation distance. The functional form (2.34) is identical to Andrews (1976, 2004, 2005) estimate obtained by somewhat different considerations.

Hence we have at least two ways to estimate the cohesive zone size and calibrate numerical resolution: the zero-speed cohesive zone size  $\Lambda_0$  given by (2.26) and the approximate solution (2.34) for  $\Lambda$  at large propagation distances. The two estimates are complementary. The  $\Lambda_0$  estimate shows that, regardless of the background stress or rupture propagation distances, the numerical resolution is already constrained by the choice of the frictional parameters and elastic bulk properties. For the parameters used in our test problem and  $C_1 = 9\pi/32$ , we find

$$\Lambda_{\text{III}_0} = 620 \text{ m}, \quad \Lambda_{\text{II}_0} = 827 \text{ m} \quad (2.35)$$

where  $\Lambda_{\text{III}_0}$  and  $\Lambda_{\text{II}_0}$  refer to the values for Mode II and Mode III, respectively. Since we need several spatial nodes within  $\Lambda_0$  to accommodate the Lorentz contraction, these estimates already indicate that good spatial resolution of our problem would involve grid sizes of order 100 meters or smaller. The  $\Lambda$  estimate attempts to incorporate the background stress level (through the stress drop  $\Delta\tau$ ) and the reduction of the cohesive zone due to the increasing crack speed  $v$  for large propagation distances  $L$ . Using expression (2.34) with the maximum anti-plane propagation distance  $L = 7.5$  km and  $C_1/C_2^2 = 9/16$ , we obtain

$$\Lambda_{\text{III}_{\min}}^{\text{est}} = 251 \text{ m}. \quad (2.36)$$

For Mode II, we cannot derive an analytical formula like equation (2.34), but we can perform the procedure numerically. For a given  $L$ , we compute  $K$  from equation (2.28–2.29) and substitute it into the crack tip balance (2.21). This result in an equation with respect to the crack speed  $v$  which can be solved numerically. Then we use that  $v$  to find from (2.26). Taking  $L = 15$  km, the largest propagation distance in the in-plane direction, we get

$$\Lambda_{\text{II}_{\min}}^{\text{est}} = 190 \text{ m}. \quad (2.37)$$

Both the  $\Lambda_0$  estimate from (2.26) and the  $\Lambda$  estimate (2.34) should give good initial guidance as to what kind of spatial resolution will be needed in dynamic rupture propagation problems. However,

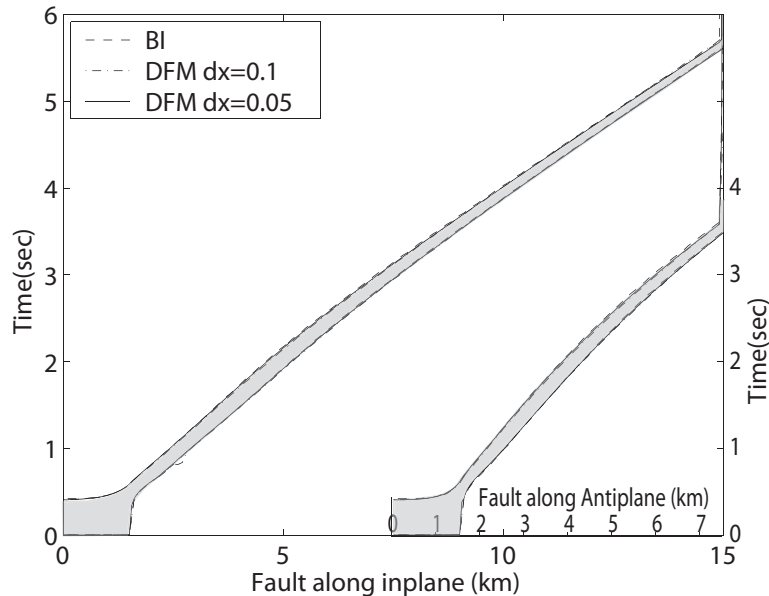


Figure 2.2: Cohesive zone during rupture, along both in-plane and anti-plane directions, for BI0.1 (dashed curve), DFM0.1 (dash-dotted curve), and DFM0.05 (solid curve) solutions

one should not expect a perfect quantitative agreement, as the estimates are derived with a number of simplifying assumptions. For example, we use the small-scale yielding assumption, the validity of which in any real situation would be only approximate. In addition, the most uncertain part of the estimate  $\Lambda$  is the set of assumptions made about the stress intensity factor. Finally, crack problems usually have features not considered in this analysis. For example, our test problem is three-dimensional, and the crack is initiated rather abruptly, by overstressing a region in the middle of the fault, which would certainly affect its development. Still, both estimates (2.36) and (2.37) compare very well, in the qualitative sense, with the actual results of our computation. Figure 2.2 shows the cohesive zone development in both anti-plane and in-plane directions. For measuring  $\Lambda$ , we define the leading edge of the cohesive zone as the spatial grid point at which the shear traction reaches  $\tau_s$ , and include in the cohesive zone the interval over which the shear traction decreases to  $\tau_d$ . The comparison between the estimates and the observed values make sense only well outside the nucleation zone, which is artificially overstressed ( $\tau_o < \tau_s$ ). We see that right outside the nucleation zone, the cohesive zone abruptly narrows and then starts to expand. These features are clearly due to the over-stressed nucleation. The smallest size of the cohesive zone right after nucleation is 300

m and it is in the anti-plane direction (all values reported in this section are based on the BI0.1 solution). Some time later the maximum sizes  $\Lambda_{\text{III min}}$  in the anti-plane direction and  $\Lambda_{\text{II min}}$  in the in-plane direction are reached:

$$\Lambda_{\text{III max}} = 460 \text{ m}, \quad \Lambda_{\text{II max}} = 560 \text{ m}. \quad (2.38)$$

After these nucleation-dominated effects, the cohesive zone progressively decreases, consistently with the theoretical developments above, reaching its subsequent smallest values at the ends of the fault:

$$\Lambda_{\text{III min}} = 350 \text{ m}, \quad \Lambda_{\text{II min}} = 325 \text{ m}. \quad (2.39)$$

Hence we see that the  $\Lambda_0$  estimate (2.35) gives a very close upper bound to all cohesive zone sizes observed in our simulation. Moreover, the BI simulation with the spatial resolution  $\Delta x = 1$  km, which is just slightly larger than both  $\Lambda_{\text{IIIo}} = 620\text{m}$  and  $\Lambda_{\text{IIo}} = 827\text{m}$ , results in very oscillatory behavior that makes the rupture arrest right after leaving the nucleation patch (that is why we do not include this run in our comparison and Table 2.2) while the BI simulation with  $\Delta x = 0.75$  km, which resolves  $\Lambda_0$  with about one cell size, still results in the rupture spreading throughout the fault, even though the results are not very accurate compared with our best-resolved and convergent solutions. Hence resolving  $\Lambda_0$  is absolutely critical, and of course more than one cell is required for good results as discussed in the next section. Notice also that  $\Lambda_{\text{IIIo}}/\Lambda_{\text{IIo}} = 3/4 = 1/(1 - \nu)$  (where  $\nu = 0.25$  is the Poisson's ratio), which predicts that, for the same propagation distances, the cohesive zone sizes in the anti-plane direction should be smaller than the cohesive zone sizes in the in-plane direction, exactly what we observe. However, the in-plane direction has a longer extent and ultimately results in a smaller cohesive zone at the end of the fault, as values (2.39) show. This is predicted by the estimates of  $\Lambda_{\text{min}}$  given in (2.36–2.37). The estimates of  $\Lambda_{\text{min}}$  are smaller than the actual values by a factor of about 1.5 (which is a constant of order 1), which we consider a very good qualitative agreement.

We conclude that one can use estimates (2.26) and (2.34) very effectively to approximately

determine cohesive zone sizes that would occur in a spontaneous rupture simulation. As we describe further in the following sections, proper resolution of the cohesive zone sizes is crucial for obtaining convergent numerical results.

To quantify our resolution, we need to report the number of spatial elements or grid points we have within the cohesive zone, given by the parameter  $N_c = \Lambda/\Delta x$  defined in (2.20). However, the cohesive zone size changes as the crack propagates, and hence  $N_c$  is not a single number but rather a variable quantity. In the next section, where we calculate some global metrics of the numerical solutions to characterize their differences, it will be convenient to have a corresponding index characterizing globally the level of cohesive-zone resolution attained in a given numerical solution. Hence we define a resolution index  $\bar{N}_c$  based on the median value of  $N_c$  obtained in the BI0.1 solution in the in-plane direction (because the in-plane direction is longer and hence likely to be representative of more points on the fault). We will also report  $N_c^{\min}$ , the minimum of  $N_c$  in the in-plane direction, as that value represents the worst local resolution achieved. Taking the spatial values in km consistently with the definition of grid sizes in Table 2.2, we get:

$$\bar{N}_c = \bar{\Lambda}_{\text{II}}/\Delta x \quad N_c^{\min} = \Lambda_{\text{IImin}}/\Delta x, \quad (2.40)$$

where  $\bar{\Lambda}_{\text{II}} = 0.44$  km and  $\Lambda_{\text{IImin}} = 0.33$  km are, respectively, the median and minimum cohesive zone sizes we observe in our simulations in the in-plane direction. Values of  $\bar{N}_c$  and  $N_c^{\min}$  are reported in Table 2.2.

## 2.5 Comparison of numerical results

We compare results in two stages. First, we quantify the differences in the DFM and BI solutions, respectively, as the grid interval  $\Delta x$  is varied. Then we focus on quantitative and qualitative comparisons of three relatively high-resolution solutions, DFM0.05, DFM0.1, and BI0.1.

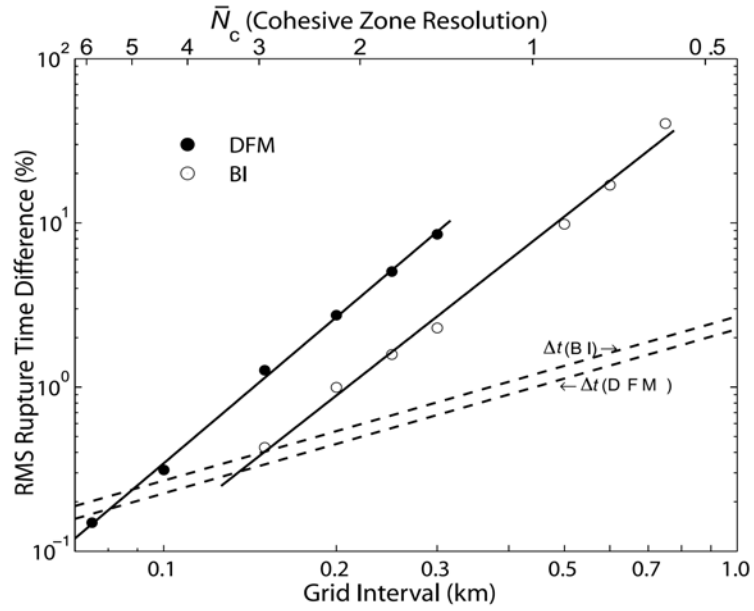


Figure 2.3: Differences in time of rupture, relative to reference solution, shown as a function of grid interval  $\Delta x$ . Differences are RMS averages over the fault plane. Open circles are BI solutions, relative to BI0.1 (the smallest grid-interval BI case). Solid circles are DFM solutions, relative to DFM0.05 (the smallest grid-interval DFM case). The dashed lines show the (approximate) dependence of time step  $\Delta t$  on  $\Delta x$ . The upper axis characterizes the calculations by their characteristic  $\bar{N}_c$  values, where  $\bar{N}_c$  is median cohesive zone width in the in-plane direction divided by  $\Delta x$ . Note the power-law convergence of both methods as the grid size is reduced. The 90% confidence intervals on the power-law exponents suggested by the regression lines are: BI [2.44–3.04]; DFM [2.77–3.15], indicating approximately equal convergence rates for the two methods.

### 2.5.1 Grid dependence of solutions

For the spontaneous rupture problem, the rupture arrival time (referred to as “rupture time” in the following) is a rather sensitive indicator of numerical precision. This sensitivity reflects the nonlinearity of the problem: Since rupture can only occur after the shear stress reaches a threshold value, relatively small inaccuracies in the calculated stress field can be expected to very significantly affect the timing of rupture breakout from the nucleation zone as well as the subsequent rupture velocity. If the rupture times are captured well, so is the rupture tip speed (or crack speed), and the rupture speed is one of the factors that influence seismic signals most. Plus, higher rupture speeds are linked to higher maximum slip rates, and hence accurate rupture times mean that the slip rates are also captured reasonably well. Therefore, we have used rupture-time differences as a primary means to quantify differences between solutions, with rupture time of a point on the interface defined here as the time at which the slip rate at that point first exceeds 1.0 mm/s.

The rupture-time comparisons are summarized in Figure 2.3. Note that the abscissa is denoted in two different ways on Figure 2.3. On the bottom, the grid size is given. On the top, we show the corresponding median cohesive-zone resolution parameter given by  $\bar{N}_c$  given by equation (2.40).

Using BI0.1 as a reference, open circles in Figure 2.3 show rupture-time difference as a function of grid interval for the BI calculations. The quantity plotted is the root mean square (RMS) difference of rupture times relative to BI0.1, with the average taken over all fault-plane nodes outside the nucleation patch; the result is then expressed as a percentage of the mean rupture time in BI0.1. The RMS differences for BI calculations appear to follow a power law in the grid size, with estimated exponent 2.74 (90% confidence interval 2.44 to 3.04). The dashed lines in Figure 2.3 show the numerical time step sizes as a function of  $\Delta x$ . The rupture-time difference between BI0.15 and BI0.1 closely approaches (within 20%) the one-time step threshold. Thus, we conclude that the BI solution has achieved rupture-time stability, to within about one time step, for  $\Delta x \leq 0.15$  km, corresponding to  $\bar{N}_c \geq 2.9$  ( $N_c^{\min} \geq 2.2$ ).

Solid circles in Figure 2.3 show the rupture-time differences for DFM, using DFM0.05 as a reference. As for DFM, the rupture time differences exhibit power law behavior in the grid size. The

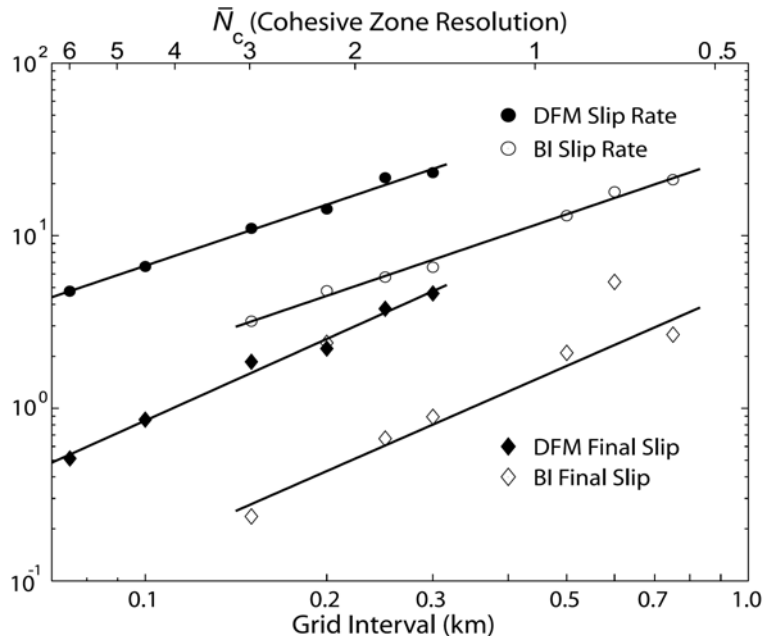


Figure 2.4: Differences in final slip (diamonds) and peak slip velocity (circles), relative to reference solution, shown as a function of grid interval  $\Delta x$ . Differences are RMS averages over the  $x$  and  $z$  axes of the fault plane. Open symbols are BI solutions, relative to BI0.1 (the smallest grid-interval BI case). Solid symbols are DFM solutions, relative to DFM0.05 (the smallest grid-interval DFM case). Note the power-law convergence of both methods as the grid size is reduced. The 90% confidence intervals on the power-law exponents suggested by the regression lines are: BI displacement [1.07–1.99]; DFM displacement [1.31–1.84]; BI velocity [1.04–1.33]; DFM velocity [1.02–1.33]. Outliers at  $\Delta x = 0.2$  km and 0.6 km were not used in estimating the BI displacement slope.

slope, 2.96 (90% confidence interval 2.77 to 3.15), is not significantly different from that for the DFM case. The DFM solution achieves rupture-time stability to within about a time step with  $\Delta x \leq 0.1$  km, corresponding to  $\bar{N}_c \geq 4.4(N_c^{\min} \geq 3.3)$ , which is an  $\bar{N}_c$  value about 3/2 the BI requirement (i.e., BI achieves the same convergence with 50% larger  $\Delta x$  than DFM).

Figure 2.4 summarizes the behaviors of two additional measures of grid-size dependence: final slip and maximum slip velocity. Each diamond (open for BI, solid for DFM) represents an RMS average (taken over the points along the  $x$  and  $z$  axes) of the difference in final slip between the solution for a given  $\Delta x$  value and a reference solution. The circles are the corresponding RMS averages for peak slip velocity. As before, BI0.1 serves as the reference for all the BI calculations, and DFM0.05 serves as the reference for all the DFM calculations. As was the case for the rupture times, the slip and slip velocity differences have roughly power-law behavior, with exponents between 1 and 2.

The displacement differences have steeper slopes than the peak velocity slopes, but 90% confidence intervals for the slopes overlap. The peak slip velocity difference falls to  $\sim 7\%$  or less for  $\Delta x \leq 0.3$  km ( $\bar{N}_c \geq 1.5$ ) for BI, and for  $\Delta x \leq 0.1$  km ( $\bar{N}_c \geq 4.4$ ) for DFM. The BI peak slip velocities and final slips converge to within a given tolerance level with  $\bar{N}_c$  about 1/3 the DFM requirements for the same tolerance level.

Note that BI slip comparisons in Figure 2.4 (open diamonds) contain two outliers, the computations with  $\Delta x = 0.2$  km and  $\Delta x = 0.6$  km. These runs have larger discrepancies in final slip because the simulated domain in these runs is slightly asymmetric with respect to the central nucleation zone. Consider the case with  $\Delta x = 0.2$  km. The nucleation region (which is 3 km  $\times$  3 km) has 15 cells in the  $x$  direction, an odd number, while the fault domain (which is 30 km  $\times$  15 km) has 150 cells in the  $x$  direction, an even number. Hence, in the  $x$  direction, there have to be different numbers of cells to the left and to the right of the nucleation zone (Figure 2.1); we choose 62 cells to the left and 63 cells to the right. This makes the nucleation zone slightly asymmetric with respect to the fault boundaries and the geometry slightly different from the runs that simulate the original symmetric problem. The slight asymmetry does not affect the rupture times and peak velocities, as these are reached before the rupture samples the boundaries of the fault zone, but the final slips depend on the arrest waves from the boundaries and are affected.

In our calculations, the time step is proportional to the grid size, as reflected by the dashed lines of Figure 2.3, and hence the resolution can be characterized by the grid spacing  $\Delta x$  only, or by  $N_c$  as its nondimensional measure. However, the BI calculation for a given  $\Delta x$  can be somewhat improved by taking smaller time steps. We do not attempt to quantify this here, but note that, as a result, for a different proportionality factor between the grid size and the time step, or for a case where lower spatial resolutions use smaller time steps, the convergence rates could be somewhat different, and hence adequate performance could be reached for slightly larger  $\Delta x$  (or smaller  $N_c$ ). We conclude that both BI and DFM solutions have achieved numerical convergence with respect to grid size reduction. Notably, the BI and DFM methods appear to have the same convergence rates, as indicated by the near-equality of the corresponding BI and DFM slopes in Figures 2.3 and 2.4.

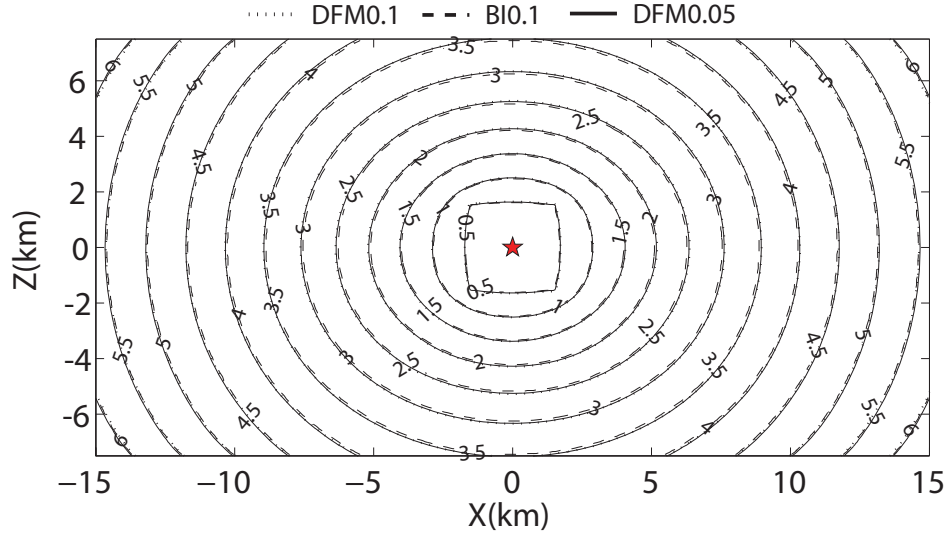


Figure 2.5: Contour plot of the rupture front for the dynamic rupture test problem. Solid curves are for DFM0.05 (grid size  $\Delta x = 0.05$  km); dotted curves are for DFM0.1 (grid size  $\Delta x = 0.1$  km); dashed curves are for BI0.1 (grid size  $\Delta x = 0.1$  km).

Note, however, that for each measure (rupture time, peak slip velocity, final slip), BI solutions, for a given  $\Delta x$ , have smaller differences with the BI best-resolved solution, BI0.1, than the corresponding DFM solutions have with their best-resolved solution, DFM0.05. For rupture time, BI achieves the given tolerance level for  $\bar{N}_c$  about a factor of 1.5 lower than DFM; for peak slip velocity and final slip, BI achieves the given tolerance level for  $\bar{N}_c$  about a factor of 3 lower than DFM.

## 2.6 Comparison of high-resolution solutions

Three relatively high-resolution solutions of the test problem are compared in Figures 2.5 to 2.6. For this purpose, we use the highest-resolution solution for each method (BI0.1 and DFM0.05, respectively), and also include DFM0.1 to provide a direct comparison between the two methods when the same grid-interval is employed. Recall that BI0.1 and DFM0.1 represent the cohesive zone with  $\bar{N}_c$  of 4.4 node points (and  $N_c^{\min} = 3.3$ ), and that DFM0.05 represents the cohesive zone with  $\bar{N}_c$  of 8.7 node points (and  $N_c^{\min} = 3.3$ ). Figure 2.5 shows contours of rupture time for these three solutions. The computed evolution of the rupture front is virtually identical for all three solutions. The level of agreement appears to be good at all distances, from the nucleation patch to the outer

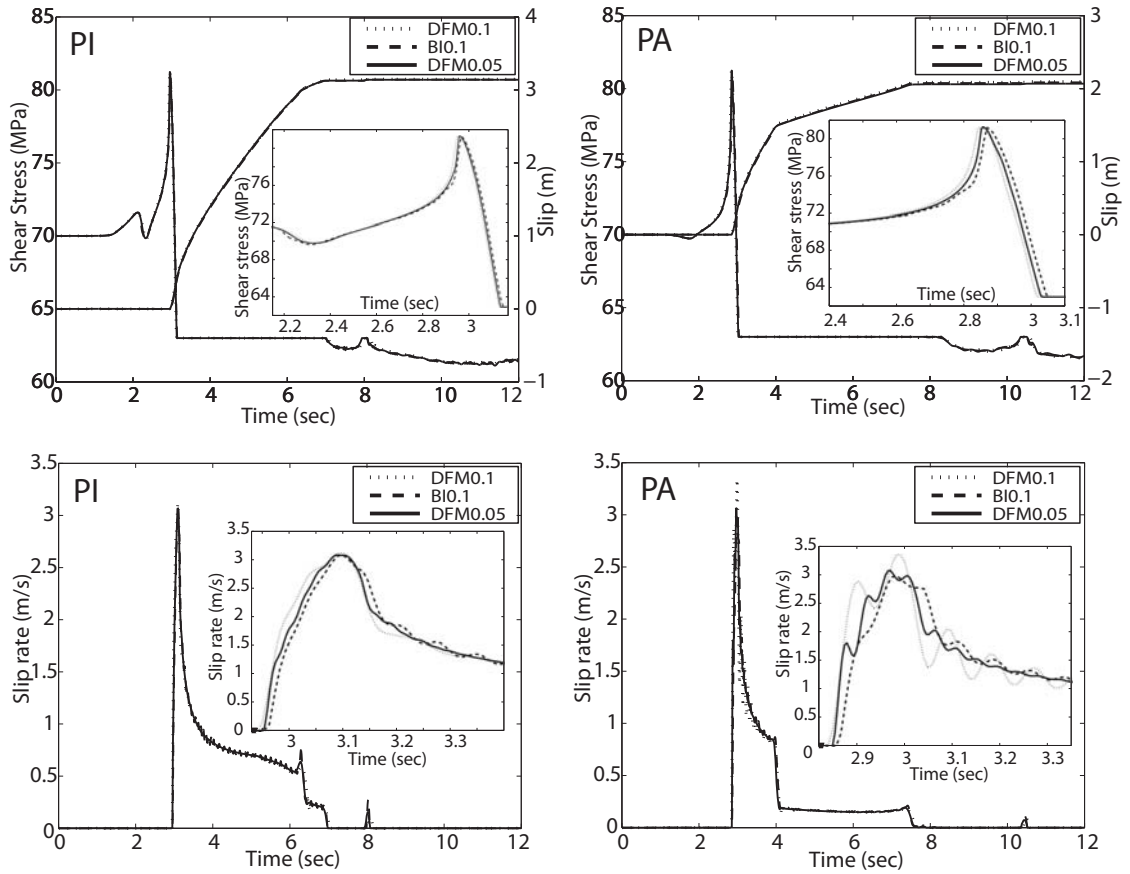


Figure 2.6: Time histories at the two fault-plane points marked in Figure 2.1. PI is on the in-plane ( $x$ ) axis, and PA is on the anti-plane ( $z$ ) axis. Shear stress, slip, and slip velocity are shown for solutions DFM0.05, DFM0.1, and BI0.1. The time histories of BI0.1 and DFM0.05 are virtually identical, with DFM0.1 also very close.

edge of the rupture surface, and even details such as the sharp corners of the 0.5 s contour, as the rupture breaks out of the nucleation patch, are virtually indistinguishable in the three solutions. The maximum difference in rupture time between DFM0.1 and BI0.1 is 0.055 s, and the RMS value (averaging over the fault plane) of the difference is 0.028 s. Based on the average rupture time on the fault of 3.57 s, this RMS difference is about 0.8%. The maximum and RMS differences between BI0.1 and DFM0.05 are 0.027 s (0.8%) and 0.045 s (1.3%), respectively.

Figure 2.6 shows the time histories at the two fault-plane points marked in Figure 2.1, one each on the in-plane (point PI) and anti-plane (point PA) axes, respectively. The time histories presented are the direct result of our simulations, with no additional filtering of any kind. In each case, the shear-stress time histories are nearly identical among the three solutions. Arrival times of rupture and several identifiable stopping phases are nearly indistinguishable in the three solutions, as are the times of arrest of sliding. Even occurrence, timing, and duration of the small reactivation of slip, at  $\sim 8$  s at PI and at  $\sim 10.3$  s at PA, are nearly identical in the three solutions. Note particularly that, at the in-plane site, both the initial stress increase associated with the  $P$  wave (arriving at  $\sim 1.5$  s), and the subsequent shear decrease associated with the  $S$  wave (arriving at  $\sim 2.2$  s) are replicated to high precision. Likewise, at the anti-plane site, the small stress decrease associated with the near-field  $P$  wave is modeled nearly identically by the three solutions. The displacement curves also agree very closely in all cases.

The only notable discrepancy is for slip velocity at PA. Even at this location, BI0.1 and DFM0.05 agree quite well. However, DFM0.1 oscillates about DFM0.05 and BI0.1, with fluctuation amplitude of about 15% of the peak velocity at the onset of motion, decaying rapidly to amplitude less than 1% of peak velocity. BI0.1 and DFM0.05 are nearly free of oscillations. The region near PA is representative of the worst case for DFM0.1 with respect to these rupture-front velocity fluctuations, which is consistent with the fact that, in that region, the cohesive zone has contracted to near its minimum (due to post-nucleation effects), with the local  $N_c$  only  $\sim 3.5$  for DFM0.1, and  $\sim 7$  for DFM0.05 (see Figure 2.2). At the PI site, where the cohesive zone width corresponds to  $N_c \sim 5$  for DFM0.1 (and to  $\sim 10$  for DFM0.05) any velocity oscillations in DFM0.1 are at least an order

of magnitude smaller: the two DFM solutions are smooth and virtually identical. All of these observations are consistent with a criterion of  $N_c \sim 5$  for obtaining slip-velocity estimates accurate to a few percent in DFM solutions, provided this criterion is satisfied locally, however, and not just in an average sense. For BI solutions, the slip velocities for BI0.1 are nearly oscillation-free, which confirms the rupture-time result that  $N_c \sim 3$  is sufficient resolution for BI.

## 2.7 Discussion

We interpret the agreement between the highest-resolution BI and DFM solutions presented above as important evidence that both solutions are accurate approximations to the continuum solution of the spontaneous rupture problem that we posed. This interpretation is further supported by the level of grid-interval independence achieved in the DFM and BI solutions.

### 2.7.1 Resolution criterion

Based on the size of the cohesive zone observed in these solutions, we propose that  $N_c \sim 3$  or about three cells within the cohesive zone is sufficient to ensure an accurate solution by the BI method, and it is  $N_c \sim 5$  by the DFM method. Note that  $N_c$  represents a local, varying quantity, and the cohesive zone resolution by about 3 cells for BI and 5 cells for DFM should be achieved everywhere locally, i.e., that should be the resolution of the minimum cohesive zone size encountered.

The criterion for uniform adherence to  $N_c \sim 3$  for BI and  $N_c \sim 5$  for DFM can probably be relaxed somewhat in many practical applications. The DFM0.1 velocity fluctuations have no effect on rupture propagation or arrest; and they decay quickly, so they do not represent an instability. Therefore, they do not interact nonlinearly with the solution. For most purposes, therefore, it would be adequate to remove them by low-pass filtering to attenuate Fourier components with wavelength shorter than the cohesive-zone width. The same applies to BI0.15 (the time histories for which are not included in Figure 2.6 for clarity of plots). In that bandlimited sense, DFM0.1 or BI0.15, although they do not quite satisfy the above criterion everywhere (since  $N_c^{\min} = 3.3$  for DFM0.1 and  $N_c^{\min} = 2.2$  for BI0.15), still provide accurate and artifact-free solutions. On the other hand, velocity

fluctuations at the level present in DFM0.1 or BI0.15 might not be acceptable when using friction models with a sensitive dependence of stress on slip velocity. In the case of rate- and state-dependent friction models (e.g., [Dieterich, 1979](#); [Ruina, 1983](#)), for example, it might prove necessary to adhere strictly to our proposed resolution criterion.

While it is reasonable to apply the obtained criterion for  $N_c$  to the class of problems considered here, in which the cohesive zone width is the smallest physical length scale present, the results will not extend to spontaneous rupture problems in which other, smaller characteristic length scales emerge. An example of the latter is the problem of rupture at a bimaterial interface. In that example, the coupling of shear and normal stress changes on the fault plane, combined with memory effects in the dependence of friction on normal stress, introduces an additional length scale ([Cochard and Rice, 2000](#); [Ranjith and Rice, 2001](#)). We conjecture that, in such cases, our criterion of  $N_c \sim 3$  for BI and  $N_c \sim 5$  for DFM would still apply, provided, however, that  $N_c$  is redefined in terms of the new minimum physical scale of the problem.

### 2.7.2 Scale collapse

The cohesive zone shrinks upon the approach of rupture speed to a terminal value (the shear wave speed in the anti-plane direction, the Rayleigh wave speed in the in-plane direction) as follows from [\(2.26\)](#). The cohesive-zone contraction could potentially make it difficult to maintain  $N_c$  sufficiently large to ensure accuracy. In the anti-plane direction, the simplest case, the cohesive-zone width will collapse as  $(1 - v^2/c_s^2)^{1/2}$ , where  $v$  is the rupture velocity. In our test problem,  $v$  reaches  $\sim 0.7c_s$  along the anti-plane axis direction. The Lorentz factor would be reduced by an additional factor of about 2, for example, if the rupture accelerated to  $\sim 0.9c_s$  and by about a factor of 4 for  $\sim 0.98c_s$ , reducing  $N_c$  in each simulation by these same factors. Thus, dealing with rupture very near terminal speed is likely to be a significant challenge for rupture simulation.

The approximate analysis ([2.21–2.34](#)) of the Lorentz contraction (in the context of the simple slip-weakening parameterization of friction) shows, for the anti-plane direction, that the cohesive-zone width scales with  $(\mu d_0/\Delta\tau)^2 L^{-1}$  and, for a given  $\Delta\tau$ , it is nearly independent of the seismic

ratio  $S$ , as long as the propagation distance  $L$  is large compared with the critical dimension for crack instability. This is identical to the scaling that [Andrews \(1976, 2004\)](#) derived from a somewhat different (but essentially equivalent) line of reasoning. The stress drop  $\Delta\tau$  used in our test calculation, 7 MPa, is about twice the average stress drop for shallow crustal earthquakes, making the test case modestly conservative in this respect (that is, had we used a more typical stress drop value of 3 MPa, the cohesive zone sizes and hence  $N_c$  would have been larger). The influence of the propagation-distance factor  $L$  on the cohesive zone size is limited by the fault width and the scale of the largest asperities. Our cohesive-zone consideration ([2.21–2.34](#)) is restricted to 2D cases but, in 3D, the smaller dimension (width) of the fault will ultimately put a bound on the stress intensity factor through which  $L$  enters the cohesive zone analysis. Our test problem has a fault width of 15 km, which is representative of the fault width for shallow crustal earthquakes. This fault-width value is equal to the maximum along-strike propagation distance of 15 km in the test problem, and the influence of the propagation-distance factor is therefore probably already at or near its limiting value ([Day, 1982a](#)). That is, even a much longer fault would not lead to much further scale contraction, so the test problem is probably also conservative with respect to the propagation-distance factor. The characteristic displacement  $d_0$ , however, is very uncertain, and values much lower than our test-problem value of 0.4 m are plausible. A  $d_0$  value of 0.1 m, for example, would have reduced  $N_c$  in each of our test problem simulations by a factor 16, putting our BI criterion of  $N_c \sim 3$  and DFM criterion of  $N_c \sim 5$  practically out of reach for a numerically tractable calculation.

Other factors, however, may limit the scale collapse associated with the approach to terminal velocity, and thus work in favor of numerical resolution (i.e., increased  $N_c$ ). Contraction of the cohesive zone is accompanied by very high strains near the fault. In an elastic model, stresses near the fault will grow inversely with the cohesive-zone dimension ([Rice, 1980](#)); and, in a more realistic model, at some stage of the cohesive zone collapse additional energy losses will occur in the form of inelastic work off the fault surface. These losses, if modeled, would limit the collapse of the cohesive zone. [Andrews \(2004\)](#) demonstrates some methods that limit scale collapse, in the context of perfect elasticity, by modifications to the friction law. Rupture simulations that incorporate off-fault

inelastic losses (Dalguer et al., 2003a,b; Andrews, 2005) provide theoretical justification for these procedures. In the simulations of Dalguer et al., for example, off-fault tension cracks open during shear rupture. This off-fault dissipation mechanism results in a reduction of the rupture velocity. Similarly, Andrews’ inelastic simulations show that when realistic off-fault inelastic energy losses are considered, fracture energy is not a constant, but rather increases with propagation distance (as does an equivalent slip-weakening displacement derived from an auxiliary elastic calculation), mitigating the collapse of scale lengths at the rupture front. When nonlinear material behavior off the fault plane dominates the energy dissipation, an appropriate length scale from which to define  $N_c$  will likely be the characteristic length over which the inelastic dissipation rate is appreciable.

### 2.7.3 Computational resources required and associated parameter limitations

The 3D spontaneous rupture calculations are quite challenging in terms of required memory and processor power. Let us consider only the memory (RAM) requirements here, as this is often the limiting factor. The memory required is 17.5 GB for BI0.1, 2.3 GB for DFM0.1, and 17.8 GB for DFM0.05. Note that the memory requirement for BI0.1 can be significantly reduced, to 2–3 GB, by using justifiable truncation of the dynamic response (e.g., as discussed by Lapusta et al. (2000) for a 2D case), which was not used here to assure the most accurate BI solution. The amount of memory needed scales with the inverse cube of the grid spacing  $\Delta x$  for both methods. Note that high-resolution runs for both methods were done on multiple processors using message passing (MPI).

Hence we immediately see the challenge in terms of computer resources one faces in studies of spontaneous ruptures. For example, suppose we would like to keep the same fracture energy in our problem, but study the effect of considering  $\xi$  times smaller critical slip  $d_0$  (and changing the frictional properties accordingly). Then, for the same stress drop, the cohesive zone sizes we would need to resolve would decrease  $\xi^2$  times according to (2.34). This means that we would need to decrease  $\Delta x$  by a factor of  $\xi^2$ , for a total increase in memory by a factor of  $\xi^6$ . That means

that just halving  $d_0$  would require 64 times as much memory, or about 150 GB for DFM and BI with truncation, and 1.1 TB for BI without truncation, which is already the scale of the largest supercomputers. Taking ten times smaller  $d_0$  would require 1,000,000 times more memory, and would clearly be impossible with present-day computers.

#### 2.7.4 Significance of BI/DFM agreement

Establishing the accuracy of numerical solution methods for the spontaneous rupture problem is challenging principally because of the nonlinearity of the problem. That nonlinearity is attributable mainly to the fact that rupture evolution and arrest are not specified a priori. In other words, we have a mixed boundary value problem in which the respective (time dependent) domains of displacement and traction boundary conditions are themselves dependent upon the displacement and stress fields. Nonlinearity allows phenomena to arise that are absent in idealized tests on linear problems, but pose significant challenges for a numerical method—the problem of scale contraction discussed above being an important example.

No analytical solutions are known for 3D spontaneous rupture problems, apart from a few special cases that reduce to linear problems (e.g., the nucleation-phase solution of [Campillo and Ionescu \(1997\)](#)) and are thus inappropriate for our purpose. We are therefore forced to make inferences about accuracy from comparison of numerical solutions. The BI method, however, could be legitimately viewed as providing at least a semi-analytical characterization of the solution to the limited class of problems to which it is applicable. The BI solution does represent the fault-plane traction and velocity discontinuity discretely, and requires purely numerical manipulations to satisfy the jump conditions. However, it represents the continuum response to a given velocity discontinuity exactly, by means of a closed-form Green’s function. It is therefore not subject to the main form of error present in volume-discretization methods such as the DFM method, which is numerical dispersion. For this reason, we would argue that agreement between DFM and BI solutions is stronger evidence of numerical accuracy (of both methods) than would be agreement between two different volume-discretization codes alone.

We note that both methods examined here are rather limited in the class of problems that they can address. The BI method, at least in the implementation presented here, is limited to uniform infinite space problems, and the DFM method, although it can address problems with a free surface and complex material properties, is limited with respect to admissible fault geometry (i.e., piecewise-planar segments, all parallel to a single coordinate plane). The numerical results presented here have been shown to be independent of both grid size and solution method, to within well-quantified tolerances, and may therefore provide a useful starting point for testing newer, more capable numerical methods for spontaneous rupture.

## 2.8 Extension to bimaterial fault interface

In Sections 2.1–2.7, we assume that the solids separated by the fault have identical material properties. However, large crustal faults usually juxtapose rocks with different mechanical properties. One example is the San Andreas Fault near Parkfield in Southern California, which separates mainly Franciscan assemblage on the Northwest side and Salinian granitic rocks on the Southwest side (Boatwright and Boore, 1982; Somerville et al., 1997). Geological observations along the San Andreas, Punchbowl, and San Jacinto faults show that the damage pattern of the fault zone rocks is asymmetric, which may be caused by preferential rupture propagation direction along these faults (Dor et al., 2005, 2006). For seismic hazard assessment, it would be important to understand whether there is a preferred rupture propagation direction on faults with material contrast (which are typically called bimaterial faults, as shown in Figure 2.7). To make our methodology more flexible, we expand it to be suitable for dynamic rupture simulations on bimaterial faults.

Breitenfeld and Geubelle (1998) presented a spectral boundary integral scheme for 2D and 3D dynamic debonding problems. Motivated by that work, we implemented our bimaterial numerical algorithm. Breitenfeld and Geubelle (1998) obtained kernels  $H_12(T)$  by performing Laplace inversion numerically. We derived a closed-form expression for  $H_{12}(T)$  (Appendix 2.10) and computed all kernels. In our simulations, a second-order Runge-Kutta procedure for updating field variables is used, similar to the case of uniform bulk, as described in the appendix of Chapter 3. Our

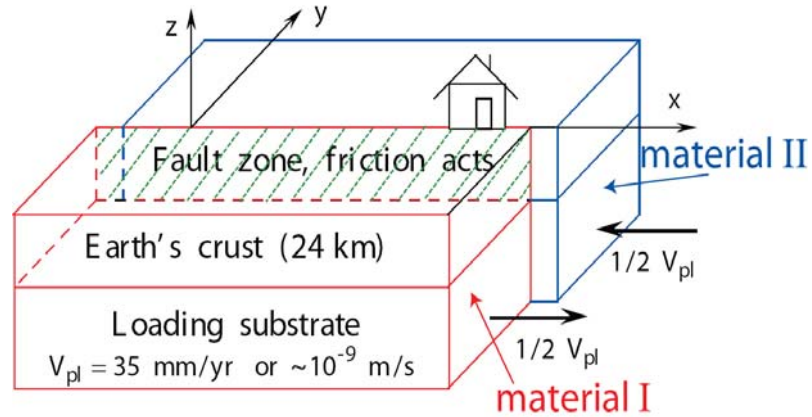


Figure 2.7: A planar fault separating materials of different elastic properties. Some theories and numerical simulations suggest that there is a preferred rupture propagation direction along bimaterial fault (Weertman, 1980; Adams, 1995; Shi and Ben-Zion, 2006).

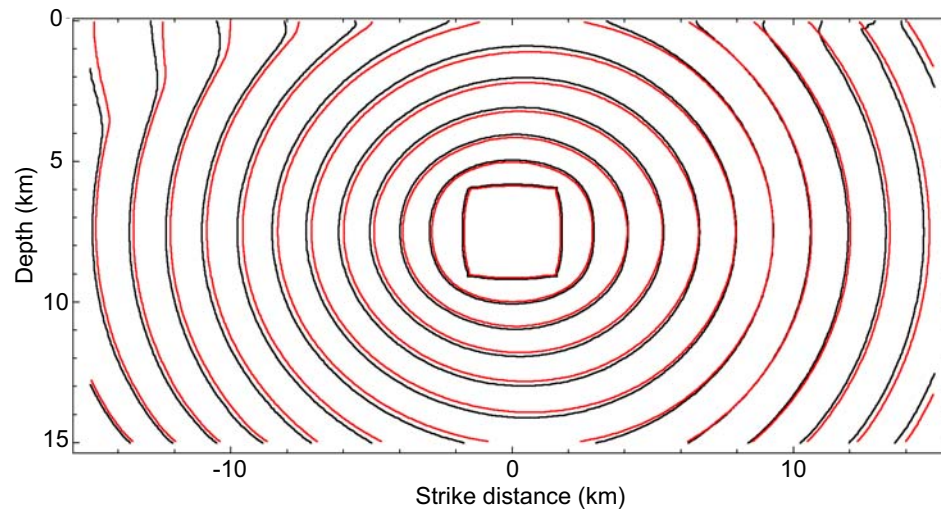


Figure 2.8: Contour plot of the rupture time on the bimaterial fault for the Southern California Earthquake Center (SCEC) Code Validation Project Problem, Version 7. Red curves are for BI method, and black curves are for DFM method. Contour lines are plotted every 0.5 seconds. Rupture propagation along horizontal direction is asymmetric due to different material properties across the fault.

numerical algorithm for bimaterial faults has been validated in the Southern California Earthquake Center (SCEC) Code Validation Project, Benchmark Problem Version 6–7. ( More information is available at <http://scecddata.usc.edu/cvws/cgi-bin/cvws.cgi> in “Public Area” → “tpv6 (tpv7)” → “liu”.) Figure 2.8 illustrates one of the test problems.

## 2.9 Conclusion

We have developed a spectral boundary integral method for simulating spontaneous rupture propagation on a frictional fault interface, and compare it with a traction-at-split-node finite difference method (DFM). The two methods give virtually indistinguishable solutions to a spontaneous-rupture test problem when both methods adequately resolve the cohesive zone (i.e., with at least 3 cells for BI and at least 5 node points for DFM). Quantitatively, we have assessed agreement between the methods in terms of the RMS differences in rupture time, final slip, and peak slip-rate, and related these to median ( $\bar{N}_c$ ) and minimum ( $N_c^{\min}$ ) resolution measures. With  $\bar{N}_c=4.4$  (and  $N_c^{\min}=3.3$ ) for both methods, the RMS time, slip, and slip-rate differences are 0.8%, 0.6%, and 9%, respectively. With the same  $\bar{N}_c$  and  $N_c^{\min}$  for BI, but better resolution ( $\bar{N}_c=8.7$  and  $N_c^{\min}=6.5$ ) for DFM, these metrics are 0.8%, 0.4%, and 3%, respectively.

Furthermore, calculations over approximately an order of magnitude range in  $\bar{N}_c$  demonstrate a well-defined power-law asymptotic behavior of both BI and DFM solutions: for each method, variations of predicted rupture time with respect to grid spacing follow a power law with exponent  $\sim 3$ . We interpret this behavior, combined with the agreement between BI and DFM solutions, as evidence of asymptotic convergence to the continuum solution. The final slip and peak slip-rate metrics show similar power-law behavior, with exponents between 1 and 2 for both methods. These numerical tests help fill a gap in our understanding of the accuracy of numerical solutions to nonlinear spontaneous rupture problems. In addition, the solutions presented here, by virtue of being demonstrably grid-independent and consistent between two very different numerical methods, may prove useful for testing new numerical methods for spontaneous rupture.

In Section 2.8, we have expanded our spectral boundary integral algorithm to be suitable for the

bimaterial fault interface, deriving analytical expressions for convolution kernels given in Appendix 2.10.

## 2.10 Appendix: closed-form expression for kernels used for bimaterial faults

Elastodynamic response on a bimaterial fault involves four convolution kernels  $H_{11}(T)$ ,  $H_{22}(T)$ ,  $H_{33}(T)$ , and  $H_{12}(T)$ . Breitenfeld and Geubelle (1998) only obtained the closed-form expressions for the first three. To make it complete, we derive the closed-form expression for the last one.

As given by Breitenfeld and Geubelle (1998), the Laplace transform  $\hat{H}_{12}(s)$  of  $H_{12}(T)$  is:

$$\hat{H}_{12}(s) = \frac{\eta s^2}{\eta - \sqrt{s^2 + \eta^2} \sqrt{s^2 + 1}} = \sum_{i=1}^3 \hat{f}_i(s), \quad (2.41)$$

where

$$\hat{f}_1(s) = \frac{\eta - \eta^2 + \eta^3}{s^2 + 1 + \eta^2}, \quad (2.42)$$

$$\hat{f}_2(s) = -\frac{\eta s}{s^2 + 1 + \eta^2} \frac{1}{\sqrt{s^2 + 1} + s}, \quad (2.43)$$

$$\hat{f}_3(s) = -\eta^3 \frac{\sqrt{s^2 + 1}}{s^2 + 1 + \eta^2} \frac{1}{\sqrt{s^2 + \eta^2} + s}. \quad (2.44)$$

In the above equations,  $\eta = c_p/c_s$ .  $\hat{f}_i(s)$  can be inverted to:

$$f_1(T) = \frac{\eta - \eta^2 + \eta^3}{\sqrt{1 + \eta^2}} \sin\left(\sqrt{1 + \eta^2} T\right), \quad (2.45)$$

$$f_2(T) = -\int_0^T \eta \cos\left(\sqrt{1 + \eta^2} u\right) \frac{J_1(T - u)}{T - u} du, \quad (2.46)$$

$$f_3(T) = \int_0^T \eta^2 g(u) \frac{J_1(\eta T - \eta u)}{T - u} du, \quad (2.47)$$

where  $J_1(T)$  is the Bessel function of the first kind, and

$$g(T) = \int_0^T \cos\left(\eta\sqrt{T^2 - u^2}\right) J_1(u) du - \cos(\eta T). \quad (2.48)$$

## Chapter 3

# 3D modeling of spontaneous earthquake sequences and aseismic slip

In Chapter 2, we have developed a 3D spectral boundary integral algorithm for simulating one instance of earthquake rupture. However, fault processes involve complex patterns of seismic events (or earthquakes) and aseismic slip. Aseismic slip may determine where earthquakes would nucleate as well as modify stress and other initial conditions before dynamic rupture. Therefore, it is important to study long-term fault slip in the context of earthquake cycles. In this chapter, we develop an algorithm for 3D modeling of spontaneous earthquake sequences and aseismic slip under slow tectonic loading, and utilize it to study interaction of fault heterogeneity with dynamic ruptures in long-term fault slip. We also compare the fully-dynamic simulations with a widely used quasi-dynamic approach.

The chapter is based on [Lapusta and Liu \(2008\)](#).

### 3.1 Methodology

We continue to consider the model of two identical elastic spaces separated by a planar fault interface  $y = 0$ . In the spectral boundary integral method, the tractions  $\tau_{yi}(x, 0, z; t) \equiv \tau_i(x, z; t)$ ,  $i = x, z$  on

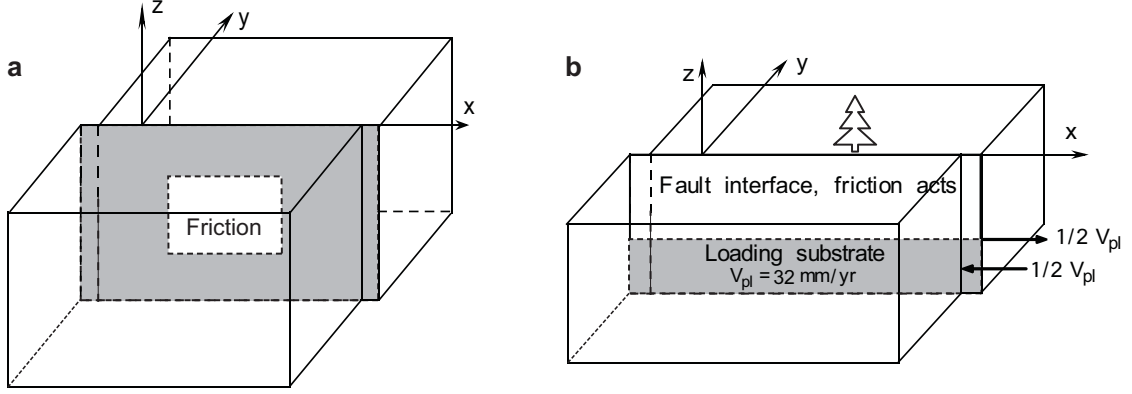


Figure 3.1: (a) A model of a planar interface embedded in an infinite and homogeneous elastic medium. (b) A vertical strike-slip fault in an elastic half-space. The top part of the fault is governed by rate and state friction, and the bottom part is steadily moving due to tectonic loading.

the interface  $y = 0$  can be expressed as:

$$\tau_i(x, z; t) = \tau_i^o(x, z; t) + f_i(x, z; t) - \eta_i V_i(x, z; t). \quad (3.1)$$

where  $\eta_x = \eta_z = \mu/(2c_s)$ . The integral relationships between displacement discontinuities and tractions on the fault interface embedded in an infinite elastic space are:

$$\begin{aligned} \begin{Bmatrix} F_x(k, m; t) \\ F_z(k, m; t) \end{Bmatrix} = & -\frac{\mu}{2\hat{q}} \begin{bmatrix} \hat{k}^2 & \hat{m}\hat{k} \\ \hat{m}\hat{k} & \hat{m}^2 \end{bmatrix} \left\{ 2 \left( 1 - \frac{c_s^2}{c_p^2} \right) \begin{pmatrix} D_x(k, m; t) \\ D_z(k, m; t) \end{pmatrix} - \int_0^t K_{\text{II}}(\hat{q}c_s(t-t')) \begin{pmatrix} \dot{D}_x(k, m; t') \\ \dot{D}_z(k, m; t') \end{pmatrix} dt \right\} \\ & -\frac{\mu}{2\hat{q}} \begin{bmatrix} \hat{m}^2 & -\hat{m}\hat{k} \\ -\hat{m}\hat{k} & \hat{k}^2 \end{bmatrix} \left\{ \begin{pmatrix} D_x(k, m; t) \\ D_z(k, m; t) \end{pmatrix} - \int_0^t K_{\text{III}}(\hat{q}c_s(t-t')) \begin{pmatrix} \dot{D}_x(k, m; t') \\ \dot{D}_z(k, m; t') \end{pmatrix} dt \right\}, \quad (3.2) \end{aligned}$$

where  $F_i(k, m; t)$  and  $D_i(k, m; t)$ ,  $i = x, z$  are the Fourier coefficients of stress functionals  $f_i(x, z; t)$  and displacement discontinuities  $\delta_i(x, z; t)$ , respectively. Elastodynamic response expressed by the convolution integrals in (3.2) can be truncated for problems that involve long deformation histories with short periods of fast slip. During slow, interseismic periods, the deformation process is quasi-static and there is no need to keep track of inertial effects. Truncation procedures for anti-plane (Mode III) problems were given by Ben-Zion and Rice (1997) and Lapusta et al. (2000). Here we develop the appropriate modifications for our 3D model.

### 3.1.1 Truncation of elastodynamic response

To implement the truncation, we compute the convolutions in (3.2) from  $t - T_w$  to  $t$  only, where  $T_w$  is the truncation time window. Convolution kernels  $K_{II}(\rho)$  and  $K_{III}(\rho)$  oscillate with decaying amplitude for larger  $\rho$  (Appendix 3.7.1). Slip velocities, and hence their Fourier coefficients  $\dot{D}_x$  and  $\dot{D}_z$ , are near-zero for most of the fault history, except during simulated earthquakes, which have durations of the order of the time for the shear wave to propagate through the simulated domain. Hence, following Lapusta et al. (2000),  $T_w$  is expressed in the form:

$$T_w = \alpha\lambda/c_s, \quad (3.3)$$

where  $\lambda$  is the largest extent of the seismogenic zone and  $\alpha$  is a truncation parameter of order 1. We call this truncation scheme “frequency-independent”, as the truncation window does not depend on the frequency of Fourier modes. Larger truncation windows make the problem closer to the one without truncation but they also increase the computational expense. In our simulations, we find that  $\alpha = 1$  gives results that do not change for larger truncation windows (Section 3.3.2).

The truncation procedure can be made more efficient by making the truncation window  $T_w$  dependent on Fourier modes. Fourier coefficients for higher frequencies are generally smaller. Even more importantly, the kernel argument  $\rho = \hat{q}c_s(t - t')$  scales with the mode frequency  $\hat{q}$  and, for larger  $\hat{q}$ , the same time window corresponds to longer integration intervals in terms of the kernel argument. Since the kernels oscillate with decaying amplitude for larger  $\rho$ , one can limit the length of kernel windows, making the corresponding time windows shorter.

In Lapusta et al. (2000), the truncation procedure and parameters used resulted in approximately  $T_w(\hat{q}) \propto \hat{q}^{-1}$ . That scheme was efficient and accurate for 2D antiplane (mode III) problems considered in Lapusta et al. (2000) but, in 3D problems, we find that it produces much lower slip velocities and rupture speeds than frequency-independent truncation. This is because both mode III and mode II kernels are involved in the 3D formulation, and the mode II kernel is more oscillatory and decays slower than the mode III kernel. From Appendix 3.7.1, for  $\rho \gg 1$ ,  $K_{II} \sim O(\rho^{-1/2})$  while

$$K_{\text{III}} \sim O(\rho^{-3/2}).$$

We have developed a new scheme that truncates less at low frequencies than the scheme and parameter choices of Lapusta et al. (2000). For low-frequency modes, the time windows are constant,  $T_w(\hat{q}) = \alpha\lambda/c_s$ , as in the frequency-independent truncation, with the kernel windows increasing for those modes. However, the kernel windows can be no larger than a given value  $\rho_c$ , which becomes a truncation parameter. Let us denote by  $\hat{q}_c$  the frequency at which the kernel windows reach the length  $\rho_c$ . Then the frequency-dependent truncation windows expressed in terms of time are given by:

$$T_w(\hat{q}) = \begin{cases} \alpha\lambda/c_s, & \hat{q} \leq \hat{q}_c, \\ \alpha\lambda/c_s \hat{q}_c/\hat{q}, & \hat{q} \geq \hat{q}_c. \end{cases} \quad (3.4)$$

Hence  $T_w(\hat{q}) \sim \hat{q}^{-1}$  for higher frequencies. Note that the lowest frequency mode  $\hat{\mathbf{q}} = (0, 0)$  with  $\hat{q} = 0$  corresponds to the uniform slip over the fault interface and has no contribution to stress transfers, so we set  $T_w(0) = 0$ . In equation (3.4),  $\hat{q}$  varies between the lowest nonzero frequency  $\hat{q}_{\min} = 2\pi/\lambda_x$  (assuming, without loss of generality, that  $\lambda_x \geq \lambda_z$ ) and the highest frequency  $\hat{q}_{\max} = \sqrt{2}\pi/\Delta x$ . In terms of the kernel argument  $\rho = \hat{q}c_s(t-t')$ , the time windows (3.4) correspond to the following kernel windows  $\rho_w(\hat{q}) = \hat{q}c_s T_w(\hat{q})$ :

$$\rho_w(\hat{q}) = \begin{cases} \alpha\lambda\hat{q}, & \hat{q} \leq \hat{q}_c, \\ \rho_c = \alpha\lambda\hat{q}_c, & \hat{q} \geq \hat{q}_c. \end{cases} \quad (3.5)$$

In our simulations,  $\rho_c \geq 100$  result in the same slip response as that with frequency-independent truncation (Section 3.3.3). Such values of the kernel argument correspond to the kernel amplitudes smaller than 0.0008 for mode III and 0.08 for mode II.

Let us estimate how much more efficient the frequency-dependent truncation is by comparing the memory requirements for the two truncation procedures. Let us assume that  $N_x \sim N_z$ . For convolution computations, each time window  $T_w(\hat{q})$  is discretized with the time interval  $\Delta t_{\min}(= \gamma\Delta x/c_s)$ , where  $\gamma$  is a constant parameter discussed in Appendix 3.7.2, resulting in  $N_T(\hat{q})$  intervals.

For the frequency-independent truncation, this number is given by:

$$N_T(\hat{q}) = \frac{T_w(\hat{q})}{\Delta t_{\min}} = \frac{\alpha N}{\gamma}, \quad (3.6)$$

where  $N = \lambda/\Delta x \sim N_x \sim N_z$ . The total number of frequency modes are  $N_x \times N_z$ . For each frequency mode, we need four arrays of the size  $N_T(\hat{q})$  to store kernels and Fourier coefficients of slip velocities. The total size of the arrays are:

$$N_{\text{tot}} = \sum_{k=-N_x/2}^{N_x/2} \sum_{m=-N_z/2}^{N_z/2} 4N_T(\hat{q}) = \frac{4\alpha}{\gamma} N N_x N_z \sim O(N^3). \quad (3.7)$$

For the frequency-dependent truncation, the total size of the arrays storing convolution values changes to:

$$N_{\text{tot}}^{\text{mod}} = \sum_{k=-N_x/2}^{N_x/2} \sum_{m=-N_z/2}^{N_z/2} 4N_T(\hat{q}) \approx \left( 2\sqrt{2}\rho_c - \frac{\rho_c^2}{\pi\alpha N} \right) \frac{N_x N_z}{\gamma} \sim \rho_c O(N^2). \quad (3.8)$$

For small values of  $\rho_c \ll \alpha\lambda\hat{q}_{\max}$ , the required memory is significantly smaller for the frequency-dependent truncation.

### 3.1.2 Fault constitutive response: rate and state friction laws

The fault resistance to sliding is described by laboratory-derived rate and state friction laws which have been widely used to model earthquake phenomena (Dieterich, 1979; Ruina, 1983; Dieterich, 2007, and references therein). A general form of rate and state friction laws is:

$$\begin{cases} \tau &= \phi(V, \theta, \sigma), \\ \dot{\theta} &= \varphi(V, \theta, \sigma), \end{cases} \quad (3.9)$$

where  $\tau = \sqrt{\tau_x^2 + \tau_z^2}$  is the magnitude of shear traction vector  $\boldsymbol{\tau} = (\tau_x, \tau_z)$ ,  $V = \sqrt{V_x^2 + V_z^2}$  is the magnitude of the slip velocity vector  $\mathbf{V} = (V_x, V_z)$ ,  $\sigma = -\tau_y$  is the normal traction (positive in compression), and  $\theta$  is the state variable. It has been experimentally established that shear traction

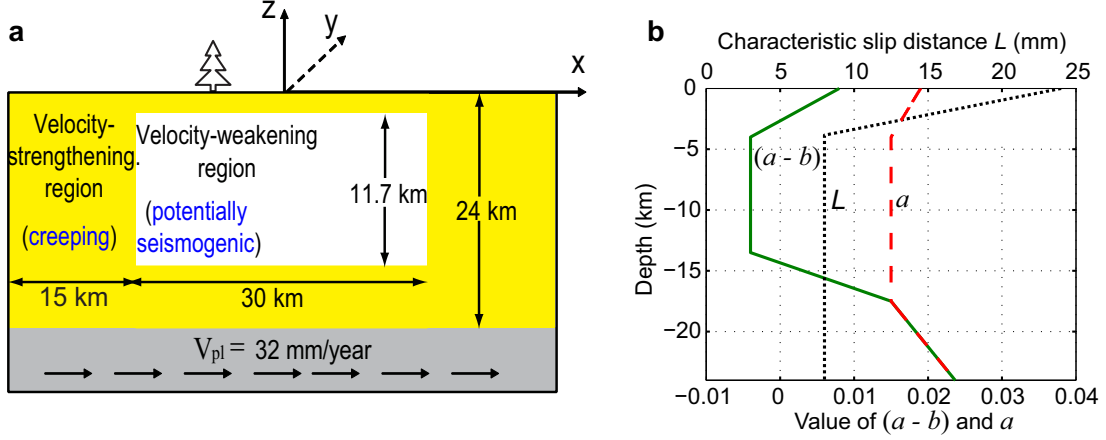


Figure 3.2: Properties of the simulated fault segment. (a) Rate and state friction acts on the top 24 km of the fault. A potentially seismogenic region of velocity-weakening properties (shown in white) is surrounded by velocity-strengthening regions (shown in yellow). Below  $z = -24$  km, steady motion of 32 mm/year is imposed. (b) Depth dependence of friction parameters  $(a - b)$ ,  $a$ , and  $L$  in the seismogenic region. The distributions are piecewise linear between the following points:  $(a - b)|_{z=0} = 0.008$ ,  $(a - b)|_{z=4} = -0.004$ ,  $(a - b)|_{z=13.5} = -0.004$ ,  $(a - b)|_{z=17.5} = 0.015$ ,  $(a - b)|_{z=24} = 0.024$ ,  $a|_{z=0} = 0.019$ ,  $a|_{z=4} = 0.015$ ,  $a|_{z=17.5} = 0.015$ ,  $a|_{z=24} = 0.024$ ,  $L|_{z=0} = 24$  mm,  $L|_{z=4} = 8$  mm,  $L|_{z=24} = 8$  mm.

instantaneously increases (decreases) in response to a sudden increase (decrease) of slip velocity (e.g., Dieterich, 1979; Ruina, 1983; Marone, 1998), which implies  $\phi(V, \theta, \sigma)/\partial V > 0$ , the feature commonly referred to as the positive direct effect. As discussed in Lapusta et al. (2000), the presence of this instantaneous positive response is essential for the numerical procedure to be able to adopt large time steps during quasi-static deformation processes while yielding stable numerical results.

Several specific forms of rate and state friction laws have been proposed. Here we adopt the aging law (Dieterich, 1979, 1981; Ruina, 1983) in the form appropriate for constant normal stress  $\sigma$ :

$$\begin{cases} \tau &= \sigma \left( f_o + a \ln \frac{V}{V_o} + b \ln \frac{V_o \theta}{L} \right), \\ \dot{\theta} &= 1 - \frac{V \theta}{L}, \end{cases} \quad (3.10)$$

where  $f_o$  and  $V_o$  are reference friction coefficient and slip velocity,  $a > 0$  and  $b > 0$  are rate and state parameters of order 0.01, and  $L$  is the characteristic slip distance. At constant slip velocity  $V$ , the state variable  $\theta$ , and hence the shear traction  $\tau$ , evolve toward steady-state values  $\theta_{ss}(V)$  and  $\tau_{ss}(V)$ , respectively, with  $\theta_{ss}(V) = L/V$  and  $\tau_{ss}(V) = \sigma [f_o + (a - b) \ln(V/V_o)]$ . The friction law is said to exhibit steady-state velocity strengthening if  $a - b > 0$ , and steady-state velocity weakening

if  $a - b < 0$ . The characteristic slip  $L$  can be interpreted as the slip necessary to renew surface contacts, and the state variable  $\theta$  ( $= L/V$  in steady state) can be interpreted as the average lifetime of contact population. In equation (3.10),  $\tau$  is not defined for  $V = 0$ . To remedy that, we use a regularized version of the law (Rice and Ben-Zion, 1996; Ben-Zion and Rice, 1997; Lapusta et al., 2000) described in Appendix 3.7.2.

Dynamic instability (i.e., an earthquake) is able to develop only if the steady-state velocity-weakening region of the fault exceeds the nucleation size  $h^*$  (e.g., Rice and Ruina, 1983; Rice, 1993; Rubín and Ampuero, 2005). Two theoretical estimates of the earthquake nucleation size for 2D problems are given by:

$$h_{\text{RR}}^* = \frac{\pi}{4} \frac{\mu^* L}{(b-a)\sigma} \text{ km}, \quad (3.11)$$

$$h_{\text{RA}}^* = \frac{2}{\pi} \frac{\mu^* b L}{(b-a)^2 \sigma} \text{ km}, \quad (3.12)$$

where  $\mu^* = \mu$  for mode III and  $\mu^* = \mu/(1 - \nu)$  for mode II. The estimate  $h_{\text{RR}}^*$  was derived from the linear stability analysis of steady sliding by Rice and Ruina (1983), while  $h_{\text{RA}}^*$  was obtained for the parameter regime  $a/b > 0.5$  by Rubín and Ampuero (2005) using the energy balance for a quasi-statically extending crack. 3D estimates would be larger by a factor of two to three;  $h_{\text{RA}}^*$  needs to be increased by a factor of  $\pi^2/4$  (A. Rubín, private communication). Chen and Lapusta (2008) have found that the resulting estimate,

$$h^* = (\pi^2/4)h_{\text{RA}}^*, \quad (3.13)$$

matches nucleation sizes in their 3D simulations quite well. Hence we adopt that estimate in our study.

The rate and state friction laws (3.10) behave similarly to standard linear-slip weakening laws during dynamic rupture propagation processes (e.g., Cocco and Bizzarri, 2002). As dynamic rupture arrives at a point along the fault, slip velocity rapidly increases with negligible slip, leading to  $V\theta/L \gg 1$ . With that condition, equation (3.10b) can be approximately rewritten as  $d\theta/dt =$

$-V\theta/L$  and integrated to express the state variable in terms of slip. From equation (3.10a), one then gets:

$$\frac{d\tau}{dt} = \sigma a \frac{d(\ln V)}{dt} - \frac{\sigma b}{L} \frac{d\delta}{dt}. \quad (3.14)$$

In (3.14),  $V$  is already in the seismic range and  $\ln V$  does not change much, making the term  $\sigma a d(\ln V)/dt$  much smaller than  $(\sigma b/L)(d\delta/dt)$ . Hence equation (3.14) describes linear decrease of shear stress with slip, with the slip-weakening rate  $W$ :

$$W = -\frac{d\tau}{d\delta} \approx \frac{\sigma b}{L}. \quad (3.15)$$

During this process, the state variable evolves with slip and the steady state is eventually reached, with shear resistance that has logarithmic dependence on slip velocity and hence does not vary much as long as slip velocity remains in the seismic range. That corresponds to the constant dynamic resistance of linear slip-weakening formulations.

Note that alternative rate and state formulations have been proposed, with different equations for the evolution of the state variable, such as the slip law (Dieterich, 1979, 1981; Ruina, 1983), the combined law of Kato and Tullis (2003), and the law in Perrin et al. (1995). Recent experiments by Bayart et al. (2006) suggest that the slip law is a better description of the friction response in velocity-jump experiments. The methodology developed in this work can be easily adopted to the alternative rate and state formulations, as well as to laws with variable normal stress (Dieterich, 2007) and modified formulations that include more significant weakening at seismic slip rates (Rice, 2006).

### 3.1.3 Criteria for spatial discretization

In numerical simulations, the spatial cell size  $\Delta x$  needs to be small enough to capture the model response. A number of studies (Rice, 1993; Ben-Zion and Rice, 1997; Lapusta et al., 2000) proposed that  $h_{\text{RR}}^*$  is the crucial length scale to resolve in 2D anti-plane earthquake cycle modeling, with  $h_{\text{RR}}^*/\Delta x$  being an important parameter. The length scale  $h_{\text{RR}}^*$  gives the critical size of a cell that

cannot become unstable on its own on a quasi-statically sliding interface (Rice and Ruina, 1983; Lapusta et al., 2000), and hence it is an important length scale governing interseismic processes and, in particular, earthquake nucleation.

However, earthquake cycle simulations also involve dynamic rupture, and that introduces another resolution criterion,  $\Lambda/\Delta x$ , where  $\Lambda$  is the cohesive zone size (Palmer and Rice, 1973; Day et al., 2005, and references therein). The cohesive zone size gives the spatial length scale over which the shear stress drops from its peak to residual values at the propagating rupture front. This length scale controls the numerical resolution during dynamic rupture. Let us denote by  $\Lambda_0$  the size of  $\Lambda$  at the rupture speed  $c \rightarrow 0^+$  ( $\Lambda$  decreases for larger rupture speeds). For the fault interface governed by linear slip-weakening law,  $\Lambda_0$  can be expressed as (Palmer and Rice, 1973; Day et al., 2005):

$$\Lambda_0 = C_1 \frac{\mu^*}{W}, \quad (3.16)$$

where  $W$  is the slip-weakening rate and  $C_1$  is a constant which is equal to  $9\pi/32$  if the stress traction distribution within the cohesive zone is linear in space. For the rate-and-state friction laws we use,  $W = b\sigma/L$  (Sections 3.1.2 and 3.2) and hence  $\Lambda_0$  is given by:

$$\Lambda_0 = C_1 \frac{\mu^* L}{b\sigma}. \quad (3.17)$$

Through 3D dynamic rupture simulations, Day et al. (2005) established that  $\Lambda_0/\Delta x$  of 3 to 5 are required to resolve dynamic rupture.

Hence the cell size  $\Delta x$  has to be small enough to resolve both  $\Lambda_0$  and  $h_{\text{RR}}^*$ . How are the two resolution criteria related? Ignoring the constants of order 1, the ratio of the two length scales for the constitutive law used in this work is:

$$\Lambda_0/h_{\text{RR}}^* = (b - a)/b. \quad (3.18)$$

The typical values are 0.015 to 0.02 for  $b$  and 0.002 to 0.004 for  $(b - a)$ , making the ratio  $\Lambda_0/h_{\text{RR}}^*$

vary from about 0.1 to 0.25. Hence the resolution criterion based on  $\Lambda_0$  dominates for these typical parameters. In this work and in Lapusta et al. (2000),  $b = 0.019$  and  $b - a = 0.004$  are used that give  $\Lambda_0/h_{\text{RR}}^* \approx 0.2$ . Hence resolving  $\Lambda_0$  with 3 to 5 spatial cells as suggested by Day et al. (2005) corresponds to resolving  $h_{\text{RR}}^*$  with 15 to 25 cells. This explains why the fully dynamic simulations of earthquake sequences by Lapusta et al. (2000) showed that  $h_{\text{RR}}^*$  needs to be discretized with about 20 cells in order to obtain resolution-independent results; that discretization was dictated by the size of the cohesive zone.

Hence resolving the cohesive zone size  $\Lambda_0$  is the more stringent requirement for the aging formulation of rate and state friction and typical rate and state parameters. This is true even for quasi-dynamic simulations (Section 3.5), in which  $\Lambda_0$  needs to be resolved with at least one cell size. For other fault constitutive relations, similar consideration should apply, in that the cell size  $\Delta x$  should be small enough to resolve all the relevant lengthscales in the problem, including the length scale governing the evolution of quasi-static deformation and nucleation of instability, as well as the length scale governing the evolution of the rupture front. For different laws, different length scales would dominate the resolution requirements. For example, in a law that combines rate and state friction with a dynamic weakening mechanism, such as pore pressure evolution, either the nucleation length scale or the rupture-front length scale may be the smallest one, depending on the values of parameters chosen for the two mechanisms.

### 3.1.4 Computational procedure

The response of faults to tectonic loading is characterized by long periods of quasi-static deformation combined with short bursts of fast slip. To simulate such response, we adopt the variable time stepping of Lapusta et al. (2000), in which the time step is set to be inversely proportional to slip velocity on the fault interface as described in Appendix 3.7.2. As the result, relatively large time steps, a significant fraction of a year, are used in the interseismic period, while small time steps, a fraction of a second, are used to simulate the evolution of each dynamic rupture. Note that the stability of the stepping procedure relies on the presence of the positive direct effect in the rate and

state formulation, the feature that has ample laboratory confirmation.

At each time step, we find updated values of the field variables by equating the elastodynamic tractions on the fault interface represented by equations (3.1) and the frictional strength of the fault given by equations (3.10). Appendix (3.7.2) describes the details of the updating procedure. Since 3D simulations are computationally expensive, parallel coding is an indispensable ingredient in our computations. We use the message passing interface (MPI) techniques to spread the storage of field variables into multiple processors. Calculation of the dynamic response, update of field variables, and fast fourier transforms (FFTs) are also done in parallel.

### 3.1.5 Model of a strike-slip fault

The elastodynamic formulation (3.1–3.2) is valid for a planar interface  $y = 0$  embedded in an infinite elastic homogeneous medium. Due to the spectral representation, the finite domain of interest is periodically replicated in both  $x$  and  $z$  directions. Hence the simulated domain needs to include buffer zones that would prevent dynamic ruptures on each replication from interacting with each other. An example is shown in Figure 3.1a, where a potentially seismogenic zone (shown in white) is surrounded by the fault region (shown in grey) that can stop dynamic ruptures. Such region can have steady-state velocity-strengthening properties and/or prescribed slip velocity (e.g., slip velocity equal to the plate rate or to zero). The methodology developed in this work has been used in such a model to study small repeating earthquakes (Chen and Lapusta, 2008).

Here, we would like to study the behavior of a strike-slip fault embedded in an elastic *half*-space, with a free surface at  $z = 0$ , as shown in Figure 3.1b. To fit this model into the formulation (3.1–3.2), we use the image method (e.g., Lapusta et al., 2000). The domain that we would like to study on the fault interface is  $x \in [-\lambda_x/2, \lambda_x/2]$ ,  $z \in [-\lambda_z/2, 0]$ , where  $z = 0$  is the free surface. We add a mirror image of that domain by imposing the following conditions in the region  $x \in [-\lambda_x/2, \lambda_x/2]$ ,  $z \in [0, \lambda_z/2]$  :

$$\begin{cases} \delta_x(x, -z; t) = \delta_x(x, z; t), & V_x(x, -z; t) = V_x(x, z; t) \\ \delta_z(x, -z; t) = -\delta_z(x, z; t), & V_z(x, -z; t) = -V_z(x, z; t). \end{cases} \quad (3.19)$$

The resulting simulated domain becomes  $x \in [-\lambda_x/2, \lambda_x/2]$ ,  $z \in [-\lambda_z/2, \lambda_z/2]$ , and it is that domain that is periodically repeated along both  $x$  and  $z$  directions to form an infinite interface in a homogeneous elastic space, making the formulation (3.1–3.2) applicable.

The mirror-image method induces the boundary conditions on  $z = 0$  as  $\tau_{zx} = \tau_{zy} = 0$  and  $u_z = 0$ , which are not exactly the traction-free boundary conditions  $\tau_{zx} = \tau_{zy} = \tau_{zz} = 0$ . However, this approximation works quite well for strike-slip faults, which slip mostly in the along-strike direction  $x$ . In the code comparison exercise organized by the Southern California Earthquake Center (SCEC), simulations of dynamic rupture on a slip-weakening strike-slip fault in an elastic half-space have been compared for different numerical methods (Harris et al., 2004, 2008). The comparison of our approach with other methods that can represent the true traction-free surface showed that this approximation captures most effects of the free surface and that the errors induced are relatively small and restricted to the region right next to the free surface. Recently, Zhang and Chen (2006a,b) derived a boundary-integral formulation with analytical kernels for a planar fault of an arbitrary dipping orientation embedded in an elastic half-space. These kernels have more complex representations and using them in the context of long-term calculations is a goal for future work.

To incorporate tectonic loading, we assume that the far-field plate motion results in the deeper extension of the fault moving with constant slip rate equal to the plate rate  $V_{\text{pl}}$  (Tse and Rice, 1986), as illustrated in Figure 3.1b. Hence we assign a constant slip rate  $V_{\text{pl}}$  in the corresponding part of our domain, and solve for slip rate everywhere else on the fault.

## 3.2 Simulation example: fault with a homogeneous seismogenic region

### 3.2.1 Parameters of the fault model

Let us use the developed methodology to simulate long-term slip history of a strike-slip fault segment which contains a potentially seismogenic region with steady-state velocity weakening properties surrounded by steady-state velocity-strengthening region (Figure 3.2a). The seismogenic region

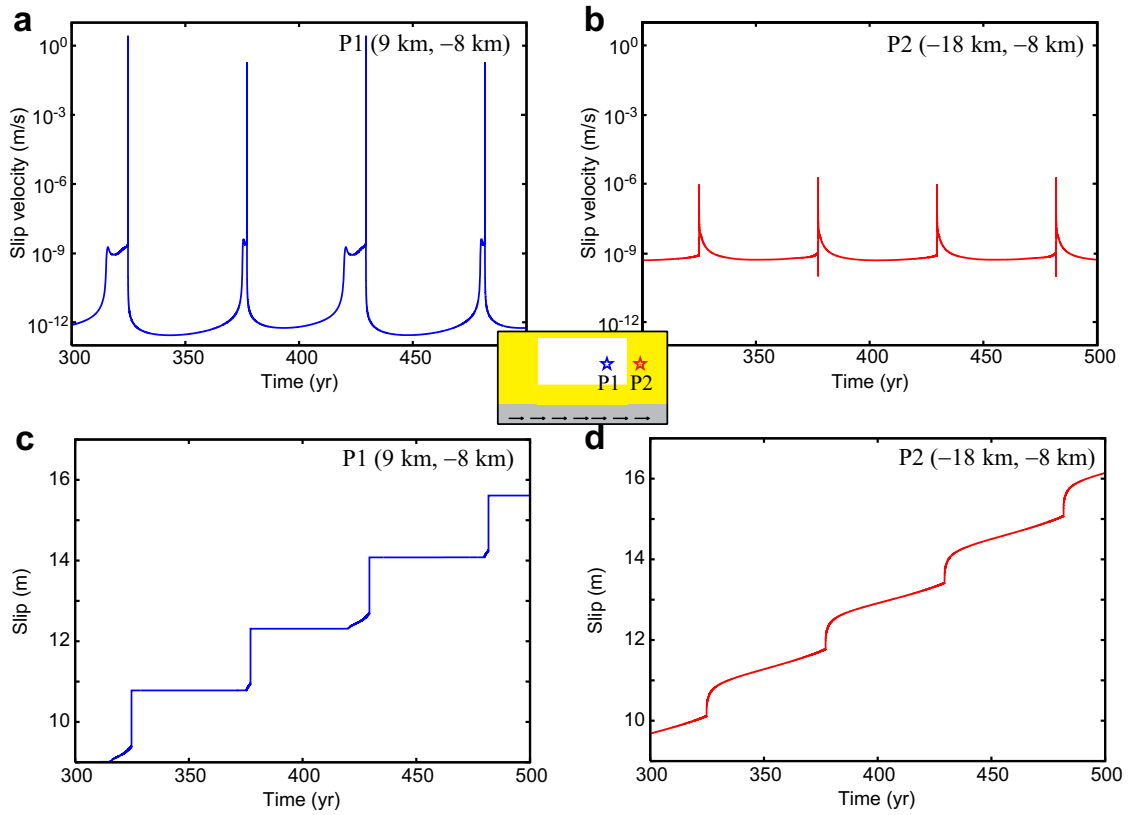


Figure 3.3: Long-term histories of slip and slip velocity history at two representative fault locations, P1 from the velocity-weakening region and P2 from the velocity-strengthening region. Slip velocity is plotted on the logarithmic scale. (a),(c) Point P1 (9 km,-8 km) exhibits stick-slip behavior. It is virtually locked for most of the time (with slip velocity three orders of magnitude below the plate rate) but occasionally slips very fast, with maximum slip velocity on the order of 1 m/s. (b),(d) Point P2 (-18 km,-8 km) moves throughout the simulated time. After each dynamic event, it has postseismic slip, with maximum slip velocity on the order of  $10^{-6}$  m/s.

incorporates gradual variations of rate and state parameters at the top and bottom rheological transitions but we call the region homogeneous in comparison to the model of Section 3.4 where the seismogenic region incorporates a compact heterogeneity in the form of higher normal stress. Model parameters are given in Figure 3.2 and Table 3.1. The fault segment is 60 km long and 30 km deep. With the mirror image, the simulated domain is  $\lambda_x = \lambda_z = 60$  km. Rate and state friction acts on the top 24 km of the fault, while the bottom fault segment,  $-30 < z < -24$  km, slips with the plate rate of  $V_{\text{pl}} = 10^{-9}$  m/s or 32 mm/year. The potentially seismogenic velocity-weakening region is located at  $-15 < x < 15$  km and  $-14.34 < z < -2.67$  km and it is  $L_{\text{seis}} = 30$  km long and  $W_{\text{seis}} = 11.7$  km wide. Within the seismogenic region, the depth distributions of rate and state parameters  $a$ ,  $(a - b)$ , and  $L$  are given in Figure 3.2b.  $L$  linearly increases at shallow depths, qualitatively modeling the plausible situation of larger frictional energy resisting sliding at shallow depths due to wider gouge layers or multiple slip surfaces. Normal traction on the fault interface is space- and time-independent,  $\sigma(x, z) = \tau_y(x, z; t) = \tau_y^o(x, z; t) = 50$  MPa. The constant value of  $\sigma$  close to the free surface is chosen for numerical tractability, to explore several issues unrelated to the free surface such as interaction of rupture with heterogeneity over several earthquake cycles (Section 3.4) and quasi-dynamic and other simplified formulations (Section 3.5). In Section 3.2.4, we compare fault behavior with other distributions of  $L$  and  $\sigma$ , including smaller values of  $\sigma$  at shallower depths and depth-independent  $L$ .

The characteristic slip  $L$  shown in Figure 3.2 is equal to 8 mm over most of the fault; we also use the distribution with twice smaller values of  $L$  for comparison, resulting in  $L = 4$  mm over most of the fault. Such values of  $L$  result in much larger 3D estimates of nucleation sizes,  $h^* = 9$  km for  $L = 8$  mm and  $h^* = 4.5$  km for  $L = 4$  mm, than what would be obtained based on laboratory values of  $L = 10\text{--}100$   $\mu\text{m}$ . Such large values of  $h^*$  may be realistic under some conditions, e.g., if effective normal stress  $\sigma$  is very low due to fluid overpressure (e.g., Liu and Rice, 2005; Suppe and Yue, 2007) or if steady-state velocity-weakening properties are close to velocity-neutral. We need such large values of  $L$  to be able to resolve the dynamic propagation of seismic events that arise in the model. As discussed in Section 3.1.3,  $h^*$  should be smaller than the size of the velocity-weakening region

in order for the model to produce dynamic events. Hence the parameter  $h^*/W_{\text{seis}}$  that relates the estimated nucleation size to the width of the velocity-weakening region is an important indicator of how unstable the behavior of the model would be (Liu and Rice, 2005; Rubin, 2008).  $h^*/W_{\text{seis}} \geq 1$  predicts quasi-static behavior, while smaller values point to unstable behavior. For  $L = 8$  mm,  $h^*/W_{\text{seis}} = 0.8$ , a value close to 1. For  $L = 4$  mm,  $h^*/W_{\text{seis}} = 0.4$ , a value appreciably smaller than 1. Hence the two cases may exhibit qualitative differences.

The simulation starts with a dynamic event that initiates on the left edge of the fault and propagates through the entire fault. This is achieved by setting higher initial shear stress  $\tau_x^o = 1.02f_o\sigma$  for  $-15 \text{ km} < x < -10 \text{ km}$  than for the rest of the fault, where  $\tau_x^o = 1.00f_o\sigma$ . The initial values of field quantities affect only the first few events, as the model evolves towards behavior dictated by the model geometry, loading, and friction properties. The fault is discretized into square elements  $\Delta x = \Delta z = 100$  m ( $N_x = N_z = 600$ ) for simulations with  $L = 8$  mm and  $\Delta x = \Delta z = 50$  m ( $N_x = N_z = 1200$ ) for simulations with  $L = 4$  mm. The numerical resolution is discussed in Section 3.3.1. The time step during dynamic events is  $\Delta t_{\text{min}} = 0.0112$  for ( $L = 8$  mm) and  $\Delta t_{\text{min}} = 0.0056$  s ( $L = 4$  mm). Simulations have been done in parallel on 20 processors for  $L = 8$  mm and 100 processors for  $L = 4$  mm, each with the memory of 2 GB. About one billion data points are manipulated at each time step, and each earthquake cycle requires on the order of ten thousand variable time steps.

### 3.2.2 Fault response: dynamic events and aseismic slip, including transients

As expected from stability properties of rate-and-state interfaces, the velocity-strengthening region steadily slips with velocities comparable to the plate rate, while the velocity-weakening region accumulates most of its slip through earthquakes. Histories of slip velocity and slip for two representative points are shown in Figure 3.3. At point P1 from the velocity-weakening region ( $x = 9$  km,  $z = -8$  km), slip velocity is three orders of magnitude smaller than the loading plate rate for most of the simulated time, indicating that the fault is typically locked at this location (Figure 3.3a). Occasion-

ally, slip velocity of P1 goes up to seismic values of the order of 1 m/s, indicating the occurrence of seismic slip. Slip accumulation of P1 has the corresponding step-like nature (Figure 3.3c). In contrast, point P2 ( $x = 18$  km,  $z = -8$  km) from the velocity-strengthening region has slip velocity that never deviates too much from the plate rate of  $10^{-9}$  m/s (Figure 3.3b). Relatively small increases of slip velocity at P2 after each earthquake correspond to postseismic slip. Slip at P2 increases steadily in time, with faster accumulation after each dynamic event (Figure 3.3d).

Typical earthquake cycles are illustrated in Figures 3.4 and 3.5 through snapshots of slip-velocity distribution on the fault at several times between two successive dynamic events. For the case of  $L = 8$  mm and  $h^*/W_{\text{seis}} = 0.8$  (Figure 3.4), the ninth earthquake nucleates on the left side of the seismogenic region, and propagates bilaterally first and then mostly to the right (panels A–C). The seismic slip causes positive static stress changes in the surrounding velocity-strengthening area, which responds with increased aseismic slip rates that decay over time (panels D–E). This is postseismic slip. During the interseismic period (panel F), the velocity-weakening region is locked, while the surrounding velocity-strengthening region moves with slip velocity of the order of the plate rate. That aseismic slip creates stress concentration at the boundary between the locked and slipping regions, causing slip there and hence continuously moving the boundary into the locked region. For  $L = 8$  mm, the locked region almost disappears (panel J), consistently with the large estimate of the nucleation zone  $h^* = 9$  km which approximates how far slow slip can penetrate into velocity-weakening region without nucleating a dynamic event. That interseismic slip contains a slip episode faster than the plate rate, i.e., an aseismic transient, which is shown in Figure 3.6 on a different slip-velocity scale. The transient develops on the left side of the locked region (panel G8) and propagates around the locked region (panels G8–I8), decreasing the locked part in the process. Maximum slip velocity during this aseismic transient is about  $10^{-7}$  m/s, and its propagation speed is about 8 km/year. Between the times of 480.43 and 481.52 years, the average slip of the seismogenic region is 0.061 m and the corresponding moment is  $6.4 \times 10^{17}$  N · m, an equivalent of a  $M_w = 5.8$  earthquake. These values are qualitatively consistent with some observations of aseismic transients (e.g., [Kawasaki, 2004](#)). At the end of the transient, the next dynamic event nucleates on the right

side of the seismogenic region (panel K of Figure 3.4) and propagates bilaterally first (panel L) and then mainly to the left.

For the smaller value of characteristic slip  $L = 4$  mm and hence for the smaller  $h^*/W_{\text{seis}} = 0.4$ , the seismogenic region is more unstable and experiences less aseismic slip in the interseismic period (Figure 3.5). Events nucleate closer to the rheological transition (panel A) and propagate more unilaterally (panels B–C). Right after postseismic slip (panels D–E), most of the seismogenic region is locked and the fault behavior for both values of  $L$  is quite similar (panels F, Figures 3.4 and 3.5). In the interseismic period, aseismic transients still occur for  $L = 4$  (Figure 3.6, panels G4–I4), but now it is clear that they are mostly confined to the areas of the velocity-weakening region close to rheological transitions that experience slow-slip penetration from the nearby velocity-strengthening region. Further discussion of aseismic transients is given in section 3.6. When the next dynamic event nucleates (panels J–L, Figure 3.5), much of the velocity-weakening region remains locked.

To visualize slip accumulation on the fault through several earthquake cycles, we plot slip along the horizontal line  $z = -8$  km (Figure 3.7). The solid green lines are plotted every 5 years, representing slip accumulations during interseismic periods. The dashed red lines are plotted every 2 seconds when the maximum slip velocity on the fault exceeds 1 mm/s, illustrating the end of earthquake nucleation and seismic slip accumulation. Only a part of the fault, from  $x = -20$  km to  $x = 20$  km, is shown. The spacing of the green lines indicates that the fault outside the velocity-weakening region moves steadily for most of the time and experiences faster postseismic motion after dynamic events. Densely spaced red lines correspond to the end of the nucleation phase, while more sparse red lines illustrate dynamic rupture propagation. For  $L = 8$  mm and  $h^*/W_{\text{seis}} = 0.8$  (Figure 3.7a), this relatively homogeneous model produces a periodic two-event pattern. For  $L = 4$  mm and  $h^*/W_{\text{seis}} = 0.4$  (Figure 3.7b), the model settles into periodic behavior, with all events starting on the left side of the fault. This is because events have larger slip at the other end of the fault and relieve more stress there, resulting in the nucleation of the next event on the same side of the fault. The behavior is more complex for  $h^*/W_{\text{seis}} = 0.8$  due to aseismic transients. The aseismic transients also always start on the side of the fault that nucleated the previous dynamic event. However, they

do not initiate dynamic slip but rather propagate towards the other side of the fault, initiating a dynamic event there.

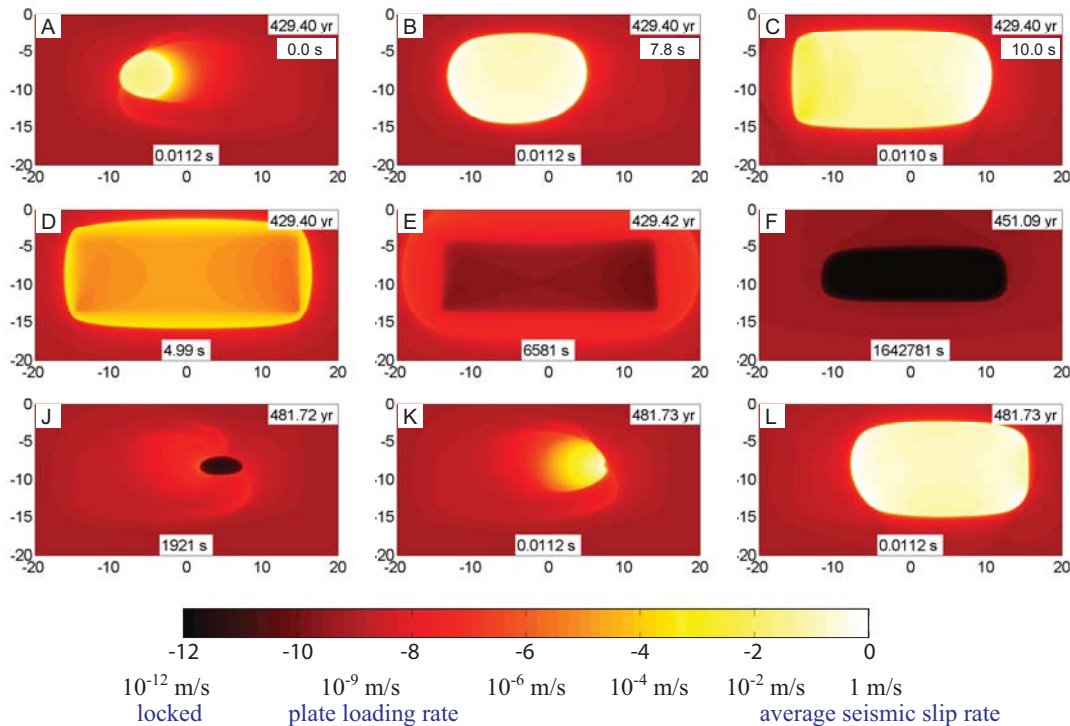


Figure 3.4: Snapshots of spatial slip-velocity distribution during a typical earthquake cycle for  $L = 8$  mm ( $h^*/W_{\text{seis}} = 0.8$ ). Slip history between the 9th and 10th events is illustrated. Colors represent slip velocity on the logarithmic scale. White and bright yellow correspond to seismic slip rates, orange and red correspond to aseismic slip, and black corresponds to locked portions of the fault. Each panel shows the time  $t$  of the snapshot in years (in the upper-right corner) and the corresponding time step  $\Delta t$  in seconds (at the bottom of each panel). Panels A–C also show the time in seconds elapsed since the time of panel A. The simulations reproduce dynamic events (panels A–C and K–L), postseismic slip (panels D–E), and the interseismic period (panel F). Aseismic transient slip occurs between panels F and J and it is shown in panels G8–I8 of Figure 3.6 on a different slip-velocity scale.

### 3.2.3 Parameters of simulated earthquakes

The model produces realistic dynamic events, with maximum slip velocity over the fault exceeding 1 m/s and rupture speeds reaching 2.5 km/s. Let us define the seismic moment  $M_0$  of each event as the moment released on the fault when maximum slip velocity exceeds 0.1 m/s:

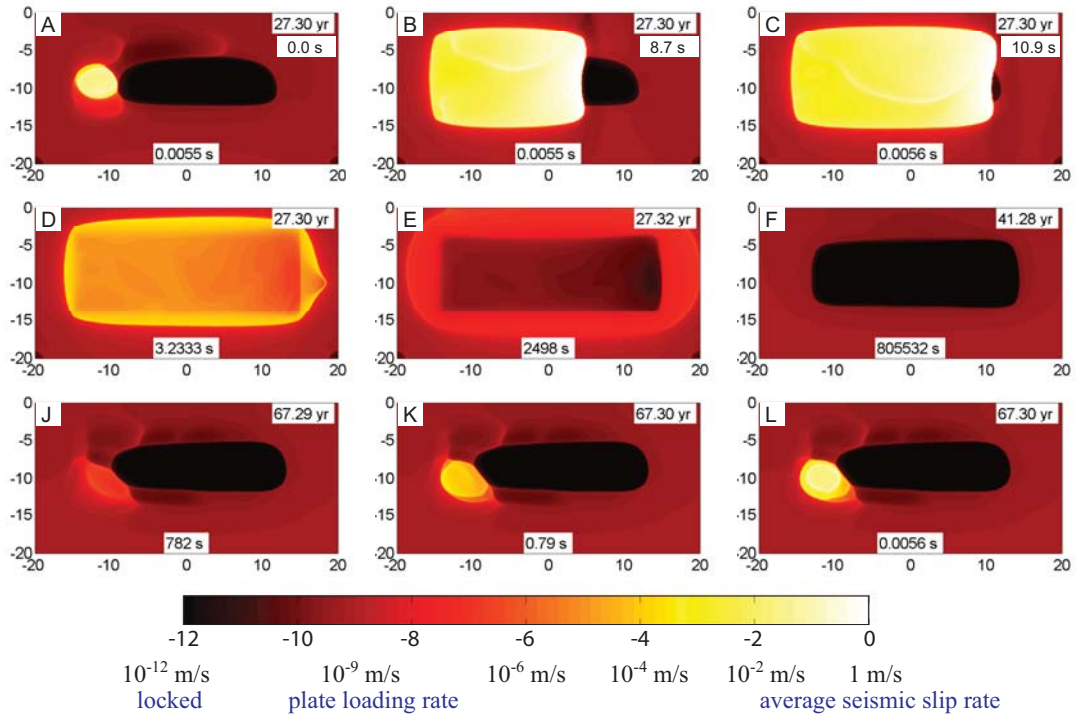


Figure 3.5: Snapshots of spatial slip-velocity distribution during a typical earthquake cycle for  $L = 4$  mm ( $h^*/W_{\text{seis}} = 0.4$ ). Slip history between the 2nd and 3d events is illustrated. Colors and time markings have the same meaning as in Figure 3.4. Compared with the case with  $L = 8$  mm (Figure 3.4), dynamic events in the case with  $L = 4$  mm have smaller nucleation size, nucleate closer to the rheological transition (panels A, L), have more unilateral propagation, and develop faster rupture speeds (panels A–C). Consistent with the smaller value of  $h^*/W_{\text{seis}}$ , the velocity-weakening region experiences less aseismic slip, with large portion of the region still locked when a seismic event nucleates (panels A, J–L). Smaller aseismic transients still occur between panels F and J; they are shown in panels G4–I4 of Figure 3.6.

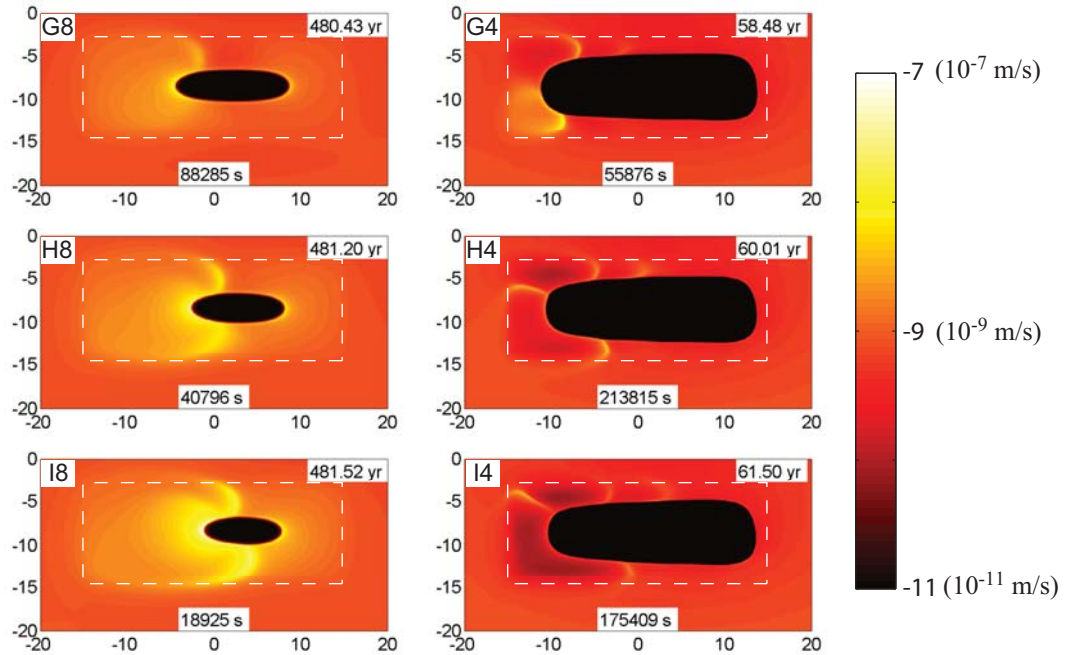


Figure 3.6: Snapshots of spatial slip-velocity distribution illustrating aseismic transients. White dashed rectangles show the extent of the velocity-weakening region. Panels G8–I8 correspond to the simulation with  $L = 8$  mm. The aseismic transient travels around the locked portion of the fault. The average rupture speed between panels G8 and I8 is about 10 km/s and the maximum slip velocity is about  $10^{-7}$  m/s. The aseismic slip accumulated in the seismogenic region is equivalent to that of a  $M_w = 5.8$  earthquake. Panels G4–I4 correspond to the simulation with  $L = 4$  mm. The spatial extent of the transients is smaller. Again, the transients travel around the locked portion of the fault. Comparison of the two cases shows that the transients are confined to the band of the velocity-weakening region next to rheological transition which experiences slow slip in the interseismic period. The width of the band scales with the nucleation size and its estimate  $h^*$ . That is why smaller values of  $h^*/W_{\text{seis}}$  lead to smaller and more localized aseismic transients.

Table 3.1: Parameters of our simulations. For depth-dependent quantities marked with the asterisk “\*”, the typical value over the velocity-weakening (potentially seismogenic) region is specified.

Parameter	Symbol	Value	
Fault length along strike	$\lambda_x$	60 km	
Fault depth	$\lambda_z/2$	30 km	
Velocity-weakening region, length	$L_{\text{seis}}$	30 km	
Velocity-weakening region, width	$W_{\text{seis}}$	11.7 km	
Loading slip rate	$V_{\text{pl}}$	32 mm/yr	
Shear wave speed	$c_s$	3.0 km/s	
Poisson’s ratio	$\nu$	0.25	
Reference slip velocity and friction coefficient	$V_o$ $f_o$	10 <sup>-6</sup> m/s 0.6	
Rate-and-state parameters* in the velocity-weakening region	$a$ $b$	0.015 0.019	
Effective normal stress*	$\sigma$	50 MPa	
Characteristic slip*	$L$	8 mm	4 mm
Cell size	$\Delta x$	100 m	50 m
Minimum time step	$\Delta t_{\text{min}}$	0.0112 s	0.0056 s

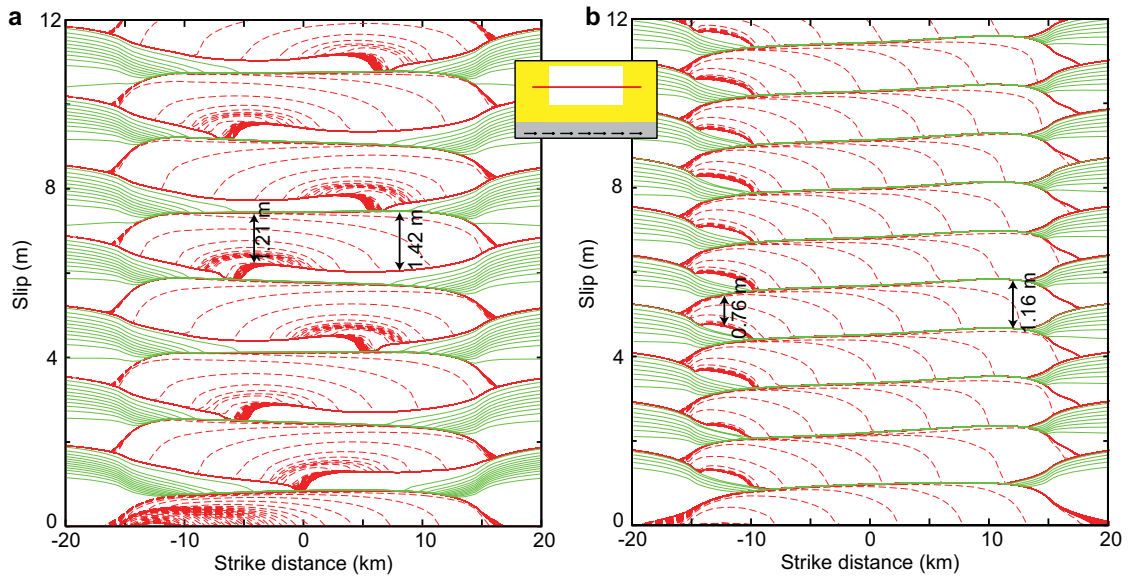


Figure 3.7: Slip accumulation along the line  $z = -8$  km for the case of the homogeneous seismogenic region. Red dashed lines illustrate fast slip; they are plotted every 2 s when maximum slip velocity over the fault exceeds 1 mm/s. Green solid lines are plotted every 5 years, representing slip accumulation in interseismic periods. (a) The case with  $L = 8$  mm settles into a periodic two-event pattern. (b) The case with  $L = 4$  mm results in periodic events. In the latter case, dynamic ruptures propagate faster and are more pulse-like. In both cases, points at the nucleation zones accumulate less slip seismically than points elsewhere on the fault.

$$M_0 = \int_{t_{\text{ini}}}^{t_{\text{end}}} \int_{\Omega} \mu V(x, z; t') d\Omega dt', \quad (3.20)$$

where  $\Omega$  is the seismogenic (velocity-weakening) region with the area  $|\Omega| = W_{\text{seis}}L_{\text{seis}}$ , and  $t_{\text{ini}}$  and  $t_{\text{end}}$  are times for each dynamic event, between which maximum slip velocity on the fault stays larger than  $V_{\text{seis}} = 0.1$  m/s. Similarly, we compute the static stress drop  $\Delta\tau$  as:

$$\begin{aligned} \Delta\tau &= \bar{\tau}_x(t_{\text{ini}}) - \bar{\tau}_x(t_{\text{end}}) \\ &= \frac{1}{|\Omega|} \int_{\Omega} \tau_x(x, z; t_{\text{ini}}) d\Omega - \frac{1}{|\Omega|} \int_{\Omega} \tau_x(x, z; t_{\text{end}}) d\Omega. \end{aligned}$$

For  $L = 8$  mm,  $M_0 = 1.1 \times 10^{19}$  N · m for each event, corresponding to the moment magnitude  $M_w = 6.6$ ,  $\bar{\tau}_x(t_{\text{ini}}) = 31.2$  MPa,  $\bar{\tau}_x(t_{\text{end}}) = 27.8$  MPa, and  $\Delta\tau = 3.4$  MPa. For  $L = 4$  mm,  $M_0 = 9.9 \times 10^{18}$  N · m,  $M_w = 6.6$ ,  $\bar{\tau}_x(t_{\text{ini}}) = 31.2$  MPa,  $\bar{\tau}_x(t_{\text{end}}) = 28.0$  MPa, and  $\Delta\tau = 3.2$  MPa. The average seismic slip on the seismogenic part of the fault per event is  $\bar{\delta}_{\text{seis}} = M_{\text{seis}}/\mu|\Omega| = 1.01$  m for  $L = 8$  mm and 0.94 m for  $L = 4$  mm. Since the plate loading rate is  $V_{\text{pl}} = 32$  mm/year and the earthquake period is  $T = 52.4$  years for  $L = 8$  mm and 37.4 years for  $L = 4$  mm, slip accumulation per earthquake cycle is  $\bar{\delta} = V_{\text{pl}}T = 1.65$  m for  $L = 8$  mm and 1.18 m for  $L = 4$  mm. Therefore, 61% and 80% of fault slip in the seismogenic region is accumulated seismically for  $L = 8$  mm and  $L = 4$  mm, respectively.

Each point ruptured dynamically exhibits effective stress-slip dependence that closely resembles linear slip-weakening laws, as discussed in Section 3.1.2. This is illustrated in Figure 3.8, which shows the behavior of three velocity-weakening points and one velocity-strengthening point. The velocity-strengthening point is located close to rheological transition. For all curves, the weakening slope is well-approximated by  $W = -\sigma b/L$ . For  $L = 8$  mm, we find that the effective slip-weakening behavior is similar for different points but not identical, with the peak stress and effective slip-weakening distance increasing with the rupture propagation. This is because the rupture accelerates as it propagates along the fault. For  $L = 4$  mm, the dependence of stress on slip is nearly identical for the velocity-weakening points, because the rupture accelerates early in the event and, afterwards,

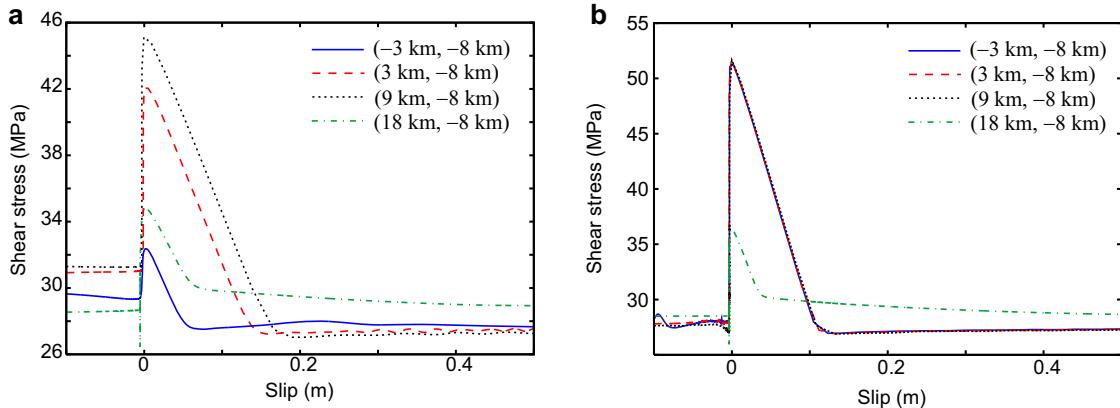


Figure 3.8: Shear stress as a function of slip during a representative dynamic event (the 9th one in the sequence) for four locations on the fault with (a)  $L = 8$  mm and (b)  $L = 4$  mm. In both cases, dynamic rupture propagates from the left side of the fault to the right side, passing the velocity-weakening locations (-3 km, -8 km), (3 km, -8 km), (9 km, -8 km), and then influencing the velocity-strengthening location (18 km, -8 km) as the rupture arrests in the velocity-strengthening region. Zero slip for each point is chosen as the slip when shear stress at the point reaches its peak during the dynamic event. We see that the effective dependence of stress on slip is similar to linear slip-weakening friction, with the slip-weakening rate  $W \approx \sigma b/L$ . The velocity-strengthening point has a smaller values of  $b$  than the other three points and hence a smaller slope. In the case with  $L = 8$  mm, rupture accelerates while propagating through the points shown (Figure 3.7a), leading to different effective peak strength and slip-weakening distances for the three velocity-weakening points. In the case with  $L = 4$  mm, the rupture has nearly reached its limiting speed and it is almost steady (Figure 3.7b), leading to similar behavior of the velocity-weakening points.

the relatively homogeneous fault properties and conditions ensure that the rupture behavior does not change much as the rupture propagates along the fault.

### 3.2.4 Effect of parameter distributions near the free surface

In the presented simulations, effective normal stress  $\sigma = 50$  MPa is constant throughout the fault and the characteristic slip  $L$  is depth-dependent near the free surface. Because of the relatively large  $\sigma$ , and hence large velocity-strengthening effect  $\sigma(a - b)$ , dynamic rupture arrests shortly upon encountering the shallow velocity-strengthening region and does not reach the free surface (Figure 3.9a). While constant  $\sigma$  at depth can be motivated by fluid overpressure (Rice, 2006),  $\sigma$  should decrease to near-zero values at the free surface. To investigate the effect of  $\sigma$  and  $L$  near the free surface, we consider the case of Lapusta et al. (2000), in which normal stress is depth-dependent near the free surface,  $\sigma = \min[2.8 + 18|z|/\text{km}, 50]$  MPa, and the characteristic slip  $L$  is constant and equal to the value at depth. In this case, the rupture propagates all the way to the free surface (Figure

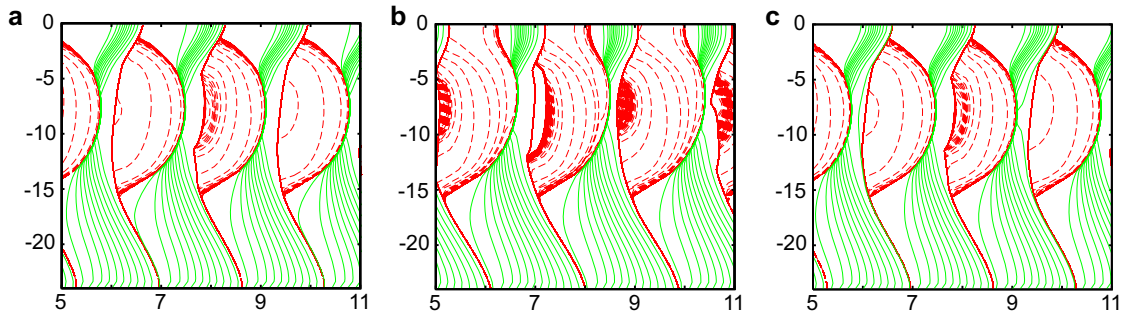


Figure 3.9: Accumulation of slip along the line  $x = 3$  km, for the fault with the homogenous seismogenic region and the case of  $L = 8$  mm. Lines have the same meaning as in Figure 3.7. Different near-surface parameter distributions are explored. (a) In the case of Section 3.2.1–3.2.2 and Figures 3.3–3.8 with constant normal stress and depth-dependent  $L$ , dynamic events do not reach the free surface, arresting in the velocity-strengthening region. The free surface accumulates large slip deficit, which is compensated by aseismic slip. (b) For depth-independent  $L$  and normal stress decreasing towards the free surface (the same distributions as in the 2D model of Lapusta et al. (2000)), dynamic ruptures propagate all the way to the free surface, consistently with the results of Lapusta et al. (2000). (c) When distributions of parameters  $a$  and  $b$  in the case of panel (b) are modified to match the distributions of  $\sigma a$  and  $\sigma b$  of the case in panel (a), the near-surface behavior becomes very similar to the case of panel (a).

3.9b), as it did in the 2D simulations of Lapusta et al. (2000). However, even with the depth-variable normal stress, we can prevent the rupture from reaching the free surface by modifying rate and state parameters  $a$  and  $b$  so that  $a\sigma$  and  $b\sigma$  are the same as in our original example (Figure 3.9c). For the problems considered in this work, it is not essential whether slip does or does not propagate to the free surface, and we use the parameters of Section 3.1 in simulations presented in the following.

### 3.3 Parameter validation

#### 3.3.1 Spatial discretization

For the model with  $L = 8$  mm, we have  $h_{RR}^* = 1.26$  km and  $\Lambda_0 = 233$  m for the mode II direction. (This theoretical estimate of  $\Lambda_0$  is close to the value of 300 m obtained in our simulations.) Hence, as discussed in Section 3.1.3,  $\Lambda_0 = 233$  m is the smaller length scale and the one we should aim to resolve. To make sure our simulations produce resolution-independent results, we run a series of simulations with cell sizes  $\Delta x = 50$  m, 100 m, 200 m, and 400 m. Figure 3.10(a) and (b) show slip accumulation along  $z = -8$  m for  $\Delta x = 50$  m and  $\Delta x = 400$  m. Comparing with the

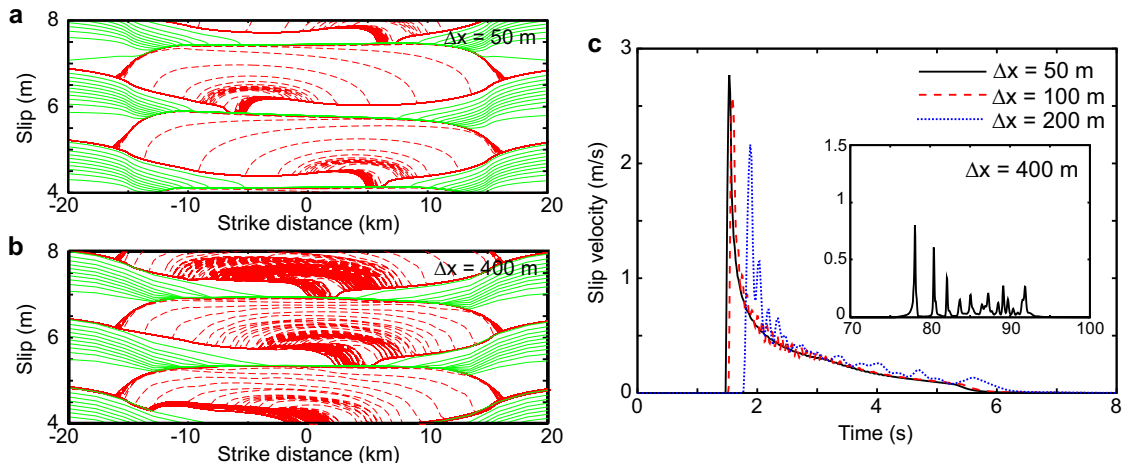


Figure 3.10: Fully dynamic simulations with different cell sizes  $\Delta x$ . (a),(b) Slip accumulation along the line  $z = -8$  km for  $\Delta x = 50$  m and 400 m, respectively. The results can be compared with Figure 3.7a that shows slip accumulation for  $\Delta x = 100$  m. (c) Slip-velocity history of the fault location (9 km,  $-8$  km) during the 5th event for  $\Delta x = 50$  m, 100 m, 200 m, and 400 m. Zero in time corresponds to rupture arrival at the location (6 km,  $-8$  km). The values  $\Delta x = 50$  m and 100 m are both several times smaller than the quasi-static cohesive zone size  $\Lambda_0 = 300$  m and produce resolution-independent results.  $\Delta x = 200$  m provides less adequate resolution and  $\Delta x = 400$  m leads to very different results. The numerical resolution in our simulations is dictated by the cohesive zone size, as the nucleation size  $h^*$ , another important length scale, is several times larger.

results for  $\Delta x = 100$  m in Figure 3.7, we find that  $\Delta x = 50$  m and  $\Delta x = 100$  m produce virtually indistinguishable slip patterns over earthquake cycles. The value  $\Delta x = 400$  m produces a completely different slip pattern, indicating poor numerical resolution. The simulation with  $\Delta x = 200$  m (not shown) produces a slip pattern which is similar to that of  $\Delta x = 50$  m and  $\Delta x = 100$  m but has notable differences, such as deeper nucleation regions and 2% smaller slip per cycle.

Figure 3.10c shows slip-velocity history of the fault location (9 km,  $-8$  km) during the 5th event. Zero time is chosen as the arrival time of rupture at the point (6 km,  $-8$  km). Again,  $\Delta x = 100$  m and  $\Delta x = 50$  m produce similar results during dynamic rupture propagation, although slip velocity has some oscillations for  $\Delta x = 100$ . These oscillations are due to the kernel discretization, as discussed in Appendix 3.7.1. For  $\Delta x = 200$ , rupture time is noticeably larger, slip velocities are smaller, and the profile is more oscillatory. As the rupture propagates, the cohesive zone becomes smaller, making  $\Delta x = 200$  m inadequate. For  $\Delta x = 400$  m (insert), the result is completely different, indicating numerical problems. Hence we confirm the finding of Day et al. (2005) that the quasi-static cohesive zone in 3D simulations needs to be resolved by about 3 cells.

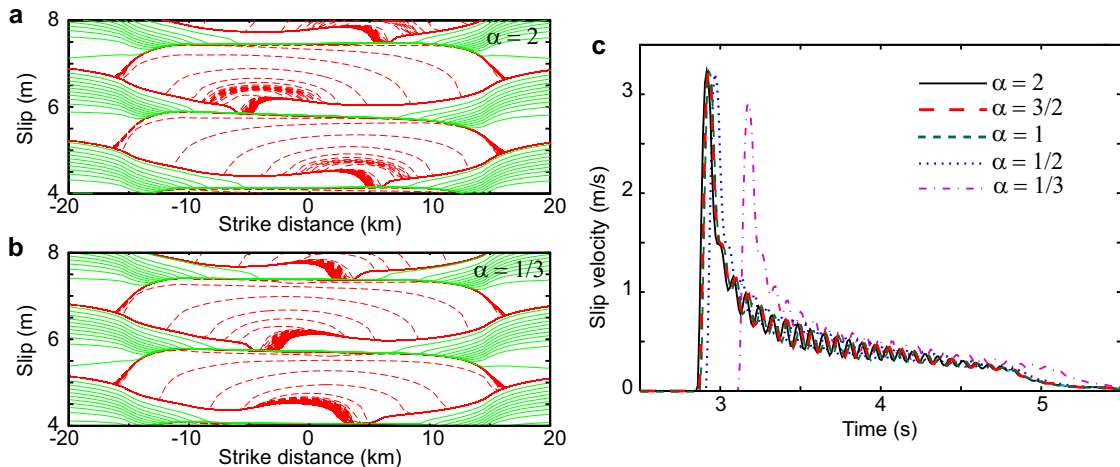


Figure 3.11: Fully dynamic simulations with different values of the truncation parameter  $\alpha$ . (a),(b) Slip accumulation along the line  $z = -8$  km for  $\alpha = 2$  and  $1/3$ , respectively. The results can be compared with Figure 3.7a that shows slip accumulation for  $\alpha = 3/2$ . (c) Slip-velocity history of the fault location (12 km,  $-8$  km) during the 5th event for  $\alpha = 1/3, 1/2, 3/2, 1$ , and  $2$ . Zero in time corresponds to rupture arrival at the location (6 km,  $-8$  km). Larger values of  $\alpha$  lead to inclusion of longer slip histories in the dynamic response calculation.  $\alpha = 2, 3/2$ , and  $1$  produce similar results, while  $\alpha = 1/2$  and  $1/3$  cause differences as discussed in the text.

### 3.3.2 Frequency-independent truncation

To determine the suitable value of parameter  $\alpha$  in the frequency-independent truncation window  $T_w = \alpha\lambda/c_s$ , we do a series of simulations with  $\alpha = 2, 3/2, 1, 1/2$ , and  $1/3$ . Simulations with  $\alpha = 2, 3/2, 1$  all produce virtually indistinguishable results in terms of both earthquake patterns and slip-velocity histories during individual events (Figures 3.11 and 3.7a), indicating that either of them can be used in the truncation procedure. We use  $\alpha = 3/2$  in most of our simulations. Simulations with  $\alpha = 1/2$  and  $1/3$  produce somewhat different behavior. For example, the rupture speed is 2% smaller for  $\alpha = 1/2$  and 9% smaller for  $\alpha = 1/3$ .

### 3.3.3 Frequency-dependent truncation

As discussed in Section 3.1.1, frequency-dependent truncation can save a lot of computational resources, including memory. It has two parameters,  $\alpha$  and  $\rho_c$ . We fix  $\alpha = 3/2$ , a value that performs well in the frequency-independent truncation, and compare results for several values of  $\rho_c$ . For  $N_x = N_z = 600$  and  $\Delta x = 100$  m, frequency-independent truncation implies  $\rho_c = \alpha\lambda\hat{q}_{\max} \approx 2000$ . To activate frequency dependence, we need to choose a smaller value of  $\rho_c$ . We try  $\rho_c = 250, 200$ ,

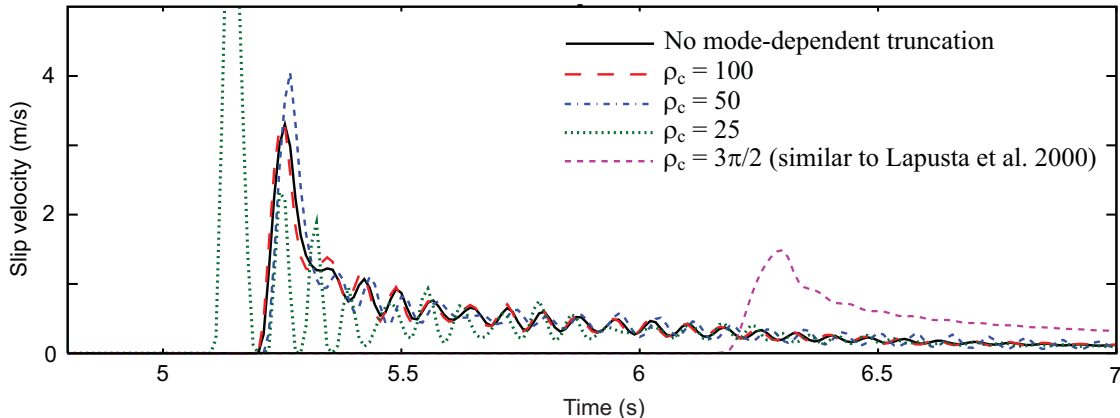


Figure 3.12: Slip-velocity history of the fault location (12 km,  $-8$  km) during the first event in fully dynamic simulations with different values of the truncation parameter  $\rho_c$ . Zero in time corresponds to the rupture arrival at the location (3 km,  $-8$  km). Larger values of  $\rho_c$  make the frequency-dependent truncation closer to the frequency-independent one. Our frequency-dependent truncation with  $\rho_c = 3\pi/2$  approximately corresponds to the truncation parameters in Lapusta et al. (2000).  $\rho_c \geq 100$  produce the same results as the frequency-independent truncation.

150, 100, 50, 25, and  $3\pi/2$ . The last value approximately reproduces the truncation scheme used in Lapusta et al. (2000). We find that simulations that use frequency-dependent truncation with  $\rho_c \geq 100$  produce the same results as simulations with frequency-independent truncation. Figure 3.12 shows slip-velocity history of the fault location (12 km,  $-8$  km) during the first event for different values of  $\rho_c$ . The simulation with  $\rho_c = 100$  has the same rupture time at this location as the simulation with frequency-independent truncation, and the difference in peak velocity between the two simulations is less than 5%. Hence truncation with  $\rho_c = 100$  gives adequate results while using only 9.7% of the memory required for frequency-independent truncation. The memory savings would be more significant for smaller cell sizes or larger fault dimensions. The simulation with  $\rho = \alpha\pi = 3\pi/2$ , which worked well in 2D antiplane models (Lapusta et al., 2000), produces rather poor results, with much more slowly rupture speeds and slip velocity. The difference between 2D anti-plane and 3D problems arises due to properties of mode II kernel as discussed in Section 3.1.1.

### 3.4 Long-term interaction of slip with compact heterogeneity

As an application example, let us investigate long-term behavior of a fault segment in the presence of compact heterogeneity. This study requires the fully dynamic 3D approach for simulating long-term slip developed in this work, as the existing 2D dynamic and 3D quasi-dynamic methodologies may not be able to capture all features of the response as explained in Section 1. We use the model of Section 3.2.1 with a stronger circular patch of 20% larger effective normal stress  $\sigma$ . The patch is centered at the location ( $x = 3$  km,  $z = -8$  km) and has the radius of 1 km. The other model parameters are the same as in Section 3.2.1, including  $L = 8$  mm, with the exception of initial shear stress outside the strip  $-15$  km  $< x < -10$  km. The value  $1.00f_o\sigma$  of section 3.2 results in the first event that is slower than subsequent events (Figure 3.7a). Since we would like to compare interaction of dynamic rupture with the stronger patch in the first event with the interaction in subsequent events, it is important for the first event to be more dynamic. To achieve that, we use initial shear stress of  $1.01f_o\sigma$  outside the strip  $-15$  km  $< x < -10$  km.

#### 3.4.1 Supershear burst in the first event

The first event nucleates in the region of higher initial shear stress on the left side of the seismogenic region and propagates towards the location of the patch. Since the patch is stronger than the surrounding fault but the initial shear stress is uniform, the front of dynamic rupture is delayed at the asperity during the first event (Figure 3.13, top row, left panel). Note that the slip-velocity scale in Figure 3.13 is different than in previous figures with slip-velocity snapshots; the scale in Figure 3.13 is chosen to illuminate the rupture front. Slip in the surrounding areas concentrates shear stress at the patch, breaking it and creating a supershear burst over a part of the rupture front (Figure 3.13, top row, middle and right panels). Along the horizontal line  $z = -8$  km, the rupture front advances 3.4 km in 0.84 s, with the average rupture speed of  $c = 4.0$  km/s, which is larger than the shear wave speed  $c_s = 3$  km/s. Such supershear bursts were studied by Dunham et al. (2003) in simulations of single earthquakes on faults governed by linear slip-weakening friction. In our simulation, the supershear part of the front transitions back to sub-Rayleigh speed shortly

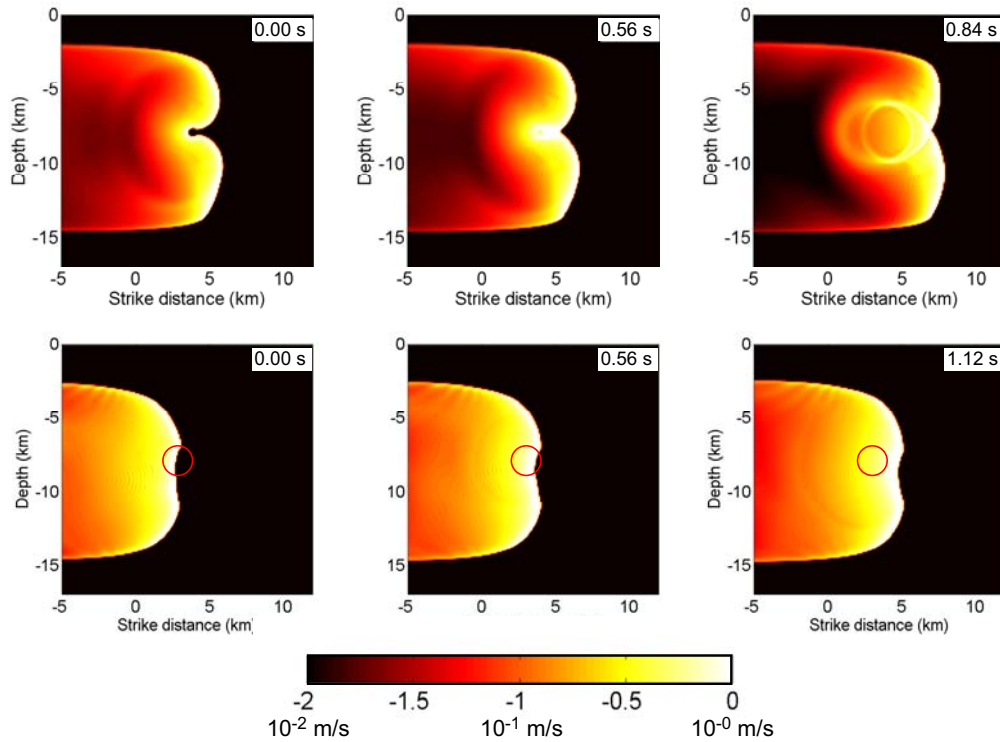


Figure 3.13: Snapshots of slip-velocity distribution during the first (top row) and second (bottom row) events for the case with a stronger patch. The slip-velocity range shown is different from Figures 3.4–3.6 and chosen to emphasize the rupture front. The number in the upper-right corner of each snapshot indicates the elapsed time (in seconds) since the first snapshot for each event. During the first event, dynamic rupture interacts with the stronger patch and produces a supershear burst. During the second event, no interaction or supershear propagation occurs; the stronger patch is indicated by a red circle in this case. Rupture behavior of the first event does not repeat in the slip history of the fault due to redistribution of shear stress.

afterwards.

### 3.4.2 No supershear burst in subsequent events

The supershear burst observed in the first event is due to interaction of dynamic rupture with the normal-stress heterogeneity. Will this interaction repeat in subsequent events? The second earthquake also nucleates on the left side of the seismogenic region and propagates towards the stronger patch. The bottom row of Figure 3.13 shows the snapshots of slip velocity distribution during the second event as the rupture front passes through the patch. The snapshots show that there is no interaction of the rupture front with the stronger patch. In the panels corresponding to the first event (top row), the patch location is obvious; in the panels corresponding to the second event (bottom row), we need to mark the patch with a red circle to indicate its location. The rupture front smoothly propagates through the patch with sub-Rayleigh speeds. The average horizontal rupture speed in the time period between the first and the third snapshot is  $c = 2.0$  km/s or about 0.7 of the Rayleigh wave speed. Rupture continues to accelerate as it propagates further along the fault interface. Note that the concave rupture-front profile in the bottom row of Figure 3.13 is also present in the case without the patch during the second event, and it is not related to the presence of the stronger patch. Rather, it is caused by higher rupture speeds close to the boundary between creeping and locked regions due to shear stress concentration there.

Hence dynamic rupture does not “notice” the patch during the second event and, in fact, during all subsequent events. This is due to redistribution of shear stress on the fault after the first event. Figure 3.14 shows two shear stress distributions along the horizontal line  $z = -8$  km, which passes through the center of the patch, during the first and second events. The distributions correspond to the time when the rupture front that propagates towards the patch is about 2 km away from the patch. Before rupture propagates through the patch in the first event, shear stress inside the patch is approximately equal to the initial shear stress of 30.3 MPa. The ratio of shear stress and effective normal stress  $\tau/\sigma$  is 0.505 inside the patch and 0.606 in the surrounding region. Therefore, the patch delays the rupture and then produces a supershear burst. However, before rupture propagation over

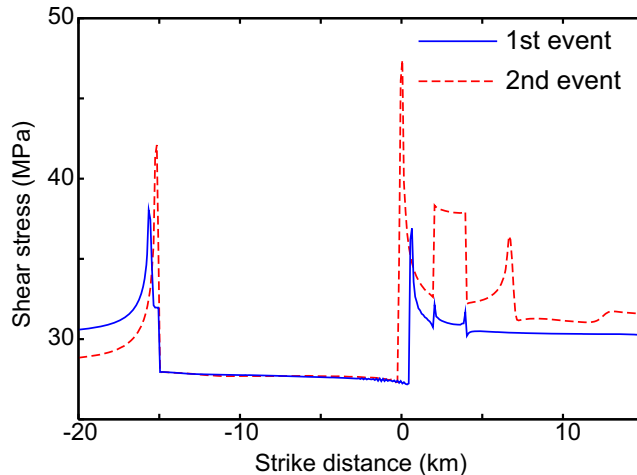


Figure 3.14: Distribution of shear stress along the line  $z = -8$  km during the 1st and 2nd events, at the time when the horizontal rupture front (at this depth) arrives approximately at the center of the fault ( $x = 0$  km). In the 1st event, the patch has similar shear stress  $\tau$  as the surrounding area but 20% larger normal stress  $\sigma$ , resulting in smaller nondimensional prestress  $\tau/\sigma$  than the rest of the fault. However, in the second event,  $\tau$  inside the patch is about 20% larger than in the surrounding area, resulting in homogeneous nondimensional prestress  $\tau/\sigma$ . This redistribution of shear stress due to prior slip history eliminates the interaction of dynamic rupture with the patch observed in the first event.

the patch in the second event, shear stress inside the patch is higher, about 37.2 MPa, and the ratio  $\tau/\sigma$  is 0.62 inside the patch and 0.63 outside of it. In other words, before the second event, shear stress is proportionally higher at the patch, compensating for its higher strength.

This simple example illustrates the necessity of long-term simulations of fault behavior for understanding effects of fault heterogeneity, even if one is concerned with dynamic events only. While any prestress can be assumed for simulations of a single dynamic rupture, stress distribution before events in long-term simulations as well as on natural faults is the result of complicated history of seismic and aseismic slip, which depends, in part, on the strength distribution. Our results suggest that distributions of fault stress and strength are related and cannot be assumed independently.

### 3.4.3 Effect of heterogeneity on long-term behavior

The 20% stronger patch occupies less than 1% of the fault area, yet it changes the long-term behavior of slip in this model. We compare the homogeneous-fault case of Section 3.2.2 and the case of one small heterogeneity considered here using plots of slip accumulation along the horizontal line  $z = -8$

km (Figures 3.7a and 3.17a). We see that while the sequence of large events maintains its two-event periodicity, the stronger patch destroys the symmetry in fault properties between the left and right sides of the fault, resulting in asymmetric behavior. In the homogeneous case, aseismic transients alternate the direction of their propagation, moving from left to right before one event and the other way before the next one. In the case with the stronger patch, all aseismic slip propagates from left to right. Once the slow slip reaches the stronger patch, an event nucleates. This is because larger effective normal stress corresponds to a smaller nucleation size, favoring rupture nucleation there. Correspondingly, the nucleation process at the right side of the fault is modified and shifted to occur at the asperity.

#### 3.4.4 Fault interaction with heterogeneity of higher normal stress

Let us denote the normal stress inside the heterogeneity as  $\sigma_h$ . In Section 3.2,  $\sigma_h = \sigma = 50$  MPa, and there is no heterogeneity. In Section 3.4,  $\sigma_h = 1.2\sigma = 60$  MPa, the heterogeneity has 20% larger effective normal stress than the surrounding area. In this section, we investigate the long-term fault interaction with heterogeneity having higher effective normal stress  $\sigma_h = 1.4\sigma, 1.6\sigma, 1.8\sigma$ , and  $2.0\sigma$ .

Simulations show that interaction of rupture with heterogeneity diminishes for events after the first one, almost disappearing after the first three events (Figure 3.15). Interestingly, for  $\sigma_h = 2.0\sigma$ , rupture does not break the heterogeneity during the first event. After the first three events, interaction of dynamic rupture with the patch is much reduced, even for twice stronger patch, as shown in Figure 3.15.

The heterogeneity does influence the long-term behavior of the fault, increasing the complexity of slip histories. Figure 3.16 shows the earthquake recurrence period  $T$  for different  $\sigma_h$ . For the simulated values of  $\sigma_h$ ,  $T$  reaches the maximum value at  $\sigma_h = 1.2\sigma$ , and then decreases for larger  $\sigma_h$ . This behavior arises from the following two competing factors. On the one hand, higher normal stress inside the heterogeneity results in larger shear stress drop in each dynamic event, and requires longer interseismic time to restrengthen the fault, and hence favors larger  $T$ . On the other hand, areas of larger normal stress have smaller earthquake nucleation sizes, which facilitates earthquake

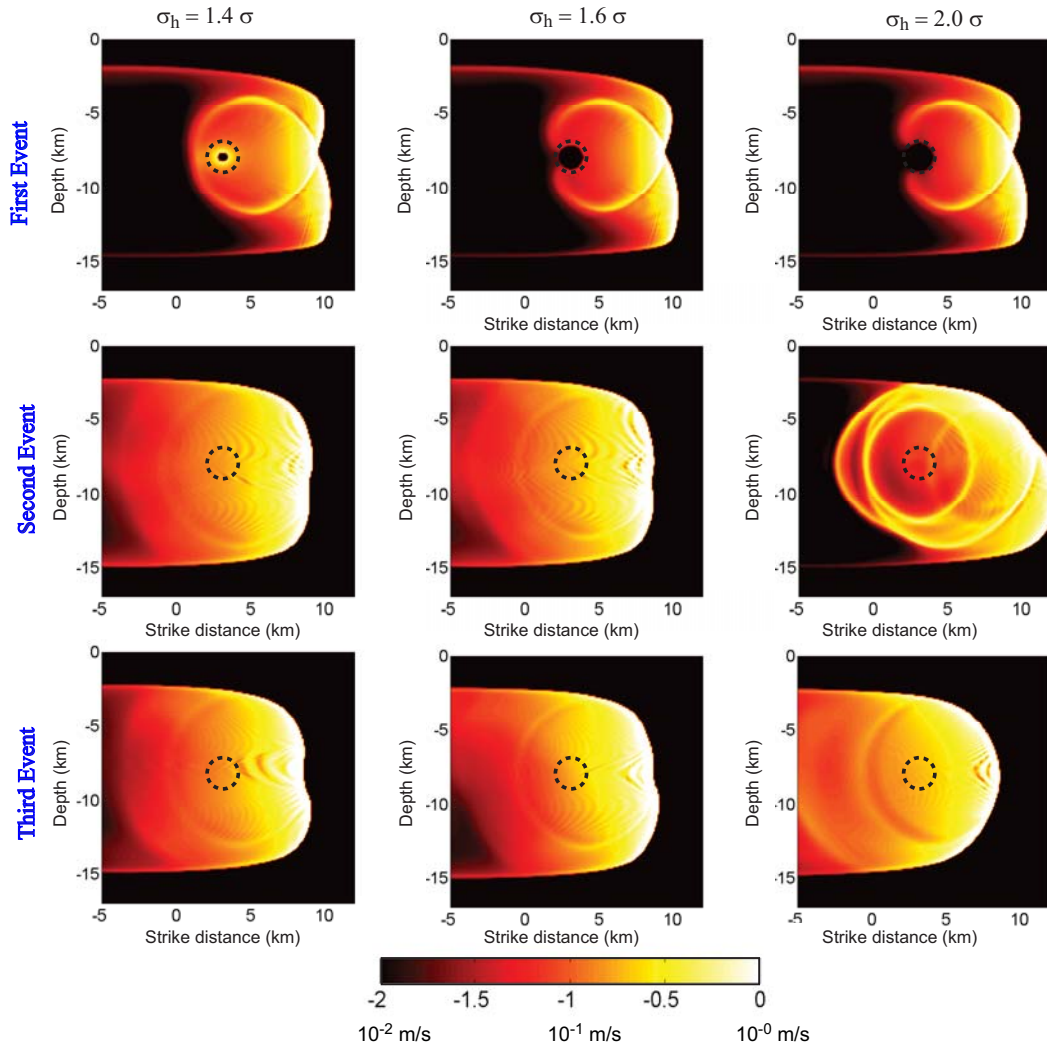


Figure 3.15: Snapshots of slip velocity during the first three events for  $\sigma_h = 1.4\sigma$ ,  $1.6\sigma$ , and  $2.0\sigma$ . Black circles are plotted to indicate the location of the heterogeneity. Due to redistribution of shear stress with slip, the interaction of dynamic rupture with heterogeneity becomes insignificant after the first three events.

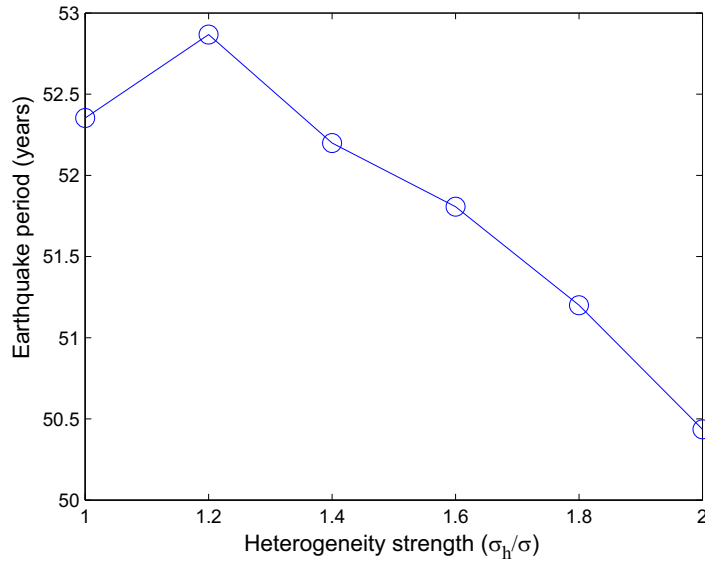


Figure 3.16: Earthquake recurrence period  $T$  for different heterogeneity strengths  $\sigma_h$ . Higher normal stress inside the patch increases the shear stress drop in dynamic events, and thus tends to increase  $T$ . On the other hand, higher normal stress decreases the earthquake nucleation size, and thus facilitates earthquake occurrence.

nucleation, and leads to smaller  $T$ . Whether  $T$  increases or decreases with  $\sigma_h$  depends on the relative importance of these two competing factors. For  $\sigma_h = 1.2$ , earthquakes nucleate outside the patch, and the first factor wins. For higher  $\sigma_h$ , some earthquakes start to nucleate at the patch, and the second factor dominates.

We also observe the models with  $\sigma_h \leq 1.6\sigma$  always produce typical large events, however, the models with  $\sigma_h \geq 1.8\sigma$  have occasional small events, which occur around the heterogeneity. For heterogeneity of high normal stress, failure of the heterogeneity can lead to either small or large events, depending on the stress distribution outside the patch.

### 3.5 Comparison of fully dynamic and quasi-dynamic approaches

If the fully dynamic formulation is replaced with the quasi-dynamic one (e.g., [Rice, 1993](#)), simulations become much simplified and computational resources needed are significantly reduced. The quasi-dynamic formulation has been widely used in earthquake studies (e.g., [Rice, 1993](#); [Ben-Zion and Rice,](#)

1995; Rice and Ben-Zion, 1996; Hori et al., 2004; Kato, 2004; Hillers et al., 2006; Ziv and Cochard, 2006). It ignores wave-mediated stress transfers expressed through convolutions integrals in equation (3.2) by setting  $T_w = 0$  for all Fourier modes. Any increment of slip induces instantaneous static stress changes everywhere on the fault. However, the quasi-dynamic formulation differs from the quasi-static one in that it retains dynamic radiation terms  $\eta_i V_i(x, z; t)$  in equation (3.1), capturing some dynamic effects and allowing solution to exist during dynamic instabilities.

Here we compare the results of quasi-dynamic 3D calculations with the fully dynamic ones and explore the suggestion of Lapusta et al. (2000) that smaller radiation damping terms in the quasi-dynamic formulation can make the comparison more favorable. For this study, we use the model with a stronger patch from Section 3.4.

### 3.5.1 Generalized quasi-dynamic formulation

Let us generalize the quasi-dynamic formulation to allow for smaller radiation damping coefficients. Shear components of tractions can be written as

$$\tau_i(x, z; t) = \tau_i^o(x, z; t) + f_i(x, z; t) - \frac{\mu}{2c_s\beta_s} V_i(x, z; t), \quad (3.21)$$

where  $i = x, z$ ,  $\beta_s$  is a constant, and the convolution integrals in  $f_i(x, z; t)$  are ignored. For the standard quasi-dynamic formulation, we have  $\beta_s = 1$ , and we are interested in  $\beta_s \geq 1$ . Wave speeds enter the quasi-static formulation through the radiation damping terms in (3.21) and through the static stress transfers in (3.2) which use the ratio  $c_p/c_s$ . Therefore, the generalized quasi-dynamic formulation (3.21) with  $\beta_s > 1$  corresponds to the standard quasi-dynamic approach with faster wave speeds:

$$\bar{c}_s = \beta_s c_s, \quad \bar{c}_p = \beta_s c_p. \quad (3.22)$$

Because of the faster wave speeds, we need to use smaller time steps  $\bar{\Delta}t_{\min}$  in calculations with  $\beta_s > 1$ :

$$\bar{\Delta}t_{\min} = \gamma \frac{\Delta x}{\bar{c}_s} = \gamma \frac{\Delta x}{\beta_s c_s} = \frac{\Delta t_{\min}}{\beta_s}. \quad (3.23)$$

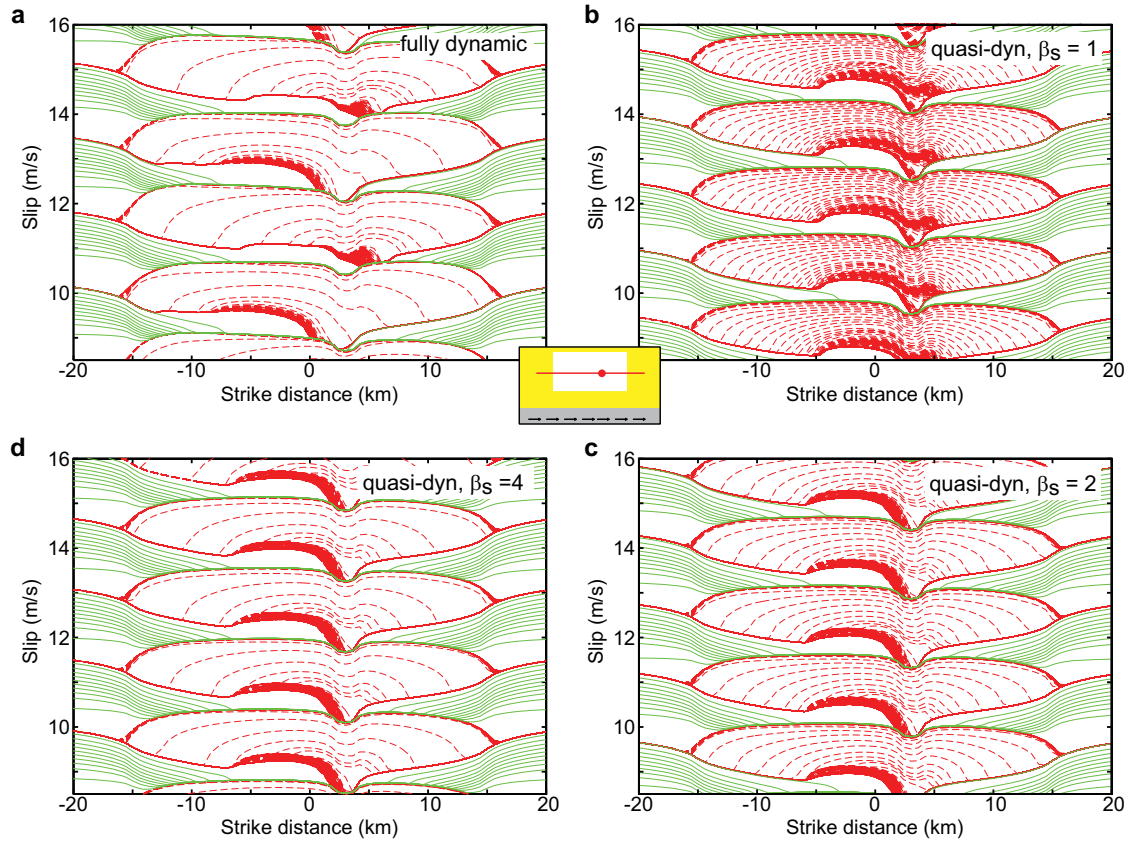


Figure 3.17: Accumulation of slip along the line  $z = -8$  km for the case with a stronger patch. Lines have the same meaning as in Figure 3.7. (a) Results for the fully dynamic simulation. The slip pattern of the fault with a small stronger patch (which occupies less than 1% of the seismogenic area) is different from the one with the homogeneous seismogenic region (Figure 3.7a). (b) The standard quasi-dynamic formulation ( $\beta_s = 1$ ) results in a modified slip pattern, smaller slip velocity, slower rupture speeds, and smaller slip per event. (c),(d) Larger values of  $\beta_s = 1$  or smaller radiation terms in the quasi-dynamic formulation accelerate rupture speed and increase slip velocity. However, all quasi-dynamic simulations produce similar slip patterns that are qualitatively different from the fully-dynamic one.

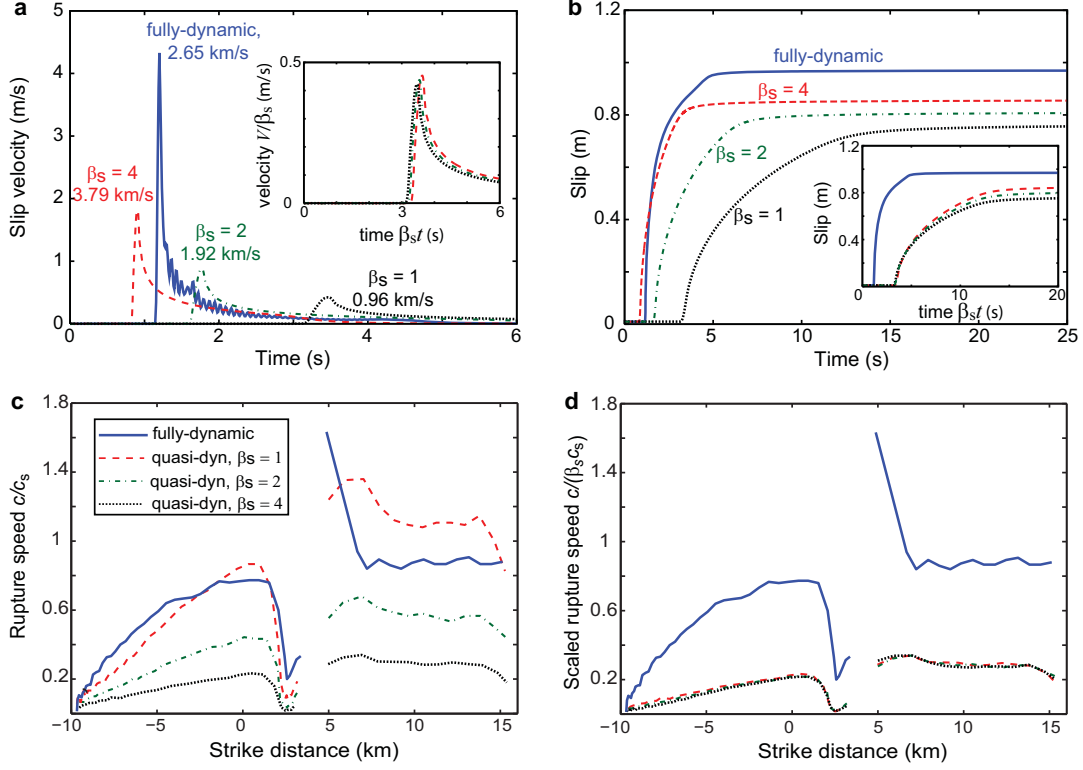


Figure 3.18: Comparison of fully dynamic and quasi-dynamic simulations of one dynamic event (the first event in the sequence). (a),(b) Slip-velocity and slip histories of the fault location (9 km, -8 km). Zero time corresponds to the time of rupture arrival at the point (6 km, -8 km). Slip velocity and slip per event in quasi-dynamic simulations is significantly smaller than in the fully-dynamic one. Simulations with larger  $\beta_s$  produce faster rupture speeds, larger slip velocity, and larger slip per event. However, when scaled appropriately, the quasi-dynamic results all collapse onto the same curves (insets in panels (a) and (b)). (c),(d) Rupture speed as a function of rupture tip location along  $z = -8$  km. The quasi-dynamic simulation with  $\beta_s = 4$  has larger rupture speeds than the fully-dynamic simulation. All quasi-dynamic simulations have nearly identical scaled rupture speed  $c/(\beta_s c_s)$ , as shown in panel (d).

We have confirmed conclusion (3.23) in our simulations. This means that simulating quasi-dynamic problems with smaller radiation damping terms is more challenging, as it requires smaller time steps and more computational time. This consideration is also consistent with the fact that the quasi-static formulation cannot be used to model dynamic rupture. For the quasi-static formulation,  $\beta_s = +\infty$  and, according to equation (3.23), the time steps should be infinitely small.

### 3.5.2 Similarity of quasi-dynamic solutions and their differences with fully dynamic results

Let us compare the fully dynamic simulation of Section 3.4 with several quasi-dynamic simulations that use different values of  $\beta_s$ . Figure 3.17 shows slip accumulation along the horizontal line  $z = -8$  km for the fully-dynamic simulation and the quasi-dynamic simulations with  $\beta_s = 1, 2,$  and  $4$ . We choose a part of slip history that already reflects the long-term behavior of the model. The first observation is that the rupture speed and slip velocity, which are related to the horizontal and vertical spacing of red dashed lines, respectively, are much lower for the standard quasi-dynamic simulation ( $\beta_s = 1$ ) than for the fully dynamic one. However, the rupture speed and slip velocity increase for larger  $\beta_s$  and, for  $\beta_s = 4$ , look comparable to that of the fully dynamic simulation.

Hence it is tempting to conclude that larger values of  $\beta_s$  result in a better match. However, further examination reveals a problem. All quasi-dynamic simulations share a qualitatively similar periodic slip pattern: earthquakes nucleate in the middle of the fault and propagate bilaterally. The fully-dynamic simulation has a different slip pattern that consists of two events, as discussed in Section 3.4.3. Hence it seems that differences that accumulate during dynamic events are sufficient to change long-term fault behavior even in this relatively simple model.

Comparison of individual events in Figure 3.18 further demonstrates the similarity among quasi-dynamic simulations and their differences with the fully dynamic one. Slip and slip-velocity histories of one point on the fault ( $x = 9$  km and  $z = -8$  km) during the first event are shown in Figure 3.18(a) and (b). Zero for each time history is chosen as the time of rupture arrival at the point with  $x = 6$  km and  $z = -8$  km. From Figure 3.18a, we can get the average rupture speed between locations  $x = 6$  km and  $x = 9$  km along the line  $z = -8$  km, which is 0.96 km/s for quasi-dynamic simulation with  $\beta_s = 1$ , 1.92 km/s for  $\beta_s = 2$ , 3.79 km/s for  $\beta_s = 4$ , and 2.65 km/s for the fully dynamic simulation. Hence the rupture speed in the quasi-dynamic simulation with  $\beta_s = 4$  is faster than the fully-dynamic simulation. At the same time, slip velocity for  $\beta_s = 4$ , while substantially higher than that for  $\beta_s = 1$ , is still much smaller than slip velocity of the fully dynamic calculation. Furthermore, the final slip is smaller for all quasi-dynamic simulations (Figure 3.18b) than for the

fully dynamic one; this is also true about average slip per event and static stress drop. Increasing  $\beta_s$  further is not a productive approach to increasing slip velocity and slip rates, as the rupture speed would also increase, and the rupture speed for  $\beta_s = 4$  is already too high, as demonstrated in Figure 3.18c. For points between  $x = 6$  km and  $x = 15$  km, the rupture speed of the quasi-dynamic simulation with  $\beta_s = 4$  is higher than that of the fully dynamic run. Note that the standard quasi-dynamic approach (with  $\beta_s = 1$ ) fails to reproduce the supershear burst during the first dynamic event discussed in Section 3.4.1.

We find that quasi-dynamic simulations with different values of  $\beta_s$  can be scaled to match each other. The insets in Figure 3.18(a) and (b) show rescaled slip velocity  $V^* = V/\beta_s$  and slip  $\delta$  as functions of the rescaled time  $t^* = \beta_s t$ . Figure 3.18d plots rescaled rupture speeds  $c/(\beta_s c_s)$ , with the fully dynamic result for comparison. We see that all quasi-dynamic curves fall almost on top of each other in rescaled plots. Hence quasi-dynamic simulations with different  $\beta_s$  are similar to each other during dynamic rupture, provided we use rescaled time  $t^* = \beta_s t$ , slip velocity  $V^* = V/\beta_s$ , and rupture speed  $c^* = c/\beta_s$  (with stress  $\tau$ , slip  $\delta$ , and spatial coordinates  $x, z$  unchanged).

### 3.5.3 Cohesive zone size and numerical resolution in quasi-dynamic simulations

From simulations, we find that the cohesive zone size in quasi-dynamic calculations is always equal to the quasi-static cohesive zone size  $\Lambda_0$ . It does not decrease as rupture propagates and it is independent of  $\beta_s$ . Figure 3.19 shows stress distribution along parts of the line  $z = -8$  km during the first event for the quasi-dynamic simulations with  $\beta_s = 1$  and  $\beta_s = 4$ . The simulated events are shown in the bottom row. Note that we use  $\Delta x = 50$  m in these simulations, instead of 100 m, to better capture the size of the cohesive zone. In Figure 3.19a of  $\beta_s = 1$ , the rupture front is at  $x = -7.9$  km and the average rupture speed before that location is only 0.12 km/s, which is less than 5% of the shear wave speed. The cohesive zone size in that situation, which is equal to 6 cell sizes or 300 m, should be very close to the quasi-static cohesive zone size. The theoretical estimate in Section 3.3.1 gives a similar value of 233 m. At the later stages of this rupture, the cohesive zone

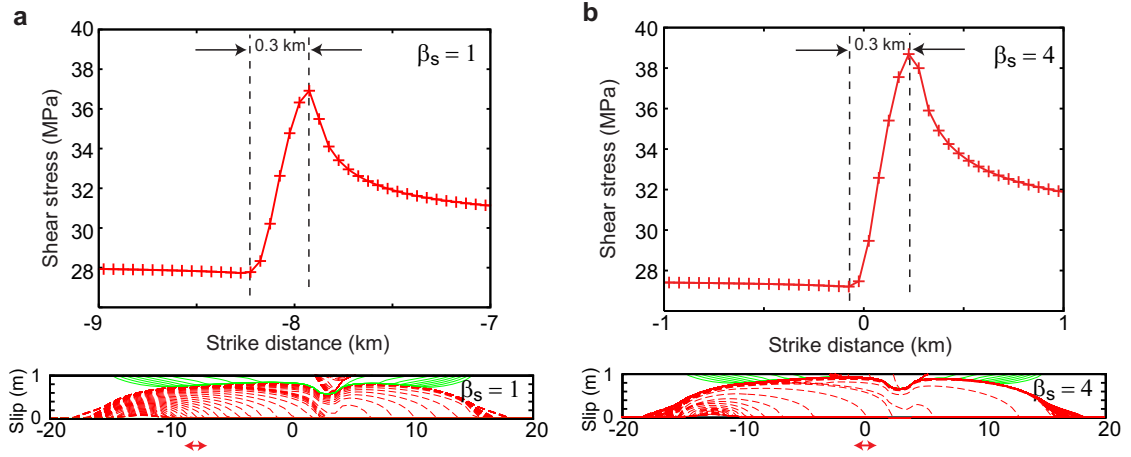


Figure 3.19: Cohesive zones in quasi-dynamic simulations. (a) Shear stress distribution along the horizontal line  $z = -8$  km at the time of rupture front arrival at point  $(-7.9$  km,  $-8$  km) during the first event in the simulation with  $\beta_s = 1$ . Crosses indicate locations of spatial cells ( $\Delta x = 50$  m). The rupture speed at that time is  $0.12$  km/s. The cohesive zone size is  $0.3$  km. The bottom panel shows the accumulation of slip in that case, with the double arrow indicating the distance plotted in the main panel. (b) Shear stress distribution along the horizontal line  $z = -8$  km at the time of rupture front arrival at  $(0.24$  km,  $-8$  km) km during the first event in the simulation with  $\beta_s = 4$ . The rupture speed at that time is  $2.45$  km/s. Despite the different value of  $\beta_s$  and the different rupture speed, the cohesive zone size is still  $0.3$  km. In quasi-dynamic simulations, the cohesive zone size does not shrink during rupture propagation and its size is independent of the parameter  $\beta_s$ .

size stays equal to  $300$  m. For the quasi-dynamic simulation with  $\beta_s = 4$ , the cohesive zone size is still  $300$  m (Figure 3.19b). At the time shown in Figure 3.19b, the rupture speed is  $2.45$  km/s, more than  $80\%$  of the shear wave speed.

The fact that the cohesive zone does not change in quasi-dynamic simulations simplifies choosing proper spatial discretization. In our study, any cell size below the quasi-static estimate of the cohesive zone size has produced well-resolved quasi-dynamic calculations (we have tried  $\Delta x = 50$  m,  $100$  m, and  $200$  m; recall that  $\Delta x = 200$  m was not adequate for the fully dynamic simulation). But larger cell sizes lead to inaccurate solutions; for example,  $\Delta x = 400$  m changes the results significantly, just like in the fully dynamic case. How much more advantageous is the quasi-dynamic simulation in terms of the spatial discretization depends on how much the cohesive zone shrinks during the corresponding fully dynamic simulation.

### 3.6 Conclusions

We have developed, based on prior studies, a 3D methodology for simulating long-term history of spontaneous seismic and aseismic slip on a vertical planar strike-slip fault subjected to slow tectonic loading. Our approach reproduces all stages of earthquake cycles, from accelerating slip before dynamic instability, to rapid dynamic propagation of earthquake rupture, to post-seismic slip, and to interseismic creep, including aseismic transients. We have extended the existing 2D methodology (Lapusta et al., 2000) to 3D, proposed a numerical resolution criterion that combines findings for long-term histories and dynamic rupture, developed a new frequency-dependent truncation procedure, determined the values of numerical parameters that lead to results independent of numerical procedures in 3D, developed a parallel implementation of the 3D code, and applied the developed methodology to several examples.

In 2D studies of earthquake sequences (e.g., Rice, 1993; Lapusta et al., 2000), the numerical discretization was based on the need to resolve the nucleation process and the associated spatial scale  $h^*$ . However, in both fully dynamic and quasi-dynamic simulations, seismic events propagate as dynamic ruptures with rapid variations of field variables at their tip. We have shown that the resolution criterion based on the near-tip cohesive zone and quantified in our previous collaborative work (Day et al., 2005) is more restrictive for the parameters typically used in earthquake-sequence simulations. Once the cohesive zone size is resolved with several spatial cells, the nucleation-related scale  $h^*$  is resolved as well, since it is several times larger. This consideration explains the finding of Lapusta et al. (2000) that  $h^*$  needs to be resolved by 20 spatial cells, a relatively large number; that level of discretization was actually required for resolving the much smaller size of the cohesive zone.

We find that the frequency-dependent truncation procedure developed for 2D anti-plane problems by Lapusta et al. (2000) is inadequate in 3D. This is because 3D problems involve elastodynamic kernels for Mode II, and those kernels decay much slower than the Mode III kernels. We have developed a new frequency-dependent truncation procedure that is based both on considerations of Lapusta et al. (2000) and on the decay of the kernel amplitude.

Slip response in the presented fault models, which have relatively simple distributions of friction properties, involves aseismic transients, i.e., episodes of spontaneous aseismic fault slip faster than the plate rate. These transients arise in the areas of velocity-weakening regions close to rheological transitions and constitute propagating nucleation attempts. Their extent depends on the nucleation size. In our simulations, we choose parameters that make nucleation sizes a significant fraction of the fault width, to make the problems numerically tractable. Large nucleation sizes may be realistic for certain fault conditions such as highly elevated pore pressure or velocity-weakening properties close to velocity-neutral. In fact, [Liu and Rice \(2005\)](#) obtained aseismic transients in a subduction model with occasional highly elevated pore pressure next to rheological transition. It is possible that aseismic transients occur only under conditions that result in large nucleation sizes, in which case the mechanism of aseismic transients presented in [Liu and Rice \(2005\)](#) and reproduced here is a viable one. However, note that many areas on natural faults should have small nucleation sizes to produce small events. Other mechanisms have been proposed to explain aseismic transients, such as inelastic dilatancy and complex dependence of friction on slip velocity (e.g., [Shibazaki and Shimamoto, 2007](#); [Segall and Rubin, 2007](#)).

We have used the developed methodology to investigate interaction of slip with a stronger fault patch of 20% higher normal stress over many earthquake cycles. The patch significantly affects the dynamic rupture in the first event, causing rupture delay followed by a supershear burst. However, the patch becomes “invisible” to dynamic rupture in subsequent events due to redistribution of shear stress. While simulations of single dynamic events play an important role in exploring earthquake dynamics, our results show that long-term simulations are also important as they can help us understand how assumptions about the distribution of fault strength influences the distribution of fault stress before large events. Our results have consequences for studies that attempt to determine parameters of strong ground motion by considering many potential scenarios of earthquake rupture on a given fault, primarily by choosing different distributions of fault strength and fault initial conditions. Our results suggest that the two distributions are related due to prior fault slip. Note that the small stronger patch, which occupies only 1% of the fault areas, significantly influences the

long-term behavior of the fault in our model, moving nucleation locations and causing asymmetric behavior.

Comparison of the fully dynamic and the standard quasi-dynamic approaches shows that the quasi-dynamic approach results in smaller slip per event and significantly smaller slip velocities and rupture speeds, confirming the results of 2D comparisons (Lapusta et al., 2000). The new observation in 3D models is that the long-term slip pattern of the model is also different between the fully dynamic and quasi-dynamic simulations, even for the simple distributions of fault properties considered. Hence the discrepancies between the fully dynamic and quasi-dynamic simulations accumulated during inertially-controlled ruptures have long-term influences over earthquake cycles in 3D. The quasi-dynamic approach also fails to reproduce the supershear burst in the first dynamic event of the simulation with a stronger patch. We have explored the possibility of improving the comparison by decreasing radiation damping terms of the quasi-dynamic formulation. We find that such a change is equivalent to the standard formulation with higher wave speeds and it only rescales the resulting solution without changing it qualitatively.

## 3.7 Appendix

### 3.7.1 Convolution kernels

The elastodynamic convolution kernels  $K_{\text{II}}$  and  $K_{\text{III}}$  from equation (3.2) can be expressed as (Geubelle and Rice, 1995):

$$\begin{aligned} K_{\text{II}}(\rho) &= 2(1 - c_s^2/c_p^2) - \int_0^\rho C_{\text{II}}(\eta) d\eta, \\ K_{\text{III}}(\rho) &= 1 - \int_0^\rho C_{\text{III}}(\eta) d\eta, \end{aligned} \tag{3.24}$$

where

$$C_{\text{II}} = \frac{J_1(\rho)}{\rho} + 4\rho \left[ W\left(\frac{c_p}{c_s}\rho\right) - W(\rho) \right] - 4\frac{c_s}{c_p} J_0\left(\frac{c_p}{c_s}\rho\right) + 3J_0(\rho), \tag{3.25}$$

$$C_{\text{III}} = \frac{J_1(\rho)}{\rho}, \tag{3.26}$$

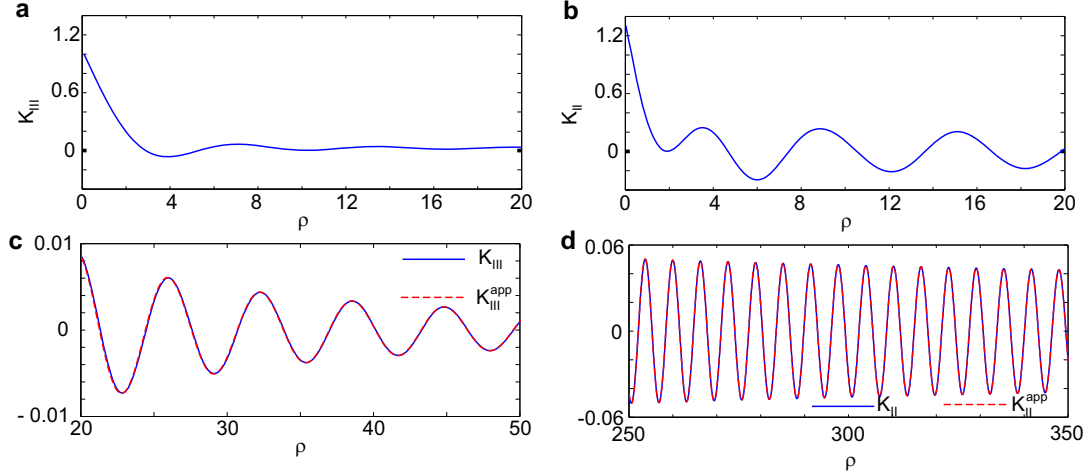


Figure 3.20: Elastodynamic kernels  $K_{\text{III}}(\rho)$  and  $K_{\text{II}}(\rho)$ . (a),(b) Values of the kernels for relatively small kernel arguments. (c),(d) Comparison of kernels with the leading terms in their asymptotic expansions. For  $\rho \gg 1$ ,  $K_{\text{III}}(\rho) \sim O(\rho^{-3/2})$  and  $K_{\text{II}}(\rho) \sim O(\rho^{-1/2})$ .  $K_{\text{II}}(\rho)$  decays much slower than  $K_{\text{III}}(\rho)$  as  $\rho$  increases.

$$W(\rho) = \int_{\rho}^{\infty} \frac{J_1(\eta)}{\eta} d\eta = 1 - \int_0^{\rho} \frac{J_1(\eta)}{\eta} d\eta, \quad (3.27)$$

and  $J_0(\rho)$  and  $J_1(\rho)$  denote Bessel functions. Kernels  $K_{\text{II}}(\rho)$  and  $K_{\text{III}}(\rho)$  have the following property:

$$\int_0^{\infty} K_{\text{II}}(\eta) d\eta = \int_0^{\infty} K_{\text{III}}(\eta) d\eta = 1. \quad (3.28)$$

Since the asymptotic form of Bessel functions  $J_n(\rho)$  for  $\rho \gg n$  is:

$$J_n(\rho) \sim \sqrt{\frac{2}{\pi\rho}} \cos\left(\rho - \frac{1}{2}n\pi - \frac{1}{4}\pi\right), \quad (3.29)$$

$K_{\text{III}}(\rho)$  can be expanded for  $\rho \gg 1$ :

$$K_{\text{III}}(\rho) = \int_{\rho}^{\infty} \frac{J_1(\eta)}{\eta} d\eta \sim \sqrt{\frac{2}{\pi}} \left\{ \frac{\cos(\rho - \pi/4)}{\rho^{3/2}} + \frac{3 \sin(\rho - \pi/4)}{2 \rho^{5/2}} + O(\rho^{-7/2}) \right\}. \quad (3.30)$$

The leading term of the expansion is given by:

$$K_{\text{III}}^{\text{app}}(\rho) = \sqrt{\frac{2}{\pi}} \frac{\cos(\rho - \pi/4)}{\rho^{3/2}}. \quad (3.31)$$

Similarly, the asymptotic expansion of  $K_{\text{II}}(\rho)$  for  $\rho \gg 1$  is:

$$K_{\text{II}}(\rho) = \sqrt{\frac{2}{\pi}} \left\{ \frac{\sin(\rho - \pi/4)}{\rho^{\frac{1}{2}}} + \frac{4(c_s/c_p)^{\frac{7}{2}} \cos(c_p \rho/c_s - \pi/4) - 3 \cos(\rho - \pi/4)}{\rho^{\frac{3}{2}}} + O\left(\frac{1}{\rho^{\frac{5}{2}}}\right) \right\}, \quad (3.32)$$

with the leading term:

$$K_{\text{II}}^{\text{app}}(\rho) = \sqrt{\frac{2}{\pi}} \frac{\sin(\rho - \pi/4)}{\rho^{\frac{1}{2}}}. \quad (3.33)$$

The kernels and their comparison with the leading terms are shown in Figure 3.20. The slower decay of  $K_{\text{II}}(\rho)$  has important implications for the frequency-dependent truncation, as discussed in Sections 3.1.1 and 3.3.3.

In our simulations, slip-velocity histories exhibit some small oscillations (e.g., Figure 3.12). For both  $\Delta x = 100$  m and  $\Delta x = 50$  m, the oscillations have the period of 6 time steps, or 0.0672 s for  $\Delta x = 100$  m and 0.0336 s for  $\Delta x = 50$  m. The amplitude of the oscillations gets smaller for  $\Delta x = 50$  m. Hence the oscillations are not physical. We find that they are due to kernel discretization. As shown above, kernels  $K_{\text{II}}(\rho)$  and  $K_{\text{II}}(\rho)$  have period of  $2\pi$  for  $\rho \gg 1$ . In simulations, time  $t$  is discretized with the minimum time step  $\Delta t_{\text{min}} = \gamma \Delta x / c_s$  and hence the kernel argument  $\rho$  is discretized with the kernel interval given by:

$$\Delta \rho_{\text{min}} = \hat{q} c_s \Delta t_{\text{min}}. \quad (3.34)$$

Therefore, for each frequency mode  $\hat{q}$ , the number of points resolving one period of the kernel is:

$$N_\rho = \frac{2\pi}{\Delta \rho_{\text{min}}} = \frac{2\pi}{\hat{q} \gamma \Delta x}. \quad (3.35)$$

$N_\rho$  is smaller for larger  $\hat{q}$ .

For the highest frequency magnitude  $\hat{q}_{\text{max}} = \sqrt{2}\pi/\Delta x$ , we get  $N_\rho = \sqrt{2}/\gamma = 4.2$  for  $\gamma = 1/3$  that we use in simulations. Therefore, one period of the kernel is resolved by only 4.2 points for the highest frequency. However, only four modes ( $k = \pm N_x/2, |m| = \pm N_z/2$ ) have such high frequency. If one considers all the modes as a rectangular array,  $-\pi/\Delta x \leq \hat{k} = 2\pi k/\lambda_x \leq \pi/\Delta x$

and  $-\pi/\Delta x \leq \hat{m} = 2\pi z/\lambda_z \leq \pi/\Delta x$  with  $\hat{q} = \hat{k}^2 + \hat{m}^2$ , and draws a circular ring of unit width centered at zero frequency, then the radius of the ring that can cover the largest area is  $\pi/\Delta x$ . Hence the largest contribution to oscillations likely comes from modes with the frequency magnitude  $\hat{q} = \pi/\Delta x$ . For these modes,  $N_\rho = 2/\gamma = 6$ , which explains the observed period of the oscillations. Smaller cell sizes  $\Delta x$  help reduce the amplitude of oscillations, as for smaller  $\Delta x$  frequencies  $\pi/\Delta x$  become much higher and hence have smaller Fourier coefficients  $\dot{D}_x(k, m; t')$  and  $\dot{D}_z(k, m; t')$ .

### 3.7.2 Updating field variables

Modeling of long deformation histories with periods of fast slip requires variable time stepping. We employ the time stepping scheme developed by [Lapusta et al. \(2000\)](#) for 2D anti-plane problems. The scheme works quite well in our 3D models. The variable time step  $\Delta t$  is chosen as:

$$\Delta t = \max\{\Delta t_{\min}, \Delta t_{\text{evol}}\}, \quad (3.36)$$

where  $\Delta t_{\min}$  is the minimum time step chosen for good resolution of dynamic rupture propagation and  $\Delta t_{\text{evol}}$  varies with slip velocity as discussed below. The value of  $\Delta t$  is always adjusted to be an integer multiple of  $\Delta t_{\min}$ , as this simplifies computation of convolution integrals. The minimum time step is given by:

$$\Delta t_{\min} = \gamma \Delta x / c_s \quad (3.37)$$

where  $\gamma$  is a constant. We use  $\gamma = 1/3$ , as this is the value suggested by our previous study of dynamic rupture in 3D ([Day et al., 2005](#)). The time step  $\Delta t_{\text{evol}}$  is set to be inversely proportional to slip velocity:

$$\Delta t_{\text{evol}} = \min_{i,j} [\xi(i,j) L(i,j) / V(i,j)], \quad (3.38)$$

where  $L(i,j)$ ,  $V(i,j)$ , and  $\xi(i,j)$  are the characteristic slip, slip velocity, and a prescribed parameter for the cell  $(i,j)$ ,  $i = 1, 2, \dots, N_x$  and  $j = 1, 2, \dots, N_z$ .  $\xi(i,j)$  is a function of friction properties from linear stability analysis ([Lapusta et al., 2000](#)). In addition,  $\xi(i,j)$  is constrained to satisfy

$\xi(i, j) \leq \xi_c$ , where  $\xi_c$  is a constant, to ensure that slip at each time step does not exceed  $\xi_c L(i, j)$ . Lapusta et al. (2000) used  $\xi_c = 1/2$ . In our 3D models, we do a series of comparison with  $\xi_c = 1/2$ ,  $1/3$ ,  $1/4$ , and  $1/5$ . We find that values  $\xi_c \geq 1/3$  produce virtually indistinguishable results, but  $\xi_c = 1/2$  results in small differences. In the simulations presented in this work, we use  $\xi_c = 1/5$ ; however,  $\xi_c = 1/3$  would have produced the same results.

To update field variables, we extend to 3D the scheme developed by Lapusta et al. (2000) for 2D antiplane problems. Instead of updating state variable  $\theta$  directly, we use the quantity  $\phi = \log(V_o\theta/L)$ . From equation (3.10), the evolution equation for  $\phi$  is:

$$\frac{d\phi}{dt} = \frac{V_o}{L}e^{-\phi} - \frac{V}{L}. \quad (3.39)$$

Suppose that, at time  $t$ , the discretized values of tangential slips  $\delta_\nu(i, j; t)$ , slip velocities  $V_\nu(i, j; t)$ ,  $\nu = x, z$ , and state variable  $\phi(i, j; t)$  are known for the cell  $(i, j), i = 1, 2, \dots, N_x, j = 1, 2, \dots, N_z$ . In addition, we also have the Fourier coefficients of tangential slips  $D_\nu(k, m; t')$ , and the history of Fourier coefficients of slip velocity  $\dot{D}_\nu(k, m; t'), |k| \leq N_x/2, |m| \leq N_z/2$  for the (discretized) prior time  $t', t - T_w < t' < t$ , where  $t$  is the current time and  $T_w$  is the truncation time window. To advance the field variables by one time step  $\Delta t$  and determine the quantities at the end of  $t + \Delta t$ , we proceed in the spirit of a second-order Runge-Kutta procedure as follows (for compactness, all explicit references to the indices  $(i, j)$  for physical space and  $(k, m)$  for Fourier space are suppressed):

1. Determine the evolution time step  $\Delta t$  using equation (3.36).
2. Make the first predictions of the values of the slips  $\delta_\nu^*(t + \Delta t)$ , their Fourier coefficients  $D_\nu^*(t + \Delta t)$  and the state variable  $\phi^*(t + \Delta t)$  for each cell, assuming that slip velocities are constant and equal to  $V_\nu(t)$  throughout the time step  $t$ . Hence we have:

$$\delta_\nu^*(t + \Delta t) = \delta_\nu(t) + \Delta t V_\nu(t) \quad (3.40)$$

$$D_\nu^*(t + \Delta t) = D_\nu(t) + \Delta t \dot{D}_\nu(t) \quad (3.41)$$

$$\phi^*(t + \Delta t) = \begin{cases} \log \{e^{\phi(t)}(1 - Vdt/L) + V_0dt/L\}, & Vdt/L \leq 10^{-6}; \\ \log \{V_0/V + (e^{\phi(t)} - V_0/V)e^{-Vdt/L}\}, & Vdt/L > 10^{-6}. \end{cases}, \quad (3.42)$$

where  $V = \sqrt{V_x^2(t) + V_z^2(t)}$  is the resultant slip rate. The update of  $\phi$  distinguishes between small and large values of  $Vdt/L$  for the following reason. For small  $V$ ,  $(e^{\phi(t)} - V_0/V) \doteq -V_0/V$  and  $e^{-Vdt/L} \doteq 1$  in the numerical sense, and then  $\phi^*(t + \Delta t) \doteq \log(0)$ , which leads to an error in computation. Using the Taylor expansions for small values of  $Vdt/L$  avoids the problem. Then we compute the first predictions of the Fourier coefficients of stress transfer functionals  $F_\nu^*(t + \Delta t)$ , using equation (3.2):

$$\begin{aligned} \begin{Bmatrix} F_x^*(t + \Delta t) \\ F_z^*(t + \Delta t) \end{Bmatrix} &= -\frac{\mu}{2\hat{q}} \begin{bmatrix} \hat{k}^2 & \hat{m}\hat{k} \\ \hat{m}\hat{k} & \hat{m}^2 \end{bmatrix} \left\{ 2 \left(1 - \frac{c_s^2}{c_p^2}\right) \begin{pmatrix} D_x^*(t + \Delta t) \\ D_z^*(t + \Delta t) \end{pmatrix} \right. \\ &\quad \left. - \int_{t+\Delta t-T_w}^t K_{\text{II}}(\hat{q}c_s(t + \Delta t - t')) \begin{pmatrix} \dot{D}_x(t') \\ \dot{D}_z(t') \end{pmatrix} dt' - \int_0^{\Delta t} K_{\text{II}}(\hat{q}c_s t') dt' \begin{pmatrix} \dot{D}_x(t) \\ \dot{D}_z(t) \end{pmatrix} \right\} \\ &\quad + \text{similarly rewritten second term of (3.2)}. \end{aligned} \quad (3.43)$$

For  $\Delta t \geq T_w$ , the second term on the right-hand side of the above expression is set to be zero. For  $\Delta t < T_w$ , the term can be computed because slip-velocity history is known. The third term is an approximation of the convolution on the time interval corresponding to the current time step. We then obtain the first prediction of stress functionals,  $f_\nu^*(t + \Delta t)$  through the inverse Fast Fourier Transform (FFT) of  $F_\nu^*(t + \Delta t)$ .

3. Find the prediction of slip velocities  $V_\nu^*(t + \Delta t)$  corresponding to the predicted values of the state variable  $\phi^*(t + \Delta t)$  and stress functionals  $f_\nu^*(t + \Delta t)$ . The direction of the slip-velocity vector  $\mathbf{V} = (V_x, V_z)$  should coincide with the direction of the shear-traction vector  $\boldsymbol{\tau} = (\tau_x, \tau_z)$ :

$$\frac{V_z^*(t + \Delta t)}{V_x^*(t + \Delta t)} = \frac{\tau_z^*(t + \Delta t)}{\tau_x^*(t + \Delta t)}. \quad (3.44)$$

Combining the above equation with (3.1), we get:

$$\frac{V_z^*(t + \Delta t)}{V_x^*(t + \Delta t)} = \frac{\Phi_z^*(t + \Delta t)}{\Phi_x^*(t + \Delta t)}, \quad (3.45)$$

$$\tau^* = \Phi^* - \frac{\mu}{2c_s} V^*, \quad (3.46)$$

where  $\Phi_\nu^*(t + \Delta t) = \tau_\nu^o(t + \Delta t) + f_\nu^*(t + \Delta t)$ ,  $\Phi^* = \sqrt{\Phi_x^{*2}(t + \Delta t) + \Phi_z^{*2}(t + \Delta t)}$ ,  $V^* = \sqrt{V_x^{*2}(t + \Delta t) + V_z^{*2}(t + \Delta t)}$ , and  $\tau^* = \sqrt{\tau_x^{*2}(t + \Delta t) + \tau_z^{*2}(t + \Delta t)}$ . Equating the shear traction (3.46) to the strength given by the regularized form of the rate and state friction law (e.g., Rice and Ben-Zion, 1996; Ben-Zion and Rice, 1997; Lapusta et al., 2000; Lapusta and Rice, 2003) results in:

$$\Phi^* - \frac{\mu}{2c_s} V^* = a \sigma \operatorname{arcsinh} \left[ \frac{V^*}{2V_o} \exp \left( \frac{f_o + b\phi^*(t + \Delta t)}{a} \right) \right]. \quad (3.47)$$

Newton-Rhapson search is used to solve the above equation for  $V^*$ . Once  $V^*$  are obtained,  $V_\nu^*(t + \Delta t)$ ,  $\nu = x, z$  can be readily found from equation (3.45).

4. Make the second predictions of the values of the slips  $\delta_\nu^{**}(t + \Delta t)$ , their Fourier coefficients  $D_\nu^{**}(t + \Delta t)$ , and the state variable  $\phi^{**}(t + \Delta t)$  :

$$\delta_\nu^{**}(t + \Delta t) = \delta_\nu(t) + \Delta t [V_\nu(t) + V_\nu^*(t + \Delta t)]/2, \quad (3.48)$$

$$D_\nu^{**}(t + \Delta t) = D_\nu(t) + \Delta t [\dot{D}_\nu(t) + \dot{D}_\nu^*(t + \Delta t)]/2 \quad (3.49)$$

$$\phi^{**}(t + \Delta t) = \left\{ \begin{array}{ll} \log \{ e^{\phi(t)} (1 - V^* dt/L) + V_o dt/L \}, & V^* dt/L \leq 10^{-6}; \\ \log \{ V_o/V^* + (e^{\phi(t)} - V_o/V^*) e^{-V^* dt/L} \}, & V^* dt/L > 10^{-6}. \end{array} \right\}, \quad (3.50)$$

where  $\dot{D}_\nu^*(t + \Delta t)$  are Fourier coefficients of  $V_\nu^*(t + \Delta t)$ ,  $\nu = x, z$ . Then we can find the corresponding prediction of stress transfer functionals,  $f_\nu^{**}(t + \Delta t)$ , using  $\delta_\nu^{**}(t + \Delta t)$  and assuming the slip velocities are constant and equal to  $[V_\nu(t) + V_\nu^*(t + \Delta t)]/2$  throughout the evolution time step. The computational procedure is analogous to (3.2) in stage 2. Note that the second term on the right-hand side of (3.2) stays the same in this stage, and hence we do not need to compute it again.

6. Find the second prediction of slip velocities  $V_\nu^{**}(t + \Delta t)$  that corresponds to the predicted state variables  $\phi^{**}(t + \Delta t)$  and stress functionals  $f_\nu^{**}(t + \Delta t)$ . The computational procedure is analogous to stage 3.

7. Declare the values of the second prediction as the values of field quantities at the time  $t + \Delta t$ . Store the values of slips  $\delta_\nu(t + \Delta t)$ , their Fourier coefficients  $D_\nu(t + \Delta t)$ , slip velocities  $\dot{\delta}_\nu(t + \Delta t)$ , and state variable  $\phi(t + \Delta t)$  for use in the next time step. In addition, store  $\dot{D}_\nu(t') = [\dot{D}_\nu(t) + \dot{D}_\nu^*(t + \Delta t)]/2, \nu = x, z$  as the Fourier coefficients of slip-velocity history for time  $t < t' < t + \Delta t$ . Go back to stage 1 to advance another time step.

## Chapter 4

# Transition of mode II cracks from sub-Rayleigh to intersonic speeds in the presence of favorable heterogeneity

Here, we use the methodology developed in Chapter 2 to study intersonic transition and propagation of shear cracks in a 2D single-rupture model. Importance of this subject and relevant observations have been discussed in Chapter 1. Inter-sonic transition in the context of a 3D fault model and long-term fault slip is considered in Chapter 5.

This chapter is based on [Liu and Lapusta \(2008\)](#).

### 4.1 Burridge-Andrews mechanism on homogeneous fault

Theoretical and numerical studies of sub-Rayleigh-to-inter-sonic transition date back to [Burridge \(1973\)](#) and [Andrews \(1976\)](#). [Burridge \(1973\)](#) considered a self-similar mode II crack and found that a shear stress peak propagates with the shear wave speed  $c_s$  in front of the crack. [Andrews \(1976\)](#) performed numerical simulations of spontaneous crack propagation on a uniformly prestressed interface governed by a linear slip-weakening law (Figure 4.1a) in which friction linearly decreases from static friction strength  $\tau^s$  to constant dynamic friction strength  $\tau^d$  over a characteristic slip  $d_o$ . This law implies a finite fracture energy given by  $1/2 (\tau^s - \tau^d) d_o$ . [Andrews \(1976\)](#) started with

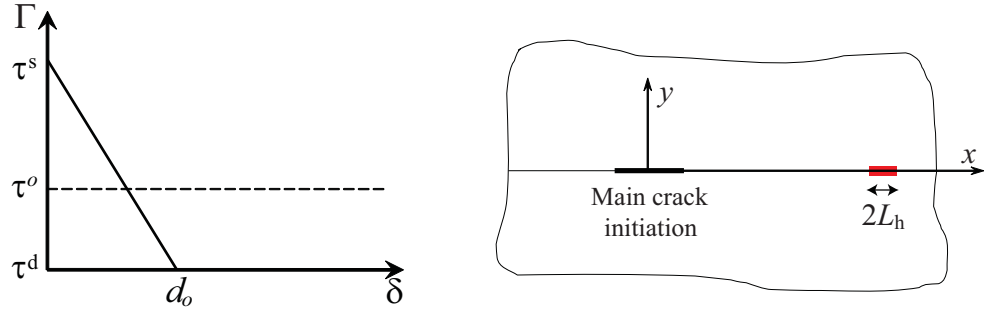


Figure 4.1: (a) Linear slip-weakening friction law.  $\tau_c$  is the shear strength of the interface and  $\delta$  is slip (or relative displacement in shear) across the interface. (b) A prescribed crack interface is embedded in an infinite, elastic, and homogeneous space. The main crack is initiated from a region around  $x = 0$ . This work considers interaction of the main crack with a region of heterogeneity that exists in front of the main crack and may initiate a secondary crack. Depending on the model, the heterogeneity is a pre-existing subcritical crack, a patch with higher prestress, or a patch with lower peak friction strength. When discussing crack tips and their speeds for both main and secondary cracks, we always refer to crack tips that propagate in the direction of increasing  $x$ , or to the right in all figures, unless specified otherwise.

shear stress and slip distributions appropriate for a critical static crack under a uniform far-field shear loading  $\tau^o$  and initiated a dynamic crack by slightly increasing shear stress along the critical crack profile. The half length of the critical crack is given by (Andrews, 1976):

$$L^c = \frac{1}{\pi(1-\nu)} \frac{\mu(\tau^s - \tau^d)d_o}{(\tau^o - \tau^d)^2}, \quad (4.1)$$

where  $\nu$  is the Poisson's ratio and  $\mu$  is the shear modulus.  $L^c$  is used as a reference length scale in this study, to facilitate comparison with Andrews (1976) and subsequent studies. Andrews (1976) confirmed and supplemented the findings of Burridge (1973) by demonstrating that a growing shear stress peak propagates with the shear wave speed  $c_s$  in front of the initially sub-Rayleigh crack and that the peak approaches the limiting value  $\tau^{\max} = \tau^o + S_{\text{crit}}(\tau^o - \tau^d)$ ,  $S_{\text{crit}} = 1.77$ , as the crack approaches the Rayleigh wave speed  $c_R$ . If  $\tau^{\max} > \tau^s$ , the shear stress peak reaches static friction strength during crack propagation, and a daughter crack is initiated in front of the main crack. The daughter crack propagates with intersonic speeds from its very beginning. This process of intersonic transition is often called the Burridge-Andrews mechanism. Figure 4.2 shows our simulation of this

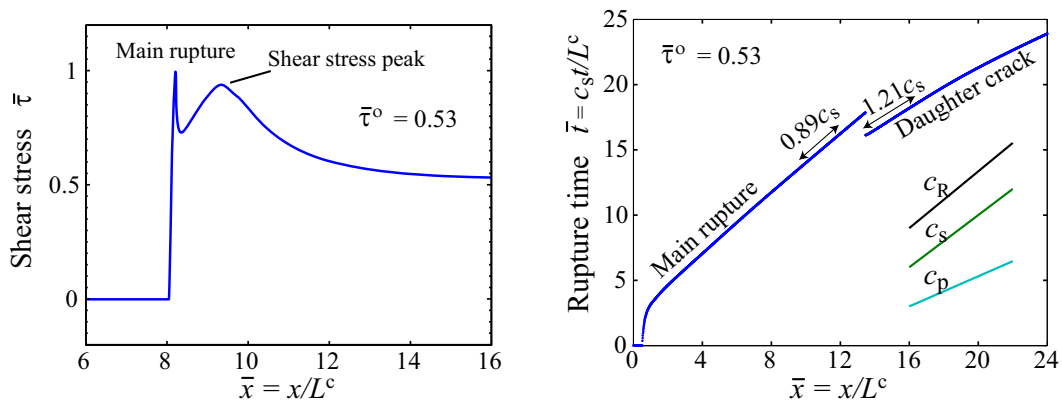


Figure 4.2: (a) Shear stress distribution for a mode II crack spontaneously propagating on an interface governed by linear slip-weakening friction. A peak in shear stress travels with the shear wave speed in front of the crack. The interface has uniform friction properties and uniform prestress  $\tau^o$  given by  $(\tau^o - \tau^d)/(\tau^s - \tau^d) = 0.53$ . (b) Rupture time along the interface, i.e., the time at which each point along the interface first acquires nonzero speeds. A daughter crack appears in front of the main crack at the location  $x/L^c = 13.5$  and propagates with intersonic speeds as described by the Burridge-Andrews mechanism. Here and in the text the word “inter-sonic” refers to speeds between the shear wave speed  $c_s$  and the dilatational wave speed  $c_p$ . For lower prestress, the daughter crack would appear further along the interface or not at all.

transition mechanism; the methodology is described in Section 4.2.

The Burridge-Andrews mechanism has been observed in the laboratory (Xia et al., 2004) and provides a plausible model for intersonic transition during earthquakes. The condition  $\tau^{\max} > \tau^s$  implies that, for given friction properties, shear prestress  $\tau^o$  on the interface has to be large enough for intersonic transition to occur, i.e.,  $(\tau^o - \tau^d)/(\tau^s - \tau^d) > 1/(1 + S_{\text{crit}}) = 0.36$ . Equivalently, the seismic ratio  $S$  defined as  $S = (\tau^s - \tau^o)/(\tau^o - \tau^d)$  has to be smaller than the critical value,  $S_{\text{crit}} = 1.77$ . If, for given friction properties, shear prestress  $\tau^o$  is not large enough, no daughter crack nucleates, and the limiting rupture speed of the main crack is the Rayleigh wave speed  $c_R$ . Note that values of  $\tau^o$  only slightly larger than the limiting value would imply transition to intersonic speeds at very large propagation distances, and larger values of  $\tau^o$  are needed for smaller transition distances. For example, transition at the location  $x/L^c = 13.5$  requires prestress  $(\tau^o - \tau^d)/(\tau^s - \tau^d) = 0.53$ , which is the case shown in Figure 4.2.

A number of other studies have addressed the issue of intersonic transition and/or intersonic

propagation. Significant advances have been made in understanding various theoretical aspects of crack propagation with speeds larger than  $c_R$  (e.g., [Burridge et al., 1979](#); [Freund, 1979](#); [Broberg, 1994, 1995](#); [Huang and Gao, 2001](#); [Samudrala et al., 2002](#); [Antipov and Willis, 2003](#)). In part, it has been established that cracks cannot propagate with speeds in the interval  $[c_R, c_s]$  due to energetic constraints, and that intersonic cracks in models with finite tractions, constant fracture energy, and uniform prestress would tend to accelerate to the dilatational wave speed  $c_p$ . [Gao et al. \(2001\)](#) studied the transition of a sub-Rayleigh mode II crack to intersonic speeds using both continuum and molecular dynamics simulations and showed that the two approaches agree. [Geubelle and Kubair \(2001\)](#) analyzed numerically intersonic transition under mixed-mode conditions and pointed out that transition from sub-Rayleigh to intersonic speeds can occur “through a sudden acceleration of the tip of the main cohesive zone”. The study of [Geubelle and Kubair \(2001\)](#) considered relatively high prestress levels that would result in intersonic transition by the Burridge-Andrews mechanism. Recently, [Festa and Vilotte \(2006\)](#) and [Shi et al. \(2007\)](#) considered dependence of intersonic transition and rupture mode on crack initiation; the former study used linear slip-weakening friction, while the latter study used a law of a rate and state type. [Dunham \(2006\)](#) proposed that transition distances for the Burridge-Andrews mechanism can be obtained from the self-similar crack model by requiring that the daughter crack reaches a critical size. Inter-sonic transition in 3D models of earthquake rupture, in some cases in the presence of heterogeneities, have been studied numerically by a number of researchers (e.g., [Day, 1982a,b](#); [Madariaga and Olsen, 2000](#); [Fukuyama and Olsen, 2002](#); [Dunham et al., 2003](#)). A number of studies addressed the issue of inter-sonic rupture speeds in a bimaterial configuration, where the interface separates two different elastic materials (e.g., [Harris and Day, 1997](#); [Cochard and Rice, 2000](#); [Adams, 2001](#); [Ranjith and Rice, 2001](#); [Shi and Ben-Zion, 2006](#)).

## 4.2 Methodology

Our goal is to study inter-sonic transition in the presence of fault heterogeneity, which is common on natural faults (Section [4.5.6](#)). We consider a mode II plane-strain shear crack propagating along a

planar interface  $y = 0$  embedded in an infinite, linear elastic, and homogeneous space (Figure 4.1). The direction of crack propagation and slip (or relative displacement in shear)  $\delta(x, t)$  is denoted by  $x$ . The Poisson's ratio  $\nu$  is chosen to be 0.25, so that  $c_R = 0.92c_s$  and  $c_p = \sqrt{3}c_s$ . The crack interface is governed by a linear slip-weakening friction law, in which its shear strength  $\tau_c$  linearly decreases from its static value  $\tau^s$  to its dynamic value  $\tau^d$  over a characteristic slip  $d_o$ :

$$\tau_c(\delta) = \begin{cases} \tau^d + (\tau^s - \tau^d)(1 - \delta/d_o), & \delta \leq d_o; \\ \tau^d, & \delta > d_o. \end{cases} \quad (4.2)$$

$\tau^s$  and  $\tau^d$  can be thought of as products of constant in time compressive normal stress  $\sigma(x)$  and static and dynamic friction coefficients, respectively.  $\tau^s$  and  $\tau^d$  are uniform in space for cases described in this study. Section 4.5 contains a comment about models with a patch of lower static friction strength  $\tau^s$ .

Rupture propagation is numerically calculated using the spectral boundary integral method (e.g., Perrin et al., 1995; Geubelle and Rice, 1995; Lapusta et al., 2000). In our 2D model, shear traction  $\tau(x, t)$  on the interface  $y = 0$  can be expressed as the sum of “loading” traction  $\tau^l(x, t)$  that would act on the interface in the absence of any displacement discontinuity (i.e., slip) plus additional terms due to time-dependent slip  $\delta(x, t)$  on the interface, in the form:

$$\tau(x, t) = \tau^l(x, t) + f(x, t) - \frac{\mu}{2c_s} V(x, t), \quad (4.3)$$

where  $f(x, t)$  is a functional of slip history on the interface and  $V(x, t) = \partial\delta(x, t)/\partial t$  is slip velocity. As  $f(x, t)$  is obtained analytically through a closed-form Green function, boundary integral methods can be considered semi-analytical and tend to be more accurate than other numerical approaches such as finite difference methods (e.g., Day et al., 2005).  $f(x, t)$  is related to  $\delta(x, t)$  and history of  $V(x, t)$  in the Fourier domain (Appendix 4.6.2), and hence the spatial extent of the simulated interface is actually infinite with the domain of interest periodically replicated along the interface. The size of the domain is chosen so that waves from its periodic replications do not reach spatial

locations of interest during the simulated time. Note that slip does not affect normal tractions  $\sigma(x)$  which remain constant in this model.

Spontaneous rupture of the interface is simulated by requiring, at each time step, that shear traction (4.3) is equal to shear strength (4.2) for points along the interface that have nonzero slip velocity, and that shear traction (4.3) is smaller than shear strength (4.2) for points along the interface that have zero slip velocity. More details about the formulation and numerical procedure are given in Appendix 4.6.2 and Day et al. (2005).

Loading is incorporated in the model by prescribing traction  $\tau^l(x, t)$  in equation (4.3) that would act on the interface if it were constrained against any slip.  $\tau^l(x, t)$  is equal to a constant value,  $\tau^o$ , on most of the interface. We call  $\tau^o$  “background prestress” and quantify it in two ways.  $\bar{\tau}^o = (\tau^o - \tau^d)/(\tau^s - \tau^d)$  gives a nondimensional value of  $\tau^o$  which increases with  $\tau^o$ . The seismic ratio  $S = (\tau^s - \tau^o)/(\tau^o - \tau^d)$  (Andrews, 1976) is smaller for larger  $\tau^o$ . In a region close to  $x = 0$ ,  $\tau^l(x, t)$  is such that a main crack spontaneously spreads from there starting at  $t = 0$ .  $\tau^l(x, t)$  is elevated above  $\tau^o$  in a region of favorable heterogeneity of the size  $2L_h$  located at  $x = D$  (Figure 4.1).  $D$  is fixed and equal to  $12L^c$ . Dependence of results on  $D$  is discussed in Section 4.4. Further specification of  $\tau^l(x, t)$  and the process of initiating the main crack are discussed in Sections 4.3 and 4.4.

Uenishi and Rice (2003) considered a quasi-static mode II crack on a linearly slip-weakening interface subjected to peaked loading. They demonstrated that the crack would become unstable when its half length reaches the nucleation half length given by

$$L^{\text{nucl}} = \frac{0.579}{1 - \nu} \frac{\mu d_o}{(\tau^s - \tau^d)} = 0.579\pi \frac{(\tau^o - \tau^d)^2}{(\tau^s - \tau^d)^2} L^c, \quad (4.4)$$

assuming that the crack half length reaches  $L^{\text{nucl}}$  while slip inside the crack is still below  $d_o$ . In other words,  $L^{\text{nucl}}$  is relevant for cracks developing in such a way that their half length reaches  $L^{\text{nucl}}$  before their slip (or relative shear displacement) exceeds  $d_o$ . In that case, the entire crack length lies within the cohesive zone up until unstable crack propagation, and the singular crack theory cannot

be used. As demonstrated by [Uenishi and Rice \(2003\)](#) and confirmed in this study, this situation is relevant for a wide range of loading conditions. We discuss the relation of  $L^{\text{nucl}}$  to our results in the following sections. Note that  $L^{\text{nucl}}$  could be chosen as a characteristic length scale in our models but we use the critical half length  $L^c$  in that capacity, to facilitate comparison with previous studies. As a reminder,  $L^c = (2\pi(1 - \nu))^{-1}\mu G/(\tau^o - \tau^d)^2$  gives the half length for a singular crack, with fracture energy  $G$  and residual shear stress  $\tau^d$ , which is in the critical state (such that, for an infinitesimal crack advance, the energy released is exactly balanced by the energy absorbed) under uniform far-field stress  $\tau^o$ .  $L^c$  is relevant for cohesive-zone models of cracks in situations when the cohesive zone sizes at the crack tips of quasi-static cracks are small compared to the overall crack size, which means that cracks are still quasi-static when slip exceeds  $d_o$  over most of the crack length. Note that  $L^{\text{nucl}}$  is independent of background prestress  $\tau^o$  but the normalized ratio  $L^{\text{nucl}}/L^c$  depends on  $\tau^o$  ([Table 4.1](#)).

Rupture propagation is simulated on a uniform spatial grid with the cell size  $\Delta x = L^c/N^c$  and constant time step  $\Delta t = \Delta x/\beta c_s$ , where  $N^c$  is the number of cells in the length  $L^c$ , and  $\beta$  determines the time step as a fraction (equal to  $1/\beta$ ) of the time for the shear wave to travel through  $\Delta x$ . An important quantity to resolve is the cohesive zone length at the crack tip ([Palmer and Rice, 1973](#); [Day et al., 2005](#)). A useful upper bound for the cohesive zone length of a sub-Rayleigh crack is given by the cohesive zone length  $\Lambda_o$  of a crack propagating at  $0^+$  speeds ([Palmer and Rice, 1973](#); [Rice, 1980](#)):

$$\Lambda_o = \frac{9\pi}{32(1 - \nu)} \frac{\mu d_o}{(\tau^s - \tau^d)}. \quad (4.5)$$

Note that, for given friction properties,  $L^{\text{nucl}}$  and  $\Lambda_o$  differ only by a prefactor of order 1. [Table 4.1](#) relates numerical resolution of  $L^c$  and  $\Lambda_0$  and gives values of  $L^{\text{nucl}}/L^c$  for different prestress levels  $\tau^o$  used in this study.

We use the following nondimensional variables: time  $\bar{t} = c_s t/L^c$ , length  $\bar{x} = x/L^c$ , slip velocity  $\bar{V} = \mu V/c_s(\tau^o - \tau^d)$ , and stress  $\bar{\tau} = (\tau - \tau^d)/(\tau^s - \tau^d)$ . All other variables and quantities are nondimensionalized accordingly and their nondimensional names are denoted by adding a bar “-”. For example,  $\bar{\tau}^o = (\tau^o - \tau^d)/(\tau^s - \tau^d)$  and  $\bar{L}^{\text{nucl}} = L^{\text{nucl}}/L^c$ . Note that  $\bar{\tau}^s = 1$ ,  $\bar{\tau}^d = 0$ , and  $\bar{L}^c = 1$ .

Table 4.1: Values of  $S$ ,  $L^{\text{nucl}}/L^c$ , and numerical resolution of  $L^c$  and  $\Lambda_o$  for different prestress levels  $\tau^o$ .  $N^c = 100$  is the lowest resolution used. Numerical convergence has been verified by considering  $N^c$  equal to 200, 400, and, in some cases, 1200, which increases the resolution of the cohesive zone by a factor of two, four, and twelve, respectively.

$\bar{\tau}^o = (\tau^o - \tau^d)/(\tau^s - \tau^d)$	0.33	0.25	0.20	0.08
$S = (\tau^s - \tau^o)/(\tau^o - \tau^d)$	2	3	4	11.5
$L^{\text{nucl}}/L^c$	0.202	0.114	0.073	0.012
$N^c = L^c/\Delta x$	100	100	100	800
$\Lambda_o/\Delta x$	30.8	17.4	11.1	14.2

For clarity, we sometimes specify nondimensional quantities in terms of their dimensional analogs.

Slip progression along the interface is tracked using the notion of rupture time. Nondimensional rupture time is defined as the non-dimensional time  $\bar{t}(\bar{x})$  when slip rate  $\bar{V}$  of point  $\bar{x}$  becomes nonzero for the first time. Our implementation of that definition is to require that slip rate exceeds a given small value,  $\bar{V}_c$ . The results do not depend on the value of  $\bar{V}_c$  as long as it is small enough to capture slip initiation. We adopt  $\bar{V}_c = 10^{-6}$ . Note that, for  $\mu = 3 \cdot 10^4$  MPa and  $c_s = 3 \cdot 10^3$  m/s typical for rocks, and  $\tau^o - \tau^d = 10$  MPa which is the order of magnitude for typical stress drops during large earthquakes,  $\bar{V}_c = 10^{-6}$  corresponds to the dimensional value of  $10^{-6}$  m/s. In all cases we checked, we find that any spatial cell with non-zero slip rate has nondimensional slip rate larger than  $10^{-6}$ , which means that this choice for  $\bar{V}_c$  appropriately captures initiation of slip.

### 4.3 Advancing main rupture towards a pre-existing subcritical crack: An example of abrupt sub-Rayleigh-to-intersonic transition

To smoothly initiate a main crack and a subcritical secondary crack, we conduct a preliminary quasi-dynamic calculation in which the part of the functional  $f(x, t)$  that accounts for wave mediated stress transfers is ignored (Appendix 4.6.2). We prescribe loading traction  $\bar{\tau}^l(\bar{x}, \bar{t}')$  which has two peaks,

at  $\bar{x} = 0$  and  $\bar{x} = \bar{D}$ :

$$\bar{\tau}^l(\bar{x}, \bar{t}') = \bar{\tau}^o + (1 - \bar{\tau}^o)(1 + R\bar{t}') \left\{ \exp \left[ - \left( \frac{\bar{x}}{\bar{L}^{\text{nucl}}} \right)^2 \right] + \exp \left[ - \left( \frac{\bar{x} - \bar{D}}{\bar{L}^{\text{nucl}}/2} \right)^2 \right] \right\}. \quad (4.6)$$

In (4.6),  $R$  is the loading rate of the imposed peaks and  $\bar{\tau}^o$  is (constant) background prestress outside of the two peaks;  $\bar{\tau}^o = 0.33$  (i.e.,  $S = 2$ ) in this section. At  $\bar{t}' = 0$ , frictional sliding initiates at  $\bar{x} = 0$  and  $\bar{x} = \bar{D}$ . We let the sliding zone centered at  $\bar{x} = 0$  expand until it reaches a certain half size  $\bar{L}_{\text{ini}}$ . This happens at the time  $\bar{t}' = \bar{t}'_{\text{ini}}$ . We save the corresponding distributions of loading tractions  $\bar{\tau}^l$ , shear tractions  $\bar{\tau}$ , slip  $\bar{\delta}$ , and slip velocity  $\bar{V}$  along the interface, and use them as initial conditions for a subsequent fully dynamic calculation, in which we reset the time by setting  $\bar{t} = \bar{t}' - \bar{t}'_{\text{ini}}$ . Note that loading tractions  $\bar{\tau}^l(\bar{x}, \bar{t})$  are unchanged thereafter (for all  $\bar{t} > 0$ ).

We choose parameters of the initiation procedure that mimic tectonically driven slow nucleation on faults in the Earth's crust and result in smooth acceleration of the main crack. For that, we first consider the initiation of the main crack separately, without the second exponential term in (4.6). We consider progressively slower loading rates  $R = 0.63$ ,  $0.063$ , and  $0.0063$ , and progressively smaller initial half sizes  $\bar{L}_{\text{ini}} = \bar{L}^{\text{nucl}}$ ,  $0.9\bar{L}^{\text{nucl}}$ , and  $0.8\bar{L}^{\text{nucl}}$ , and compare stress conditions that the resulting main crack creates at the location  $\bar{x} = \bar{D} = 12$  of the preexisting subcritical crack. For  $\bar{L}_{\text{ini}} = \bar{L}^{\text{nucl}}$ , loading rates  $R = 0.063$  and  $R = 0.0063$  give virtually identical stressing conditions as shown in Figure 4.3; we use  $R = 0.0063$  in the simulations described in this work. For  $R = 0.0063$ ,  $\bar{L}_{\text{ini}} = 0.8\bar{L}^{\text{nucl}}$  does not initiate spontaneous crack propagation, while both  $\bar{L}_{\text{ini}} = 0.9\bar{L}^{\text{nucl}}$  and  $\bar{L}_{\text{ini}} = \bar{L}^{\text{nucl}}$  create a spontaneously propagating main crack that smoothly accelerates from near-zero tip speeds.  $\bar{L}_{\text{ini}} = 0.9\bar{L}^{\text{nucl}}$  and  $\bar{L}_{\text{ini}} = \bar{L}^{\text{nucl}}$  result in virtually indistinguishable stressing conditions at the location of the subcritical crack. We choose  $\bar{L}_{\text{ini}} = \bar{L}^{\text{nucl}}$  because it results in shorter computation time. The importance of the initiation procedure and related results of Festa and Vilotte (2006), Shi et al. (2007), and Geubelle and Kubair (2001) are discussed in Section 4.5.4.

The shear stress distribution at the beginning of a dynamic simulation is shown in Figure 4.4. At  $\bar{t} = 0$ , the secondary crack centered at  $\bar{x} = 12$  is much smaller than the main crack (which has

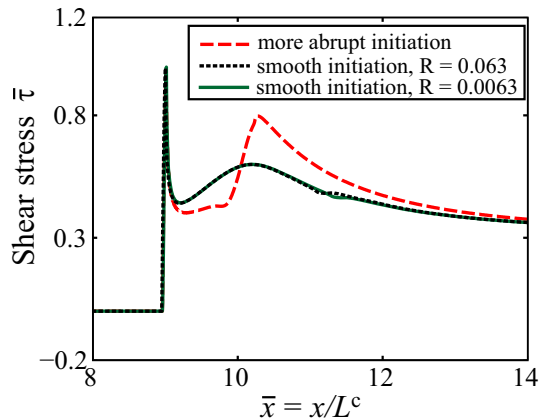


Figure 4.3: Stress distribution on the interface for different initiation procedures. To compare stress fields created by the main crack, no heterogeneity at  $\bar{x} = 12$  is imposed for these simulations. The more abrupt initiation procedure that results in a higher shear stress peak is discussed in Section 4.4.

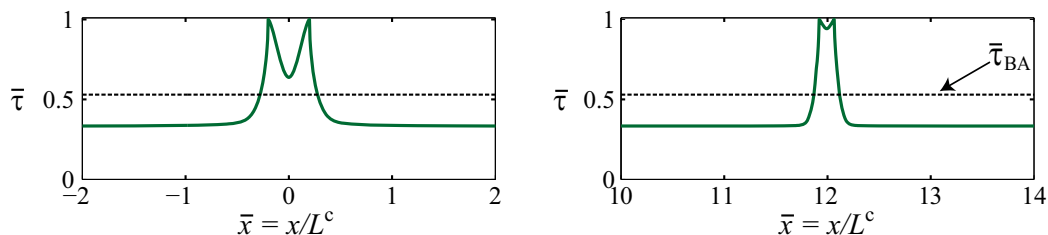


Figure 4.4: Stress distribution around the main crack and pre-existing subcritical crack at  $\bar{t} = 0$  (solid green line). The main crack centered at  $\bar{x} = 0$  is poised to propagate spontaneously for  $t > 0$ , while the secondary crack centered at  $x = 12L^c$  remains a subcritical crack. Prestress outside of zones affected by cracks is equal to  $\bar{\tau}^o = 0.33$ .  $\bar{\tau}_{BA} = 0.53$  (black dashed line) is the prestress level required for intersonic transition at the location  $\bar{x} = 13.5$  by the Burridge-Andrews mechanism.

length  $\bar{L}^{\text{nuc}}$ ), constituting a subcritical crack. The background prestress level  $\bar{\tau}^o = 0.33$  is below the critical value 0.36 of the Burridge-Andrews mechanism.  $\bar{\tau}^o = 0.33$  is even lower if compared to the value  $\bar{\tau}_{BA} = 0.53$  needed for the Burridge-Andrews transition at the location  $\bar{x} = 13.5$  which is close to the location of the subcritical crack. Hence no intersonic transition would occur under such prestress in the homogeneous case (with no preexisting subcritical crack).

For  $\bar{t} > 0$ , the spontaneously propagating main crack sends out dilatational and shear waves, which impose an intersonic loading stress field (Appendix 4.6.1) on the secondary subcritical crack. Figure 4.5 (left panel) shows rupture time on the interface. The secondary crack begins to spread at

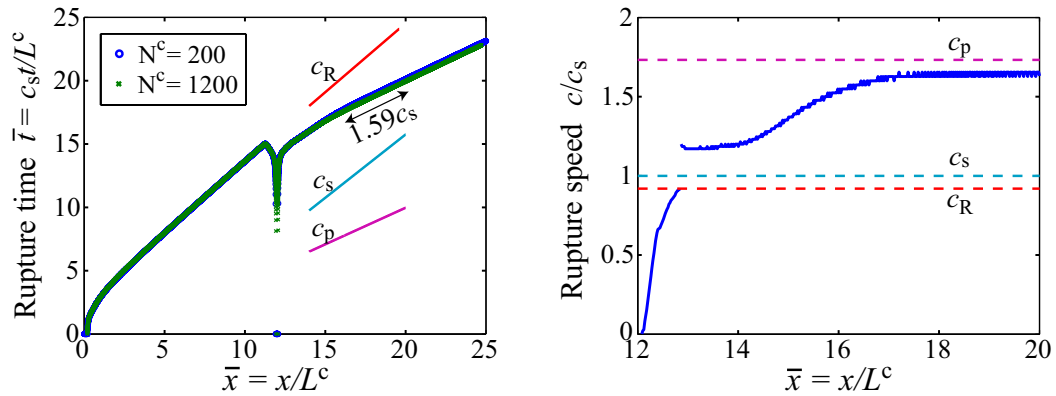


Figure 4.5: Left panel: Rupture time along the interface for the case with a preexisting subcritical crack. Under the stress field of the advancing main crack, the secondary subcritical crack begins to spread at  $\bar{t} = c_s t / L^c = 7.9$  and eventually propagates with intersonic speeds. Note that the results of simulations with two resolutions,  $N^c = 200, \beta = 4$  and  $N^c = 1200, \beta = 4$ , are almost indistinguishable on the scale of the plot. More resolution comparisons are shown in Figure 4.6. Right panel: Rupture speed of the secondary crack. It approaches the Rayleigh-wave speed and then abruptly jumps to intersonic speeds. Rupture speed is determined for the case with resolution  $N^c = 1200, \beta = 4$  by dividing the interface into intervals of 24 cells each, computing average rupture speed over each interval, and plotting the obtained value with respect to the middle of the interval. Care is taken to make the location of the rupture speed jump correspond to a beginning or end of an interval.

the time  $\bar{t} = c_s t / L^c = 7.9$  with rupture speeds close to zero. At that time, the main crack tip arrives at the position  $5.4L^c$ . As the main crack approaches, the secondary crack rapidly accelerates to the Rayleigh wave speed  $c_R$  and then jumps to an intersonic speed (Figure 4.5, right panel). The crack tip speed of the secondary crack before the jump is numerically indistinguishable from  $c_R$ , so it is possible that the crack tip speed reaches  $c_R$  momentarily before the jump. Note that while steady crack propagation with  $c_R$  would result in zero cohesive zone length and infinite slip velocities and hence would be impossible, transient propagation with  $c_R$  cannot be excluded.

To confirm the abrupt nature of the sub-Rayleigh-to-intersonic transition of the secondary crack, we have done simulations with several levels of resolution, from  $N^c = 200, \beta = 4$  to  $N^c = 1200, \beta = 4$ . Figure 4.6 shows the space-time progression of the rupture front of the secondary crack close to the location and time of the transition. The results have converged with respect to the discretization of space and time. For example, the location of the transition is 12.862 for  $N^c = 800$  and 12.855 for  $N^c = 1200$ , a relative difference of less than 0.1%. As Figure 4.6 demonstrates, the sub-Rayleigh-to-intersonic transition occurs within one spatial grid cell  $\Delta x$  and one time step  $\Delta t$  for all resolutions we have considered. Hence, in the limit of  $\Delta x \rightarrow 0$  and  $\Delta t \rightarrow 0$ , the crack tip should abruptly jump from  $c_R$  to an intersonic speed.

Figure 4.7 illustrates abrupt transition of the secondary crack tip to intersonic speeds by giving snapshots of slip velocity and stress distributions at the crack tip. At time  $\bar{t} = c_s t / L^c = 15.02$ , the tip of the secondary crack propagates with the speed numerically equal to  $c_R$ . At  $\bar{t} = 15.04$ , sliding initiates just *one* cell ahead of the crack tip and the sliding region propagates with intersonic speeds immediately. This process is the same in simulations with different  $\Delta x$  and time step  $\Delta t$ . In the limit of  $\Delta x \rightarrow 0$  and  $\Delta t \rightarrow 0$ , intersonic sliding should be inseparable from the crack tip, and initiate exactly at the tip.

Hence we conclude that the secondary crack transitions from sub-Rayleigh to intersonic speeds by abruptly changing the speed of its tip. This transition mechanism is different from the Burridge-Andrews mechanism, in which a daughter crack starts out as an intersonic crack. Note that once the secondary crack transitions to intersonic speeds, it accelerates to speeds close to  $c_p$  and maintains

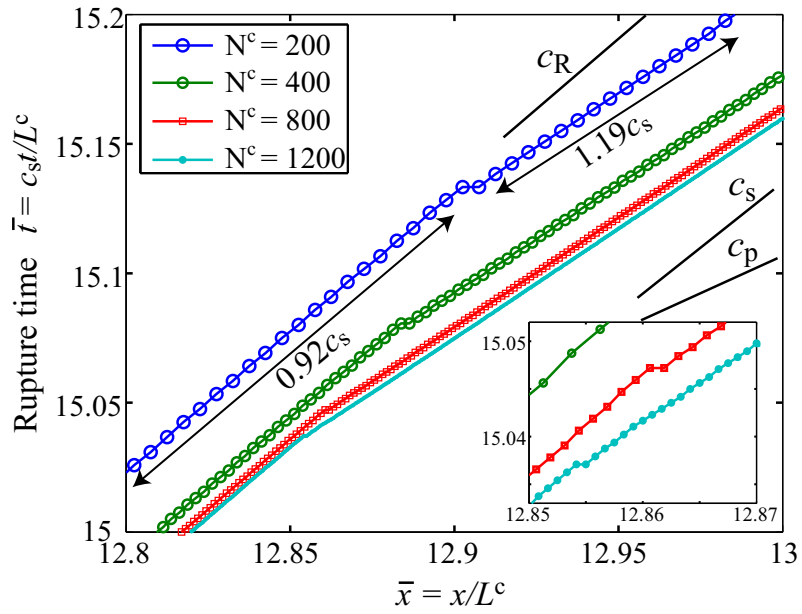


Figure 4.6: Propagation of the secondary crack in the region where sub-Rayleigh-to-isonic transition occurs. Rupture time of each spatial cell is indicated using different symbols for different resolution. For progressively finer resolution (i.e., larger  $N^c$ ), transition occurs within one cell size  $\Delta x$  and one time step  $\Delta t$ , which means that, in the limit of  $\Delta x \rightarrow 0$  and  $\Delta t \rightarrow 0$ , the rupture front abruptly jumps from speeds numerically equal to  $c_R = 0.92c_s$  to an isononic speed.

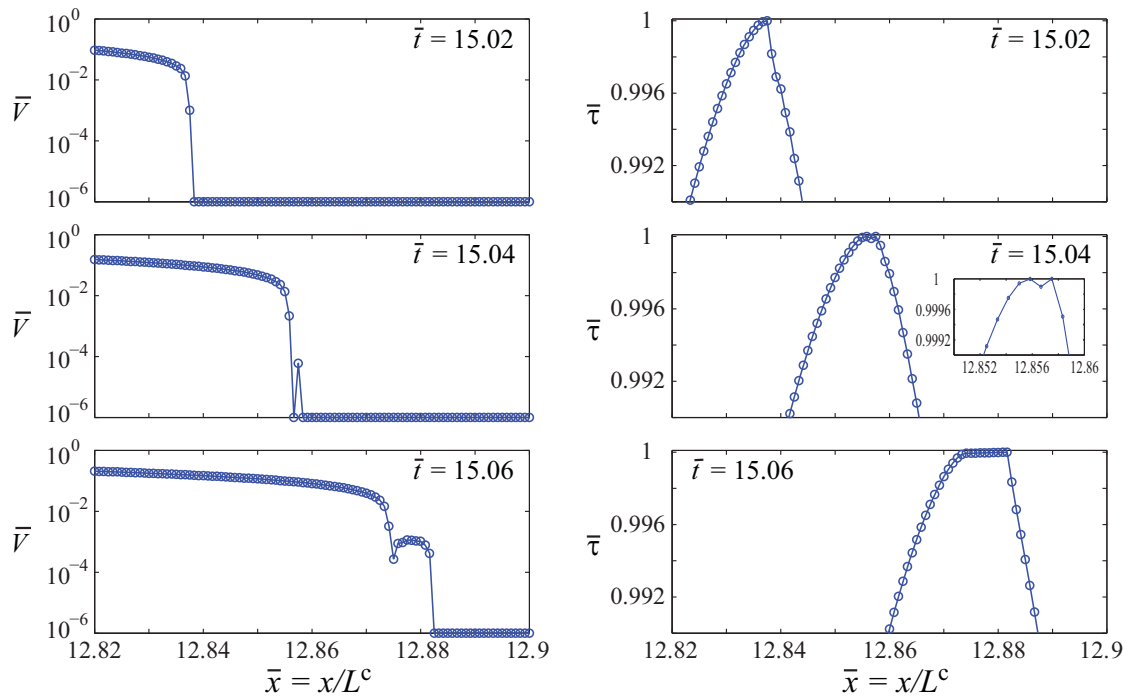


Figure 4.7: Snapshots of slip velocity (left) and shear stress distributions (right) on the interface during sub-Rayleigh-to-intersonic transition for the case  $N^c = 1200, \beta = 4$ , zooming in on the crack tip. Slip velocity is plotted on the logarithmic scale. For plotting convenience, slip velocity shown is the actual slip velocity plus  $10^{-6}$  and hence zero slip velocity appears as  $10^{-6}$  on the plot. At time  $\bar{t} = c_s t / L^c = 15.02$ , the crack tip propagates with the speed numerically equal to  $c_R$ . At  $\bar{t} = 15.04$ , sliding initiates just *one* cell ahead of the crack tip and propagates with intersonic speeds.

them for long propagation distances. Further discussion of this mechanism is given in Section 4.5.1 and Appendix 4.6.3. Whether the transition occurs or not should depend on the size of the preexisting crack, background prestress  $\bar{\tau}^o$ , and loading provided by the main crack. (The loading significantly depends on the initiation procedure for the main crack, as explained in Sections 4.4, 4.5.4.) We explore these dependencies for a related case of a patch of higher prestress discussed in the next section.

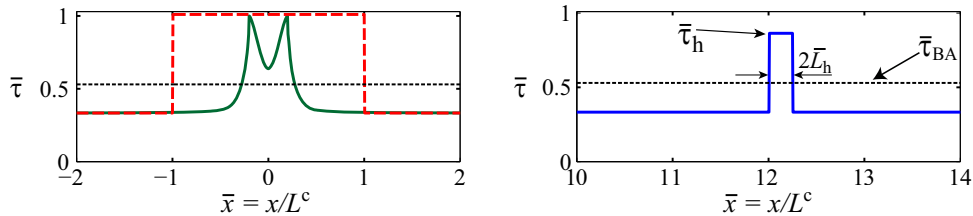


Figure 4.8: Shear stress distribution around the main crack (left panel) and the patch of higher prestress (right panel) at  $\bar{t} = 0$  ( $\bar{\tau}^o = 0.33$ ). In the left panel, the solid green and dashed red lines correspond to the smooth and more abrupt initiation procedures, respectively.  $\bar{\tau}_{BA} = 0.53$  is the level of prestress required to achieve Burridge-Andrews intersonic transition at the location  $\bar{x} = 13.5$  with the smooth initiation procedure.

#### 4.4 Advancing main crack towards a patch of higher prestress: dependence on patch size, prestress, and location

Instead of a preexisting crack (Section 4.3), let us consider higher prestress  $\bar{\tau}_h^o = (\tau_h^o - \tau^d)/(\tau^s - \tau^d)$  in a small patch  $\bar{D} < \bar{x} < \bar{D} + 2\bar{L}_h$ , where  $\bar{L}_h = L_h/L^c$  is the half size of the patch (Figure 4.8). We select  $\bar{D} = 12$ . Sliding in the patch starts from its end  $\bar{x} = \bar{D}$  (closer to the main crack) at the same time for all patch sizes, everything else being equal. We use two ways to initiate the main crack: (i) the same smooth initiation as in Section 4.3, and (ii) a more abrupt initiation for which, at  $\bar{t} = 0$ , prestress within  $|\bar{x}| < 1$  is set to be 1% larger than the static strength  $\tau^s$  of the interface. In the case of (ii), the main crack initiates at once in the entire region  $|\bar{x}| < 1$ . It accelerates and acquires speeds close to  $c_R$  much sooner than in the case of the smooth initiation procedure. This results in a significantly higher shear stress peak as shown in Figure 4.3. For the smooth initiation, such a shear stress peak would result only after much longer rupture propagation along the interface. As in Section 4.3, background prestress  $\bar{\tau}^o$  is chosen low  $\bar{x}$  compared to prestress required for intersonic transition by the Burridge-Andrews mechanism. If there were no patch of higher prestress, no intersonic transition and propagation would occur.

Spontaneous propagation of the main crack for times  $\bar{t} > 0$  imposes an additional dynamic stress field on the patch of higher prestress. For a range of patch sizes  $L_h/L^c$  and values of background prestress  $\bar{\tau}_h^o$ , as discussed in the following, shear stress in the patch overcomes the static friction

strength  $\tau^s$  before the arrival of the shear stress peak, and secondary sliding (or crack) initiates at the patch corner  $\bar{x} = 12$  closest to the main crack. The secondary crack spreads along the patch with intersonic speeds, driven by intersonic stress increase due to the advancing main crack. So far, the behavior is intuitively obvious. However, it is not intuitively clear how this intersonic secondary crack would behave after it enters the surrounding region of lower background prestress. While intersonic propagation over the higher-stressed patch is an interesting phenomenon, we would like to study whether the patch can induce sustained intersonic propagation for long distances beyond the patch. Hence in the following we call “sub-Rayleigh” those scenarios that result in the eventual sub-Rayleigh propagation of the crack, despite the fact that all scenarios include intersonic propagation of the secondary crack over the higher-stressed patch.

Our simulations show that behavior of the secondary crack after it leaves the patch of higher prestress is quite complicated. First, its tip speed momentarily reduces to zero, at least for small patch sizes studied here. Its subsequent behavior depends on background prestress  $\bar{\tau}^o$ , on the additional loading provided by the main crack, on the level  $\bar{\tau}_h^o$  of prestress in the patch, and on the patch size  $\bar{L}_h = L_h/L^c$ . Loading provided to the patch by the main crack depends on background prestress  $\bar{\tau}^o$ , the position of heterogeneity  $\bar{D}$ , and the procedure of main crack initiation. For each initiation procedure, we fix  $\bar{D} = 12$  and consider the dependence of results on the patch prestress  $\bar{\tau}_h^o$  and size  $\bar{L}_h$  for different values of  $\bar{\tau}^o$ . Intuitively, the larger the patch and the higher prestress it has, the more likely it is to cause transition to intersonic speeds. Yet the simulation results are more complex.

We start by describing results for the more abrupt initiation (ii) of the main crack. Results of our simulations in terms of intersonic vs. sub-Rayleigh propagation of rupture beyond the patch of higher prestress are summarized in Figure 4.9. To determine the eventual crack speed, we simulate rupture propagation until the location  $\bar{x} = x/L^c = 16$  is ruptured. For cases that require further clarification, and for selected conceptually important cases, we redo calculations until the location  $\bar{x} = 25$  is ruptured. Note that our methodology periodically repeats the simulated domain. Hence, to simulate a bilateral main crack and to avoid waves arriving from periodic replications of the

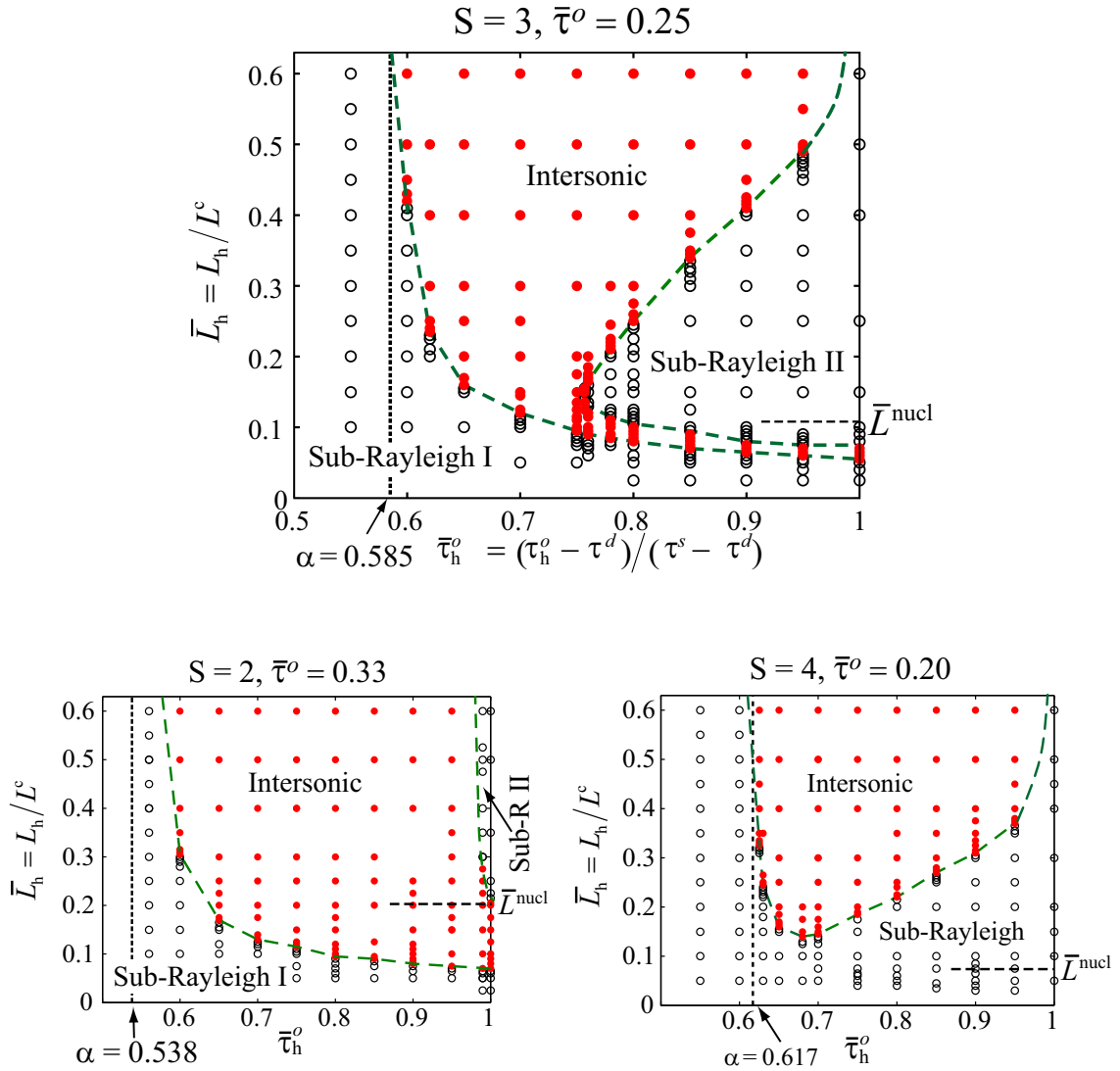


Figure 4.9: Influence of patch parameters on eventual intersonic vs. sub-Rayleigh propagation for three different values of background prestress and more abrupt initiation of the main crack. The horizontal and vertical axes indicate the patch prestress and patch size, respectively. Red filled dots indicate simulated cases for which rupture has sustained intersonic speeds beyond the higher-stressed patch. Black open dots indicate simulated cases for which rupture stays sub-Rayleigh. Dashed green lines indicate approximate boundaries of different behavior. The value  $\alpha$  of the patch prestress is discussed in the text.

rupture process into the region of observation, we use domain lengths of 50 and 80 to determine the crack speed at locations  $\bar{x} = 16$  and  $\bar{x} = 25$ , respectively.

Figure 4.9 (top panel) shows results for  $\bar{\tau}^o = 0.25$  ( $S = 3$ ). We find two regions of sub-Rayleigh behavior, marked “Sub-Rayleigh I” and “Sub-Rayleigh II” in the figure, and one connected region of intersonic behavior. Boundaries separating regions of intersonic and sub-Rayleigh behavior are approximate in Figure 4.9, inferred based on simulated cases shown as dots. We have studied many cases close to the boundaries, and that is why dots close to the boundaries overlap. Results for cases  $\bar{\tau}^o = 0.33$  ( $S = 2$ ) and  $\bar{\tau}^o = 0.2$  ( $S = 4$ ) are shown in Figure 4.9, bottom panels. Comparison of cases  $\bar{\tau}^o = 0.25$  and  $\bar{\tau}^o = 0.33$  shows that regions of sub-Rayleigh behavior shrink for the higher background prestress  $\bar{\tau}^o = 0.33$ , especially region “Sub-Rayleigh II”. Comparison of cases  $\bar{\tau}^o = 0.25$  and  $\bar{\tau}^o = 0.2$  shows that for the lower background prestress  $\bar{\tau}^o = 0.2$ , regions of sub-Rayleigh behavior expand and overlap, creating a single larger sub-Rayleigh region. Hence larger background prestress favors intersonic propagation, as could be expected, and causes consistent motion of the boundaries separating sub-Rayleigh and intersonic behavior.

Simulations for the smooth main crack initiation, which results in a smaller shear stress peak as the main crack approaches the patch of higher prestress, are summarized in Figure 4.10. We see qualitatively similar behavior in terms of where regions of sub-Rayleigh and intersonic propagation are located. As could be expected, a smaller shear stress peak results in smaller regions of intersonic propagation for the same values of background prestress.

To explain the existence and location of regions of sub-Rayleigh and intersonic behavior in Figures 4.9 and 4.10, let us consider some limiting cases. If there were no patch of higher prestress, the main crack would stay sub-Rayleigh, as all background prestress values  $\bar{\tau}^o$  considered here are lower than prestress required for transition by the Burridge-Andrews mechanism. A very small patch should have the same effect as no patch, and hence we should have sub-Rayleigh propagation for patch half sizes  $\bar{L}_h = L_h/L^c$  close to zero, regardless of the patch prestress. This explains the existence of the region marked “Sub-Rayleigh I” close to the  $\bar{L}_h = 0$  line for any value of  $\bar{\tau}_h^o$ . For most cases in region “Sub-Rayleigh I”, the main crack overtakes secondary sliding, and continues its sub-Rayleigh

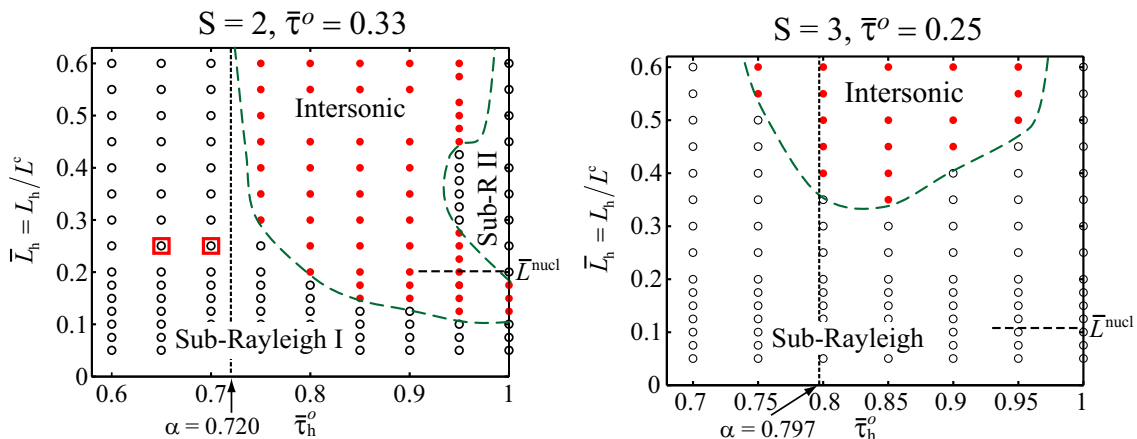


Figure 4.10: Influence of patch parameters on intersonic vs. sub-Rayleigh propagation for smooth initiation of the main crack that results in a smaller shear stress peak. The horizontal and vertical axes indicate the patch prestress and patch size, respectively. Red filled dots indicate simulated cases for which rupture has sustained intersonic speeds beyond the higher-stressed patch. Black open dots indicate simulated cases for which rupture stays sub-Rayleigh. Dashed green lines indicate approximate boundaries of different behavior. The value  $\alpha$  of the patch prestress, blue star, and two cases marked by small red squares are discussed in the text.

propagation. An example of such case is shown in Figure 4.11 (left panel,  $\bar{L}_h = 0.055 = 0.48\bar{L}^{\text{nucl}}$ ). Only for cases close to the boundary with the intersonic region, the secondary crack either just manages to propagate with sub-Rayleigh speed itself, or even transitions to intersonic speeds for a brief time and then reverts back to sub-Rayleigh speeds (Figure 4.11, right panel).

If the prestress level in the patch is equal to the static strength,  $\bar{\tau}_h^o = 1$ , then secondary sliding starts in the patch at  $\bar{t} = 0$ , when the main crack is still far away. If the patch is large enough, as approximately given by  $\bar{L}_h \geq \bar{L}^{\text{nucl}}$ , then the secondary crack develops into a spontaneous sub-Rayleigh crack and runs away with speeds close to  $c_R$  before the main crack can approach and interact with that process. Similar behavior occurs for  $\bar{\tau}_h^o$  close to 1. Case  $\bar{L}_h = 0.2 = 1.75\bar{L}^{\text{nucl}}$ ,  $\bar{\tau}_h^o = 0.85$  in Figure 4.11 is an example of such behavior. This argument explains the existence of the region marked “Sub-Rayleigh II” which includes a part of the line  $\bar{\tau}_h^o = 1$ .

If the patch with  $\bar{\tau}_h^o = 1$  is small, as approximately given by  $\bar{L}_h \leq \bar{L}^{\text{nucl}}$ , then it develops into a subcritical crack and, similarly to the preexisting crack case of Section 4.3, such subcritical cracks

can be driven, under the right conditions, to intersonic speeds by the stress field of the advancing main crack. Such intersonic cases separate the two sub-Rayleigh regions for background prestress values  $\bar{\tau}^o = 0.25$  and  $0.33$  in Figure 4.9 and  $\bar{\tau}^o = 0.33$  in Figure 4.10. An example of such intersonic behavior is the case of  $\bar{L}_h = 0.075 = 0.66\bar{L}^{\text{nucl}}$  in Figure 4.11. However, regions “Sub-Rayleigh I” and “Sub-Rayleigh II” merge for lower levels of background prestress and smaller shear stress peaks, as Figures 4.9 and 4.10 show. The resulting connected sub-Rayleigh region consists of two distinct areas, one in which the eventual sub-Rayleigh propagation is due to the main crack, and the other in which the eventual sub-Rayleigh propagation is due to the secondary crack. Note that large patches (i.e., larger than  $L^{\text{nucl}}$ ) with uniform prestress  $\bar{\tau}_h^o = 1$  (or close to 1) are unlikely to exist on the path of another crack in a realistic situation (i.e., on faults in the Earth’s crust). Any small heterogeneities or perturbations would lead to development of unstable sliding in those patches, effectively nucleating a main crack there. Such patches are considered in this study mostly to have a better understanding of the parameter space.

If the shear stress peak traveling in front of the main crack does not initiate sliding in the patch, lower shear stresses behind the peak cannot do that either, and sliding in the patch initiates only due to high stresses very close to the main crack tip. In this situation, a small patch can no longer create a preexisting subcritical crack that could be driven to intersonic speeds by the approaching main crack. Hence small patches can only cause intersonic transition for large enough values of the patch prestress,  $\bar{\tau}_h^o > \alpha$ , where  $\alpha$  is the patch prestress which would be brought to the static strength by the maximum of the shear stress peak. Prestress  $\alpha$  satisfies  $1 - \alpha = \bar{\tau}^{\text{peak}} - \bar{\tau}^o$ , where  $\bar{\tau}^{\text{peak}}$  is the maximum of the shear stress peak when it arrives at the patch. The value of  $\bar{\tau}^{\text{peak}}$  depends on the history of the main crack; in our simulations, it is determined by the initiation procedure, background prestress, and location of the patch (which is fixed at  $\bar{x} = 12$ ). For  $\bar{\tau}^o = 0.25$  ( $S = 3$ ) and more abrupt initiation of the main crack, simulations show that  $\bar{\tau}^{\text{peak}} = 0.665$ , which leads to  $\alpha = 0.585$ . The values of  $\alpha$  for other values of  $\bar{\tau}^o$  and for smooth initiation of the main crack are determined analogously. Lines  $\bar{\tau}_h^o = \alpha$  are marked in Figures 4.9 and 4.10 as vertical black lines with short dashes. Inter-sonic transition should be inhibited for  $\bar{\tau}_h^o < \alpha$ , at least for small patches,

and that is what we observe in Figures 4.9 and 4.10.

For patches with  $\bar{\tau}_h^o > \alpha$ , intersonic loading stress provided by the main crack creates intersonic secondary crack in the patch. When the intersonic secondary crack exits from the patch into the region of lower background prestress, it slows down first but, for large enough patch sizes, accelerates back at once and jumps abruptly to intersonic speeds (e.g., case  $\bar{L}_h = 0.34 = 2.98\bar{L}^{\text{nucl}}$  in Figure 4.11). That behavior can be understood as follows. Inter-sonic propagation in the patch radiates stress waves and most of them are left behind by the intersonic secondary crack. When the secondary crack exits the patch and slows down, the stress field radiated by sliding in the patch catches up with the secondary crack and loads it. The duration of this loading depends on the patch size, and hence it would be increasingly important for larger patches, causing acceleration of the secondary crack and transition to intersonic speeds. Note that for patches with prestress lower than  $\alpha$  but close to it, sliding in the patch is still intersonic but it is separated from the main crack only by a few cell sizes, and the behavior of the two cracks after exiting the patch cannot be well separated. Subsequent sustained intersonic propagation occurs only for large enough patches, as it is driven exclusively by stress radiation from the patch. For patch prestress levels much smaller than  $\alpha$ , the main crack and secondary sliding in the patch cannot be separated, and the only effect of the patch is to increase the sub-Rayleigh propagation speed of the main crack.

More abrupt initiation of the main crack results in a larger shear stress peak and hence should provide an approximate picture of the model behavior for a patch located much farther from the initiation of the main crack (i.e., for larger  $\bar{D}$ ). Consider the case of  $\bar{\tau}^o = 0.33$ . Through simulations we find that the more abrupt initiation procedure results in the same maximum of the shear stress peak at the location of  $\bar{x} = 12$  as the smooth initiation procedure at the location of  $\bar{x} = 80$ . Given the high resolution we would like to achieve in this study, such long propagation distances are hard to study even in 2D. To check the correspondence between the smooth initiation procedure with  $\bar{D} = 80$  and abrupt initiation procedure with  $\bar{D} = 12$ , we have done simulations with the smooth initiation procedure where we put a patch of higher prestress  $\bar{\tau}_h^o = 0.65$  or  $0.7$  and size  $\bar{L}_h = 0.25$  at the location  $\bar{D} = 80$ , with background prestress  $\bar{\tau}^o = 0.33$  ( $S = 2$ ). These cases are sub-Rayleigh for  $\bar{D} = 12$  and

smooth initiation (Figure 4.10, left panel, open black dots surrounded by red squares). However, they are intersonic for  $\bar{D} = 12$  and more abrupt initiation (Figure 4.9, bottom left panel). For smooth initiation and  $\bar{D} = 80$ , these cases are also intersonic, indicating that more abrupt initiation and its higher shear stress peak can indeed approximate long propagation distances for the smooth initiation. The correspondence cannot be exact, however, since the shear stress distribution in front of the main crack keeps extending in space for longer propagation distances; the height of the peak may be the same, but its width would be different. Since the intersonic vs. sub-Rayleigh behavior depends not just on the stress field ahead of the main crack but also on other factors such as, for example, the patch size in relation to  $\bar{L}^{\text{nucl}}$ , this discrepancy cannot be resolved by simply scaling the patch size in accordance with its location.

We have demonstrated that a small patch of higher prestress can completely change rupture behavior. To illustrate the complexity of the response that results when the stress field of the main crack interacts with the patch, let us consider the case of background prestress  $\bar{\tau}^o = 0.25$  ( $S = 3$ ), patch prestress  $\bar{\tau}_h^o = 0.85$ , and more abrupt initiation of the main crack (Figure 4.9, top panel). Rupture times for four values of the patch size  $\bar{L}_h = L_h/L^c$  are shown in Figure 4.11 (left panel) but more cases (shown as dots in Figure 4.9 for  $\bar{\tau}_h^o = 0.85$ ) are enumerated in the following. Note that  $\bar{L}^{\text{nucl}} = 0.11$  in this case.

For  $\bar{L}_h \leq 0.06$ , the main crack overtakes the secondary crack, and continues its sub-Rayleigh propagation beyond the patch of higher stress (Figure 4.11,  $\bar{L}_h = 0.055$ ). For  $\bar{L}_h = 0.065$ , the secondary crack survives but stays sub-Rayleigh. For  $0.07 \leq \bar{L}_h \leq 0.085$ , the secondary crack accelerates after a pause and acquires sustained intersonic speeds by the abrupt transition mechanism described in Section 4.3 (Figure 4.11,  $\bar{L}_h = 0.075$ ). For  $0.09 \leq \bar{L}_h \leq 0.105$ , the secondary crack accelerates to sub-Rayleigh speeds and creates an intersonic daughter crack in front; the daughter crack subsequently dies and the secondary crack continues its propagation with sub-Rayleigh speeds. For  $\bar{L}_h = 0.125$ , the secondary crack accelerates to sub-Rayleigh speeds and there is no intersonic propagation beyond the patch. For  $0.15 \leq \bar{L}_h \leq 0.25$ , the secondary crack accelerates after its momentary stop and briefly acquires intersonic speeds but then continues its sub-Rayleigh

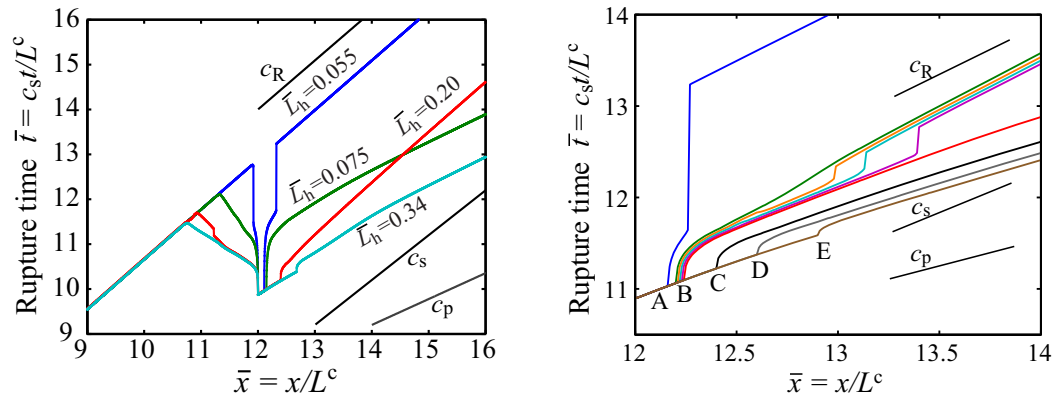


Figure 4.11: Rupture time for different patch sizes, with  $\bar{\tau}^o = 0.25$  ( $S = 3$ ) and more abrupt initiation of the main crack. Left panel: Patch prestress  $\bar{\tau}_h^o = 0.85$ . Rupture eventually propagates with intersonic speeds for  $\bar{L}_h = L_h/L^c = 0.075$  and  $0.34$  and sub-Rayleigh speeds for  $\bar{L}_h = 0.055$  and  $0.20$ . Behavior for these and other patch sizes is discussed in the text. Right panel: Patch prestress  $\bar{\tau}_h^o = 0.70$ , note a different scale of  $\bar{x}$ . The behavior is much simpler than for  $\bar{\tau}_h^o = 0.85$ . Cases with different  $\bar{L}_h$  are marked by letters A–E at the location  $\bar{x} = 12 + 2\bar{L}_h$  where the secondary crack for each case leaves the patch.  $\bar{L}_h = 0.08$ , line A: the secondary crack is overtaken by the main crack for this and smaller  $\bar{L}_h$ .  $\bar{L}_h = 0.1, 0.105, 0.11, 0.115, 0.12$ , line B: for  $0.1 \leq \bar{L}_h \leq 0.115$ , the secondary crack accelerates to  $c_R$  and abruptly transitions to intersonic speeds, but reverts back to sub-Rayleigh speeds after short (but progressively longer) intersonic propagation; for  $\bar{L}_h = 0.12$ , the crack manages to stay intersonic and results in eventual intersonic propagation.  $\bar{L}_h = 0.20, 0.30, 0.45$ , lines C, D, E: same behavior as for  $\bar{L}_h = 0.12$

propagation (Figure 4.11,  $\bar{L}_h = 0.2$ ). This seems contradictory with eventual intersonic propagation of smaller patches, for example,  $\bar{L}_h = 0.075$ . Closer examination of these two cases shows that the secondary rupture accelerates faster after leaving the patch in the case of  $\bar{L}_h = 0.20$ , as expected for a larger patch and hence a larger secondary crack. However, this means that the secondary crack in the case of  $\bar{L}_h = 0.20$  reaches the same locations along the interface sooner than in the case of  $\bar{L}_h = 0.075$ , and hence those locations are less stressed by the advancing main crack. For  $0.3 \leq \bar{L}_h \leq 0.335$ , the secondary crack transitions to intersonic speeds, reverts back to sub-Rayleigh speeds, nucleates an intersonic daughter crack in front which shortly dies, so that eventual propagation is sub-Rayleigh; such complicated behavior results from complicated dynamic stressing that combines the stress field of the main crack and the stress field released by intersonic sliding in the patch. For  $0.34 \leq \bar{L}_h \leq 0.6$ , the secondary crack only briefly pauses after leaving the patch, accelerating and transitioning abruptly to intersonic speeds while the main crack is still relatively far. For these larger patches, stress release during intersonic propagation within the patch must play a significant role in inducing the subsequent intersonic transition as already discussed. Figure 4.11 shows the case of  $\bar{L}_h = 0.34$ .

This rich response is consistent with our discussion of regions of intersonic vs. sub-Rayleigh behavior in Figures 4.9 and 4.10. Note that the illustrated case of  $\bar{\tau}_h^o = 0.85$  is especially complicated since, for increasing patch size, we cross three boundaries separating regions of sub-Rayleigh and intersonic behavior (Figure 4.9, top panel,  $\bar{\tau}_h^o = 0.85$ ). The response in other cases can be much simpler, as it is, for example, in the case of  $\bar{\tau}_h^o = 0.70$ , where only one boundary is crossed (Figure 4.9, top panel, and Figure 4.11, right panel). This is because the patch prestress  $\bar{\tau}_h^o = 0.70$  is relatively far from the nondimensional static strength of 1 and hence the region “Sub-Rayleigh II” does not come into play.

To illustrate the behavior of the secondary crack, we show snapshots of stress and slip rate on the interface close to the patch of higher prestress. Figure 4.12 compares two cases from the left panel of Figure 4.11: the case of  $\bar{L}_h = 0.075$  (which results in intersonic transition) and the case of a larger patch,  $\bar{L}_h = 0.20$  (for which the crack stays sub-Rayleigh). The case with no patch is also

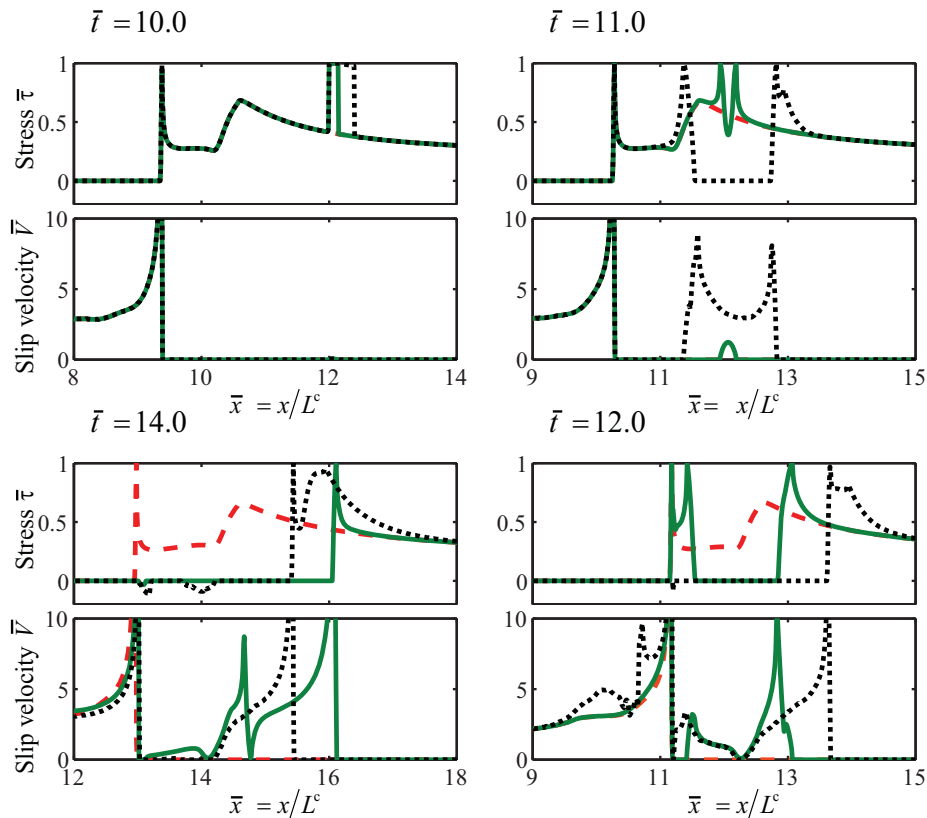


Figure 4.12: Snapshots of stress and slip velocity for the cases of  $\bar{L}_h = 0.075$  (solid green line) and  $\bar{L}_h = 0.20$  (black dashed line with smaller dashes) with  $\bar{\tau}^o = 0.25$ ,  $\bar{\tau}_h^o = 0.85$ , and more abrupt initiation of the main crack. Propagation of the main crack with no patch of higher prestress is also shown (red dashed line with larger dashes).

shown.

$\bar{t} = 10.0$ : Stress and slip rate are the same for all three cases, with the only difference being higher stress at the location of the patch. Stress at the left corner of the patch ( $\bar{x} = x/L^c = 12$ ) has just reached the static strength, due to the additional stress provided by the main crack. The front of the main crack is located between  $\bar{x} = 9$  and  $\bar{x} = 10$ .

$\bar{t} = 11.0$ : The range of  $\bar{x}$  is shifted in this snapshot. The secondary crack is still subcritical and close to the boundaries of the patch for  $\bar{L}_h = 0.075$  but it is well-developed and propagates outside the patch for  $\bar{L}_h = 0.20$ . This is not unexpected, since for  $\bar{L}_h = 0.20$  the secondary crack is much larger when it exits the patch. Note that  $\bar{L}^{\text{nucl}} = 0.114$ .

$\bar{t} = 12.0$ : The front of the secondary crack for  $\bar{L}_h = 0.075$  is already intersonic (it is located

close to  $\bar{x} = 13$ ). Note that the shear stress peak of the main rupture, plotted for the case with no patch, has not yet reached this location. The secondary crack for  $\bar{L}_h = 0.20$ , located close to  $\bar{x} = 14$ , continues its sub-Rayleigh propagation and a clear shear stress peak develops in front of it.

$\bar{t} = 14.0$ : The range of  $\bar{x}$  is shifted in this snapshot. The intersonic secondary crack front for  $\bar{L}_h = 0.075$  has passed  $\bar{x} = 16$ , which means that its average speed since  $\bar{t} = 12.0$  has been larger than  $1.5c_s$ . The sub-Rayleigh front for  $\bar{L}_h = 0.20$  is now behind, at about  $\bar{x} = 15.5$ . The shear wave peak ahead of that front has increased, almost reaching the static strength, raising the possibility of a Burridge-Andrews-type daughter crack. However, examination of further crack history (not shown) reveals that this peak starts to decrease for subsequent times and does not reach the static strength. (However, for similar situations with other parameters, a daughter crack does sometimes nucleate and either dies or leads to sustained intersonic propagation.) The tip of the main crack is at about  $\bar{x} = 13$ , but, at this time, all points behind the secondary crack tip have already slipped for both cases, so we have one compound rupture with the tip that coincides with the secondary crack tip.

Note that the patch makes prestress distribution on the interface discontinuous at the patch edges (Figure 4.8). We have done several simulations in which prestress is smooth and differentiable between the background level  $\bar{\tau}^o$  and the patch level  $\bar{\tau}_h^o$ . We find that simulation results with the continuous prestress distribution around the patch are very similar to those with discontinuous prestress distribution and reproduce all qualitative features, including abrupt intersonic transition and rupture behavior beyond the location of the patch.

## 4.5 Conclusions and discussion

We find that sub-Rayleigh-to-intersonic transition of mode II cracks occurs in a number of models that subject cracks to intersonic loading fields. A natural example of such stress field is stress between the shear wave peak and earliest dilatational waves propagating in front of a spontaneously expanding sub-Rayleigh Mode II crack (Appendix 4.6.1). If a secondary developing crack is subjected to such stress field, it can transition to intersonic speeds and maintain that intersonic propagation

under a range of conditions. The Burridge-Andrews mechanism is a special case of such models. We have demonstrated sub-Rayleigh-to-intersonic transition and sustained intersonic propagation for two more models that contain “favorable heterogeneity”, i.e., places susceptible to nucleation of secondary cracks. Models with a preexisting subcritical crack and with a small patch of higher prestress have been considered. Similar behavior is expected in a model with a small patch of lower static strength, and we confirm that in our simulations (not shown in this work).

In the models, a secondary crack nucleates at the location of the favorable heterogeneity and, for a range of parameters, it is driven to intersonic speeds by the advancing main crack. In models with a patch of higher prestress, interaction between the advancing stress field of the main crack and the patch results in a complicated behavior which is described in Section 4.4 and can be understood by considering limiting cases. We note that propagation of a secondary crack before the intersonic transition is not only nonlinear (due to friction) but also highly unsteady dynamic process and its analytical treatment, beyond qualitative arguments provided in this study, may be rather difficult. However, once crack tips become intersonic, their behavior is consistent with analytical inferences for intersonic cracks (e.g., [Burridge et al., 1979](#); [Freund, 1979](#); [Broberg, 1994, 1995](#); [Huang and Gao, 2001](#); [Samudrala et al., 2002](#); [Antipov and Willis, 2003](#)).

In the following, we summarize and discuss other findings and their implications.

#### 4.5.1 Abrupt change of crack tip speeds

In the presented models, tips of secondary cracks exhibit abrupt change of their speed from the value numerically equal to the Rayleigh wave speed  $c_R$  to an intersonic speed, and that change occurs right at the crack tip. This is different from the Burridge-Andrews mechanism, in which the daughter crack is intersonic from its very beginning. The abrupt change of a crack tip speed described in this work is an alternative way of avoiding the forbidden speed regime  $[c_R, c_s]$ .

[Freund \(1990\)](#) pointed out that, under some general assumptions, crack front speeds change in phase with applied driving stress. That implies that smooth variations in applied driving stress should result in smooth variations of the resulting crack speed. This is indeed the case in our

simulations for crack speed changes within the sub-Rayleigh regime and within the intersonic regime. However, in the preexisting subcritical crack case of Section 4.3, all stress-related fields are continuous in time and space, but we still observe an abrupt front speed jump from speeds approaching  $c_R$  to an intersonic speed. These simulations imply that jumps from  $c_R$  to intersonic speeds may be possible, in highly unsteady situations, even if the driving stress is continuous. We emphasize that, for all cases of abrupt intersonic transition presented in this study, (i) the corresponding crack tip has been under action of an intersonic stress field of an advancing crack and, in some cases, an additional intersonic stress field radiated during intersonic sliding in the patch of higher prestress, with the latter field playing either minor or dominating role depending on the patch size, and (ii) the fronts have been highly unsteady prior to transition, rapidly accelerating from near-zero speeds to  $c_R$ .

Once the crack tip starts to propagate with intersonic speeds, the sliding process behind the tip retains larger slip velocities at the place of the old crack tip propagating with  $c_R$  and tends to create a region of decreased slip velocities propagating with  $c_s$  (which is a general feature of intersonic mode II cracks which propagate faster than shear and Rayleigh waves). This creates an impression of the old front (close to  $c_R$ ) falling behind and an intersonic daughter-like crack emerging from the old front. In that sense, the abrupt transition resembles a daughter crack originating right at the secondary crack front. The region of decreased slip velocities propagating with  $c_s$  behind the intersonic crack tip tends to separate the sliding region, further reinforcing the daughter-crack analogy. (That separation also creates intersonic pulses.) Whether this is just a visual resemblance or a useful way of thinking about this transition theoretically remains a question for future study. In some cases, intersonic transition of the secondary crack beyond the patch of higher prestress is followed by transition back to sub-Rayleigh speeds. Such intersonic-to-sub-Rayleigh transition is only observed after short intersonic propagation distances, less than 1-2  $L^c$ . When the “reverse” transition happens, the crack reverts back to the old crack front. This further supports the notion of a daughter crack originating right at the crack tip and expanding but then, in the case of the “reverse” transition, shrinking and disappearing, presumably because the intersonic loading stress due to the approaching main crack and, in some cases, due to stress waves released from the higher-stressed

patch, has passed by without creating a large enough intersonic daughter crack. This consideration supports the notion of a critical crack size for intersonic transition introduced in a different context by [Dunham \(2006\)](#).

#### 4.5.2 Prestress levels for intersonic transition and propagation

In models with favorable heterogeneities, intersonic transition and propagation can occur under much lower background prestress levels than those required by the Burridge-Andrews mechanism. This means that the level of prestress required by the Burridge-Andrews mechanism is only needed to nucleate a daughter crack on a homogeneously prestressed interface, and not to drive the daughter crack to intersonic speeds or to maintain that intersonic propagation. In Sections 4.3 and 4.4, intersonic transition and propagation occur with background prestress  $\bar{\tau}^o = (\tau^o - \tau^d)/(\tau^s - \tau^d) = 0.33, 0.25,$  and  $0.2$ , while the Burridge-Andrews mechanism has critical prestress of  $0.36$  and needs prestress of  $0.53$  to achieve intersonic transition at a comparable transition length.

How low can prestress levels be and still allow intersonic transition and propagation? To investigate that question, we have considered progressively lower background prestress values  $\bar{\tau}^o = 0.15, 0.10,$  and  $0.08$  in the model with a patch of higher prestress (Section 4.4). Inter-sonic transition and sustained intersonic propagation beyond the patch occur for all these prestresses. (The other parameters of the model are: patch location  $D/L^c = 12$ , patch size  $L_h/L^c = 0.25$ , patch prestress  $\bar{\tau}_h^o = 0.8$ , and more abrupt initiation of the main crack.) Note that the smaller  $\bar{\tau}^o$ , the more challenging numerical simulations are if we would like to consider the same size of the simulated domain in terms of  $L^c$  and ensure that the cohesive zone length is adequately resolved. Combining equations (4.1), (4.5), and  $N^c = L^c/\Delta x$  gives the following resolution estimate:  $\Lambda^o/\Delta x = (9\pi^2/32)(\bar{\tau}^o)^2 N^c$ , where  $\Lambda^o$  is the cohesive zone length for  $0^+$  crack tip speeds. We use  $N^c = 800$  for low prestress values which gives, for the lowest value  $\bar{\tau}^o = 0.08$ ,  $\Lambda^o/\Delta x = 14$ . For sub-Rayleigh crack speeds higher than  $0^+$ , the cohesive zone length would decrease; we verify cohesive zone resolution by plotting stress distributions on the interface for various stages of the crack development and observing that there are several cell sizes within the cohesive zone, which means that the cohesive zone is

adequately resolved (e.g., [Day et al., 2005](#)). In addition, there are virtually no cell-by-cell numerical oscillations of slip velocities behind crack tips in our simulations; such oscillations are usually a sign of inadequate numerical resolution. To the best of our knowledge, this is the first demonstration, in a simulation of spontaneous propagation of cracks, that shear cracks can propagate with intersonic speeds under such low prestress levels.

Based on our simulations, we hypothesize that, in the presence of a sufficiently large favorable heterogeneity, intersonic transition and propagation of mode II cracks are possible for any background prestress  $\bar{\tau}^o > 0$  (or equivalently  $\tau^o > \tau^d$ ). This would be analogous to sub-Rayleigh cracks, for which any background prestress  $\tau^o$  higher than dynamic strength  $\tau^d$  would lead to sustained crack propagation assuming that the initial crack is large enough (recall that the critical size  $L^c \sim 1/(\tau^o - \tau^d)^2$  and  $L^c$  increases rapidly as  $\tau^o$  approaches  $\tau^d$ ).

### 4.5.3 Transition distance

Models with favorable heterogeneities have transition distances that depend on the position of heterogeneity. Transition lengths determined by [Andrews \(1976\)](#) for homogeneous stress and strength provide an upper bound for transition lengths in models considered here.

[Andrews \(1976\)](#) numerically showed that nondimensional transition distance  $L_{BA}/L^c$  on a homogeneously prestressed interface, with initial conditions appropriate for a quasi-static critical crack, is a function of the seismic ratio  $S$  (or, equivalently, prestress  $\bar{\tau}^o$ ). For high enough prestress (i.e.,  $S < S_{\text{crit}}$ ), transition length  $L_{BA}/L^c$  of the Burridge-Andrews mechanism is determined by the position where the maximum of the shear stress peak reaches static strength. For smaller prestress (i.e.,  $S \geq S_{\text{crit}}$ ), no intersonic transition is possible by the Burridge-Andrews mechanism, and  $L_{BA}/L^c$  is infinity. This study shows that if favorable heterogeneity is located closer to the main crack initiation region than  $L_{BA}/L^c$ , then intersonic transition may occur due to the heterogeneity, with the transition length approximately given by the location of the heterogeneity. For example, all models with sustained intersonic propagation in [Sections 4.3 and 4.4](#) have transition lengths dictated by the location of heterogeneity  $D/L^c = 12$ . If heterogeneities were not present in the models, transition

lengths by the Burridge-Andrews mechanism would be infinite for the prestress values studied.

#### 4.5.4 Importance of crack initiation procedure

The procedure of main crack initiation significantly affects subsequent crack propagation and hence the loading provided by the main crack to the location of favorable heterogeneity. That, in turn, affects the crack tip speed beyond the location of heterogeneity (Section 4.4, Figures 4.9 vs. 4.10).

In the smooth initiation procedure (described in Section 4.3), we stop the time-dependent loading increase when the initial half size  $L_{\text{ini}}$  of the main crack reaches the nucleation half size  $L^{\text{nucl}}$  determined by Uenishi and Rice (2003). That, plus the slow loading we choose, ensures that the initiation procedure mimics tectonically driven slow nucleation on faults in the Earth’s crust. Our more abrupt crack initiation (Section 4.4) initiates the main crack by imposing prestress 1% larger than static strength over length  $2L^c$ , a procedure typical in modeling single earthquakes. For the background prestress levels used in this study,  $2L^c$  is appreciably larger than  $2L^{\text{nucl}}$  (Table 4.1). That creates larger initial crack sizes and faster acceleration of the main crack, by overstressing the main crack initially in comparison with a slow, quasi-static nucleation process. The resulting higher shear stresses ahead of the main crack promote intersonic transition. This more abrupt initiation procedure can be considered a proxy for larger propagation distances as explained in Section 4.4.

Note that similar overstressing of the crack can be achieved with our smooth initiation procedure by using faster time-dependent loading and continuing it until initial crack half sizes larger than  $L^{\text{nucl}}$  would be created. Under slow tectonic loading characteristic for earthquakes, nucleation zones should become unstable after reaching half lengths of  $L^{\text{nucl}}$ , as shown by Uenishi and Rice (2003) and confirmed in this work, making subsequent tectonic loading irrelevant on the time scale of the dynamic event. Hence nucleation half sizes larger than  $L^{\text{nucl}}$  cannot be obtained under slowly increasing loading. In a model, any loading added to the nucleation zone after a developing nucleation site reaches the half size  $L^{\text{nucl}}$  represents extra loading or overstressing. More abrupt initiation procedure similarly provides the crack with extra loading. It is possible that such extra loading can result on real faults for some dynamic triggering scenarios or rapid strength variations. However, it

is important to keep in mind that nucleation procedures that are abrupt and/or overstress the crack initially may not be the most common ones on tectonically loaded faults.

In Sections 4.3 and 4.4, we have considered relatively low background prestress levels, lower than the ones needed for intersonic transition by the Burridge-Andrews mechanism. We have conducted additional simulations that use the more abrupt initiation procedure with higher prestress levels in the absence of heterogeneities. In those simulations, the main crack achieves intersonic speeds much sooner than predicted by the Burridge-Andrews mechanism. If we load the nucleation region even more, we can make the main crack transition to intersonic speeds right outside the nucleation zone. In those cases, transition to intersonic speeds happens by either the abrupt transition mechanism described in this work, or by the Burridge-Andrews daughter mechanism, or both (that is, in some cases, the crack experiences abrupt speed changes twice, once by the abrupt mechanism described in this study, and the second time by nucleating an intersonic Burridge-Andrews daughter crack in front of the already intersonic crack).

These results for overstressed cracks are consistent with the studies of Festa and Vilotte (2006) and Shi et al. (2007) who considered, in the absence of stress heterogeneity beyond the nucleation region, the dependence of intersonic transition and rupture mode on the initiation procedure, and with the study of Geubelle and Kubair (2001) and Shi and Ben-Zion (2006). In Shi et al. (2007), the initiation procedure is similar to the more abrupt procedure of this work, in that a value of shear stress about 3% above the static strength is used over a zone which is about three to six times larger than  $2L^{\text{nucl}}$ . That may explain the rapid transition of rupture to intersonic speeds in the model of Shi et al. (2007) for high background prestress levels. (Note that their study uses a friction law of a rate and state type.) In Festa and Vilotte (2006), a nucleation procedure with a peaked stress in the nucleation zone is used. They find that intersonic transition is enhanced, and transition distances are shorter, when peaked loading with widths progressively larger than  $2L^{\text{nucl}}$  is used. Geubelle and Kubair (2001), while concentrating on mixed-mode failure, considered, in part, intersonic transition for a purely mode II crack. They found that the crack transitions to intersonic speeds by abruptly changing the speed of its tip at distances very close to the crack initiation zone. The initiation

procedure in [Geubelle and Kubair \(2001\)](#) is not described in detail but short transition distances obtained in that work suggest that the initiation procedure provided some overstressing, in the sense defined above.

#### 4.5.5 Propagation speeds in the intersonic regime

Once a crack acquires intersonic speeds, it tends to accelerate, in our models, to speeds larger than  $\sqrt{2}c_s$  and close to the dilatational wave speed  $c_p$ . This is consistent with the theoretical study of [Burridge et al. \(1979\)](#) who concluded that intersonic ruptures in models with finite tractions, constant fracture energy, and homogeneous prestress would accelerate to  $c_p$  (our models have homogeneous prestress after the location of favorable heterogeneity). This result is also consistent with experiments (e.g., [Xia et al., 2004](#)). [Samudrala et al. \(2002\)](#) found that, for velocity-weakening interfaces, the open interval of speeds from  $\sqrt{2}c_s$  to  $c_p$  corresponds to stable rupture growth, so speeds larger than  $\sqrt{2}c_s$  should be typical for velocity-weakening interfaces as well. Note that, for singular cracks,  $\sqrt{2}c_s$  is the only possible intersonic speed, as this is the only speed at which the energy release rate is positive ([Freund, 1990](#)), but that is no longer the case for cohesive-zone models with finite tractions.

#### 4.5.6 Implications for earthquake dynamics

Models for intersonic transition and propagation proposed here may have important consequences for earthquake dynamics. Favorable heterogeneities considered in this work are likely to be present on real faults. Earthquake models predict that seismic events are preceded by quasi-static slip in so-called nucleation zones (e.g., [Lapusta et al., 2000](#); [Lapusta and Rice, 2003](#)) that are analogous to preexisting subcritical cracks considered in [Section 4.3](#). Faults are likely to harbor multiple nucleation zones. When one of these zones gives rise to an earthquake, the other developing nucleation zones would find themselves under the stress field of an approaching dynamic crack, creating the scenario considered in [Section 4.3](#). How heterogeneous stress and strength are on faults and on what scales is an active area of current research. Seismic inversions typically contain regions of high and low slip, which likely indicate variations in fault prestress and/or strength. In particular, faults may contain

patches of higher prestress considered in Section 4.4 or patches of lower strength. We do not present results for patches of lower strength in this work but our simulations show that they are similar to results for patches of higher prestress.

Our modeling indicates that intersonic transition may be dominated by those heterogeneities. In that case, interpretation of inferred intersonic propagation using the Burridge-Andrews mechanism for homogeneous prestress and strength could lead to misleading constraints on background prestress levels or friction properties.

Note that even when sustained intersonic propagation does not occur in our models, the presence of favorable heterogeneity often mimics intersonic propagation locally by producing significant advance in the crack tip location. For a preexisting subcritical crack or a patch of sufficiently high prestress (higher than  $\alpha$  defined in Section 4.4), the tip of combined rupture propagating beyond the patch is that of the secondary crack for patches close to and larger than  $L^{\text{nucl}}$  (for smaller patches, the secondary crack is overtaken by the main crack). Even if the secondary crack is sub-Rayleigh, average rupture speed would appear to be intersonic in the region that surrounds the patch. Consider, for example, the case with a patch of the size  $L_h/L^c = 0.20$  from the left panel of Figure 4.11. Eventual propagation is sub-Rayleigh in that case, but the secondary crack tip is about  $2L^c$  ahead of where the main crack front would have been if there were no patch. Hence the average crack speed in the space interval shown in Figure 4.11 (from  $\bar{x} = 9$  to  $\bar{x} = 16$ ) is  $1.4 c_s$ . In addition, favorable heterogeneity provides the main crack with additional stress release which temporarily increases stresses in front of the crack. That makes intersonic transition due to another heterogeneity or due to the Burridge-Andrews mechanism more likely.

In a broader context, this study shows the importance of incorporating heterogeneities into models of rupture dynamics. This study indicates that a small preexisting crack or higher-stressed patch can completely change the failure process on the interface, perturbing a sub-Rayleigh crack into becoming intersonic. This emphasizes the need to systematically study effects of stress and strength heterogeneities on rupture behavior.

## 4.6 Appendix

### 4.6.1 Intersonic loading field due to an accelerating sub-Rayleigh mode II crack

For a sufficiently smooth dynamic shear stress field  $\tau(x, t)$ , let us define its propagation speed  $c(x, t)$  as

$$c(x, t) = -\frac{\partial\tau(x, t)/\partial t}{\partial\tau(x, t)/\partial x}. \quad (4.7)$$

A stress field with  $c(x, t) > c_s$  and  $\partial\tau(x, t)/\partial t > 0$  represents stress increase that travels along the interface with an intersonic speed. We call such stress fields “intersonic loading fields” in this study. Intersonic loading fields should promote failure of the interface with intersonic speeds (and they indeed do as this study demonstrates). Simulations show that a sub-Rayleigh mode II crack spontaneously accelerating on a uniformly prestressed interface governed by linear slip-weakening friction develops a shear stress peak ahead of its tip (e.g., [Andrews \(1976\)](#), Figures 4.2 and 4.3), and stress in front of the peak represents an intersonic loading field.

This can be theoretically understood by considering a self-similar singular crack model, in which the stress field takes a general form of  $\tau(x, t) = \tilde{\tau}(x/t)$ . If a self-similar crack expands bilaterally with rupture speed  $v_r < c_R$  under uniform prestress  $\tau^o$  on an interface with dynamic resistance  $\tau^d$ , the stress field ahead of the crack between the dilatational and shear wave fronts can be expressed as (e.g., [Burridge, 1973](#); [Freund, 1990](#)):

$$\tau(x, t) = \tilde{\tau}(c = x/t) = \tau^o + (\tau^o - \tau^d) \frac{F(h, \omega)}{I(h)}, \quad (4.8)$$

$$h = 1/v_r, \quad a = 1/c_p, \quad b = 1/c_s, \quad \omega = t/x = 1/c, \quad (4.9)$$

$$F(h, \omega) = \int_a^\omega \frac{4\xi^2 \sqrt{\xi^2 - a^2}}{(h^2 - \xi^2)^{3/2} \sqrt{b^2 - \xi^2}} d\xi, \quad (4.10)$$

$$I(h) = \int_0^\infty \frac{(b^2 + 2\xi^2)^2 - 4\xi^2 \sqrt{a^2 + \xi^2} \sqrt{b^2 + \xi^2}}{(h^2 + \xi^2)^{3/2} \sqrt{b^2 + \xi^2}} d\xi. \quad (4.11)$$

The propagation speed of a self-similar stress field  $\tau(x, t)$  is  $c(x, t) = x/t$ . For points located between the dilatational and shear wave fronts  $c_s < x/t < c_p$ , stress propagates with intersonic speeds and increases if  $v_r < c_R$ :

$$\frac{\partial \tau}{\partial t} = (\tau^o - \tau^d) \frac{\partial F}{\partial \omega} \frac{\partial \omega}{\partial t} = \frac{\tau^o - \tau^d}{x} \frac{4\omega^2 \sqrt{\omega^2 - a^2}}{(h^2 - \omega^2)^{3/2} \sqrt{b^2 - \omega^2}} > 0. \quad (4.12)$$

Therefore, the stress field between the dilatational and shear wave fronts of a sub-Rayleigh self-similar crack represents an intersonic loading field.

Larger sub-Rayleigh crack front speeds  $v_r$  correspond to larger stress between the dilatational and shear wave fronts. To show that, let us define  $G(1/v_r, 1/c) = (\tilde{\tau}(c) - \tau^o)/(\tau^o - \tau^d)$ , hence  $G(h, \omega) = F(h, \omega)/I(h)$ , and

$$\frac{\partial G(h, \omega)}{\partial h} = \frac{I(h) \partial F(h, \omega) / \partial h - F(h, \omega) \partial I(h) / \partial h}{I^2(h)} = \frac{\frac{\partial F}{\partial h} / F - \frac{\partial I}{\partial h} / I}{F I^3}. \quad (4.13)$$

Notice that  $F(h = 1/v_r, \omega = 1/c) > 0$  and  $I(h = 1/v_r) > 0$  for any  $0 < v_r < c_R$  and  $c_s \leq c < c_p$ , and

$$\frac{\partial F}{\partial h} = -\frac{3}{h} \int_a^\omega \frac{h^2}{h^2 - \xi^2} \frac{4\xi^2 \sqrt{\xi^2 - a^2}}{(h^2 - \xi^2)^{3/2} \sqrt{b^2 - \xi^2}} d\xi < -\frac{3}{h} F, \quad (4.14)$$

$$\frac{\partial I}{\partial h} = -\frac{3}{h} \int_0^\infty \frac{h^2}{h^2 + \xi^2} \frac{(b^2 + 2\xi^2)^2 - 4\xi^2 \sqrt{a^2 + \xi^2} \sqrt{b^2 + \xi^2}}{(h^2 + \xi^2)^{3/2} \sqrt{b^2 + \xi^2}} d\xi > -\frac{3}{h} I. \quad (4.15)$$

Combining equations (4.13–4.15), we get:

$$\frac{\partial G(h, \omega)}{\partial h} < 0; \quad h = 1/v_r > 1/c_R \quad \text{and} \quad 1/c_p \leq \omega < 1/c_s. \quad (4.16)$$

One can also find that  $G(1/v_r, 1/c_s) \rightarrow 1.775$  as  $v_r \rightarrow c_R$ , as shown in Figure 4.13a, which is consistent with the value of  $S_{\text{crit}}$  computed by Andrews (1976).

The theoretical considerations above are based on a self-similar crack model, in which stress is inverse square-root singular at the rupture tip for sub-Rayleigh propagation. However, as Andrews (1976) pointed out, a crack governed by a linear slip-weakening law can be well approximated by

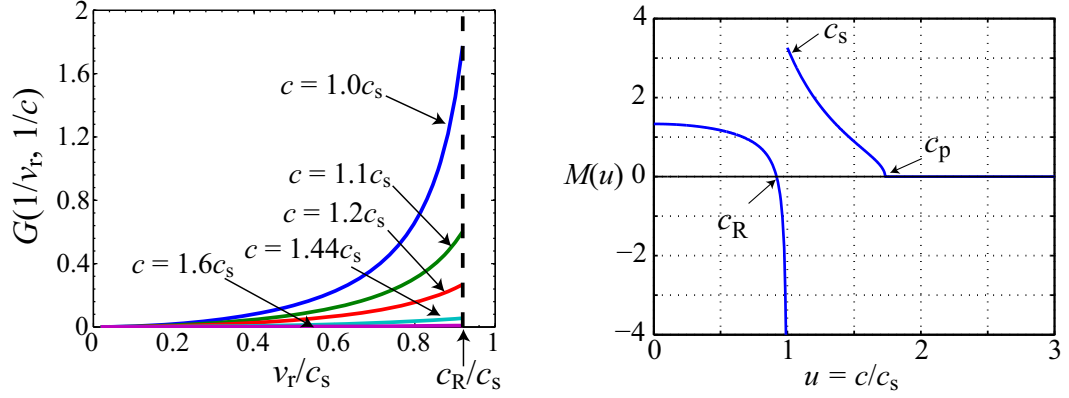


Figure 4.13: Left:  $G(1/v_r, 1/c) = (\tilde{\tau}(c) - \tau^o)/(\tau^o - \tau^d)$  for different  $c > c_s$  and rupture speed  $v_r$ . Right: Mode II kernel  $M(u)$  of the space-time representation of  $f(x, t)$

the self-similar solution after it propagates through several critical lengths  $L^c$ .

#### 4.6.2 Expressions for stress transfer functional in the spectral boundary integral method

In simulations, we use a spectral boundary integral method (Section 4.2), in which Fourier coefficients of the stress transfer functional  $f(x, t)$  are related to Fourier coefficients of slip  $\delta(x, t)$  and its history (Perrin et al., 1995; Geubelle and Rice, 1995; Lapusta et al., 2000). The simulated domain of length  $L$  is discretized into  $N$  elements and we write:

$$\delta(x, t) = \sum_{k=-N/2}^{N/2} \hat{\delta}(k, t) \exp(i2\pi kx/L), \quad (4.17)$$

$$f(x, t) = \sum_{k=-N/2}^{N/2} \hat{f}(k, t) \exp(i2\pi kx/L). \quad (4.18)$$

The Fourier coefficients  $\hat{f}(k, t)$  and  $\hat{\delta}(k, t)$  are related by:

$$\hat{f}(k, t) = -\frac{\mu \tilde{k}}{2} \int_0^t C_{\text{II}}(\tilde{k}c_s t') \hat{\delta}(k, t - t') \tilde{k}c_s dt', \quad (4.19)$$

$$C_{\text{II}}(T) = J_1(T)/T + 4T[W(c_p T/c_s) - W(T)] - 4\frac{c_p}{c_s} J_0(c_p T/c_s) + 3J_0(T), \quad (4.20)$$

where  $\tilde{k} = 2\pi k/L$ ,  $C_{\text{II}}(T)$  is the mode II convolution kernel (Geubelle and Rice, 1995),  $J_0(T)$  and  $J_1(T)$  are Bessel functions, and

$$W(T) = 1 - \int_0^T \frac{J_1(x)}{x} dx. \quad (4.21)$$

Integration of equation (4.19) by parts separates the stress functional into static (long-term) and transient dynamic parts:

$$\hat{f}(k, t) = -\mu\tilde{k} \left(1 - \frac{c_s^2}{c_p^2}\right) \hat{\delta}(k, t) + \frac{\mu\tilde{k}}{2} \int_0^t K_{\text{II}}(\tilde{k}c_s t') \frac{\partial \hat{\delta}(k, t-t')}{\partial t} dt', \quad (4.22)$$

$$K_{\text{II}}(T) = \int_T^\infty C_{\text{II}}(\eta) d\eta = 2\left(1 - \frac{c_p^2}{c_s^2}\right) - \int_0^T C_{\text{II}}(\eta) d\eta. \quad (4.23)$$

The integral term on the right-hand side of equation (4.22) describes dynamic stress changes due to waves. If it is neglected, the resulting formulation is referred to as “quasi-dynamic”. The quasi-dynamic formulation differs from the quasi-static formulation in that it contains the radiation damping term,  $\mu V/(2c_s)$ , which captures some dynamic effects. The quasi-dynamic formulation is widely used in earthquake studies to simplify computations. We use the quasi-dynamic formulation during slow and relatively long smooth initiation phases discussed in Section 4.3, to speed up computations and to ensure that no stress waves from the initiation procedure exist in the model at later times. After the initiation phase, we use fully dynamic formulation. Note that kernel  $C_{\text{II}}(T)$  oscillates with decaying amplitude which allows to truncate the integral term (e.g., Lapusta et al., 2000; Day et al., 2005). However, in this study we do not employ any truncation, to compute dynamic stress fields as accurately as possible.

### 4.6.3 Some aspects of crack tip behavior during abrupt intersonic transition

As we show in Sections 4.3 and 4.4, if a secondary crack finds itself under the action of an intersonic loading field generated by an approaching main crack, the tip of the secondary crack can rapidly accelerate to values numerically indistinguishable from  $c_R$  and then abruptly jump to an intersonic

speed. While steady crack propagation with  $c_R$  would result in zero cohesive zone length and infinite slip velocities and hence it is impossible, our simulations show that transient propagation with  $c_R$  may be possible. The crack tip jumps to an intersonic speed by initiating sliding just one cell  $\Delta x$  away from the crack tip (Figures 4.6, 4.7). At that moment, shear stress in the cell immediately in front of the tip is below static strength, and shear stress in the next cell has reached static strength (Figure 4.7). The same process is observed for smaller and smaller  $\Delta x$ , with the shear stress in the intermediate cell closer and closer to static strength. Hence, in the limit  $\Delta x \rightarrow 0$ , we expect intersonic transition to occur right at the crack tip.

To understand why shear stress is lower immediately next to the crack tip than farther ahead, let us consider a mode II crack tip that has propagated (for a short time) with the Rayleigh wave speed  $c_R$ . How does the wave radiation from that tip at time  $t_o$  influence the stress field in front of the tip at the time  $t > t_o$ ? To answer that question, let us consider the stress transfer functional  $f(x, t)$  (equation 4.3) in the space-time domain (e.g., [Cochard and Rice, 1997](#)):

$$f(x, t) = \frac{\mu c_s}{2\pi} \int_{-\infty}^t \int_{-\infty}^{+\infty} M\left(\frac{x - \zeta}{c_s(t - \theta)}\right) \frac{\delta_{,\zeta\zeta}(\zeta, \theta)}{c_s(t - \theta)} d\zeta d\theta, \quad (4.24)$$

$$M(u) = \begin{cases} \frac{4\sqrt{1-u^2}\sqrt{1-(c_s^2/c_p^2)u^2} - (2-u^2)^2}{u^2\sqrt{1-u^2}} & \text{if } |u| < 1, \\ \frac{4\sqrt{1-(c_s^2/c_p^2)u^2}}{u^2} & \text{if } 1 < |u| < c_p/c_s, \\ 0 & \text{if } |u| > c_p/c_s \end{cases} \quad (4.25)$$

The integral kernel  $M(u)$  is plotted in Figure 4.13b. Note that  $M(u) < 0$  for  $c_R/c_s < u < 1$ . Let us denote the location of the crack tip at the time  $t$  by  $x_r(t)$ , where  $x_r(t) = x_r(t_o) + c_R(t - t_o)$ .

Numerical calculation approximates the above integral with discretized space and time, effectively assuming constant  $\delta_{,\zeta\zeta}$  within the cell size  $\Delta x$  and time step  $\Delta t$ . Therefore rupture tip located at  $x_r(t_o)$  at the time  $t_o$  contributes to the stress functional  $f(x, t)$  by an amount  $\Delta f(x_r(t_o), t_o)$ :

$$\Delta f(x_r(t_o), t_o) = \frac{\mu c_s}{2\pi} M\left(\frac{x - x_r(t_o)}{c_s(t - t_o)}\right) \frac{\delta_{,\zeta\zeta}(x_r(t_o), t_o)}{c_s(t - t_o)} \Delta t \Delta x. \quad (4.26)$$

In (4.26),  $\delta_{,\zeta\zeta}(x_r(t_o), t_o)$  is the value for the spatial cell located in the ruptured region ( $x < x_r(t_o)$ ) and, for sufficiently small cell size, its sign can be obtained by considering  $\zeta \rightarrow x_r^-(t_o)$ . Since  $\delta(\zeta \geq x_r(t_o), t_o) = 0$  and  $\delta_{,\zeta}(x_r^-(t_o), t_o) = \delta_{,\zeta}(x_r^+(t_o), t_o) = 2\varepsilon_{xx}(x_r(t_o), t_o) = 0$ , where  $\varepsilon_{xx}$  is the normal strain in  $x$  direction, we find:

$$0 < \delta(\zeta < x_r(t_o), t_o) = \frac{1}{2}\delta_{,\zeta\zeta}(x_r^-(t_o), t_o)(\zeta - x_r(t_o))^2 + o((\zeta - x_r(t_o))^2), \quad (4.27)$$

and hence  $\delta_{,\zeta\zeta}(x_r^-(t_o), t_o) > 0$ . From properties of kernel  $M$  and equations (4.26) and (4.27), we obtain for  $t > t_o$ :

$$\begin{cases} \Delta f(x_r(t_o), t_o) < 0 & x_r(t_o) + c_R(t - t_o) < x < x_r(t_o) + c_s(t - t_o), \\ \Delta f(x_r(t_o), t_o) > 0 & x_r(t_o) + c_s(t - t_o) < x < x_r(t_o) + c_p(t - t_o). \end{cases} \quad (4.28)$$

At time  $t$ , the crack tip is at  $x_r(t) = x_r(t_o) + c_R(t - t_o)$ . Therefore  $\Delta f(x_r(t_o), t_o) < 0$  for  $x \in [x_r(t), x_r(t) + (c_s - c_R)(t - t_o)]$ , and  $\Delta f(x_r(t_o), t_o) > 0$  for  $x \in [x_r(t) + (c_s - c_R)(t - t_o), x_r(t) + (c_p - c_R)(t - t_o)]$ . This means that the crack tip traveling with  $c_R$  at time  $t_o$  contributes negatively to shear stress at the part of the interface immediately in front of the current rupture tip (at time  $t$ ) and positively to shear stress a little farther ahead. This relation holds for all times  $t_o < t$  for which the crack has propagated with a speed at or close to  $c_R$ . Piling up of these contributions from different  $t_o < t$  may explain the observed stress distribution during intersonic transition in our simulations (Figure 4.7), where shear stress is lower in the cell immediately in front of the crack tip and reaches static strength in the next cell. In the continuum solution, the negative contribution of the crack tip to location immediately ahead may be exactly balanced by contributions from other parts of the crack, as our simulations suggest for decreasing cell sizes. But in a discretized calculation, contributions from the crack front are evidently overemphasized, which is not surprising since one would expect largest numerical errors to come from crack tips where slip velocity and stress vary rapidly.

## Chapter 5

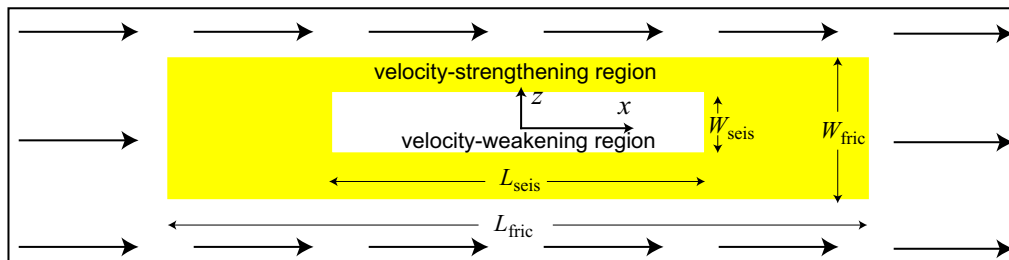
# Intersonic rupture in 3D simulations of earthquake sequences and aseismic slip: effect of rheological boundaries and weaker patches

The results of Chapter 4 suggest that heterogeneity can have significant effect on intersonic transition and propagation. The 2D in-plane model of Chapter 4 is a widely used tool to study earthquake dynamics, yet it has a number of simplifications that can affect its applicability to natural earthquakes, as discussed in Chapters 1 and 4. 2D models simplify the fault to one dimension, which was shown to promote intersonic transition in comparison with more realistic 3D models (e.g., Day, 1982a,b; Fukuyama and Olsen, 2002; Dunham, 2006). Moreover, as demonstrated in Chapter 3, it is important to model earthquakes under stress conditions that naturally develop in the model due to prior slip, as artificially chosen initial conditions may never repeat in the long-term history of the fault. The outcome of single-event simulations of Chapter 4 depends on the chosen initial conditions.

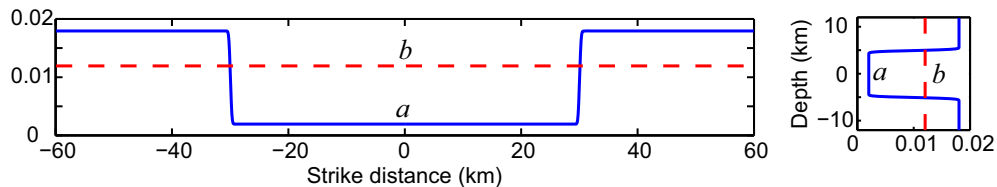
In this Chapter, we remove some of the simplifications of Chapter 4 by studying intersonic transition and propagation in simulations of earthquake sequences and aseismic slip using the 3D fault model developed in Chapter 3. Our goal is to verify the qualitative conclusion of Chapter 4 that fault heterogeneity favors intersonic transition and can, in fact, be the dominating factor.

As reported in the following, we indeed find that intersonic transition is dominated by fault heterogeneity in 3D models. In part, we discover that rheological boundaries play an important role, favoring intersonic transition. The boundaries separate regions of different slip behavior in the interseismic period, concentrating stress and hence promoting larger rupture speeds during occasional earthquakes. This behavior was not captured by any of the prior studies in 3D models (e.g., [Day, 1982a](#); [Madariaga and Olsen, 2000](#); [Fukuyama and Olsen, 2002](#); [Dunham, 2006](#)), as they considered a single instance of dynamic rupture in fault models that do not incorporate rheological boundaries. Presence of such rheological boundaries on natural faults has ample laboratory and observational evidence (e.g., [Blanpied et al., 1991](#); [Marone et al., 1991](#); [Blanpied et al., 1995](#); [Ellsworth et al., 2000](#); [Marone, 1998](#); [Lyons and Sandwell, 2002](#); [Schaff et al., 2002](#); [Waldhauser et al., 2004](#); [Shearer et al., 2005](#)). Seismogenic regions, which are locked during interseismic period, are likely to have slowly moving, velocity-strengthening regions above (at shallow depths, 0–3 km) and below (deeper than 15 km or so in Southern California). Existence of shallow velocity-strengthening regions is supported by laboratory experiments, in which rock friction at low normal stress typically exhibits velocity-strengthening behavior due to unconsolidated fault gouge (e.g., [Marone et al., 1991](#); [Marone, 1998](#)), observations of interseismic shallow creep (e.g., [Lyons and Sandwell, 2002](#)), shallow afterslip of large earthquakes (e.g., [Marone et al., 1991](#); [Marone, 1998](#)), and the deficit of seismicity at shallow depths (e.g., [Shearer et al., 2005](#)). The deeper velocity-strengthening regions may be caused by elevated temperatures, which are shown to favor such behavior in the lab (e.g., [Blanpied et al., 1991, 1995](#)). Such regions are further supported by clustering of small earthquakes and limits on the depth extent of seismicity (e.g., [Ellsworth et al., 2000](#); [Schaff et al., 2002](#); [Waldhauser et al., 2004](#)) and deep postseismic slip (e.g., [Reilinger et al., 2000](#)). In single-event rupture models, velocity-strengthening regions have been often approximated as unbreakable regions, with no special stress distribution on their boundary. Further comparison between our and prior studies is given in Section 5.5. In the cases when the rheological boundary does not cause the entire rupture to transition to intersonic speeds, we find that compact heterogeneity of lower seismic ratio further promotes intersonic transition.

(a): Fault model for Cases I and II



(b): Friction parameters for Case I



(c): Friction parameters for Case II

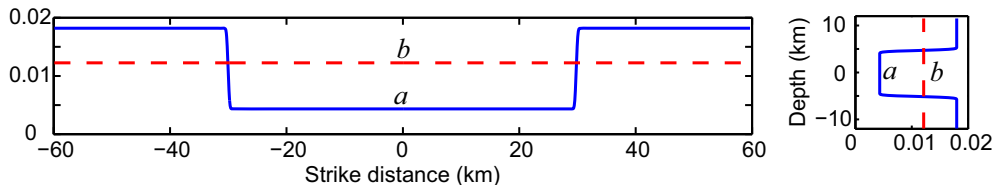


Figure 5.1: (a) A buried strike-slip fault model which is 180 km long and 36 km wide. The region where friction acts is  $L_{\text{fric}} = 120$  km long and  $W_{\text{fric}} = 24$  km wide. It is separated into a potentially seismogenic velocity-weakening region (white color,  $L_{\text{seis}} = 60$  km,  $W_{\text{fric}} = 10$  km), and a velocity-strengthening region (yellow color). The outside region moves with the constant loading rate  $V_{\text{pl}} = 10^{-9}$  m/s = 32 mm/year. Figure (b) and (c) show distributions of friction parameters  $a$  and  $b$  along horizontal line  $z = 0$  km and vertical line  $x = 0$  km in Cases I and II, respectively.

## 5.1 Fault model

We consider a buried strike-slip fault segment that contains a potentially seismogenic region with steady-state velocity-weakening properties surrounded by steady-state velocity-strengthening region (Figure 5.1). The fault segment is loaded by the constant tectonic loading rate  $V_{\text{pl}} = 10^{-9}$  m/s = 32 mm/year. The simulated fault domain is  $\lambda_x = 180$  km long and  $\lambda_z = 36$  km wide; it is periodically repeated along  $x$  and  $z$  direction to form an infinite plane. The fault segment where friction acts is  $L_{\text{fric}} = 120$  km long and  $W_{\text{fric}} = 24$  km wide, and the velocity-weakening (potentially seismogenic) region is  $L_{\text{seis}} = 60$  km by  $W_{\text{fric}} = 10$  km. The seismogenic region in this Chapter is longer than that of Chapter 3, and it has the potential to host larger strike-slip earthquakes.

The fault interface is governed by rate and state friction (3.10). The distributions of friction

parameters  $a$  and  $b$  are:

$$a(x, z) = \bar{a}_{vw} + (\bar{a}_{vs} - \bar{a}_{vw})B(x; L_{\text{seis}}; w_x)B(z; W_{\text{seis}}; w_z) \quad (5.1)$$

$$b(x, y) = \bar{b} \quad (5.2)$$

where

$$B(\xi; \lambda; w) = \begin{cases} 0; & |\xi| \leq (\lambda - w)/2 \\ \frac{1}{2} \left\{ 1 - \tanh \left( \frac{w}{|\xi| - (\lambda - w)/2} + \frac{w}{|\xi| - (\lambda + w)/2} \right) \right\}; & (\lambda - w)/2 < |\xi| < (\lambda + w)/2 \\ 1; & |\xi| \geq (\lambda + w)/2 \end{cases} \quad (5.3)$$

In equations (5.1–5.3),  $x$  and  $z$  are the horizontal and vertical coordinates of the fault, with the origin  $(0, 0)$  located at the center of the fault, and  $\bar{a}_{vw}$ ,  $\bar{a}_{vs}$ , and  $\bar{b}$  are constants that satisfy  $(\bar{a}_{vw} - \bar{b}) < 0$  and  $(\bar{a}_{vs} - \bar{b}) > 0$ . The region of  $|x| < (L_{\text{seis}} - w_x)/2$  and  $|z| < (W_{\text{seis}} - w_z)/2$  is uniformly velocity-weakening, with  $a(x, z) = \bar{a}_{vw}$  and  $b(x, z) = \bar{b}$ ; the region of  $|x| > (L_{\text{seis}} + w_x)/2$  or  $|z| > (W_{\text{seis}} + w_z)/2$  is uniformly velocity-strengthening, with  $a(x, z) = \bar{a}_{vs}$  and  $b(x, z) = \bar{b}$ ; friction properties smoothly transition from velocity-weakening to velocity-strengthening in between the two regions.  $w_x = 2$  km and  $w_z = 2$  km are the horizontal and vertical sizes of the transition region, which are a small fraction of  $L_{\text{seis}}$  and  $W_{\text{seis}}$ , respectively. Approximately (up to a fraction of  $w$ ), the region of  $|x| < L_{\text{seis}}/2$  and  $|z| < W_{\text{seis}}/2$  is velocity-weakening, and the outside region is velocity-strengthening.

We show results for four simulated cases. For all cases, we use  $\sigma = 50$  MPa,  $V_o = 10^{-6}$  m/s,  $f_o = 0.6$ ,  $\bar{a}_{vs} = 0.018$ , and  $\bar{b} = 0.012$  (Table 5.1). The parameters  $\bar{a}_{vw}$  and  $L$  are case-dependent, as shown in Table 5.2. Cases I and II contain uniform velocity-weakening regions with properties given by (5.1–5.3), with Case I favoring intersonic transition. Case IIIh1 and IIIh2 incorporate heterogeneity favorable to intersonic transition. More details about the cases are given in Sections 5.3– 5.4.

Our choice of spatial resolution and numerical parameters is motivated by our studies in Chapter

Table 5.1: Case-independent parameters

Parameter	Symbol	Value
Overall fault length	$\lambda_x$	180 km
Overall fault width	$\lambda_z$	36 km
Frictional fault, length	$L_{\text{fric}}$	120 km
Frictional fault, width	$W_{\text{fric}}$	24 km
Seismogenic region, length	$L_{\text{seis}}$	60 km
Seismogenic region, width	$W_{\text{seis}}$	10 km
Transition region, horizontal	$w_x$	2 km
Transition region, vertical	$w_z$	2 km
Loading slip rate	$V_{\text{pl}}$	32 mm/yr
Shear modulus	$\mu$	30 GPa
Shear wave speed	$c_s$	3.0 km/s
Poisson's ratio	$\nu$	0.25
Reference slip velocity	$V_o$	$10^{-6}$ m/s
Reference friction coefficient	$f_o$	0.6
Effective normal stress	$\sigma$	50 MPa
Rate-and-state parameter	$\bar{b}$	0.012
Rate-and-state parameter	$\bar{a}_{\text{vs}}$	0.018

Table 5.2: Case-dependent parameters

Case	Friction parameter $\bar{a}_{\text{vw}}$	Characteristic slip distance $L$ (m)	heterogeneity		
			$\Delta a$	$L_h$ (km)	$x_h$ (km)
I	0.002	0.02	None		
II	0.004	0.016	None		
IIh1	0.004	0.016	0.003	9	-5
IIh2	0.004	0.016	0.003	9	5

3. For rate and state friction, the quasi-static cohesive zone size  $\Lambda_0$  is (Chapter 3):

$$\Lambda_0 = C_1 \frac{\mu^* L}{b\sigma}, \quad (5.4)$$

where  $C_1$  is a constant equal to  $9\pi/32$  if the shear traction distribution within the cohesive zone is linear in space,  $\mu^* = \mu$  for a mode III crack and  $\mu^* = \mu/(1 - \nu)$  for a mode II crack. In all simulations, we use  $L = 0.016$  m to 0.02 m, leading to  $\Lambda_0 = 706$  m to 882 m for mode III.  $\Lambda_0$  for mode II is  $1/(1 - \nu) = 4/3$  times larger. In all simulations, we use cell size  $\Delta x = 100$  m, which resolves the quasi-static cohesive zone size by at least seven points. According to Chapters 2 and 3, such resolution is adequate to correctly resolve the evolution of rupture at its tip.

The horizontal length of the seismogenic zone is  $L_{\text{seis}} = 60$  km, and the time window  $T_w$  for computing stress-transfer convolutions and storing previous slip history is chosen as:

$$T_w = \alpha \frac{L_{\text{seis}}}{c_s}. \quad (5.5)$$

In all simulations, we use  $\alpha = 1$ , which is proven large enough to accurately capture the inertial effects (Chapter 3). We do not adopt any mode-dependent truncation in simulations presented in this chapter.

To start the first event, the initial shear stress  $\tau_o$  is set to be larger in a circular region:

$$\tau_o = \begin{cases} f_o\sigma \left[ 1 + 1\% \exp\left(\frac{r^2}{r^2 - r_0^2}\right) \right], & r < r_0 \\ f_o\sigma, & r \geq r_0 \end{cases} \quad (5.6)$$

where  $r = \sqrt{(x - x_0)^2 + (z - z_0)^2}$ ,  $x_0 = -20$  km,  $z_0 = 0$  km, and  $r_0 = 3$  km. The distribution of initial shear stress has smooth variation over space. It peaks at  $r = 0$  with the maximum value of  $1.01f_o\sigma$ , smoothly decreases to  $f_o\sigma$  as  $r$  increases to  $r_0$ , and then stays constant for  $r > r_0$ , as shown in Figure 5.2. The state variable  $\theta$  is initially set to be  $L/V_o$ , steady state value for slip velocity  $V_o$ . In Chapter 3, we have shown that the initial values of field quantities affect only the first few events,

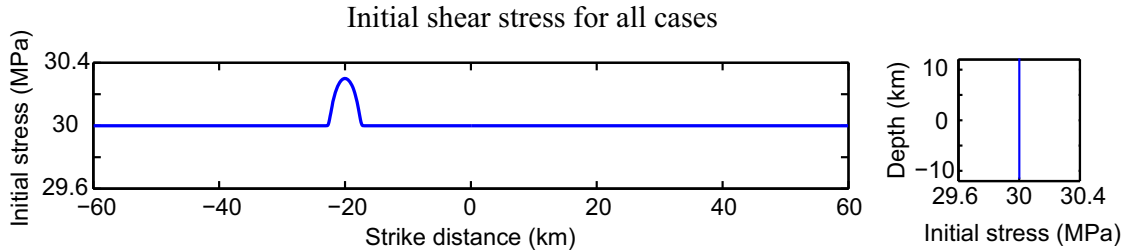


Figure 5.2: Distribution of shear stress at the beginning of each simulation along  $z = 0$  km (left panel) and  $x = 0$  km (right panel)

as the model later evolves toward behavior dictated only by the model geometry, fault loading, and friction properties.

## 5.2 Connection between rate and state friction and linear slip-weakening friction during dynamic rupture

Most previous studies on intersonic transition have used linear-slip weakening friction, in which friction linearly decreases from a static peak value  $\tau_p$  to a constant dynamic value  $\tau_d$  over a characteristic slip  $d_0$ . The seismic ratio  $S$  defined by

$$S = \frac{\tau_p - \tau_i}{\tau_i - \tau_d} \quad (5.7)$$

has been found to be an important parameter controlling rupture behavior in single-rupture models (e.g., [Andrews, 1976](#)), where  $\tau_i$  is the initial shear stress or the shear stress on the fault before rupture propagates. Intersonic transition is favored by higher initial stress  $\tau_i$ , and hence smaller seismic ratio  $S$  (e.g., [Burridge, 1973](#); [Andrews, 1976](#)).

In this study, we use rate and state friction, which behaves similarly to linear slip-weakening friction during dynamic rupture (e.g., [Cocco and Bizzarri, 2002](#), Chapter 3). The advantage of using rate-and-state friction is that it enables us to simulate many earthquake cycles due to its property of restrengthening during interseismic periods and due to its positive direct effect, which is essential for the numerical algorithm to be able to adopt large time steps during quasi-static deformation processes while yielding stable numerical results ([Lapusta et al., 2000](#)). Figure 5.3(a) shows shear

stress vs. slip of the fault location (0 km, 0 km) during the third event in our simulated Case I. The behavior is similar to linear slip-weakening friction: after shear stress reaches a peak value, it linearly decreases to a residual level, with the slip weakening rate  $W = b\sigma/L$  and equivalent slip weakening distance  $d_0 \approx 20L = 0.4$  m (e.g., [Cocco and Bizzarri, 2002](#); [Lapusta and Liu, 2008](#)). However, for rate and state friction, the peak strength  $\tau_p$  and the dynamic frictional resistance  $\tau_d$  are not known a priori. Instead,  $\tau_p$ ,  $\tau_d$ , and hence  $S$ , depend on slip velocity and state variable.

We derive an approximate formula to relate the seismic ratio  $S$  to friction parameters  $a$  and  $b$  for a fault governed by rate and state friction with a number of assumptions motivated by our simulations. During dynamic processes before the arrival of the main rupture, the seismogenic velocity-weakening region is essentially locked with slip velocity  $V_{bg}$  which is several orders of magnitude smaller than the plate loading rate  $V_{pl} = 10^{-9}$  m/s. The value of the state variable  $\theta$  is approximately equal to the earthquake recurrence period  $T$  ([Kaneko and Lapusta, 2008](#)). Hence, the shear stress inside the seismogenic region before an earthquake can be estimated as:

$$\tau_i = \sigma \left\{ f_o + a \ln \frac{V_{bg}}{V_o} + b \ln \frac{V_o T}{L} \right\}. \quad (5.8)$$

As the rupture tip arrives, slip velocity increases to the seismic level  $V_{dyn}$  with negligible slip such that the state variable  $\theta = T$  cannot evolve, and the stress reaches its peak value  $\tau_p$ :

$$\tau_p = \sigma \left\{ f_o + a \ln \frac{V_{dyn}}{V_o} + b \ln \frac{V_o T}{L} \right\}. \quad (5.9)$$

After that, the state variable  $\theta$  evolves to a steady-state value  $L/V_{dyn}$  for slip velocity  $V_{dyn}$ , and the stress reaches its dynamic friction level  $\tau_d$ :

$$\tau_d = \sigma \left\{ f_o + a \ln \frac{V_{dyn}}{V_o} - b \ln \frac{V_{dyn}}{V_o} \right\}. \quad (5.10)$$

Slip velocity  $V_{dyn}$  varies during this process but its variation is within an order of magnitude and has a small effect as  $V_{dyn}$  enters the expression (5.8-5.9) under the natural logarithm. The estimate

of the seismic ratio  $S$  therefore is:

$$S = \frac{\tau_p - \tau_i}{\tau_i - \tau_d} = \frac{a \ln(V_{\text{dyn}}/V_{\text{bg}})}{(b - a) \ln(V_{\text{dyn}}/V_o) - a \ln(V_{\text{dyn}}/V_{\text{bg}}) + b \ln(V_o T/L)}. \quad (5.11)$$

The estimate (5.11) cannot be used in a predictive manner, before finding the solution through simulations, because values of  $V_{\text{bg}}$ ,  $V_{\text{dyn}}$ , and  $T$  depend on the solution itself. However, since  $V_{\text{dyn}} > V_{\text{bg}}$  and  $V_{\text{dyn}} > V_o$ , (5.11) suggests that smaller values of  $a$  may decrease the seismic ratio  $S$ , hence promoting intersonic transition. This consideration motivates the selection of the four cases presented in this chapter (Table 5.2), where we achieve different intersonic behaviors in homogeneous seismogenic regions and induce heterogeneity favorable to intersonic transition mainly by varying the value of parameter  $a$ .

For all simulations in this chapter, we define the starting time of a dynamic event as the time when maximum slip velocity on the fault reaches  $V_{\text{seis}} = 0.1$  m/s, and the ending time as the time when maximum slip velocity on the fault becomes less than  $V_{\text{seis}}$ . The initial stress  $\tau_i(x, z)$  of an individual point is defined as the shear stress of that point at the starting time, residual stress  $\tau_e(x, z)$  is the shear stress at each point at the ending time of the event, peak strength  $\tau_p(x, z)$  is the maximum shear stress at a point during the event, and dynamic frictional resistance  $\tau_d(x, z)$  at each point is the stress when the slip velocity at that point is larger than  $V_{\text{seis}} = 0.1$  m/s for the last time before the end of the event. The static stress drop is given by  $\Delta\tau = \tau_i - \tau_e$ . Values of  $\tau_i$ ,  $\tau_e$ ,  $\tau_p$ , and  $\tau_d$  for point (0 km, 0 km) are marked by black crosses in Figure 5.3. Slips corresponding to times when  $\tau_i$ ,  $\tau_p$ ,  $\tau_d$ , and  $\tau_e$  are reached are marked as  $D_i$ ,  $D_p$ ,  $D_d$ , and  $D_e$  in Figure 5.3. Figures (a), (b), and (c) are for the third event of Case I, and (d) is for the third event of Case II. In both Case I and Case II,  $V_{\text{dyn}}$  is of the order of 1 m/s, and  $T$  is of the order of 100 years. Due to the smaller value of  $a$ , the seismic ratio  $S$  in Case I is smaller than in Case II, which is consistent with formula (5.9).

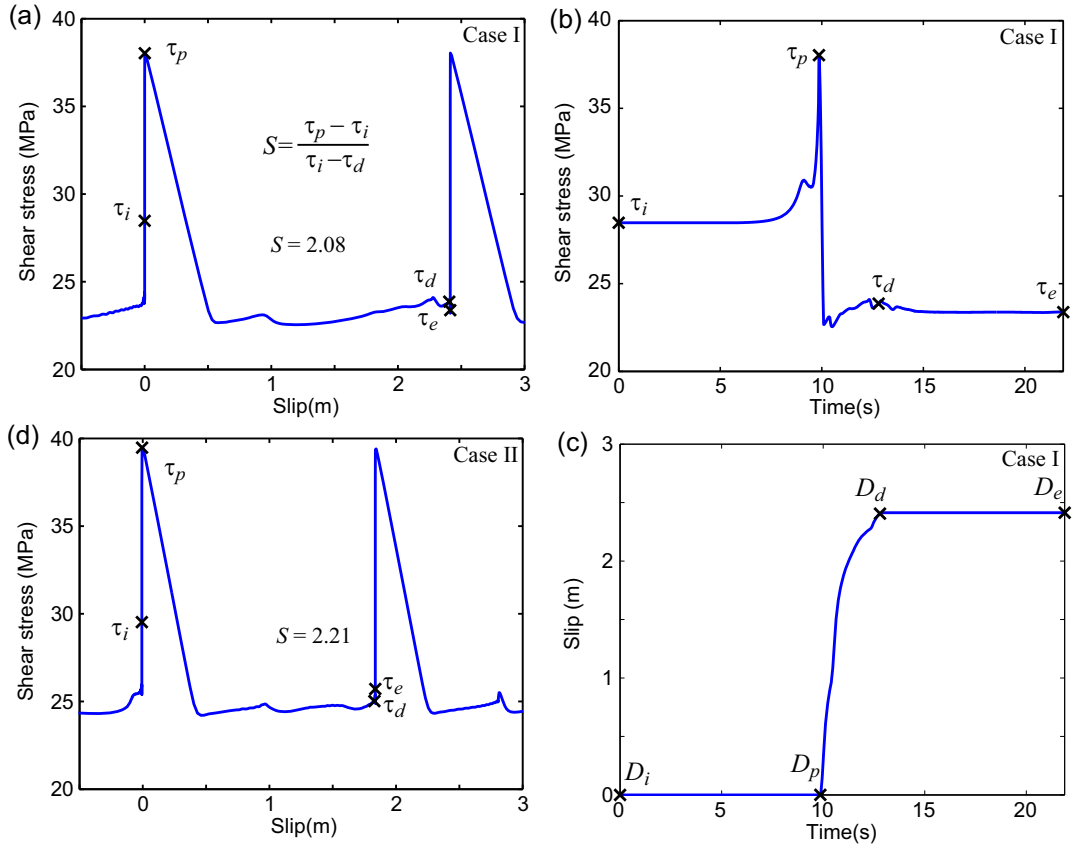


Figure 5.3: Typical behavior of a location within the seismogenic region, with (0 km, 0 km) used as an example. (a)–(c) Shear stress vs. slip, shear stress vs. time, slip vs. time for Case I. Zero time is the starting time of the third event, and slip is set to be zero at the zero time. Seismic ratio at this location is  $2.08 > S_{\text{crit},3D} (= 1.19)$  in this event. Nonetheless, rupture passes this location with an intersonic speed.  $\tau_p$ ,  $\tau_i$ ,  $\tau_d$ , and  $\tau_e$  are defined in the text. (d) Shear stress vs. slip for Case II. Zero time is the starting time of the third event. Seismic ratio is 2.21, and rupture passes this location with a subsonic speed. For both Cases I and II,  $V_{\text{dyn}}$  is of the order of 1 m/s, and  $T$  is of the order of 100 years. Larger  $a$  results in higher seismic ratio  $S$  in Case II, making Case II less susceptible to intersonic propagation.

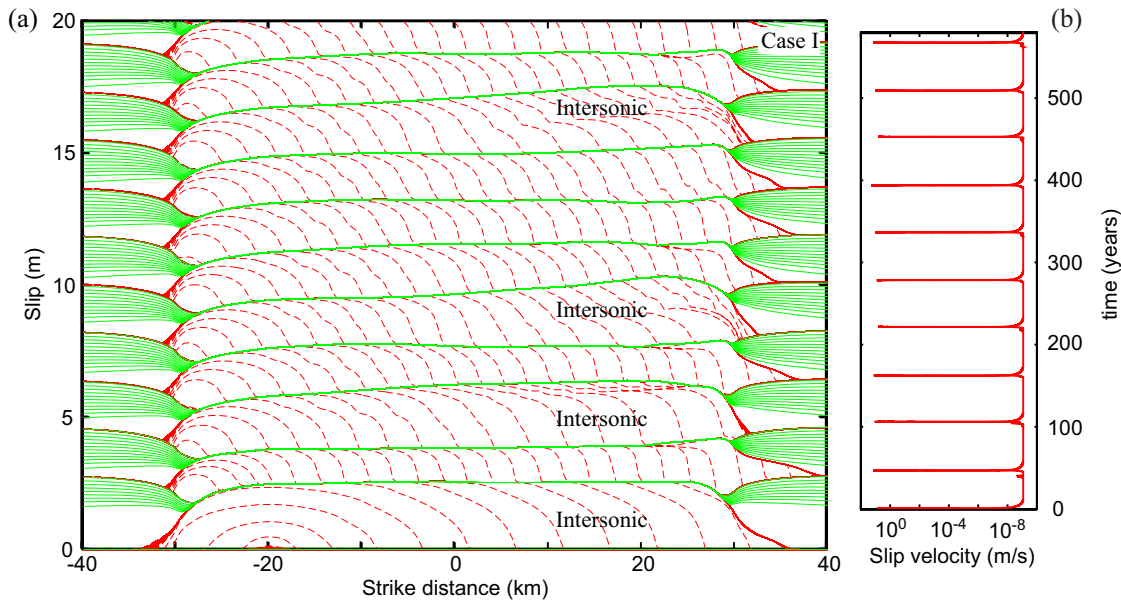


Figure 5.4: (a) Slip accumulation along the horizontal line  $z = 0$  km in Case I. Red dashed lines are plotted every 1 second when maximum slip velocity on the fault exceeds 1 mm/s, representing slip accumulation during seismic periods, and green solid lines are plotted every 5 years, representing slip accumulation in aseismic periods. The 1st, 3rd, 5th and 9th events have global intersonic propagation. (b) Maximum slip velocity on the logarithmic scale vs. time in years. Each vertical line represents a seismic event.

### 5.3 Intersonic transition due to rheological boundaries for Case I of a homogeneous seismogenic region

We start by presenting results for Case I, which has a homogeneous velocity-weakening (seismogenic) region. It also has a smaller value of friction parameter  $a$  than other cases (Table 5.2), which promotes intersonic transition (Section 5.2). Note that this case cannot be called homogeneous overall, as the homogeneous velocity-weakening region is surrounded by velocity-strengthening regions, creating heterogeneity in fault properties and, as we will see, in fault stress. Figure 5.1(b) shows distributions of friction parameters  $a$  and  $b$  along the horizontal line  $z = 0$  km and vertical line  $x = 0$  km, respectively.

The simulated earthquake sequence for Case I contains events of two distinct types. Figure 5.4 (a) shows slip accumulation along the horizontal line  $z = 0$  km in earthquake sequences, and Figure 5.4(b) shows maximum slip velocity on the fault as a function of time. The maximum slip velocity

is on the order of  $10^{-9}$  m/s during interseismic periods, and 10 m/s during dynamic events. Seismic events occur every  $T = 56 - 59$  years, and all events nucleate from the left rheological boundary and propagate to the right. However, as shown in Figure 5.4(a), slip per event along  $z = 0$  km is larger and rupture speed is faster in some events (e.g., 1st, 3rd, 5th, 9th) than others (e.g., 2nd, 4th, 6th, 7th, 8th).

We study the propagation of dynamic rupture for representative events from each category, and find that one of them is intersonic while the other is subsonic. Figure 5.5 shows snapshots of slip velocity of the third and sixth events for Case I. A part of the fault region is shown  $[-35 \text{ km}, 35 \text{ km}] \times [-8 \text{ km}, 8 \text{ km}]$ . The seismogenic velocity-weakening region occupies the area  $[-30 \text{ km}, 30 \text{ km}] \times [-5 \text{ km}, 5 \text{ km}]$  in the middle, and the fault area shown contains parts of velocity-strengthening regions of about 5 km on each side along the horizontal direction, and 3 km along the vertical direction. Slip velocity is shown on the logarithmic scale, ranging from  $10^{-12}$  m/s to 1 m/s. The plate loading rate is  $10^{-9}$  m/s. White and bright yellow colors correspond to seismic slip velocity, orange and red correspond to aseismic slip velocity, and black corresponds to locked portions of the fault. For each event, zero time is the starting time of the event, i.e., the time when maximum slip velocity reaches  $V_{\text{seis}} = 0.1$  m/s. The first panel shows slip velocity distribution at 1.11 seconds after the beginning of the event, and the time interval between two successive snapshots is 2.22 seconds. The blue line is plotted as a reference, to indicate the shear wave speed  $c_s$ , which is 3 km/s. For both events, most of the seismogenic region is locked before the dynamic rupture. The velocity-strengthening region slips with slip velocity of the order of the plate loading rate. Rupture initiates from the lower left corner of the seismogenic region. Initial stages of rupture propagation are similar for the two events: dynamic rupture propagates faster along the vertical and horizontal rheological boundaries than along the mid-depth of the velocity-weakening region, forming a concave rupture front. Rupture is similar in the two events up to the time of 7.78 seconds. At that time, both ruptures have intersonic speeds locally, in areas close to velocity-strengthening regions. After that, the two events behave differently. In the third event, the intersonic propagation along the rheological boundaries causes the entire rupture to transition to intersonic speeds. The average rupture speed along the horizontal

line  $z = 0$  between the time of 7.78 s and 16.67 s is 4.1 km/s, which is an intersonic speed. In the sixth event, the intersonic propagation along the rheological boundaries dies out and the overall rupture speed is subsonic. It is 2.7 km/s between the time of 7.78 s and 16.67 s.

Let us compute the distribution of rupture speed over the fault in the two events. Figures 5.6 (a) and (b) show contours of rupture time  $t_r(x, z)$  for the two events respectively, where  $t_r(x, z)$  of each point is defined as the time when its slip velocity reaches  $V_{\text{seis}} = 0.1$  m/s for the first time during the dynamic event. All points with same rupture time form the rupture front at that time. In both events, rupture initially spreads both along the mode II horizontal direction and the mode III vertical direction, up to the time of 4 seconds. After that, rupture saturates the entire depth of the fault and propagates predominantly along the mode II horizontal direction, before hitting the vertical rheological boundary on the right, which occurs around the time of 16 seconds for the third event and 23 seconds for the sixth event. For both events, the predominantly mode II propagation in the  $x$  direction occurs within the horizontal range  $x \in [-L_{\text{seis}}/2 + 1.5W_{\text{seis}}, L_{\text{seis}}/2 - 0.5W_{\text{seis}}] = [-15 \text{ km}, 25 \text{ km}]$ . In that fault region, we can regard the rupture speed  $c(x, z)$  to be the speed of rupture propagation in the horizontal  $x$  direction. The calculation scheme for  $c(x, z)$  is presented in Appendix 5.7. Figures 5.6 (c) and (d) show the distribution of  $c(x, z)$  on the fault for the two events, respectively. In both events, rupture has local intersonic propagation close to rheological boundaries. In the third event, most of the region within  $x \in [-15 \text{ km}, 25 \text{ km}]$  is ruptured with intersonic speeds, while in the sixth event, most of the region within  $x \in [-15 \text{ km}, 25 \text{ km}]$  is ruptured with subsonic speeds.

To categorize events and compare with seismic observations, we need a definition of rupture speed  $c^*(x)$  that is independent of depth  $z$ , and only a function of the along-strike position  $x$ . Kanamori (2004) defined rupture speed as the speed of rupture propagation at the depth  $z$  where the largest slip occurs. We follow his definition. In our model, the largest slip always occurs approximately at the depth of  $z = 0$  km, we define  $c^*(x) = c(x, z = 0)$ . We call an event intersonic if and only if rupture speed  $c^*(x)$  is intersonic for along-strike stretches longer than  $W_{\text{seis}}$ , the width of the seismogenic region. Otherwise, we call the event subsonic. Note that a subsonic event can have

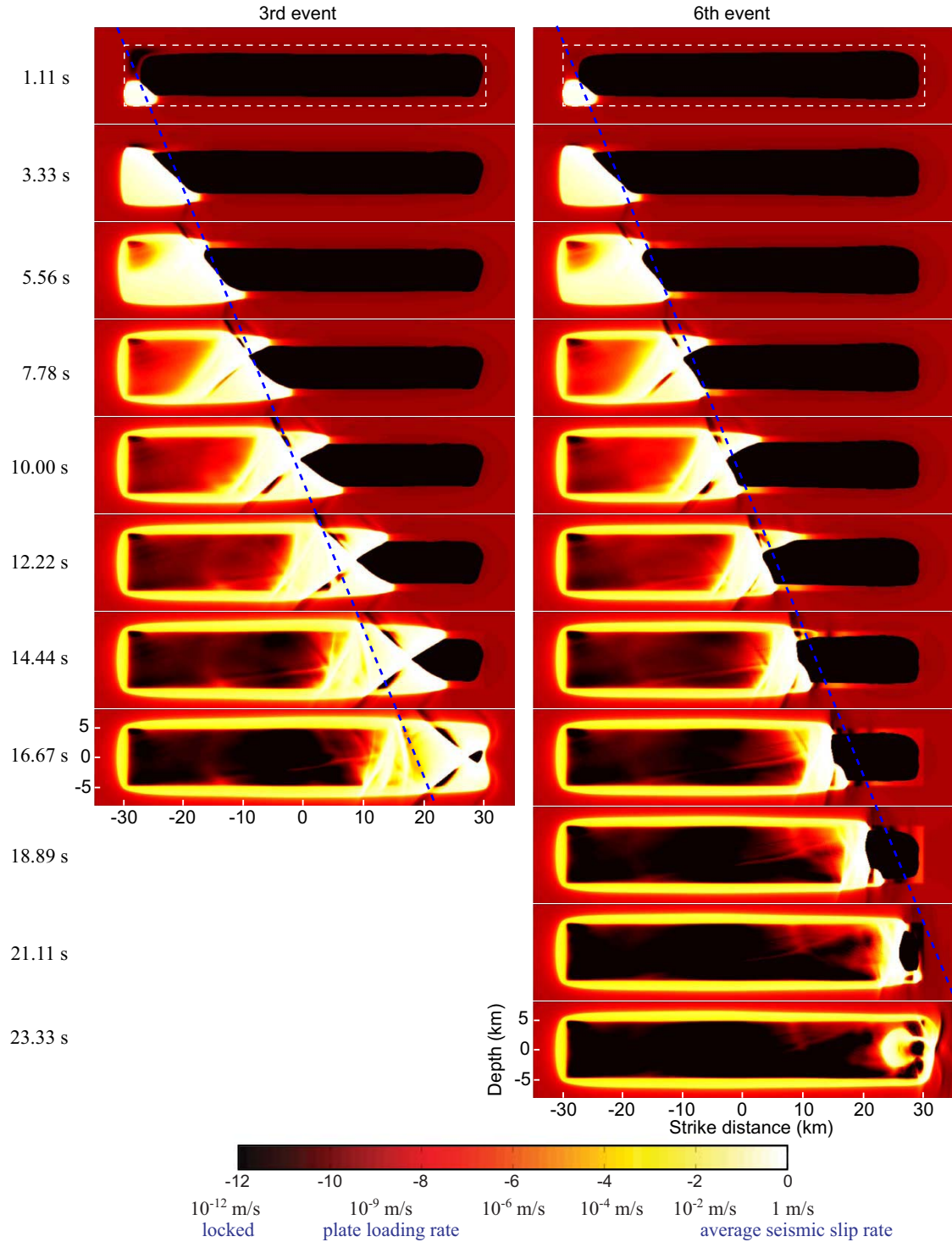


Figure 5.5: Snapshots of slip velocity in the third and sixth events for Case I. Slip velocity is shown on the logarithmic scale, ranging from  $10^{-12}$  m/s to 1 m/s. White and bright yellow correspond to seismic slip velocity, and black corresponds to locked portions of the fault. The white dashed boxes in the top panels indicate the location of the velocity-weakening region. Zero time is the starting time of each event. The time interval between two successive panels is 2.22 s. The blue dashed line is plotted to indicate the position of the rupture front (at depth  $z = 0$  km) if it propagates with the shear wave speed of 3 km/s. The two events have similar initial rupture propagation (before the time of 7.78 s), but afterwards the third event propagates appreciably faster than the sixth event.

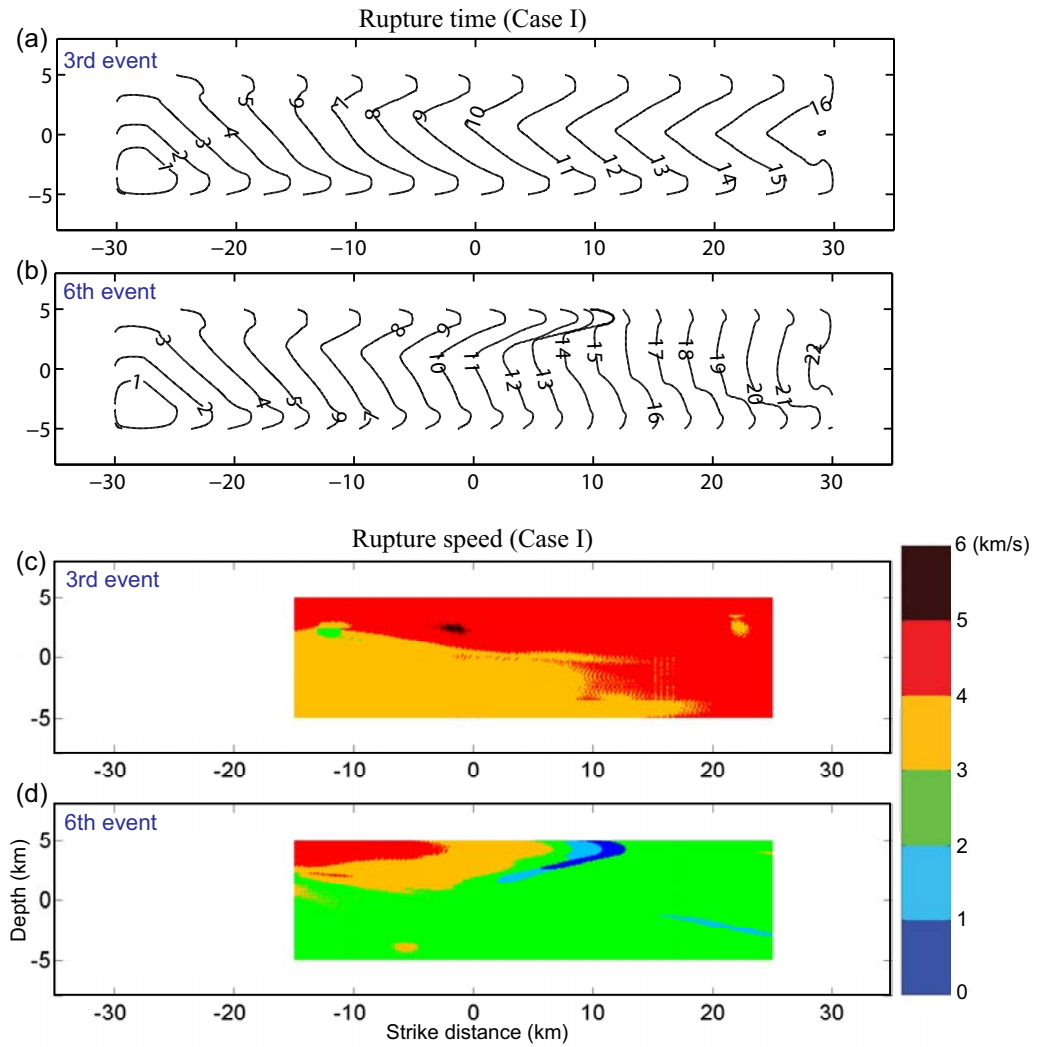


Figure 5.6: (a) and (b): Rupture time of the third and sixth events for Case I; (c) and (d): Horizontal rupture speed  $c(x, z)$  for the same events

local intersonic transients. The rupture speed  $c^*(x)$  in the third and sixth events is shown in Figure 5.7(a). In the third event, the rupture speed is intersonic throughout the along-strike distance [-15 km, 25 km], therefore the third event is an intersonic event. In the sixth event, the rupture speed is subsonic throughout the along-strike distance [-15 km, 25 km], and hence it is a subsonic event.

To compare the observed rupture speeds with seismic ratios, let us define the average seismic ratio  $\bar{S}$  for the velocity-weakening region. We define the average seismic ratio  $\bar{S}$  as the average of the seismic ratio  $S(x, z)$  over the seismogenic velocity-weakening region:

$$\bar{S} = \frac{1}{L_{\text{seis}}W_{\text{seis}}} \int_{-W_{\text{seis}}/2}^{W_{\text{seis}}/2} \int_{-L_{\text{seis}}/2}^{L_{\text{seis}}/2} S(x, z) dx dz. \quad (5.12)$$

The average shear stress before dynamic events  $\bar{\tau}_i$ , peak resistance  $\bar{\tau}_p$ , dynamic friction resistance  $\bar{\tau}_d$ , and residual stress  $\bar{\tau}_e$  are defined analogously. Table 5.3 shows the comparison of the defined values in the third and sixth events for Case I (The table also shows other cases discussed in later sections). The two events have the same  $\bar{\tau}_p$  and  $\bar{\tau}_d$ , but the third event (intersonic) has larger  $\bar{\tau}_i$  and  $\overline{\Delta\tau}$ , and hence smaller  $\bar{S}$ , than the sixth event (subsonic). Hence intersonic events have smaller values of  $\bar{S}$ , consistent with earlier studies (e.g., Andrews, 1976; Day, 1982a; Dunham, 2006).

Table 5.3: Some simulated quantities from dynamic events

Event #	$\bar{\tau}_i$ (MPa)	$\bar{\tau}_p$ (MPa)	$\bar{\tau}_d$ (MPa)	$\overline{\Delta\tau}$ (MPa)	$\bar{S}$	Rupture behavior
Case I, 3rd	31.0	37.6	24.1	7.2	1.16	intersonic
Case I, 6th	30.2	37.6	24.1	6.1	1.45	subsonic
Case II, 3rd	31.3	38.7	25.0	5.8	1.23	subsonic
Case IIh1, 3rd	31.6	38.1	25.1	6.8	1.10	intersonic
Case IIh2, 3rd	31.6	38.1	25.2	6.5	1.15	intersonic

### 5.3.1 Effects of stress concentration at rheological boundaries on inter-sonic transition

In the third event, intersonic propagation starts in areas close to the top and bottom rheological boundaries. Later, the entire rupture transitions to intersonic speeds. This transition process is quite different from most single-rupture models, where intersonic propagation first initiates at the

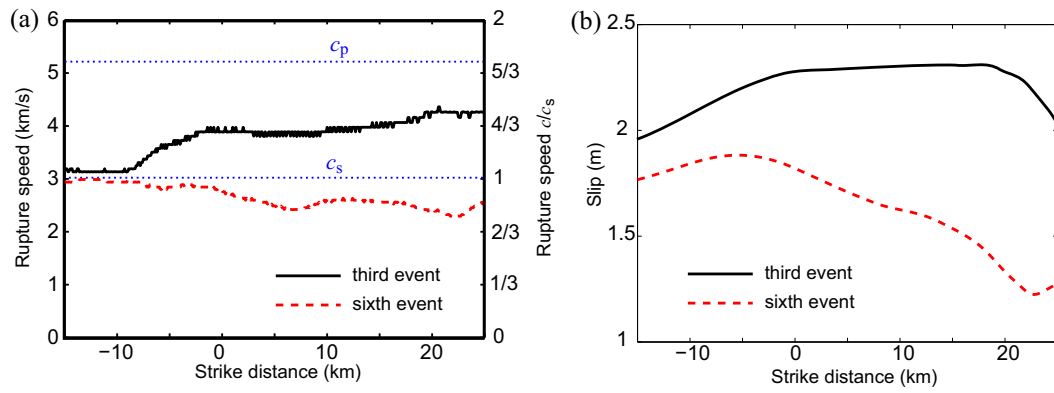


Figure 5.7: (a) Rupture speed  $c^*(x)$  as a function of strike distance  $x$  for the third and sixth events in Case I. The third event has global intersonic propagation, but the sixth event does not. (b) Average slip  $\bar{\delta}(x)$  as a function of strike distance  $x$  for the third and sixth events in Case I

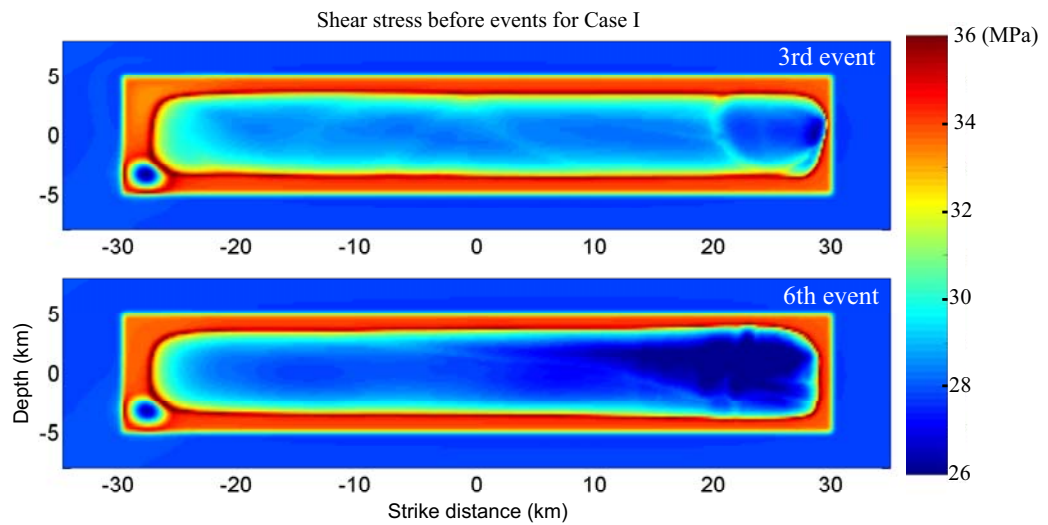


Figure 5.8: Distribution of initial shear stress  $\tau_i$  for the third (inter-sonic) and sixth (sub-sonic) events of Case I

mid-depth of the fault (e.g., Madariaga and Olsen, 2000; Fukuyama and Olsen, 2002; Dunham, 2006). The difference comes from the heterogeneous stress distribution in earthquake cycles.

After long-term history of slip on the fault in earthquake cycles, the distribution of shear stress becomes much more complicated and heterogeneous than that at the beginning of the simulation, and hence it significantly influences rupture behavior. Figure 5.8 shows distributions of shear stress on the fault before the third and sixth events in Case I. For both events, the shear stress in the velocity-strengthening region is almost uniform and approximately equal to 28 MPa ( $\approx \sigma \{f_o + (\bar{a}_{vs} - b) \ln(V_{pl}/V_o)\}$ , steady-state value for slip velocity  $V_{pl}$ ). Within the velocity-weakening seismogenic region, shear stress close to rheological boundaries is higher (33–36 MPa), than in the mid-depth of the seismogenic region (less than 30 MPa). The high initial shear stress near the rheological boundaries results from the prior aseismic slip. In interseismic periods, the velocity-strengthening regions steadily slip with slip velocities of the order of the plate rate ( $10^{-9}$  m/s), while most of the velocity-weakening region is essentially locked, with slip velocities of the order of  $10^{-50}$  m/s to  $10^{-40}$  m/s in Case I. The slip disparity between velocity-strengthening and velocity-weakening regions concentrates shear stress, creating areas of high shear stress along rheological boundaries.

To illustrate that the stress concentration along rheological boundaries is a generic feature in our model, we consider a simplified analytic model. We consider a 2D anti-plane model subjected to the following slip distribution  $\delta(z)$  along depth  $z$  on the fault:

$$\delta(z) = \begin{cases} 0, & |z| \leq W_{\text{seis}}/2 \\ \bar{\delta} = V_{pl}T, & |z| > W_{\text{seis}}/2, \end{cases} \quad (5.13)$$

where  $\delta(z) = 0$  in the region  $|z| \leq W_{\text{seis}}/2$ , which mimics the behavior of velocity-weakening region during interseismic periods, and  $\bar{\delta} = V_{pl}T$  in the outside region, which mimics the slip accumulation of velocity-strengthening region during interseismic periods. Therefore, the slip distribution of equation (5.13) mimics the interseismic slip accumulation along depth for Case I, in a simplified way.

The static stress transfer  $\tau_{\text{sf}}(z)$  resulting from this slip distribution is (e.g., Freund, 1979):

$$\tau_{\text{sf}}(z) = -\frac{\mu}{2\pi} \int_{-\infty}^{+\infty} \frac{\partial\delta/\partial\xi}{z-\xi} d\xi. \quad (5.14)$$

Substituting equation (5.13) into (5.14), we have

$$\tau_{\text{sf}}(z) = \frac{\mu}{2\pi} \frac{V_{\text{pl}}TW_{\text{seis}}}{(W_{\text{seis}}/2)^2 - z^2}. \quad (5.15)$$

$\tau_{\text{sf}}$  is positive and linearly proportional to  $\bar{\delta} = V_{\text{pl}}T$  in the region  $|z| \leq W_{\text{seis}}/2$ , indicating shear stress increases in the locked region during interseismic periods, with larger amplitude for higher slip disparity  $\bar{\delta} = V_{\text{pl}}T$ . Static stress transfer at depth  $z = 0$  is  $(2\mu/\pi)(V_{\text{pl}}T/W_{\text{seis}})$ , which is inversely proportional to the width of seismogenic region  $W_{\text{seis}}$ . Static shear transfer  $\tau_{\text{sf}}$  is much higher near the boundaries  $z = \pm W_{\text{seis}}/2$  than the center  $z = 0$ . The fault regions next to rheological boundaries have larger stress accumulation than the mid-depth region. Figure 5.9 compares this analytic model with our simulation. Blue solid lines represent the distributions of slip  $\delta(z)$  and static stress transfer  $\tau_{\text{sf}}$  of the 2D anti-plane model, and red dashed lines represent the distributions of simulated interseismic slip and stress accumulation along  $x = 0$  km for the time period between the second and third events. Overall, they are qualitatively consistent with each other. The analytical model even matches the simulation quantitatively in the mid-depth seismogenic regions. However, in the 2D analytic model (5.13 - 5.15), the slip distribution abruptly jumps from 0 to  $\bar{\delta}$  at the boundaries, leading to infinitely large  $\tau_{\text{sf}}$  there. In any realistic fault model, the high stress right at the boundary between slipping and locked regions would cause slip, extending the slipping region into the locked region. We observe such penetration of slip into the locked region in our models.

The high shear stress, and hence low seismic ratio, next to rheological boundaries before dynamic events explains local intersonic propagation there (for both the third and sixth events). Figure 5.10 shows distributions of seismic ratio  $S$  for the third and sixth event. Single-rupture simulations showed that lower seismic ratio favors intersonic transition; for example, for intersonic transition and propagation to occur on 3D homogenous faults, seismic ratio  $S$  should be smaller than a critical

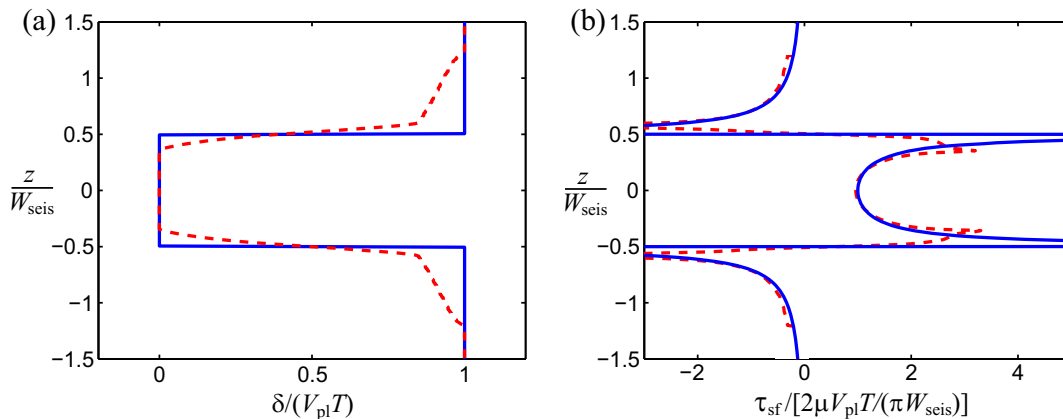


Figure 5.9: (a) Interseismic slip accumulation along central vertical line  $x = 0$  km between the second and third events of Case I (red dashed line) and slip distribution assumed in a 2D anti-plane model (blue solid line). (b) The corresponding shear stress accumulation

value  $S_{\text{crit},3\text{D}} = 1.19$  (Dunham, 2006). In Figure 5.10, regions close to rheological boundaries have low seismic ratios (red color) and favor intersonic propagation. At the same time, the mid-depth locked region has high seismic ratios (blue color) and favors subsonic propagation. That is why rupture propagates with intersonic speeds next to rheological boundaries, and subsonic speeds in mid-depth region, and forms a concave front in both events (Figure 5.5).

The third and sixth events behave differently after rupture saturates over depth, due to the different distributions of shear stress, and hence seismic ratio in the mid-depth of the velocity-weakening region. As shown in Figures 5.8 and 5.10, shear stress in most of the mid-depth region is higher, and hence the seismic ratio is lower, in the third event than in the sixth event. In the third event, the intersonic propagation along the areas next to rheological boundaries is able to prompt faster propagation of the mid-depth region and activate the global intersonic propagation on the fault. However, in the sixth event, the intersonic propagation along the rheological boundaries, is overcome by subsonic rupture propagation of the mid-depth region. The difference in shear stress before events comes from the irregularity in the event recurrence time. The interseismic periods before intersonic events (59.3 years for the third event) are slightly larger than before subsonic events (56.9 years for the sixth event), causing larger shear stress build-up, consistently with estimate (5.15). More discussion about distributions of shear stress and seismic ratio over the seismogenic

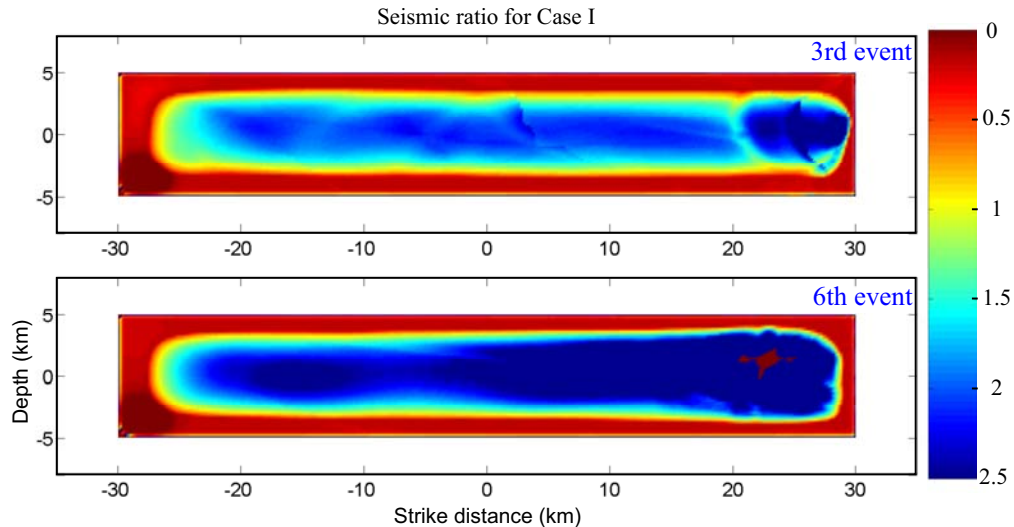


Figure 5.10: Distribution of seismic ratio  $S = (\tau_p - \tau_i)/(\tau_i - \tau_d)$  on the fault (within velocity-weakening seismogenic region) for the third and sixth event of Case I

region is in Section 5.5.2.

## 5.4 Intersonic transition due to favorable compact heterogeneity

Intersonic transition due to rheological boundaries does not occur for all parameter choices. For example, consider slip response in our fault model with  $\bar{a}_{vw} = 0.004$  and  $L = 0.016$  m (Case II). Larger values of  $\bar{a}_{vw}$  in Case II increase seismic ratio, which makes intersonic transition less likely than in Case I. A smaller  $L$  in Case II is chosen to keep the earthquake nucleation size  $h^*$  approximately same as in Case I. The distribution of friction parameters  $a$  and  $b$  are shown in Figure 5.1. Figure 5.11 shows slip accumulation along the horizontal line  $z = 0$  km for Case II. The average earthquake recurrence time is  $T = 52$  years. We find that after the first event, all subsequent events are similar and there are no intersonic events. Figure 5.12(a) shows snapshots of slip velocity on the fault for the third event of Case II. The blue dashed line is plotted to indicate the position of the rupture front (at depth  $z = 0$  km) if it propagates with the shear wave speed  $c_s$ . Local intersonic propagation occurs next to rheological boundaries, but the overall rupture speed is subsonic. More

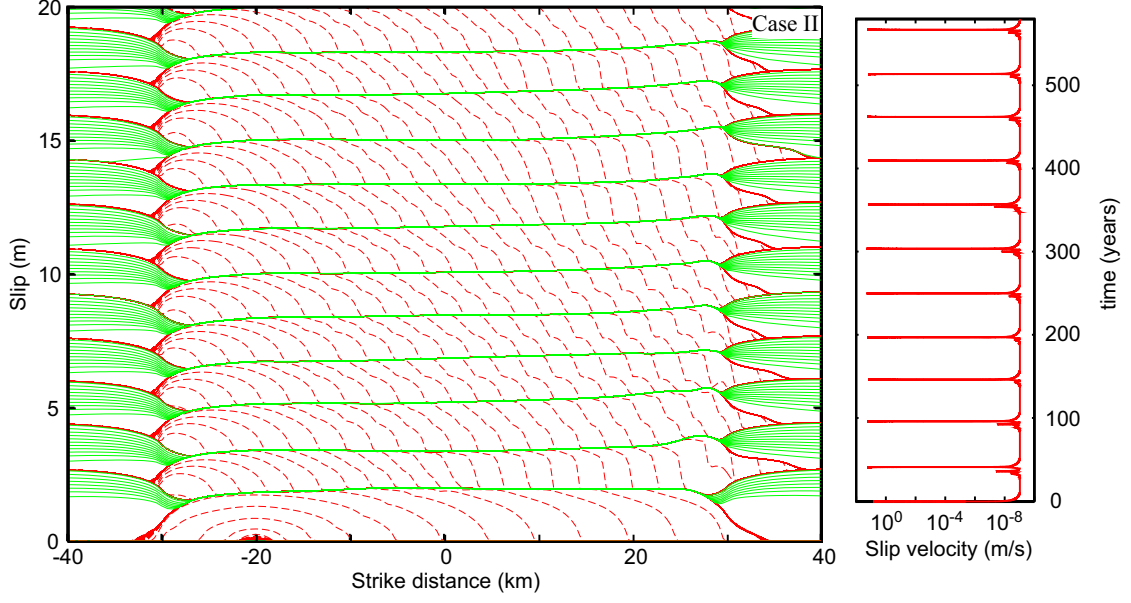


Figure 5.11: (a) Slip accumulation along the horizontal line  $z = 0$  km in Case II, with a homogeneous velocity-weakening region. All events after the first one are subsonic. (b) Maximum slip velocity on the logarithmic scale vs. time in unit of years.

discussion about Case II is in Section 5.4.1.

In the single-rupture model of Chapter 4, we find that a compact heterogeneity can completely change failure processes of the fault, perturbing subsonic crack into becoming intersonic. Guided by this idea, we consider the possibility of intersonic transition on the fault if Case II is implemented with a favorable heterogeneity in the form of a square patch of smaller  $a$  and  $b$  (Case IIh1). In Case IIh1, the patch is centered at  $x_h = -5$  km,  $z_h = 0$  km, and the distributions of friction parameters  $a$  and  $b$  are given by:

$$a(x, z) = a_{\text{II}}(x, z) + \Delta a [B(x - x_h; L_h; w_h)B(z - z_h; L_h; w_h) - 1] \quad (5.16)$$

$$b(x, z) = b_{\text{II}}(x, z) + \Delta a [B(x - x_h; L_h; w_h)B(z - z_h; L_h; w_h) - 1] \quad (5.17)$$

where  $a_{\text{II}}(x, z)$  and  $b_{\text{II}}(x, z)$  are distribution of  $a, b$  from Case II,  $\Delta a = 0.003$ ,  $L_h = 9$  km, and  $w_h = 1$  km. Outside the patch with  $|x - x_h| > (L_h + w_h)/2 = 5$  km or  $|z - z_h| > (L_h + w_h)/2 = 5$  km, we get  $a(x, z) = a_{\text{II}}(x, z)$ , and  $b(x, z) = b_{\text{II}}(x, z)$ , which are the same as in Case II. Inside the patch given by  $|x - x_h| < (L_h - w_h)/2 = 4$  km and  $|z - z_h| < (L_h - w_h)/2 = 4$  km, we get

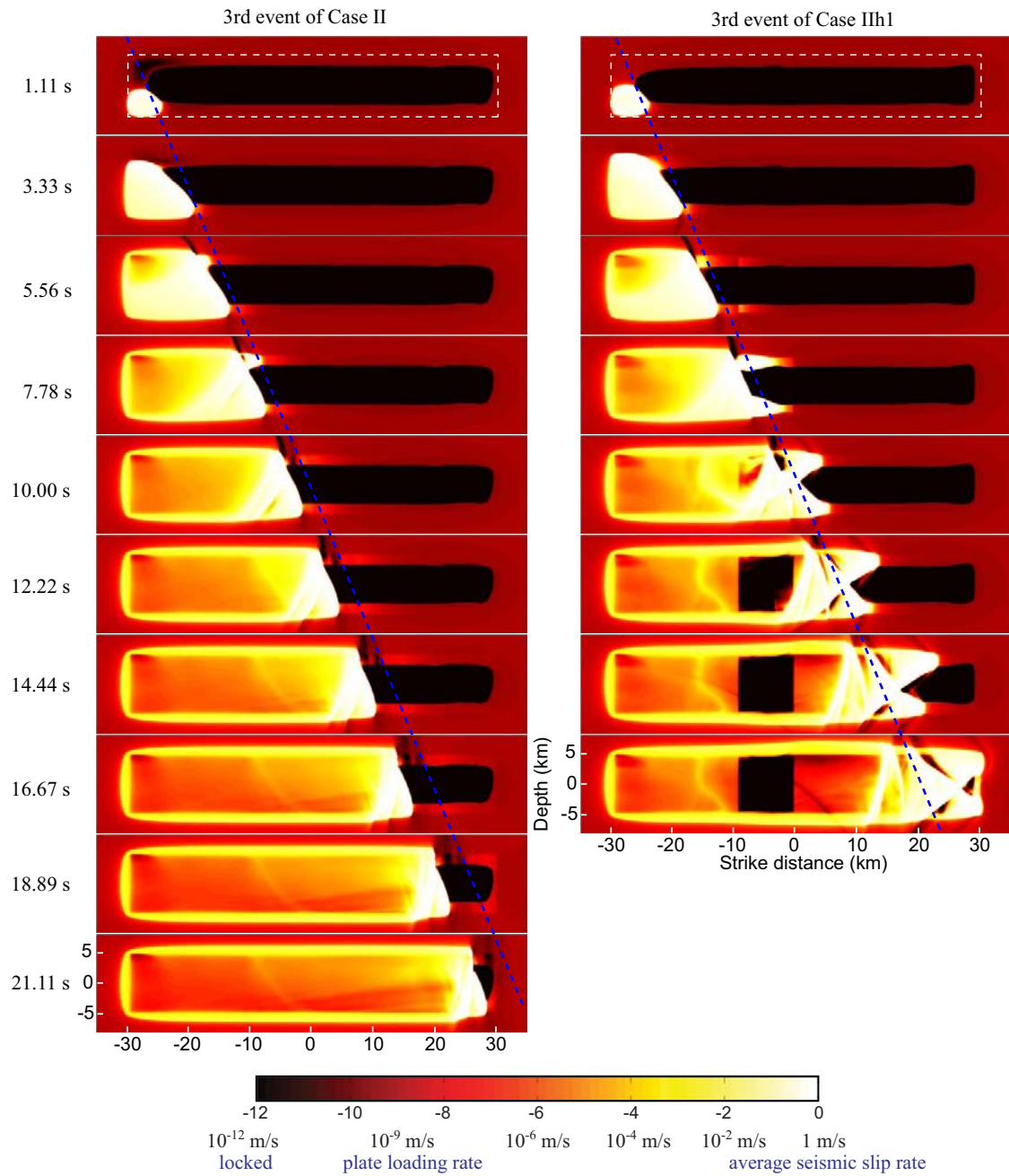


Figure 5.12: Snapshots of slip velocity on the fault for the third event of Cases II and IIIh1. The blue line is plotted to indicate the shear wave speed  $c_s$  of 3 km/s. A weaker patch of lower peak resistance in Case IIIh1 makes the entire rupture transition to intersonic speeds.

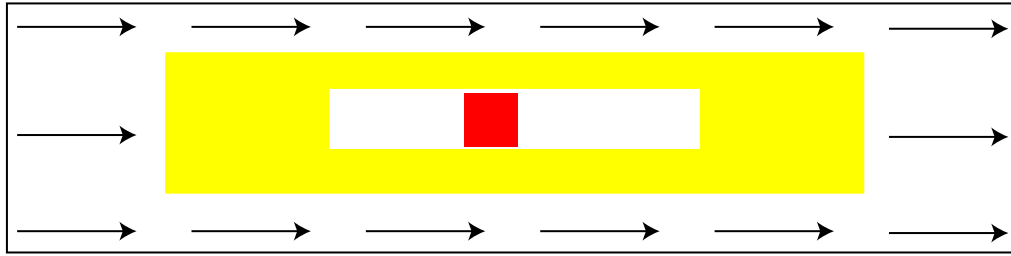
$a(x, z) = a_{\text{II}}(x, z) - \Delta a$ , and  $b(x, z) = b_{\text{II}}(x, z) - \Delta a$ , with both  $a(x, z)$  and  $b(x, z)$  smaller by  $\Delta a$  than in Case II. Friction parameters smoothly vary in between the two regions. The patch centered at  $(x_h, z_h)$  is approximately square with length  $L_h = 9$  km. The patch has smaller friction parameter  $a$ , and hence potentially smaller peak resistance during dynamic rupture (equation (5.9)). The fault model and distribution of friction parameters  $a$  and  $b$  are shown in Figure 5.13(b).

#### 5.4.1 Weaker patch as favorable heterogeneity for intersonic transition

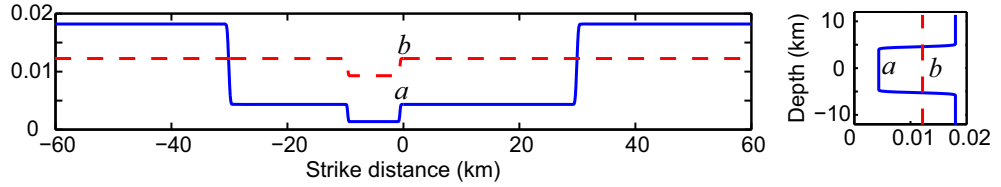
By introducing a weaker patch of lower peak resistance, Case IIIh1 produces occasional and repeated global intersonic transition and propagation in earthquake sequences. As shown in Figure 5.14, global intersonic propagation occurs in the first, third, sixth, and ninth events out of eleven events. (For Case IIIh1 and IIIh2 with a weaker patch, we call an event having global intersonic propagation only if rupture speed  $c^*(x)$  is intersonic for longer than  $W_{\text{seis}}$  in the region outside the patch.)

We pick the third event for Cases II and IIIh1 to illustrate the effect of a weaker patch in detail. Figure 5.12 shows the snapshots of slip velocity on the fault for these two events. In Case II, rupture next to the upper rheological boundary has some local intersonic propagation, which transitions back to subsonic speeds at the location  $x = -6$  km. The average rupture speed at depth  $z = 0$  km between the times of 3.3 s and 21.11 s is 2.7 km/s. In Case IIIh1, the rupture front at depth  $z = 0$  km initially propagates with subsonic speeds, and the upper rheological boundary has some local intersonic propagation. Around the time of 7.78 s, secondary ruptures initiate at the weaker patch near top and bottom rheological boundaries. The ruptures propagate with intersonic speeds in front of the main rupture, and induce transition of the overall rupture to intersonic speeds. Between the times of 3.33 s and 16.67 s, the average rupture speed along  $z = 0$  km is 3.6 km/s, which is intersonic. Figure 5.16 shows the distributions of rupture time and rupture speed in the seismogenic region for the two events. In Case IIIh1, secondary cracks initiate in the weaker patch before the arrival of main rupture, leading to a rupture front jump. The regions between the front of main rupture and secondary cracks are left white in Figure 5.16(e). The third event in both cases nucleates from the lower left corner of the velocity-weakening region. Case II does not have global intersonic

(a): Fault model for Case IIIh1



(b): Friction parameters for Case IIIh1



(c): Friction parameters for Case IIIh2

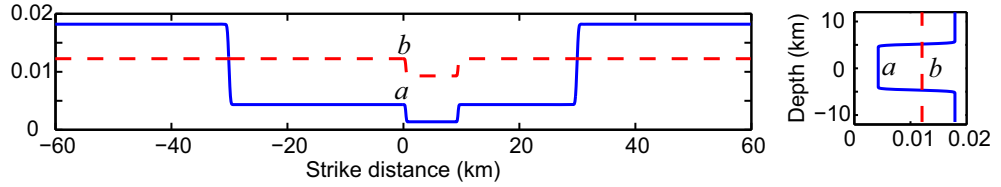


Figure 5.13: (a) Fault model of Case IIIh1: a buried strike-slip fault model with a weaker patch (red) centered at  $(-5 \text{ km}, 0 \text{ km})$ . Figure (b) and (c) show the distributions of friction parameters  $a$  and  $b$  along horizontal line  $z = 0 \text{ km}$  and vertical line  $x = 0 \text{ km}$  in Cases IIIh1 and IIIh2, respectively. In Case IIIh2, the heterogeneity is of the same size as in Case IIIh1 but centered at  $(5 \text{ km}, 0 \text{ km})$ .

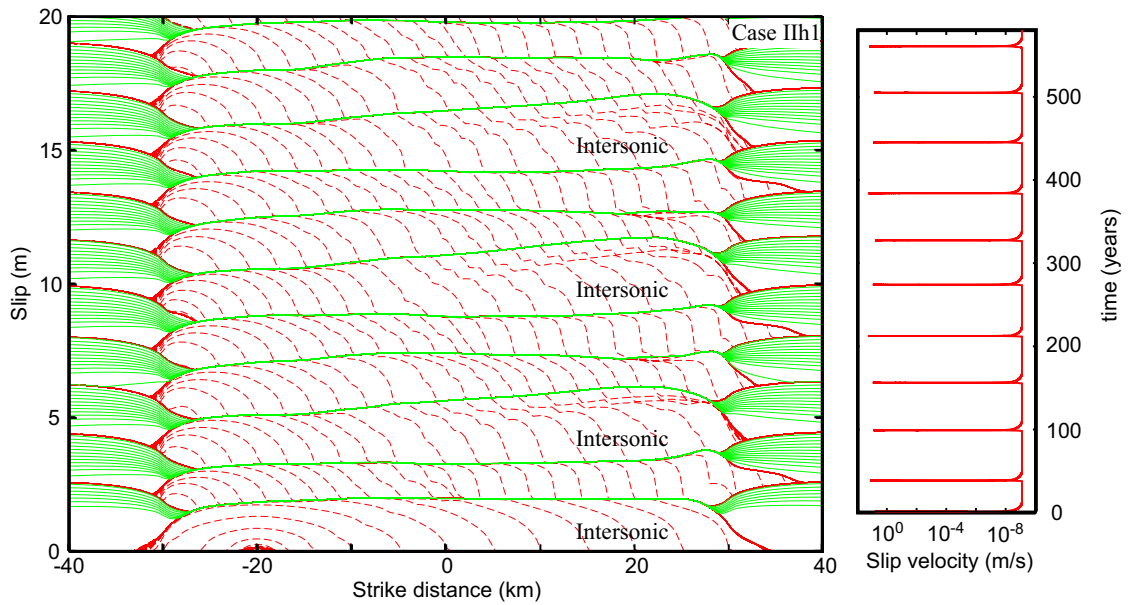


Figure 5.14: (a) Slip accumulation along the horizontal line  $z = 0 \text{ km}$  in Case IIIh1. (b) Maximum slip velocity in logarithmic scale vs. time in unit of years

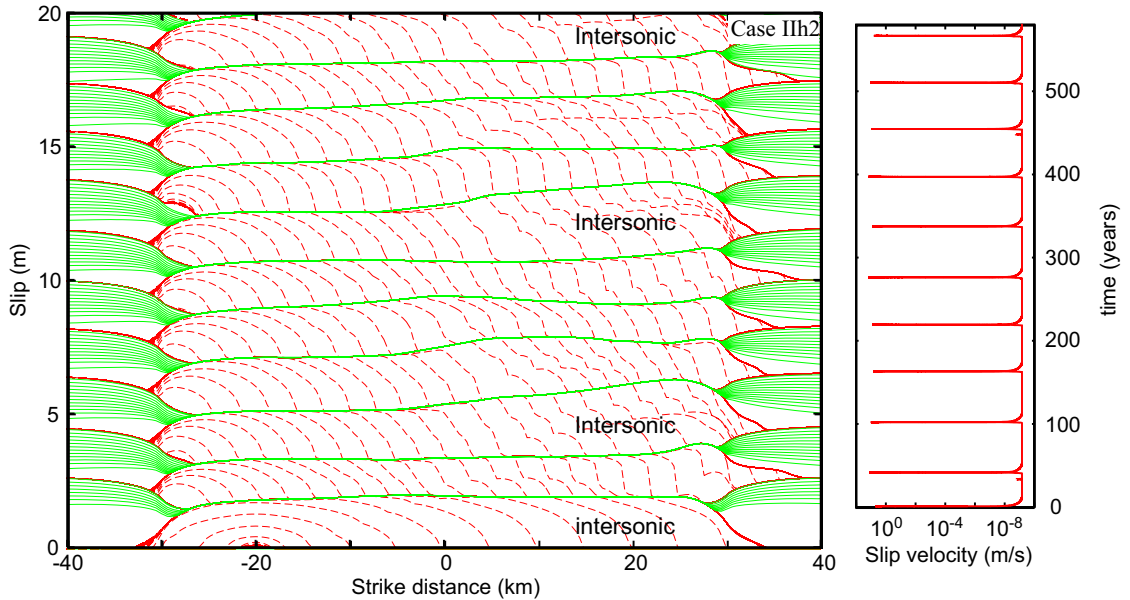


Figure 5.15: (a) Slip accumulation along the horizontal line  $z = 0$  km in Case IIIb. (b) Maximum slip velocity in logarithmic scale vs. time in unit of years

propagation. In Case IIh1, rupture mainly propagates with subsonic speeds before the weaker patch (green color in Figure 5.16(e)); intersonic transition occurs in the patch, and intersonic propagation is maintained after exiting the patch (with yellow and red colors). If we measure the horizontal distance between the center of earthquake nucleation (at the location of  $x = -27$  km) and the center of the patch ( $x = -5$  km), and define it as transition distance  $L_{\text{tran}}$ , then  $L_{\text{tran}} = 22$  km in Case IIh1. We compare this value with theoretical estimates for homogeneous faults in Section 5.5.4. Figure 5.17 shows the distribution of seismic ratio  $S$  over the seismogenic region before the third events for Case II and Case IIh1. The patch in Case IIh1 has smaller value of the friction parameter  $\bar{a}_{\text{vw}}$ , and hence smaller seismic ratio  $S = (\tau_p - \tau_i)/(\tau_i - \tau_d)$  than the surrounding areas. Due to concentrated shear stress  $\tau_i$  near the rheological boundaries, seismic ratio  $S$  is further reduced in parts of the patch next to the rheological boundaries. That is why, secondary intersonic cracks nucleate there before the arrival of the main rupture.

Hence we find that a weaker patch significantly changes rupture behavior and long-term fault slip in Case IIh1, resulting in occasional intersonic events in the fault model that has no intersonic events without the patch.

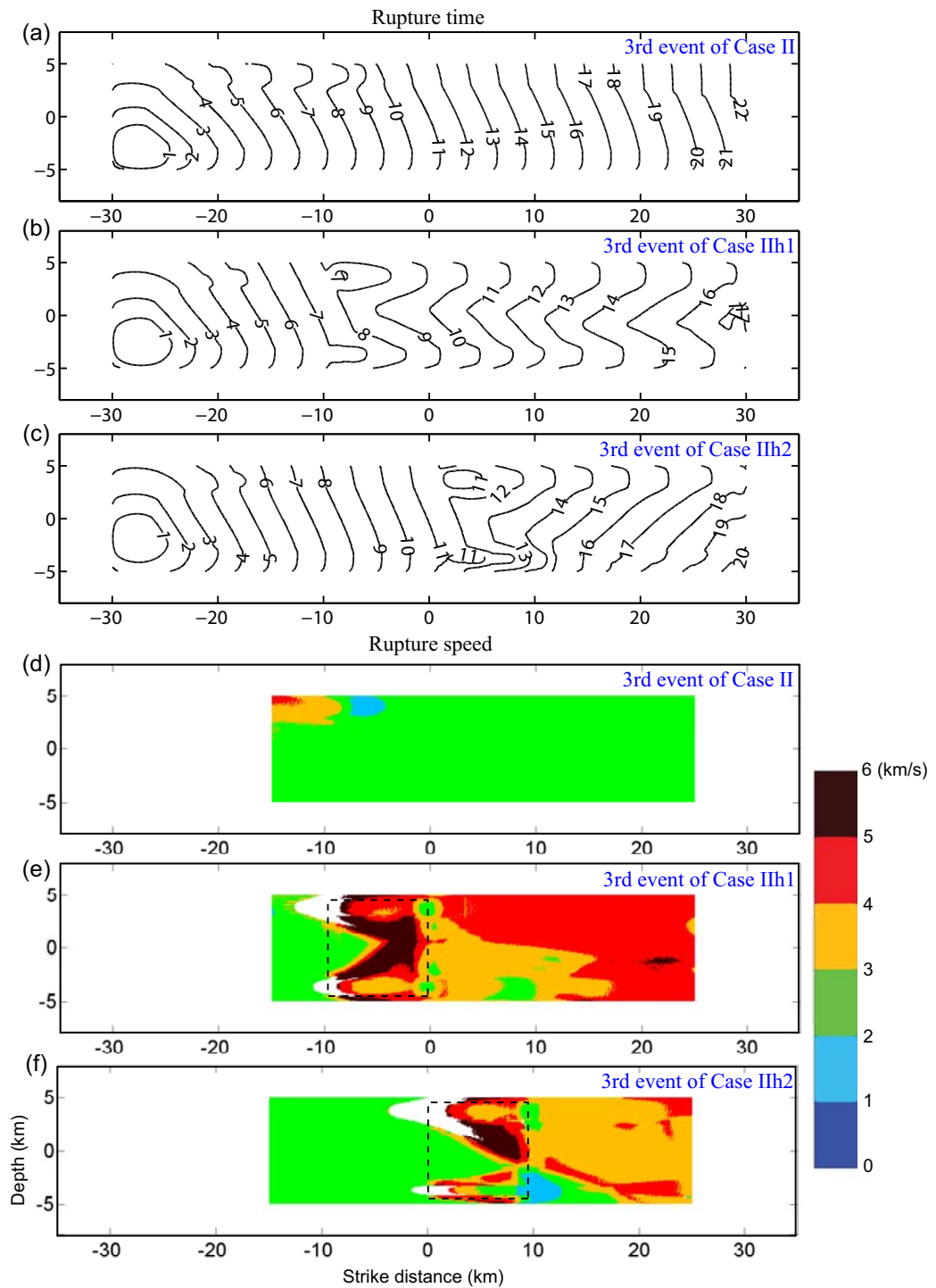


Figure 5.16: Figure (a), (b), and (c): rupture time of the third event for Case II, IIIh1, and IIIh2, respectively; Figure (c), (d), and (e): horizontal rupture speed  $c(x, z)$  on the fault of the third event for Case II, IIIh1, and IIIh2, respectively. The black dashed boxes in Figures (e) and (f) indicate the locations of the weaker patch. Global intersonic transition occurs in Case IIIh1 and IIIh2, and the transition occurs approximately at the location of the weaker patch.

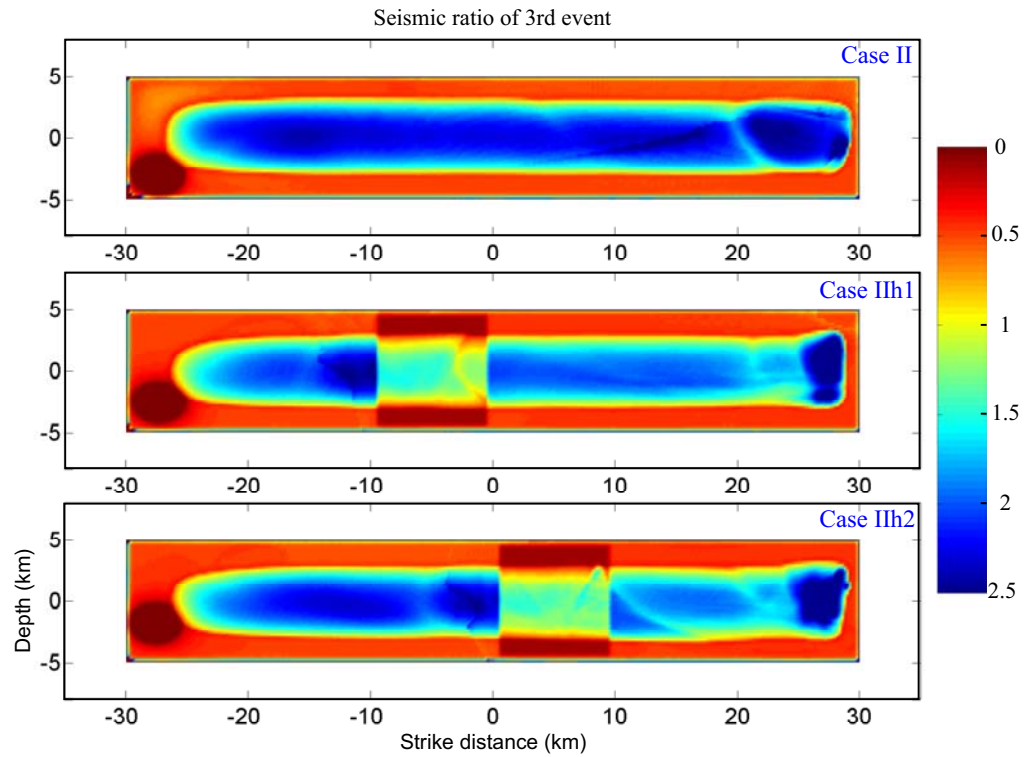


Figure 5.17: Distribution of seismic ratio  $S = (\tau_p - \tau_i)/(\tau_i - \tau_d)$  on the fault (within velocity-weakening seismogenic region) of the third event for Cases II, IIh1, and IIh2, respectively. Due to low seismic ratio in the patch in Case IIh1 and IIh2, secondary cracks are initiated there in front of the main rupture, and driven to intersonic speeds by the intersonic loading stress field in front of the shear wave front of the main rupture.

### 5.4.2 Initiation of secondary cracks in the weaker patch by an intersonic loading field

In Section 4.3, we demonstrate that a secondary rupture can be initiated ahead of the main rupture and driven to intersonic speeds by the intersonic loading field of the main rupture. That result is the generalization of the finding by [Burridge \(1973\)](#) and [Andrews \(1976\)](#) that a secondary rupture can nucleate at the peak of the shear stress traveling ahead of the main rupture in cases of sustained in-plane sliding. The results of Chapter 4 show that the secondary rupture does not have to be initiated by the peak, and it can be initiated by the elevated stress ahead of the peak if fault heterogeneity is present.

Here we show that sustained secondary cracks in the third event of Case IIIh1, which eventually lead to intersonic transition of the entire rupture, are indeed initiated not at the shear stress peak but rather ahead of the peak, due to the presence of the weaker patch, consistently with our findings in Chapter 4. Figure 5.18 shows snapshots of shear stress (panels a–c) and slip velocity (panels d–e) along the horizontal line  $z = 4$  km (near the top rheological boundary) for the third event of Case IIIh1. The time interval between panels is 1 s. In Figure 5.18(a), we find a typical picture for in-plane sliding, with a sharp shear stress increase (at about  $x = -15.3$  km) corresponding to the main rupture front and a shear stress peak ahead of the rupture front, at about  $x = -14.0$  km. The stress peak is the result of pile-up of shear waves, and it travels with the shear wave speed. The rupture front is subsonic at this time. Note that the rupture front along the  $z = 4$  km line has intersonic speeds before the time of 6.1 s shown in Figure 5.16(a), but that instance of intersonic propagation is short-lived. The shear stress field ahead of the stress peak,  $-14.1$  km  $< x < 0$  km, is an intersonic loading field (Section 4.6.1). One second later (Figure 5.18(b)), the main rupture front advances to  $x = -12.4$  km, and the shear stress peak advances to  $x = -11.0$  km. Yet, in Figure 5.18(e), we see nonzero slip velocity farther ahead, for  $-10$  km  $< x < -7$  km. Hence this secondary rupture has initiated due to the shear stress increase ahead of the shear stress peak, at the edge of the weaker patch. Figures 5.18(c) and (f) show the subsequent propagation of the rupture. The slip velocity of the secondary rupture continues to grow, and the stress peak of the main rupture front

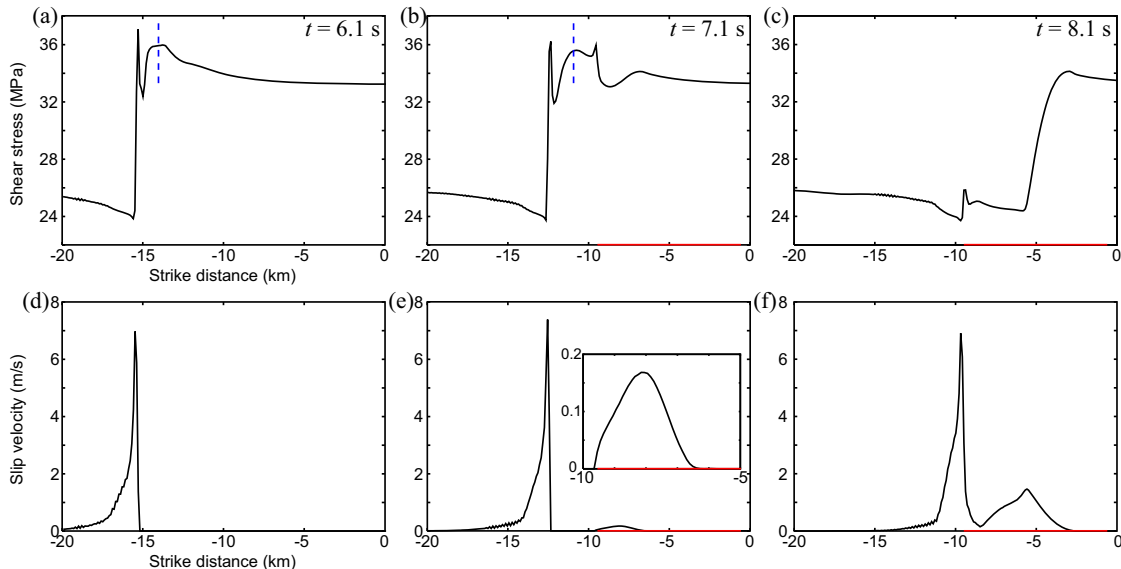


Figure 5.18: Initiation of an intersonic secondary rupture in the third event of Case IIh1. (a)–(c): Snapshots of shear stress distribution along the strike distance at  $z = 4$  km depth, next to a rheological boundary, at the times  $t = 6.1$  s,  $7.1$  s, and  $8.1$  s, respectively. (d)–(f): Corresponding snapshots of slip velocity. Red solid lines represent the location of the weaker patch. Blue dashed lines represent the horizontal locations of shear stress peak. The secondary rupture initiates in the weaker patch ahead of the shear stress peak, consistent with our findings in Chapter 4.

decreases. At the time of  $8.1$  s, the secondary crack front arrives at  $x = -2.8$  km, and the average rupture speed between the time of  $7.1$  s and  $8.1$  s is  $4.4$  km/s. The secondary crack initiated in the weaker patch propagates with intersonic speeds driven by the intersonic loading field of the main rupture.

### 5.4.3 Influence of the location of the weaker patch

In Case IIh1, intersonic transition occurs at the weaker patch. To investigate the influence of the patch location on intersonic transition, we consider a case with the patch centered at  $x_h = 5$  km,  $z_h = 0$  km (Case IIh2). The other model parameters in Case IIh2 are the same as in Case IIh1. The distributions of friction parameters  $a$  and  $b$  for Case IIh2 are shown in Figure 5.13(c).

Despite the different location of the patch, Case IIh2 results in similar fault behaviors, with some earthquakes transitioning to intersonic speeds, due to the weaker patch. We again select the third event in Case IIh2 for comparison with Cases II and IIh1. Figures 5.16(c) and (f) show distributions

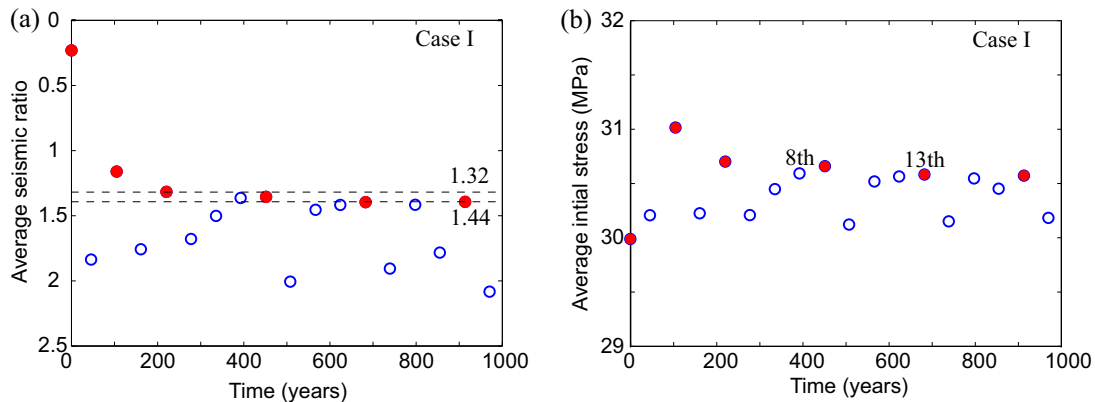


Figure 5.19: (a) Average shear stress  $\bar{\tau}_i$  before each event in Case I. (b) Effective seismic ratio  $\bar{S}$  for each event in Case I. Red solid dots represent intersonic events and blue empty circles represent subsonic events.

of rupture time and rupture speed, respectively, and Figure 5.17(c) shows the distribution of seismic ratio. Comparing Cases IIh1 and IIh2, we find that their intersonic transition processes are qualitatively similar. In both cases, the rupture is mainly subsonic before the patch. Inter-sonic transition occurs in the patch, and rupture maintains intersonic speeds after exiting the patch. Table 5.3 lists several rupture parameters of the third event for Cases II, IIh1, and IIh2. All parameters, e.g.,  $\bar{\tau}_i$ ,  $\bar{\tau}_p$ ,  $\bar{\tau}_d$ ,  $\overline{\Delta\tau}$ , and  $\bar{S}$ , are similar for Cases IIh1 and IIh2. The weaker patch dominates intersonic transition in Cases IIh1 and IIh2, and the transition distance  $L_{\text{tran}}$  depends on the location of the heterogeneity.

## 5.5 Discussion

### 5.5.1 Influence of seismic ratio $\bar{S}$ on rupture behavior

From the four simulated cases, we observe that there exists a simple correspondence between the average seismic ratio  $\bar{S}$  and intersonic/subsonic rupture propagation during dynamic events. Figure 5.19 shows the average seismic ratio  $\bar{S}$  and average shear stress  $\bar{\tau}_i$  before each event for Case I, and Figure 5.20 shows  $\bar{S}$  and  $\bar{\tau}_i$  for Cases II, IIh1, and IIh2. We select Case I for discussion, but the arguments are qualitatively applicable to Cases II, IIh1, and IIh2. In Figure 5.19, red solid dots

represent intersonic events and blue empty circles represent subsonic events. There are two critical values  $S_{c,\min} = 1.32$  and  $S_{c,\max} = 1.42$ . Events with  $\bar{S} < S_{c,\min}$  have global intersonic propagation; events with  $\bar{S} > S_{c,\max}$  do not have global intersonic propagation; events with average seismic ratio in a narrow range  $S_{c,\min} < \bar{S} < S_{c,\max}$  may be intersonic or subsonic, depending on other fault conditions, e.g., the distribution of seismic ratio. However, there is no such correspondence between shear stress  $\bar{\tau}_i$  before events and rupture behavior: most intersonic events have higher  $\bar{\tau}_i$ , but there are some exceptions. The first event has global intersonic propagation, but its  $\bar{\tau}_i = 30.00$  MPa is the lowest among all events shown in Figure 5.19.

The correspondence between  $\bar{S}$  and rupture behavior in our model is qualitatively consistent with previous studies using single-rupture models (e.g., Andrews, 1976; Dunham, 2006). In a 2D in-plane model of an unbounded fault with uniform initial shear stress, Andrews (1976) found that intersonic transition can occur on faults with seismic ratio  $S < S_{\text{crit},2\text{D}} = 1.77$  after rupture propagates long enough distance, and no intersonic transition can occur for  $S < S_{\text{crit},2\text{D}}$ . Dunham (2006) found that the critical seismic ratio in 3D is  $S_{\text{crit},3\text{D}} = 1.19$ . However, there are differences between our model and the models of Andrews (1976) and Dunham (2006). In the models of Andrews (1976) and Dunham (2006), the fault has uniform peak resistance, dynamic frictional resistance, and seismic ratios  $S$ , all of which are known before simulations. In our model, the seismic ratio  $S$  is unknown before the simulation, as it depends on  $\tau_p$ ,  $\tau_d$ , and  $\tau_i$  obtained from the simulation. Moreover,  $S$  is nonuniform on the fault. Average seismic ratio  $\bar{S}$  describes fault conditions only in an average sense. And the critical seismic ratio for intersonic transition is higher in our model than in the 3D model of Dunham (2006). For certain values of seismic ratio, e.g.,  $1.19 < \bar{S} < 1.32$ , intersonic transition would occur in our model, but not in the 3D homogeneous fault model of Dunham (2006). This shows that rheological boundaries indeed act as favorable heterogeneity, enhancing intersonic transition with respect to the homogeneous model.

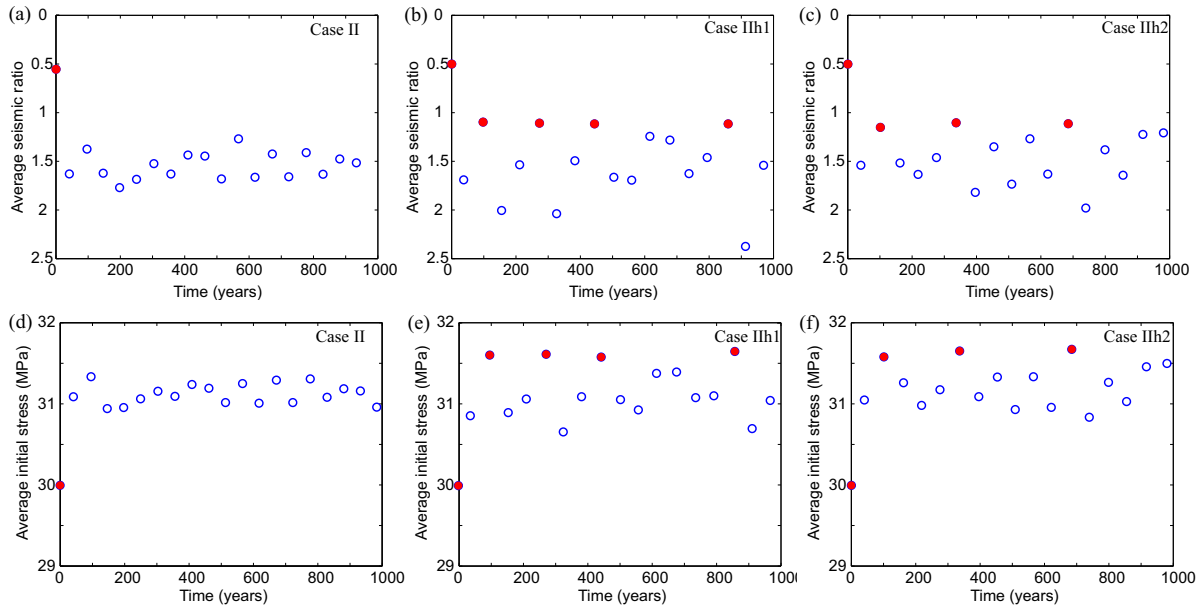


Figure 5.20: Effective seismic ratio  $\bar{S}$  and average initial shear stress  $\bar{\tau}_i$  before each dynamic event for Cases II, IIh1, and IIh2. Red solid dots represent intersonic events and blue empty circles represent subsonic events.

### 5.5.2 Distribution of seismic ratio over seismogenic region

The distribution of seismic ratio  $S$  before dynamic events is heterogeneous and separates the velocity-weakening region into two areas: the area next to rheological boundaries that creeps during interseismic periods and has lower seismic ratio, and the mid-depth area that is locked during interseismic periods and has higher seismic ratio (Figures 5.10 and 5.17). In this section, we estimate the different seismic ratios in the two regions.

The low-seismic-ratio area next to rheological boundaries creeps steadily with slip velocity of the order of plate rate  $V_{pl}$  before dynamic events, therefore the state variable is  $\theta \approx L/V_{pl}$ , and the shear stress before a dynamic event can be estimated as:

$$\tau_i = \sigma \left\{ f_o + (a - b) \ln \frac{V_{pl}}{V_o} \right\}. \quad (5.18)$$

Following the same arguments as for the formulae (5.9– 5.10), we estimate the peak resistance  $\tau_p$

and dynamic friction resistance  $\tau_d$  as:

$$\tau_p = \sigma \left\{ f_o + a \ln \frac{V_{\text{dyn}}}{V_o} - b \ln \frac{V_{\text{pl}}}{V_o} \right\}, \quad (5.19)$$

$$\tau_d = \sigma \left\{ f_o + (a - b) \ln \frac{V_{\text{dyn}}}{V_o} \right\}. \quad (5.20)$$

Then the estimate of seismic ratio  $S_{\text{slip}}$  in the slow slipping region near rheological boundaries is

$$S_{\text{slip}} = \frac{\tau_p - \tau_i}{\tau_i - \tau_d} = \frac{a}{b - a}. \quad (5.21)$$

$S_{\text{slip}} = 0.2$  in Case I and  $S_{\text{slip}} = 0.5$  in Cases II, III1, and III2, which match the simulated results quite well (Figure 5.10 and 5.17). Equation (5.21) suggests that seismic ratio in the area next to rheological boundaries is determined by friction parameters  $a$  and  $b$ , and smaller  $a/b$  promotes faster rupture propagation there.

In the mid-depth area which is locked, the peak resistance  $\tau_p$  and the dynamic frictional resistance  $\tau_d$  are approximately described by equations (5.9) and (5.10), respectively. During interseismic periods, the shear stress accumulation in the mid-depth locked region is governed by formula (5.15). The stress shear  $\tau_i$  before a dynamic event can be estimated as

$$\tau_i = \tau_d + \tau_{\text{sf}}(z) = \sigma \left\{ f_o + (a - b) \ln \frac{V_{\text{dyn}}}{V_o} \right\} + \frac{\mu}{2\pi} \frac{V_{\text{pl}} T W_{\text{seis}}}{(W_{\text{seis}}/2)^2 - z^2}, \quad (5.22)$$

which is a function of depth  $z$ . By equating the above equation with equation (5.8), we can get the background slip velocity  $V_{\text{bg,lock}}(z)$  of the locked region before a dynamic event:

$$V_{\text{bg,lock}}(z) = V_{\text{dyn}} \left( \frac{L}{V_{\text{dyn}} T} \right)^{b/a} \exp \left\{ \frac{\mu}{2\pi \sigma a} \frac{V_{\text{pl}} T W_{\text{seis}}}{(W_{\text{seis}}/2)^2 - z^2} \right\}. \quad (5.23)$$

$V_{\text{bg,lock}}(z)$  decreases as  $|z|$  decreases and reaches its minimum value at depth  $z = 0$ :

$$V_{\text{bg,lock}}(z = 0) = V_{\text{dyn}} \left( \frac{L}{V_{\text{dyn}} T} \right)^{b/a} \exp \left\{ \frac{2\mu V_{\text{pl}} T}{\pi \sigma a W_{\text{seis}}} \right\}. \quad (5.24)$$

The seismic ratio  $S_{\text{lock}}(z)$  at mid-depth locked region is:

$$S_{\text{lock}}(z) = \frac{\tau_p - \tau_i}{\tau_i - \tau_d} = \frac{2\pi\sigma b \left( (W_{\text{seis}}/2)^2 - z^2 \right)}{\mu W_{\text{seis}} V_{\text{pl}} T} \ln \frac{V_{\text{dyn}} T}{L} - 1. \quad (5.25)$$

$S_{\text{lock}}(z)$  increases as  $|z|$  decreases and reaches its maximum value at depth  $z = 0$ :

$$S_{\text{lock}}(z = 0) = \frac{\tau_p - \tau_i}{\tau_i - \tau_d} = \frac{\pi\sigma b W_{\text{seis}}}{2\mu V_{\text{pl}} T} \ln \frac{V_{\text{dyn}} T}{L} - 1. \quad (5.26)$$

These estimates of  $S_{\text{lock}}(z = 0)$  match the simulated values (Figure 5.10 and 5.17) within a factor of 1.5. An interesting observation from equation (5.26) is that smaller seismogenic width  $W_{\text{seis}}$  may actually decrease the seismic ratio at the mid-depth region, promoting faster ruptures. This effect directly comes from the static stress transfer term (5.15) at the mid-depth, which is larger for narrower seismogenic faults.

The above analysis suggests that the seismic ratio is almost uniform in the slipping region next to rheological boundaries, and increases as  $|z|$  decreases in the mid-depth region. This kind of distribution is qualitatively consistent with the simulated results.

### 5.5.3 Significance of rheological boundaries for rupture dynamics

Presence of rheological boundaries on natural faults have been inferred from a number of laboratory experiments and fault observations, as discussed in the beginning of Chapter 5. An important consequence of their presence is shear stress concentration that occurs on rheological boundary between the aseismically creeping region and the locked region, due to accumulated disparity of aseismic slip. From 2D modeling of earthquake cycles, [Lapusta et al. \(2000\)](#) found that earthquakes nucleate and small earthquakes cluster at the rheological boundaries due to this stress concentration, which is consistent with observations of fault seismicity (e.g., [Ellsworth et al., 2000](#); [Schaff et al., 2002](#)).

This study shows that stress concentration at rheological boundaries strongly influences dynamic rupture propagation. Once earthquake rupture nucleates, it propagates faster over the fault areas

next to rheological boundaries than over the rest of the seismogenic region, making the rupture transition to intersonic speeds in some cases, e.g., the third event of Case I. In some other cases, e.g., the sixth event of Case I, the high shear stress next to rheological boundaries only promotes local intersonic propagation there.

The effect of rheological boundaries observed in this study illustrates the necessity of conducting 3D modeling of long-term fault slip, as some conclusions drawn from single-rupture models may be inadequate. In many single-rupture models, the aseismic region (the velocity-strengthening region considered in this work) is simplified as an unbreakable region that can absorb infinitely large stress without failure. In these models, the finite width of the seismogenic region has the effect of depressing intersonic transition and propagation (e.g., [Day, 1982a](#); [Fukuyama and Olsen, 2002](#); [Madariaga and Olsen, 2000](#); [Dunham, 2006](#)). [Dunham \(2006\)](#) found that when the width of the seismogenic region is smaller than a critical value, the arrest waves sent out by the rheological boundaries will inhibit intersonic propagation of the fault. Many intersonic events in our model would have been subsonic events in Dunham's model. For example, with  $\bar{S} = 1.16$  and  $W_{\text{seis}} = 10$  km in the third (intersonic) event of Case I, Dunham's model would predict a subsonic rupture, as the seismogenic width  $W_{\text{seis}} = 10$  km is much narrower than the critical value given in his study. These single-rupture models do not account for the fact that the aseismic regions on natural faults are not completely unbreakable, or that, due to complicated prior slip history, stress distribution before events is not uniform, but higher at the rheological boundaries, where earthquakes tend to nucleate and propagate faster.

Note that the presence of rheological boundaries results in heterogeneous stress drop over the seismogenic region. [Figure 5.21](#) shows distribution of the stress drop  $\Delta\tau = \tau_i - \tau_e$  for the third and sixth events of Case I. As expected, in both events, areas next to the rheological boundaries have the largest positive stress drop, due to high shear stress before events. Stress drop in the velocity-strengthening region is negative, as it absorbs energy emitted by dynamic waves during seismic events, releasing it later during postseismic periods. Interestingly, higher stress drop near the rheological boundaries does not correspond to higher slip there than on the rest of the fault

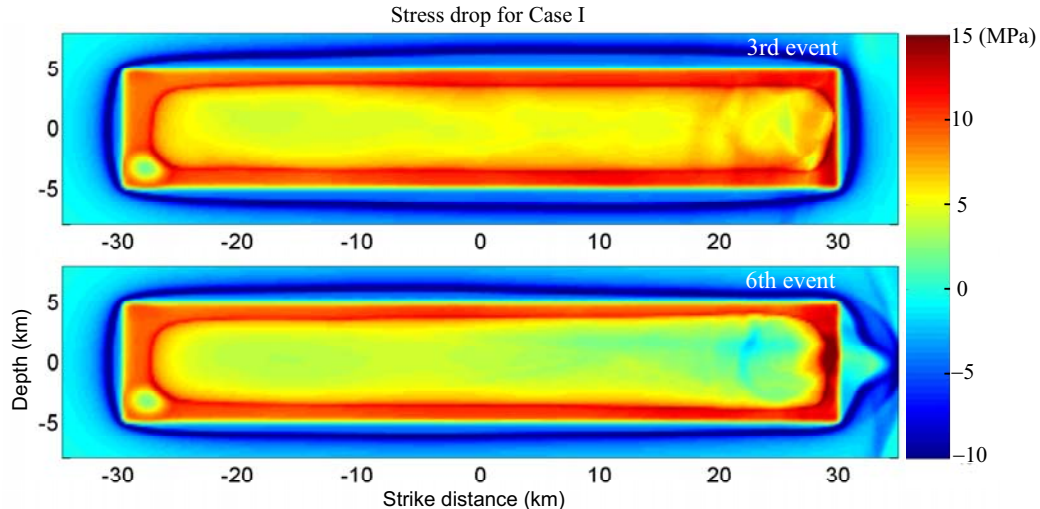


Figure 5.21: Distribution of stress drop  $\Delta\tau = \tau_i - \tau_e$  for the third and sixth events of Case I. The distribution is heterogeneous due to the presence of rheological boundaries.

(Figure 5.22).

#### 5.5.4 Effect of weaker patches on earthquake sequences

From earthquake sequences in Cases IIh1 and IIh2, we find that the weaker patches have two main effects on fault slip. They lead to more irregular earthquake sequences than the fault would have produced without the patches. They also promote intersonic transition on the fault and determine transition distance  $L_{\text{tran}}$ .

The first effect is demonstrated in Figures 5.11, 5.14, and 5.20. Figures 5.11 and 5.14 illustrate earthquake sequences and show that Case II of a homogeneous seismogenic region exhibits period behavior, while Case IIh1 with a weaker patch has a more complex earthquake sequences. Figure 5.20 shows average seismic ratio  $\bar{S}$  and average initial shear stress  $\bar{\tau}_i$  for Cases II, IIh1, and IIh2. If we exclude the first event in Figure 5.20, which has artificially assigned initial conditions,  $\bar{S}$  in subsequent events varies in a smaller range in Case II than in Cases IIh1 and IIh2. The average shear stress before dynamic events has similar behavior.

The weaker patch also induces transition to intersonic speeds (Section 5.4) and determines transition distance. We take the third event of Case IIh1 as an example. The transition distance in

that event is  $L_{\text{tran}} = 22$  km (we define  $L_{\text{tran}}$  as the horizontal distance between the center of the nucleation zone and the center of the patch). For a comparison, we compute intersonic transition distances of a homogenous fault. Let us consider a linear slip-weakening fault with uniform  $\tau_i$ ,  $\tau_p$ ,  $\tau_d$ , and  $d_0$  that are equal to the average values of Case III1. In the 2D model, the transition distance  $L_{\text{tran}}^{\text{sw},2\text{D}}$  can be approximately expressed as (Andrews, 1976; Xia et al., 2004):

$$L_{\text{tran}}^{\text{sw},2\text{D}} = \frac{9.2}{(S_{\text{crit},2\text{D}} - S)^3} L^c, \quad (5.27)$$

where  $S_{\text{crit},2\text{D}} = 1.77$ , and  $L^c$  is the half-length of quasi-static critical crack, given by:

$$L^c = \frac{1}{\pi(1-\nu)} \frac{\mu(\tau_p - \tau_d)d_0}{(\tau_i - \tau_d)^2}. \quad (5.28)$$

Therefore we have

$$L_{\text{tran}}^{\text{sw},2\text{D}} = 48 \text{ km}. \quad (5.29)$$

The intersonic transition distance  $L_{\text{tran}}^{\text{sw},3\text{D}}$  in the 3D unbounded fault model is larger than  $L_{\text{tran}}^{\text{sw},2\text{D}}$  in 2D. Interpolating from Figure 5 of Dunham (2006), we get

$$L_{\text{tran}}^{\text{sw},3\text{D}} \approx 2L_{\text{tran}}^{\text{sw},2\text{D}} = 96 \text{ km}. \quad (5.30)$$

$L_{\text{tran}} = 22$  km of Case III1 is about four times smaller than  $L_{\text{tran}}^{\text{sw},3\text{D}} \approx 96$  km for the 3D homogenous fault. Hence the presence of weaker patch can considerably shorten transition distance.

### 5.5.5 Effect of rupture speed on slip distribution

In our simulations, intersonic and subsonic events lead to different distributions of slip during dynamic rupture. We take the third (intersonic) and sixth (subsonic) events of Case I as examples. We define the final slip  $\delta_e(x, z)$  due to an event as the difference of slip between the starting time

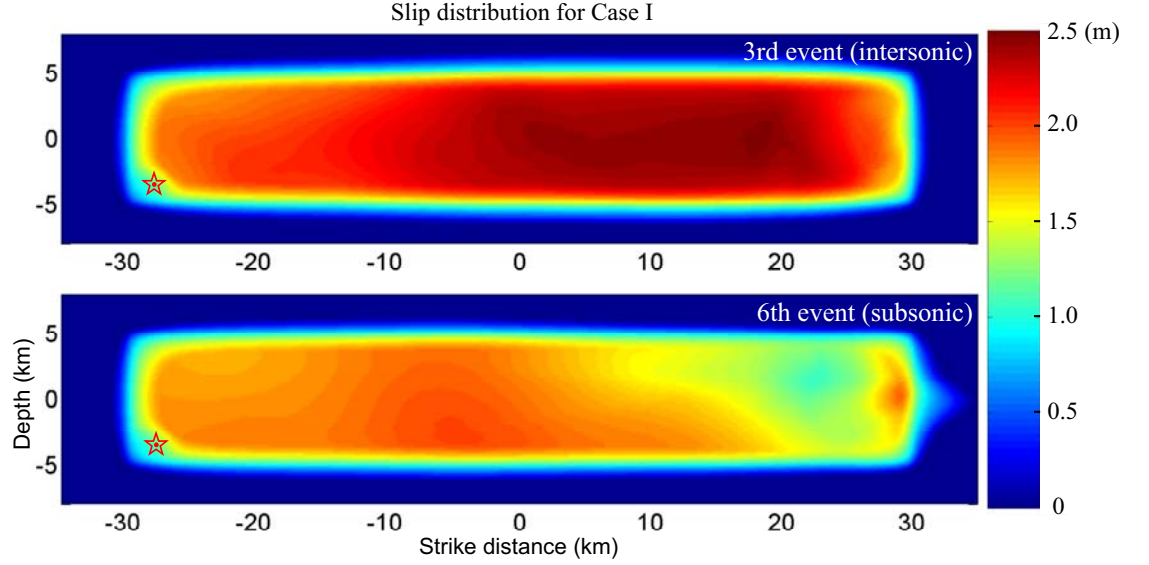


Figure 5.22: Distribution of final slip  $\delta_e(x, z)$  on the fault due to the third (intersonic) and sixth (subsonic) events for Case I. In each panel, the red star indicates the event hypocenter.

and the ending time of the event. The average slip over depth  $\bar{\delta}_e(x)$  is then:

$$\bar{\delta}_e(x) = \frac{1}{W_{\text{seis}}} \int_{-W_{\text{seis}}/2}^{W_{\text{seis}}/2} \delta_e(x, z) dz, \quad (5.31)$$

and the overall average slip in the velocity-weakening region  $\bar{\delta}_e$  is:

$$\bar{\delta}_e = \frac{1}{L_{\text{seis}}} \int_{-L_{\text{seis}}/2}^{L_{\text{seis}}/2} \bar{\delta}_e(x) dx. \quad (5.32)$$

Figure 5.22 shows the distribution of slip during the third and sixth events. The red stars indicate the event hypocenters. In both events, slip near the hypocenter is smaller compared with most of the seismogenic region. This is because earthquakes nucleate at the corner of the seismogenic region, where stress concentration is maximum, and the rheological boundaries restrict the slip growth at the hypocenter during dynamic event. Overall, the intersonic event has larger slip than the subsonic event.  $\bar{\delta}_e$  is 2.06 m in the third event, which is 26% larger than  $\bar{\delta}_e$  (= 1.63 m) in the sixth event. Note that the average stress drop  $\overline{\Delta\tau}$  in the third event is only 18% larger than the sixth event. Figures 5.7(a) and (b) show the rupture speed  $c^*(x)$  and average slip over depth  $\bar{\delta}_e(x)$  for the two

events. Larger  $c^*(x)$  usually corresponds to larger  $\bar{\delta}_e(x)$ . In Figure 5.7,  $c^*(x)$  and  $\bar{\delta}_e(x)$  are positively correlated.

### 5.5.6 On friction behavior during dynamic rupture

Rate and state friction laws were developed from laboratory rock experiments for slip velocity from  $10^{-8}$  m/s to  $10^{-3}$  m/s (e.g., Dieterich, 1979; Ruina, 1983; Blanpied et al., 1991, 1995; Marone, 1998). During dynamic rupture, many additional weakening mechanisms, e.g., flash heating, thermal pressurization of pore fluids (Rice, 2006, and references therein), may be activated and may dominate the constitutive response of the fault. In this chapter, we use rate and state friction as a proxy for linear slip-weakening friction during dynamic rupture, which has been widely used in the study of intersonic transition (e.g., Andrews, 1976; Day, 1982a,b; Fukuyama and Olsen, 2002; Dunham, 2006). Rate and state friction in its aging formulation is a unique tool that adequately represents rock behavior during interseismic periods and earthquake nucleation, allowing us to simulate long-term fault slip, while turning into approximately linear slip-weakening behavior during dynamic rupture, allowing us to represent the dynamic events as realistically as most single-rupture simulations currently do. A future step would be to study intersonic transition with a more physical friction law, e.g., a combined friction law that incorporates rate and state friction at slow slip velocities and laws motivated by thermal-weakening mechanisms at high slip velocities. We hypothesize that more physical friction laws would yield results that are qualitatively similar, as the results are due to the presence of rheological boundaries and favorable heterogeneities, and not to a particular feature of the friction law used.

## 5.6 Conclusion

We study intersonic transition and propagation of dynamic ruptures in the context of earthquake sequences and aseismic slip in a 3D fault model. The model of a planar strike-slip fault governed by rate-and-state friction contains a potentially seismogenic velocity-weakening region surrounded by velocity-strengthening regions.

We find that the rheological boundary between the velocity-weakening and velocity-strengthening regions promotes intersonic transition. The interseismic slip disparity between a velocity-strengthening region and velocity-weakening region causes stress concentration. Once earthquake rupture nucleates, it propagates faster over these areas of higher prestress than over the rest of the seismogenic region, transitioning to intersonic speeds in some cases. Since the presence of such rheological boundaries on natural faults can be inferred from laboratory studies and fault observations, this factor may significantly contribute to intersonic transition on natural faults. The occurrence of intersonic transition in our 3D model depends on friction properties and fault stress that develops in the model before large earthquakes and can be explained by the distribution of the average seismic ratio on the fault before large events. In a broader context, the rheological transition boundary can be considered as a favorable heterogeneity of higher initial shear stress naturally arising from earthquake cycles.

We also find that intersonic transition in 3D models of long-term slip can be further promoted by favorable compact fault heterogeneity, as suggested by the 2D single-event study of Chapter 4. Our simulations show that adding a fault patch of lower effective peak frictional resistance can qualitatively modify the behavior of the simulated fault, resulting in occasional intersonic earthquakes in a model that has no intersonic events without the patch. The intersonic transition distance is determined by the location of the heterogeneity. Secondary crack initiated in the heterogeneity is driven to intersonic speeds by the intersonic loading stress field of the main rupture. This study shows that the intersonic transition mechanism due to favorable heterogeneity described in Chapter 4 is qualitatively valid in the fault model with long-term history of seismic and aseismic slip.

We emphasize that the phenomenon of intersonic transition due to rheological boundaries could not be established in prior studies, as it can only be observed in simulations that include all the of the following factors: First, the numerical methodology needs to be fully-dynamic and include inertial effects to enable intersonic transition in simulations. Second, the fault model needs to be 3D in order to include the rheological boundary in the direction of rupture propagation. Third, the methodology should be able to simulate long-term slip history of faults to establish stress distribution on the fault before large events. So far, earthquake cycles modeling has shown that rheological boundaries

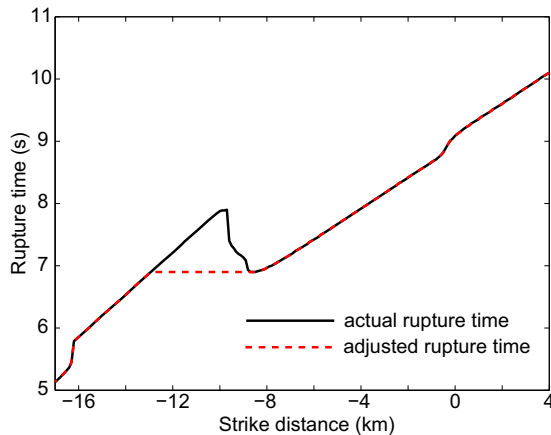


Figure 5.23: Rupture time along the line  $z = -4$  km in the third event of Case III1. The black solid line is the original rupture time  $t_r$ , and the red dashed line is the adjusted rupture time  $t_r^*$ , used to compute horizontal rupture speed.

promote earthquake nucleation (Lapusta et al., 2000), clustering of small earthquakes (Lapusta and Rice, 2003), and intersonic transition and propagation (this work). Further studies of the effect of rheological boundaries would enhance our understanding of rupture dynamics on natural faults.

## 5.7 Appendix: calculation of horizontal rupture speed $c(x, z)$

A straightforward way of computing horizontal rupture speed at a fault location  $(x, z)$  is to calculate the average rupture speed in a horizontal interval  $[x - N\Delta x, x + N\Delta x]$ , where  $\Delta x$  is the discretized cell size and  $N$  is an integer defining the width of the interval. Then we have

$$c^{(1)}(x, z) = \frac{x + N\Delta x - (x - N\Delta x)}{t_r(x + N\Delta x, z) - t_r(x - N\Delta x, z)}. \quad (5.33)$$

The drawback of the above formula is that it does not account for the possibility of a rupture front jump. The black solid line in Figure 5.23 is the rupture time along strike at depth  $z = 4$  km in the third event of Case III1. When the main rupture arrives at  $x = -13$  km (at the time of about 7 seconds), a secondary crack initiates at the location of  $x = -9$  km. The rupture front instantaneously jumps from the location of  $x = -13$  km to  $x = -9$  km, and the rupture speed of

the region between  $x \approx -13$  km to  $x \approx -9$  should not be defined, or have a special value such as infinity which can be interpreted as a jump. However, equation (5.33) yields finite values (which can be negative) of the horizontal rupture speed in the above region.

To remedy the drawback of equation (5.33), we first computed the adjusted rupture time  $t_r^*(x, z)$  at every point  $(x, z)$ .

1. At every depth  $z$ , we set the adjusted rupture time at  $x = L_{\text{seis}}/2$  (the right edge of the seismogenic region) to be equal to its actual rupture time:

$$t_r^*(x = L_{\text{seis}}/2, z) = t_r(x = L_{\text{seis}}/2, z). \quad (5.34)$$

2. Starting from  $x = L_{\text{seis}}/2 - \Delta x$ , we move towards  $x = -L_{\text{seis}}/2$ , setting:

$$t_r^*(x, z) = \min \{t_r(x, z), t_r^*(x + \Delta x, z)\}. \quad (5.35)$$

After the procedure (5.34–5.35), the adjusted rupture time  $t_r^*(x, z)$  is a monotonously non-decreasing function of the horizontal coordinate  $x$ . The red dashed line in Figure 5.23 shows the adjusted rupture time  $t_r^*(x, z)$  along  $z = 4$  km.  $t_r^*(x, z)$  is equal to  $t(x, z)$  in the region where no rupture front jumps over, and  $t_r^*(x, z)$  is set to the time of the rupture jump in the region of a jump.

3. Then we compute horizontal rupture speed  $c(x, z)$  as:

$$c(x, z) = +\infty, \quad \text{if } t_r^*(x, z) = t_r^*(x + \Delta x, z) = t_r^*(x - \Delta x, z) \quad (5.36)$$

else

$$c(x, z) = \frac{x + i_{\text{max}}\Delta x - (x + i_{\text{min}}\Delta x)}{t_r^*(x + i_{\text{max}}\Delta x, z) - t_r^*(x + i_{\text{min}}\Delta x, z)}, \quad \text{otherwise.} \quad (5.37)$$

In equation (5.37),  $i_{\text{max}}$  is the maximum value of index  $i$  ( $i \leq N$ ) satisfying:

$$t_r^*(x + j\Delta x, z) > t_r^*(x + (j - 1)\Delta x, z), \quad \forall 1 \leq j \leq i; \quad (5.38)$$

and  $i_{\min}$  is the minimum value of index  $i$  ( $i \geq -N$ ) satisfying:

$$t_r^*(x + j\Delta x, z) < t_r^*(x + (j + 1)\Delta x, z), \forall i \leq j \leq -1. \quad (5.39)$$

The above procedure ensures that rupture speed is computed as the average rupture speed in a horizontal spatial interval of  $2N\Delta x$  for most regions; and that it is set to be infinity in the region where rupture front jumps occur. In all simulations, we use  $N = 10$  and  $\Delta x = 0.1$  km.

## Chapter 6

# Conclusions and future work

We have developed three-dimensional (3D) boundary-integral methodology for simulating long-term history of spontaneous seismic and aseismic slip on a planar rate-and-state fault subjected to slow tectonic loading. Our approach is the first one to combine long-term deformation histories and the resulting stress redistribution on faults with full inclusion of inertial effects during simulated earthquakes in the context of 3D models. It reproduces all stages of earthquake cycles, from accelerating slip before dynamic instability, to rapid inertially driven propagation of earthquake rupture, to post-seismic slip, and to interseismic creep, including aseismic transients. Such problems are highly nonlinear and lack analytic solutions. The accuracy of our solutions to 3D dynamic rupture propagation problems is verified by comparison with a finite difference method that was developed for simulations of single dynamic events. Solutions to test problems converge through grid reduction and are consistent between the two methods, validating both numerical approaches and providing useful data for testing future numerical methods.

The developed methodology is applied to evaluation of simplified quasi-dynamic approaches, to investigation of rupture interaction with compact fault heterogeneity, and to intersonic rupture transition. We find that the 3D quasi-dynamic approaches not only result in much slower slip and rupture velocities, as was already established in 2D models, but also produce different long-term slip patterns. Our study of a fault model with a stronger patch shows that interaction of dynamic rupture with the heterogeneity in the first dynamic event and subsequent events is quite different, due to redistribution of fault stress by slip. This illustrates the importance of considering long-term

slip histories even if one is interested only in the behavior of dynamic ruptures.

The main application of the developed computational tools is the study of intersonic transition and propagation of dynamic rupture. Inter-sonic ruptures have been inferred from seismic observations and recorded in the lab. They have the potential to cause strong ground motion farther from the fault than subsonic ruptures. Using 2D in-plane simulations of single rupture events, we demonstrate that transition to intersonic speeds may be dominated by favorable fault heterogeneities. This qualitative finding is confirmed by considering intersonic transition and propagation in the developed 3D models over long-term deformation histories. We discover that rheological boundaries, the presence of which on faults has ample laboratory and observational evidence, act as favorable heterogeneity, concentrating stress and promoting intersonic transition. Compact fault heterogeneity in the form of weaker patches further promotes intersonic transition in 3D models.

The results of this thesis demonstrate that 3D simulations of long-term fault slip that fully account for inertial effects can uncover phenomena that cannot be discovered with simpler models. In 2D models, the fault is simplified to a line which limits the nature of heterogeneous fields that can be assumed. Simulations of one instance of dynamic rupture strongly depend on the chosen initial conditions and do not allow the model to evolve towards behavior consistent with the model geometry, friction, and other parameters. Quasi-dynamic formulations lead to modified rupture properties and cannot reproduce wave-induced phenomena such as intersonic transition.

The study also demonstrates the importance of incorporating fault heterogeneities into earthquake models. A small stronger patch alters slow slip and nucleation, resulting in a different earthquake pattern on the fault. A simple combination of rectangular velocity-weakening and velocity-strengthening fault regions creates areas of stress concentrations due to interseismic slip and promotes faster rupture speeds. Finally, a favorable fault region of higher prestress or lower strength promotes intersonic transition. Hence it is important to understand which distributions of friction and other parameters are realistic for natural faults.

The next step in improving the developed methodology would be to include dynamic weakening mechanisms. Rate and state friction laws were derived from laboratory rock experiments for low

slip velocity (e.g., [Dieterich, 1979](#); [Ruina, 1983](#); [Blanpied et al., 1991, 1995](#); [Marone, 1998](#)). During dynamic rupture, thermal weakening mechanisms, such as thermal pressurization of pore fluid and flash heating ([Rice, 2006](#), and references therein), may be activated, and they are likely to dominate fault response. In the future, it is important to extend the rate and state formulation to include these and other weakening processes at high slip rates. This is a nontrivial task, as the existing small-scale descriptions of several weakening mechanisms involve lengthscales and timescales that are intractable in 3D models of long-term slip.

The developed approach can be used to study a number of fault slip phenomena, such as postseismic slip, earthquake nucleation in heterogeneous regions, and slip response of faults with complex patterns of velocity-weakening and velocity-strengthening properties. Recent improvements in availability and quality of seismic and geodetic data have revealed complex interactions of seismic and aseismic slip, with more heterogeneous fault coupling than previously believed, slow earthquakes, and aseismic transients that are often accompanied by seismic tremor. We can use the developed simulation methodology to interpret this rich information through forward modeling, with the goal of determining constitutive behavior and properties of natural faults.

As an example, consider the results obtained in the work by [Chen and Lapusta \(2008\)](#) which used the developed methodology to study small repeating earthquakes. Since their recurrence times range from a fraction of a year to several years and their locations are known, small repeating earthquakes are an excellent observation target. They are used to study an increasingly richer array of problems, from fault creeping velocities and postseismic slip to earthquake interaction and stress drops. An intriguing observation about repeating earthquakes is their scaling of recurrence time with seismic moment which is significantly different from the scaling based on a simple conceptual model of circular ruptures with stress drop independent of seismic moment and no aseismic slip. [Chen and Lapusta \(2008\)](#) simulated long-term slip on a small velocity-weakening fault patch surrounded by a much larger velocity-strengthening region. They found that the patch produces not only earthquakes but also aseismic slip, and the proportion of seismic and aseismic slip varies with the patch radius and hence with the earthquake size. The model reproduces the observed scaling of the seismic moment

with the recurrence time and results in source parameters comparable with inversions. The simple conceptual model cannot match the observed scaling because it does not account for the aseismic slip on the patch. This is yet another example of the importance of simulating aseismic slip, even if one is only interested in earthquakes.

# Bibliography

- Aagaard, B., and T. Heaton (2008), Constraining fault constitutive behavior with slip heterogeneity. *J. Geophys. Res.*, *113*, B04301, doi:10.1029/2006JB004793.
- Adams, G.G. (1995), Self-excited oscillations of two elastic half-spaces sliding with a constant coefficient of friction. *J. Appl. Mech.*, *62*, 867–872.
- Adams, G.G. (2001), An intersonic slip pulse at a frictional interface between dissimilar materials. *J. Appl. Mech.*, *68*, (1), 81–86.
- Andrews, D.J. (1976), Rupture velocity of plane strain shear cracks. *J. Geophys. Res.*, *81*, 5679–5687.
- Andrews, D.J. (1985), Dynamic plane-strain shear rupture with a slip-weakening friction law calculated by a boundary integral method. *Bull. Seismol. Soc. Am.*, *75*, (1), 1–21.
- Andrews, D.J. (2004), Rupture models with dynamically-determined breakdown displacement. *Bull. Seismol. Soc. Am.*, *94*, 769–775.
- Andrews, D.J. (2005), Rupture dynamics with energy loss outside the slip zone. *J. Geophys. Res.*, *110*, B01307.
- Antipov, Y.A., and J.R. Willis (2003), Transient loading of a rapidly advancing Mode-II crack in a viscoelastic medium. *Mech. Mater.*, *35*, 415–431.
- Aochi, H., E. Fukuyama, and M. Matsu'ura (2000), Selectivity of spontaneous rupture propagation on a branched fault. *Geophys. Res. Lett.*, *27*, 3635–3638.
- Archuleta, R.J. (1984), A fault model for the 1979 Imperial Valley Earthquake. *J. Geophys. Res.*, *89*, 4559–4585.

- Arthur, F. (2004), Rupture process of the M 7.9 Denali fault, Alaska, earthquake: subevents, directivity, and scaling of high-frequency ground motions. *Bull. Seismol. Soc. Am.*, *94* (6B), 234–255.
- Bayart, E., A.M. Rubin, and C. Marone (2006), Evolution of fault friction following large velocity jumps, *AGU Fall Meeting*, S31A0180B.
- Beeler, N.M., T.E. Tullis, and J.D. Weeks (1994), The roles of time and displacement in the evolution effect in rock friction, *Geophys. Res. Lett.*, *21*, 1987–1990.
- Ben-Zion, Y., and J.R. Rice (1995), Slip patterns and earthquake populations along different classes of faults in elastic solids, *J. Geophys. Res.*, *100*, 12959–12983.
- Ben-Zion, Y., and J.R. Rice (1997), Dynamic simulations of slip on a smooth fault in an elastic solid, *J. Geophys. Res.*, *102*, 17771–17784.
- Ben-Zion, Y. (2001), Dynamic ruptures in recent models of earthquake faults. *J. Mech. Phys. Solids*, *49*, 2209–2244.
- Bernard, P., and D. Baumont (2005), Shear Mach wave characterization for kinematic fault rupture models with constant supershear rupture velocity. *Geophys. J. Int.*, *162*, (2), 431–447.
- Bhat, H.S., R. Dmowska, G.C.P. King, Y., Klinger, and J.R. Rice (2007), Off-fault damage patterns due to supershear ruptures with application to the 2001 Mw 8.1 Kokoxili (Kunlun) Tibet earthquake. *J. Geophys. Res.*, in press.
- Blanpied, M.L., D.A. Lockner, and J.D. Byerlee (1991), Fault stability inferred from granite sliding experiments at hydrothermal conditions, *J. Geophys. Res.*, *18*, 609–612.
- Blanpied, M.L., D.A. Lockner, and J.D. Byerlee (1995), Frictional slip of granite at hydrothermal conditions, *J. Geophys. Res.*, *100*, 13045–13064.
- Boatwright, J., and D.M. Boore (1982), Analysis of the ground accelerations radiated by the 1980 Livermore Valley earthquakes for directivity and dynamic source characteristics, *Bull. Seismol. Soc. Am.*, *72*, 1843–1865.

- Bouchon, M., M.P. Bouin, H. Karabulut, M.N. Toksöz, M. Dietrich, and A.J. Rosakis (2001), How fast is rupture during an earthquake? New insights from the 1999 Turkey earthquakes. *Geophys. Res. Lett.*, 28 (14), 2723–2726.
- Bouchon, M., and M. Vallée (2003), Observation of Long Supershear Rupture During the Magnitude 8.1 Kunlunshan Earthquake. *Science*, 301, 824–826.
- Bouchon, M., and H. Karabulut (2008), The aftershock signature of supershear earthquakes. *Science*, 320, 1323, DOI: 10.1126/science.1155030.
- Breitenfeld, M.S., and P.H. Geubelle (1998), Numerical analysis of dynamic debonding under 2D in-plane and 3D loading. *Intl. J. Fracture*, 13–38.
- Broberg, K.B. (1994). Intersonic bilateral slip. *Geophys. J. Int.*, 119, 706–714.
- Broberg, K.B. (1995), Intersonic mode II crack expansion. *Arch. Mech.*, 47, 859–871.
- Broberg, K.B. (1999), *Cracks and fracture*. Academic Press, San Diego.
- Burridge, R. (1973), Admissible speeds for plane-strain shear cracks with friction but lacking cohesion. *Geophys. J. Astr. Soc.*, 35, 439–455.
- Burridge, R., G. Conn, and L.B. Freund (1979), The stability of a rapid mode II shear crack with finite cohesive traction. *J. Geophys. Res.*, 85, B5, 2210–2222.
- Campillo, M., and I.R. Ionescu (1997), Initiation of antiplane shear instability under slip dependent friction. *J. Geophys. Res.*, 102, 20363–20371.
- Chen, T., and N. Lapusta (2008), Rate-and-state friction laws can explain scaling of small repeating earthquakes. *J. Geophys. Res.*, submitted.
- Cocco, M., and A. Bizzarri (2002), On the slip-weakening behavior of rate- and state dependent constitutive laws. *J. Geophys. Res.*, 29, 11, 1516, doi:10.1029/2001GL013999.
- Cochard, A., and R. Madariaga (1994), Dynamic faulting under rate-dependence friction. *J. Geophys. Res.*, 142, 419–445.

- Cochard, A., and R. Madariaga (1996), Complexity of seismicity due to highly rate dependent friction. *J. Geophys. Res.*, *101*, 25, 321–336.
- Cochard, A., and J.R. Rice (1997), A spectral method for numerical elastodynamic fracture analysis without spatial replication of the rupture event. *J. Mech. Phys. Solids*, *45*, 1393–1418.
- Cochard, A., and J.R. Rice (2000), Fault rupture between dissimilar materials: Ill-posedness, regularization, and slip-pulse response. *J. Geophys. Res.* *105*, B11, 25891–25907.
- Dalguer, L.A., K. Irikura, J.D. Riera, and H.C. Chiu (2001), The importance of the dynamic source effects on strong ground motion during the 1999 Chi-Chi, Taiwan, earthquake: Brief interpretation of the damage distribution on buildings. *Bull Seismol. Soc. Am.*, *91*, 1112–1127.
- Dalguer, L.A., K. Irikura, and J.D. Riera (2003), Simulation of tensile crack generation by three-dimensional dynamic shear rupture propagation during an earthquake. *J. Geophys. Res.*, *108*(B3), 2144, doi:10.1029/2001JB001738.
- Dalguer, L.A., K. Irikura, and J.D. Riera (2003), Generation of new cracks accompanied by the dynamic shear rupture propagation of the 2000 Tottori (Japan) earthquake. *Bull. Seismol. Soc. Am.*, *93*, 2236–2252.
- Dalguer, L.A., and S.M. Day (2004), Split nodes and fault zone models for dynamic rupture simulation. *Eos Trans. AGU*, *85*(47), *Fall Meet. Suppl.*, Abstract S41A–0944.
- Das, S., and K. Aki (1977), Fault planes with barriers: A versatile earthquake model. *J. Geophys. Res.*, *82*, 5648–5670.
- Das, S. (1980), A numerical method for determination of source time functions for general three-dimensional rupture propagation. *Geophys. J. R. Astr. Soc.*, *62*, 591–604.
- Das, S., and B.V. Kostrov (1988), An investigation of the complexity of the earthquake source time function using dynamic faulting models. *J. Geophys. Res.*, *93*, 8035–8050.
- Day, S.M. (1982), Three-dimensional finite difference simulations of fault dynamics: Rectangular faults with fixed rupture velocity. *Bull. Seismol. Soc. Am.*, *72*, 705–727.

- Day, S.M. (1982), Three-dimensional simulations of spontaneous rupture: The effect of nonuniform prestress. *Bull. Seismol. Soc. Am.*, *72*, 1881–1902.
- Day, S.M., L.A. Dalgner, N. Lapusta, and Y. Liu (2005), Comparison of finite difference and boundary integral solutions to three-dimensional spontaneous rupture. *J. Geophys. Res.*, *110*, B12307, doi:10.1029/2005JB003813.
- Dieterich, J.H. (1979), Modelling of rock friction, 1. Experimental results and constitutive equations. *J. Geophys. Res.*, *84*, 2161–2168.
- Dieterich, J.H. (1981), Constitutive properties of faults with simulated gouge, in *Mech. Behavior Crustal Rocks*, edited by N.L. Carter et al., *Geophys. Monogr. Ser.*, *24*, 103–120. AGU, Washington, D.C.
- Dieterich, J.H. (1992), Earthquake nucleation on faults with rate- and state-dependent strength. *Tectonophysics*, *211*, 115–134.
- Dieterich, J.H. (1994), A constitutive law for rate of earthquake production and its application to earthquake clustering. *J. Geophys. Res.*, *99*, 2601–2618.
- Dieterich, J.H. (2007), Application of rate- and state-dependent friction to models of fault slip and earthquake occurrence. *Treatise on Geophysics*, *4*, 107–129.
- Dor, O., Y. Ben-Zion, T.K. Rockwell, and J. Brune (2005), Geological signal for preferred rupture direction: updated observations from large strike-slip faults in Southern CA. *Seismol. Res. Lett.* *76* (2), 252–253.
- Dor, O., T.K. Rockwell, and Y. Ben-Zion (2006), Geologic observations of damage asymmetry in the structure of the San Jacinto, San Andreas and Punchbowl faults in southern California: A possible indicator for preferred rupture propagation direction. *Pure Appl. Geophys.*, *163*, 301–349, doi:10.1007/s00024-005-0023-9.
- Duan, B., and D. Oglesby (2005), The dynamics of thrust and normal faults over multiple earthquake cycles: effects of dipping fault geometry. *Bull. Seismo. Soc. Am.*, *95*, 5, 1623–1636.

- Dunham, M., P. Favreau, and J.M. Carlson (2003), A supershear transition mechanism for cracks, *Science*, *299*, 1557–1559.
- Dunham, M., and R.J. Archuleta (2004), Evidence for a supershear transition during the 2002 Denali fault earthquake. *Bull. Seismol. Soc. Am.*, *94*, 256–268.
- Dunham, M., and R.J. Archuleta (2005), Near-source ground motion from steady state dynamic rupture pulses. *J. Geophys. Res.*, *32*, L03302.
- Dunham, M. (2006), Conditions governing the occurrence of supershear ruptures under slip-weakening friction. *J. Geophys. Res.*, submitted.
- Ellsworth, W.L., F. Waldhauser, and A. Cole (2000), A new view of the San Andreas Fault: implications for earthquake interaction at Parkfield (extended abstract), *International School of Geophysics*, Erice-Sicily.
- Ellsworth, W.L., M. Celebi, J.R. Evans, E.G. Jensen, R. Kayen, M.C Metz, D.J. Nyman, J.W. Roddick, P. Spudich, and C.D. Stephens (2004), Near-field ground motion of the 2002 Denali fault, Alaska, earthquake recorded at Pump Station 10. *Earthquake spectra*, *20* (3), 597–615.
- Festa, G., and J.P. Vilotte (2006), Influence of the rupture initiation on the intersonic transition: Crack-like versus pulse-like modes. *Geophys. Res. Lett.*, *33* (15), L15320.
- Freund, L.B. (1979), The mechanics of dynamic shear crack propagation. *J. Geophys. Res.*, *84*, 2199–2209.
- Freund, L.B. (1990), *Dynamic fracture mechanics*. Cambridge University Press. New York.
- Fukuyama, E., and K.B. Olsen (2002), A condition for supershear rupture propagation in a heterogeneous stress field. *Pure. Appl. Geophys.*, *157*, 2047–2056.
- Gao, H., Y. Huang, and F.A. Abraham (2001), Continuum and atomistic studies of intersonic crack propagation. *J. Mech. Phys. Solids*, *49*, 2113–2132.

- Geubelle, P.H., and D.V. Kubair (2001), Intersonic crack propagation in homogeneous media under shear-dominated loading: numerical analysis. *J. Mech. Phys. Solids*, *49* (3), 571–587.
- Geubelle, P., and J.R. Rice (1995), A spectral method for 3D elastodynamic fracture problems, *J. Mech. Phys. Solids*, *43*, 1791–1824.
- Harris, R.A., and S.M. Day (1997), Effects of a low-velocity zone on a dynamic rupture. *Bull. Seismol. Soc. Am.*, *87*, (5), 1267–1280.
- Harris, R.A., et al. (2004), The source physics of large earthquakes: Validating spontaneous rupture methods. *Eos Trans. AGU*, *85* (47), *Fall Meet. Suppl.*, Abstract S12A-05.
- Harris, R.A., M. Barall, R. Archuleta, E. Dunham, B. Aagaard, J.-P. Ampuero, D.J. Andrews, H. Bhat, V. Cruz-Atienza, L. Dalguer, S. Day, B. Duan, G. Ely, Y. Kaneko, Y. Kase, N. Lapusta, Y. Liu, S. Ma, D. Oglesby, K. Olsen, A. Pitarka, S. Song, and E. Templeton (2008), The SCEC/USGS dynamic earthquake-rupture code verification exercise. *Seismol. Res. Lett.*, submitted.
- Heaton, T.H. (1990), Evidence for and implications of self-healing pulses of slip in earthquake rupture. *Phys. Earth Planet. Inter.*, *64*, 1–20.
- Hillers, G., Y. Ben-Zion, and P.M.Mai (2006), Seismicity on a fault controlled by rate- and state-dependent friction with spatial variations of the critical slip distance. *J. Geophys. Res.*, *111*(B0), 1403, doi:10.1029/2005JB003859.
- Hori, T., N. Kato, K. Hirahara, T. Bada, and Y. Kaneda (2004), A numerical simulation of earthquake cycles along the Nankai trough, southwest Japan: Lateral variation in frictional property due to slab geometry controls the nucleation position. *Earth. Planet. Sci. Lett.*, *228*, 215–226.
- Huang, Y., and H. Gao (2001), Intersonic crack propagation - Part I: The fundamental solution. *J. Appl. Mech.*, *68* (2), 169–175.
- Hsu, Y.J., M. Simons, J.P. Avouac, J. Galetzka, K. Sieh, M. Chlieh, D. Natawidjaja, L. Prawirodirdjo, and Y. Bock (2006), Frictional afterslip following the 2005 Nias-Simeulue earthquake, Sumatra. *Science*, *312*, 5782, DOI: 10.1126/science.1126960.

- Ida, Y. (1972), Cohesive force across the tip of a longitudinal-shear crack and Griffith's specific surface energy. *J. Geophys. Res.*, *77*, 3796–3805.
- Kame, N., and T. Yamashita (1999), Simulation of the spontaneous growth of a dynamic crack without constraints on the crack tip path. *Geophys. J. Int.*, *139*, 345–358.
- Kanamori, H. (2004), The diversity of physics of earthquakes. *Proc. Jpn. Acad., Ser., B*, *80*, 297–316.
- Kaneko, Y., and N. Lapusta, (2008), Variability of earthquake nucleation in continuum models of rate-and-state faults and implications for aftershock rates. *J. Geophys. Res.*, submitted.
- Kato, N. and T.E. Tullis (2003), Numerical Simulation of Seismic Cycles with a composite rate- and state-dependent friction law. *Bull. Seismo. Soc. Am.*, *93*, *2*, 841–853.
- Kato, N. (2004), Interaction of slip on asperities: Numerical simulation of seismic cycles on a two-dimensional planar fault with nonuniform frictional property. *J. Geophys. Res.*, *109*, B12306, doi:10.1029/2004JB003001.
- Kawasaki, I. (2004), Silent earthquakes occurring in a stable-unstable transition zone and implications for earthquake prediction. *Earth Plant. Space*, *56*, 813–821.
- Lachenbruch, A.H. (1980), Frictional heating, fluid pressure and the resistance to fault motion. *J. Geophys. Res.*, *85*, 6097–6112.
- Lapusta, N., J.R. Rice, Y. Ben-Zion and G. Zheng (2000), Elastodynamic analysis for slow tectonic loading with spontaneous rupture episodes on faults with rate- and state-dependent friction. *J. Geophys. Res.*, *105*, 23765–23789.
- Lapusta, N., and J.R. Rice (2003), Nucleation and early seismic propagation of small and large events in a crustal earthquake model. *J. Geophys. Res.*, *108*(B4), 2205, doi:10.1029/2001JB000793.
- Lapusta, N., and Y. Liu (2006), Three-dimensional elastodynamic simulations of seismic and aseismic slip history of a planar strike-slip fault. *Eos Trans. AGU*, *87* (52), *Fall Meet. Suppl.*, Abstract S34A-07.

- Lapusta, N., and Y. Liu (2008), 3D boundary-integral modeling of spontaneous earthquake sequences and aseismic slip. *J. Geophys. Res.*, submitted.
- Liu, Y., and N. Lapusta (2008), Transition of mode II cracks from sub-Rayleigh to inter-sonic speeds in the presence of favorable heterogeneity. *J. Mech. Phys. Solids*, *56*, 25–50, doi:10.1016/j.jmps.2007.06.005.
- Liu, Y., and J.R. Rice (2005), Aseismic slip transients emerge spontaneously in three-dimensional rate and state modeling of subduction earthquake sequences. *J. Geophys. Res.*, *110*, B08307, doi:10.1029/2004JB003424.
- Lu, X., N. Lapusta, and A.J. Rosakis (2006), Constraining friction laws by experimental observations and numerical simulations of various rupture modes. *Eos Trans. AGU*, *87*(52), *Fall Meet. Suppl.*, Abstract S33C-04.
- Lyons, S., and D. Sandwell (2002), Fault creep along the southern San Andreas from interferometric synthetic aperture radar, permanent scatterers, and stacking source. *J. Geophys. Res.*, *108*, 2047.
- Madariaga, R., K.B. Olsen, and R.J. Archuleta (1998), Modeling dynamic rupture in a 3-D earthquake fault model. *Bull. Seismol. Soc. Am.*, *88*, 1182–1197.
- Madariaga, R., and K.B. Olsen (2000), Criticality of rupture dynamics in 3D. *Pure. Appl. Geophys.*, *157*, 1981–2001.
- Marone, C.J., C.H. Scholz, and R. Bilham (1991), On the mechanics of earthquake afterslip. *J. Geophys. Res.*, *96*, 8441–8452.
- Marone, C. (1998), Laboratory-derived friction laws and their application to seismic faulting. *Ann. Rev. Earth Planetary Sci.*, *26*, 642–696.
- Mase, C.W., and L. Smith (1985), Pore-fluid pressures and frictional heating on a fault surface. *Pure Appl. Geophys.*, *122*, 583–607.
- Mase, C.W., and L. Smith (1987), Effects of frictional heating on the thermal, hydrologic, and mechanical response of a fault. *J. Geophys. Res.*, *92*, 6249–6272.

- Olsen, K.B., R. Madariaga, and R.J. Archuleta (1997), Three-dimensional dynamic simulation of the 1992 Landers earthquake. *Science*, *278*, 834–838.
- Needleman, A., and A.J. Rosakis (1999), The effect of bond strength and loading rate on the conditions governing the attainment of intersonic crack growth along interfaces. *J. Mech. Phys. Solids*, *47*, 2411–2449.
- Nielsen, S.B., J.M. Carlson, and K.B. Olsen (2000), Influence of friction and fault geometry on earthquake rupture. *J. Geophys. Res.*, *105*, 6069–6088.
- Palmer, A.C., and J.R. Rice (1973), The growth of slip surfaces in the progressive failure of over-consolidated clay slopes. *Proc. R. Soc. London Ser.*, *332*, 527–548.
- Perrin, G., J.R. Rice, and G. Zheng (1995), Self-healing slip pulse on a frictional surface. *J. Mech. Phys. Solids*, *43*, 1461–1495.
- Ranjith, K., and J.R. Rice (2001), Slip dynamics at an interface between dissimilar materials. *J. Mech. Phys. Solids*, *49* (2), 341–361.
- Reilinger, R.E., S. Ergintav, R. Burgmann, S. McClusky, O. Lenk, A. Barka, O. Gurkan, L. Hearn, K.L. Feigl, R. Cakmak, B. Aktug, H. Ozener, and M.N. Toksoz (2000), Coseismic and Postseismic Fault Slip for the 17 August 1999,  $M = 7.5$ , Izmit, Turkey Earthquake. *Science*, *289*, 5484, 1519–1524.
- Rice, J.R. (1980), The mechanics of earthquake rupture, in *Physics of the Earth's Interior*. Proc. Int. Sch. Phys. Enrico. Fermi, Course 78, edited by A.M. Dziewonski and E. Boschi, 555–649. Elsevier, New York.
- Rice, J.R., and A.L. Ruina (1983), Stability of steady frictional slipping. *J. Appl. Mech.*, *50*, 343–349.
- Rice, J.R. (1968), A path independent integral and the approximate analysis of strain concentration by notches and cracks. *J. Appl. Mech.*, *35*, 379–386.
- Rice, J.R. (1993), Spatio-temporal complexity of slip on a fault. *J. Geophys. Res.*, *98*, 9885–9907.

- Rice, J.R., and Y. Ben-Zion (1996), Slip complexity in earthquake fault models. *Proc. Natl. Acad. Sci. U.S.A.*, *93*, 3811–3818.
- Rice, J.R. (2006), Heating and weakening of faults during earthquake slip. *J. Geophys. Res.*, *111*, B05311, doi:10.1029/2005JB004006.
- Rice, J.R., and Cocco, M., (2007). Seismic fault rheology and earthquake dynamics, in *The Dynamics of Fault Zones*, edited by M. R. Handy, Dahlem Workshop (Berlin, January 2005) Report 95. The MIT Press, Cambridge, MA.
- Rosakis, A.J., O. Samudrada, and D. Coker (1999), Cracks faster than the shear wave speed. *Science*, *284*, 1337–1340.
- Rosakis, A.J. (2002), Intersonic shear cracks and fault ruptures. *Adv. Phys.*, *51* (4), 1189–1257.
- Rubin, A.M, and J.P. Ampuero (2005), Earthquake nucleation on (aging) rate and state faults. *J. Geophys. Res.*, *110* (B1), 1312, doi:10.1029/2005JB003686.
- Rubin, A.M. (2008), Episodic slow slip events and rate-and-state friction. *J. Geophys. Res.*, submitted.
- Ruina, A.L. (1983), Slip instabilities and state variable friction laws. *J. Geophys. Res.*, *88*, 10359–10370.
- Samudrala, O., Y. Huang, and A.J. Rosakis (2002), Subsonic and intersonic shear rupture of weak planes with a velocity weakening cohesive zone. *J. Geophys. Res.*, *107*, B8, 2170.
- Schaff, D.P., G.H.R. Bokelmann, G.C. Beroza, F. Waldhauser, and W.L. Ellsworth (2002), High-resolution image of Calaveras Fault seismicity. *J. Geophys. Res.*, *107* (B9), 2186, doi:10.1029/2001JB000633.
- Segall, P., and A. Rubin (2007), Dilatancy stabilization of frictional sliding as a mechanism for slow slip events. *Eos Trans. AGU*, *88* (52), Abstract T13F-08.

- Shearer, P., E. Hauksson, and G.Q. Lin (2005), Southern california hypocenter relocation with waveform cross-correlation, part 2: Results using source-specific station terms and cluster analysis. *Bull. Seismol. Soc. Am.*, *95* (3), 904–915.
- Shi, Z.Q., and Y. Ben-Zion (2006), Dynamic rupture on a bi-material interface governed by slip-weakening friction. *Geophys. J. Int.*, *165*, 469–484.
- Shi, Z.Q., Y. Ben-Zion, and A. Needleman (2007), Property of dynamic rupture and energy partition in a solid with a frictional interface. *J. Mech. Phys. Solids*, submitted.
- Shibazaki, B., and M. Matsu'ura (1992), Spontaneous processes for nucleation, dynamic propagation, and stop of earthquake rupture. *Geophys. Res. Lett.*, *19*, 1189–1192.
- Shibazaki, B., and T. Shimamoto (2007), Modelling of short-interval silent slip events in deeper subduction interfaces considering the frictional properties at the unstable transition regime. *Geophys. J. Int.*, *171*, 191–205.
- Somerville, P.G., N.F. Smith, R.W. Graves, and N.A. Abrahamson (1997), Modification of empirical strong ground motion attenuation relations to include the amplitude and duration effects of rupture directivity. *Seismol. Res. Lett.*, *68*, 199–222.
- Spudich, P., and E. Cranswick (1984), Direct observation of rupture propagation during the 1979 Imperial Valley earthquake using a short baseline accelerometer array. *Bull. Seismol. Soc. Am.*, *74* (6), 2083–2114.
- Suppe, J., and L. Yue (2007), Pore-fluid pressures and crustal strength. *Eos Trans. AGU*, *88* (52), *Fall Meet. Suppl.*, Abstract T41F-01.
- Templeton, E.L., and J.R. Rice (2006), Extent and distribution of off-fault plasticity during seismic rupture including bimaterial effects. *Eos Trans. AGU*, *87* (52), *Fall Meet. Suppl.*, Abstract S34A-01.
- Tse, S.T., and J.R. Rice (1986), Crustal earthquake instability in relation to the depth variation of frictional slip properties. *J. Geophys. Res.*, *91*, 9452–9472.

- Uenishi, K., and J.R. Rice. (2003), Universal nucleation length for slip-weakening rupture instability under nonuniform fault loading. *J. Geophys. Res.*, *108*, B1, 2042.
- Waldhauser, F., W.L. Ellsworth, D.P. Schaff, and A. Cole (2004), Streaks, multiplets, and holes: High-resolution spatio-temporal behavior of Parkfield seismicity. *Geophys. Res. Lett.*, *31*, L18608, doi:10.1029/2004GL020649.
- Weertman, J. (1980), Unstable slippage across a fault that separates elastic media of different elastic constants, *J. Geophys. Res.*, *85*, 1455–1461.
- Xia, K., A.J. Rosakis, and H. Kanamori (2004), Laboratory earthquakes: the sub-rayleigh-to-supershear rupture transition. *Science*, *303*, 1859–1861.
- Xia, K., A.J. Rosakis, H. Kanamori, and J.R. Rice (2005), Laboratory earthquakes along inhomogeneous faults: directionality and supershear. *Science*, *308*, 681–684.
- Zhang, H.M, and X.F. Chen (2006a), Dynamic rupture on a planar fault in three-dimensional half-space—I. Theory. *Geophys. J. Int.*, *164*, 633–652.
- Zhang, H.M, and X.F. Chen (2006b), Dynamic rupture on a planar fault in three-dimensional half-space—II. Validations and numerical experiments. *Geophys. J. Int.*, *167*, 917–932.
- Zheng, G., and J.R. Rice (1998), Conditions under which velocity-weakening friction allows a self-healing versus a crack-like mode of rupture. *Bull. Seismol. Soc. Am.*, *88*, 1466–1483.
- Ziv, A., and A. Cochard (2006), Quasi-dynamic modeling of seismicity on a fault with depth-variable rate- and state-dependent friction. *J. Geophys. Res.*, *111*, B08310, doi: 10.1029/2005JB004189.